

Innovative incorporation of pearl and calcium phosphate composite in bone regenerative scaffolds



Zhiyi Li

**This dissertation is submitted for the degree of
Doctor of Philosophy**

May 2024

School of Engineering

Declaration

This thesis has not been submitted in support of an application for another degree at this or any other university. It is the result of my own work and includes nothing that is the outcome of work done in collaboration except where specifically indicated. Many of the ideas in this thesis were the product of discussion with my supervisor Dr Ihtesham ur Rehman and Dr Timothy Douglas.

If others have worked on this research too, an explanation of their contribution goes here.

Excerpts of this thesis have been published in the following conference manuscripts and academic publications.

Presentation of work in:

- 32nd Conference on Biomaterials in Medicine and Veterinary Medicine. (October 12-15, Poland), presentation
- Engineering Postgraduate Research Conference. (July 2020, July 2022, Lancaster University), presentation

Zhiyi Li

Lancaster University, UK

Abstract

Bone regeneration by tissue engineering has extensively employed hydroxyapatite (HA) for bone regeneration due to its positive biological properties. However, the high crystallinity of commercial HA results in a slower biodegradation rate. This study explored the incorporation of pearl powder with calcium phosphate. Two successful synthesis methods yielded pearl/CaP composite particles with different crystallinity, confirmed through XRD patterns.

Physiochemical evaluations, including TGA, FTIR, Raman spectroscopy, XRD, XPS, and SEM, provided a comprehensive understanding of structural aspects, revealing chemical bonding between pearl and HA particles. FTIR-PAS results confirmed the presence of both A and B types of carbonated HA. Integration of these particles with chitosan (CS) through freeze-drying produced composite scaffolds with enhanced compressive strength and improved cytocompatibility compared to HA-based CS scaffolds. In vitro cell culture analyses demonstrated a higher proliferation ratio for p/CaP composite scaffolds, especially a 30:70 pearl to CaP ratio. SEM analysis corroborated the positive crosslinking and osteogenesis performance of these scaffolds, emphasizing their potential in bone tissue engineering. However, scaffolds with a high pearl: CaP ratio (50:50) and elevated p/CaP concentrations (50 wt.%) exhibited poor or non-osteogenic behaviour, underscoring the importance of carefully balanced pearl: CaP ratios and p/CaP concentrations for effective osteogenesis.

Acknowledgements

I would like to thank my supervisors, Prof. Ihtesham ur Rehman and Dr Timothy Douglas, for accepting me as part of their research group, their support, guidance, and encouragement throughout my PhD. They allowed me to have freedom in work, but always providing me his guidance and support. I would also like to thank Dr Rebecca Shepherd, Dr Jemma Kerns, Dr John Hardy, and everyone in the School of Engineering, Biomedical and Life Sciences at the Lancaster University, who contributed in one way or the other towards my research.

I am grateful to all members of the research group who helped me with my experiments and presentations. Specially to Dr Abdullah Talari for his company in the lab and his constant support and help throughout my research project. Also, Daniel Baines, the PhD candidate who gave me huge help and support for the research and the experience to the conference.

My deepest appreciation goes to my dad, my mother, my grandmother, for their understanding, patience, and support during the long term I spent away from them.

Additionally, my gratitude goes to Lancaster University Graduate College for funding me with a travel grant for conference and presentation of my work.

My final thank you goes to Ihtesham, Timothy, and Rebecca again, without whom none of this would have been possible. I am grateful for their unfailing support all through my PhD.

Contents

1 INTRODUCTION.....	1
1.1 Introduction	1
1.2 Background	1
1.3 Project Aim	5
1.4 Hypothesis.....	5
1.5 Objectives.....	5
1.6 Thesis Outline and Chapter Summary	7
2 LITERATURE REVIEW	8
2.1 Introduction	8
2.2 Bone.....	9
2.2.1 Bone classification	9
2.2.2 The structure of bone.....	11
2.2.3 The remodelling process of bone	12
2.2.4 Bone diseases.....	14
2.2.5 Biomaterials applications for bone regeneration.....	17
2.3 Hydroxyapatite	19
2.3.1 Structure of nano and macro HA.....	20
2.3.2 Carbonated hydroxyapatite.....	22
2.3.3 Methodologies for HA synthesis	25
2.3.4 HA and HA based applications in bone regeneration.....	31
2.4 Pearl.....	31
2.4.1 Inorganic components of pearl	35
2.4.2 Organic components of pearl.....	36
2.4.3 Pearls in bone regeneration.....	38
2.5 Bioactive scaffolds.....	40
2.5.1 Chitosan (CS) scaffolds.....	40
2.5.2 Properties of chitosan.....	42
2.5.3 Molecular weight (MW).....	43
2.5.4 Degree of deacetylation (DD).....	44
2.5.5 Processing of chitosan	45
2.6 Characterization techniques.....	47
2.6.1 Chemical characterization	47
2.6.2 Physical characterization	52
2.6.3 Mechanical characterization	56
2.6.4 Biological characterization	59
3 MATERIALS AND METHODOLOGIES.....	67
3.1 Introduction	67
3.2 Hydroxyapatite and pearl/calcium phosphate composite	67
3.2.1 Synthesis of HA	68
3.2.2 Chemical precipitation of HA.....	68
3.2.3 Sol-gel synthesis of hydroxyapatite.....	70
3.2.4 Hydrothermal method synthesis of hydroxyapatite.....	71
3.3 Synthesis of pearl/calcium phosphate (p/CaP) composite.....	73
3.4 Scaffold fabrication	73

3.4.1 Freeze drying fabrication method	75
3.5 Physical characterization	76
3.5.1 TGA.....	76
3.5.2 SEM	77
3.5.3 Porosity estimation.....	77
3.5.4 BET.....	78
3.6 Chemical characterization	79
3.6.1 FTIR spectroscopy	79
3.6.2 Raman spectroscopy	80
3.6.3 X-ray diffraction (XRD) spectroscopy.....	81
3.6.4 X-ray Photoelectron Spectroscopy (XPS)	81
3.7 Compressive strength characterization.....	82
3.8 Biological characterization.....	83
3.8.1 Cultured cells.....	84
3.8.2 In-vitro degradation tests.....	86
3.8.3 3-Dimensional cell culture.....	87
3.8.4 Cell viability (AlamarBlue® assay).....	88
4 PHYSICAL AND CHEMICAL STUDIES OF SYNTHESIZED POWDERS AND COMPOSITE SCAFFOLDS	91
4.1 Introduction	91
4.2 Physical study of powder and scaffold samples.....	93
4.2.1 TGA results and discussion of powders samples	93
4.2.2 SEM analysis of powders and scaffold samples.....	99
4.2.3 Porosity estimation.....	110
4.3 Chemical study of powder and scaffold samples.....	112
4.3.1 FTIR spectroscopy analysis	112
4.3.2 Raman spectroscopy analysis of powder samples	123
4.3.3 XRD spectroscopy analysis of powder samples	127
4.3.4 XPS analysis of powder samples.....	131
4.4 Mechanical studies of composite scaffolds.....	133
4.5 Discussions	138
5 BIOLOGICAL STUDIES OF COMPOSITE SCAFFOLDS.....	144
5.1 Introduction	144
5.2 In-vitro degradation tests.....	145
5.2.1 Preparation of test samples and degradation media	147
5.2.2 pH analysis	148
5.2.3 Weight analysis	148
5.2.4 Results and discussion	149
5.3 Cell viability-AlamarBlue® (AB) assay.....	153
5.3.1 AB assay results and discussion	154
5.3.2 Cell proliferation/migration observation by SEM	161
5.4 Discussion	163
6 CONCLUSIONS AND FUTURE WORKS	166
6.1 Introduction	166
6.2 Conclusions	166
6.3 Future work	169

7 BIBLIOGRAPHY 171

List of Tables

Table 2.1 Characteristic, functions, and examples for different classifications of bones.	10
Table 2.2 Physical and chemical properties of hydroxyapatite.	21
Table 2.3 Various pearl/nacre biomedical applications in recent years.	39
Table 2.4 Key mechanical properties of human bone, HA, and pearl.	57
Table 2.5 Critical mechanical properties of a compact human bone.	58
Table 4.2.1 Details of porous chitosan scaffold composite samples prepared in this study. Pearl: CaP ratios are in equivalence of the mass ratio of pearl to CaP weight percentages (wt.%), which are related to the weight of chitosan.	100
Table 4.2.2 Diameters of pores from the SEM images of all scaffolds.	109
Table 4.2.3 Densities and porosities of all sample scaffolds.	110
Table 4.3.4 Typical FTIR peaks of pearl.	114
Table 4.3.5 Characteristic FTIR peaks of stoichiometric HA.	115
Table 4.4.1 Elastic modulus of all CS and CS composite scaffolds.	136
Table 5.1 One factor linear regression study of the 14-day AB assay fluorescent intensity changes for cell proliferation on different samples.	158

List of Figures

Fig 2.1 General structure of a long bone in 5 parts: Epiphysis (Top and bottom), metaphysis (between epiphysis and diaphysis), and diaphysis (WikiJornal of Medicine, 2014).12

Fig 2.2 Overview of bone remodelling process with 4 process and cells included: Lining cells, Osteoclasts, Osteoblasts, Hematopoietic stem cells, Osteoblastic stromal cells, Mesenchymal stem cells, and Omensteoblast precursor (Proff et al., 2009).13

Fig 2.3 Major milestones of biomaterials application in timeline (modified, Koons et al., 2020).17

Fig 2.4 The flowchart diagram for HA synthesis using emulsion technique (Bose et al., 2003). Reprinted (adapted) with permission from {Bose, S. and Saha, S.K., 2003. Synthesis and characterization of hydroxyapatite nanopowders by emulsion technique. Chemistry of materials, 15(23), pp.4464-4469}. Copyright {2024} American Chemical Society.28

Figure 2.5 Schematic of the bivalve molluscan shell anatomy nacre structure (Sun and Bhushan, 2012).32

Fig. 2.6 “Brick and Mortar” structure of the pearl nacre layer: mainly consists of aragonite crystals and connected by protein layers between crystal layers. The upper scheme is the modified diagram for demonstration of the structure, and the bottom images are the SEM scans of lacklustre pearls (Parker et al., 2010; Qiao et al., 2007). Reprinted (adapted) with permission from { Qiao, L., Feng, Q.L. and Li, Z., 2007. Special vaterite found in freshwater lackluster pearls. Crystal growth & design, 7(2), pp.275-279. }. Copyright {2024} American Chemical Society.34

Fig. 2.7 Crystal structure of Aragonite (L, Face-centred orthorhombic system) and Vaterite (R, hexagonal crystal system).	36
Fig. 2.8 Structure and formation of taurine. A: The chemical structure of taurine (NH ₂ (CH ₂) ₂ SO ₂ OH). B: This diagram generally displays the main steps of the formation of taurine in the body. The enzyme cysteine dioxygenase (CDO) catalyses the conversion of L-cysteine to cysteine sulfinic acid, and the oxidation of hypotaurine (2-aminoethane sulfinate) results in taurine (modified) (Marcinkiewicz et al., 2014).	37
Figure 2.9 Chemical structure of a disaccharide segment of chitosan taken from the study by Kumar et al.(2004). Reprinted (adapted) with permission from { Kumar, M.R., Muzzarelli, R., Muzzarelli, C., Sashiwa, H. and Domb, A.J., 2004. Chitosan chemistry and pharmaceutical perspectives. Chemical reviews, 104(12), pp.6017-6084.}. Copyright {2024} American Chemical Society.	42
Fig. 2.10 Hydroxyl and carbonate bands of the carbonated (a) and hydroxyapatite (b) powders (Rehman et al., 1997).	48
Figure 2.11 The energy level and different scattering phenomenon inside a Raman spectroscopy.	50
Figure 3.1 HA synthesis reaction set-up: A white HA solution formed during the reaction, which took place by the constant stirring of reagents in a round-bottom two-necked reactor placed in a silicone oil bath at 75 °C on a stirring heating plate. A glass condenser with water flow in the outer layer provides refluxing NH ₃ ·H ₂ O and water, which was fitted on top neck of the reactor a dropping funnel for feeding reagent solution ((NH ₄) ₂ HPO ₄ solution), and a thermometer to monitor the temperature.	69
Figure 3.2 The flow chart of one-pump hydrothermal synthesis system (3.2a and 3.2c), and the helical stainless steel scaffold design (3.2b). The whole system used a peristaltic pump that can continuously drag both Ca ²⁺ and PO ₄ ²⁻ solutions into the heating oven with a constant speed. The helical scaffold with	

small holes inside the oven helped to increase the heat exchange area, in which the mixed solution flow through the reaction tubes, so that CaP/HA particles were generated along the reaction flow tube.72

Figure 3.3 Image of the setup of compression testing of a composite porous scaffold specimen placed onto a lower compression plate in the Instron® UTM instrument (Instron® 3345, Norwood, MA, USA).83

Fig 4.2.1 Thermal gravimetric analysis (TGA) data curves displaying the mass loss of hydroxyapatite (HA), pearl and pearl/CaP (p/CaP) composite powders. HA is in black line; pearl is in blue line and p/CaP is in red line.94

Fig. 4.2.2 TGA data curves demonstrating the weight loss versus temperature, including the 1st derivative of weight for the HA sample. (a) weight loss and derivative of weight against temperature. (b) 1st derivative of weight against temperature curve. (c) weight loss versus temperature curve. (d) DTA and weight loss against temperature curve.95

Fig. 4.2.3 TGA data curves demonstrating the weight loss versus temperature, including the 1st derivative of weight for the pearl sample. (a) weight loss and derivative of weight against temperature. (b) 1st derivative of weight against temperature curve. (c) weight loss versus temperature curve. (d) DTA and weight loss against temperature curve.97

Fig. 4.2.4 TGA data curves demonstrating the weight loss versus temperature, including the 1st derivative of weight for the p/CaP composite sample. (a) weight loss and derivative of weight against temperature. (b) 1st derivative of weight against temperature curve. (c) weight loss versus temperature curve. (d) DTA and weight loss against temperature curve.98

Fig. 4.2.5 SEM microstructure images of pearl powder samples with increasing magnifications. Magnifications increased from a. to d. by x5,000, x10,000, and x20,000, respectively. Scale bars at the bottom of images represent at a. is 10 μm and at b. to d. are 1 μm.101

Fig. 4.2.6 SEM microstructure images of synthesized HA samples and commercial HA samples with the same x20,000 magnification. **(a)** HA samples synthesized by hydrothermal methodology, **(b)** HA samples obtained from the sol-gel technique, **(c)** HA samples synthesized with the precipitation method, and **(d)** the HA commercial samples.102

Fig. 4.2.7 SEM microstructure images of p/CaP samples with increasing magnifications, newly formed crystals would be noticed attached to the pearl platelets. Magnifications increased from **a.** to **f.** by x2,000, x5,000, x10,000, and x20,000, respectively. Scale bars at the bottom of images represent at **a.** is 10 μm and at **b.** to **f.** are 1 μm103

Fig. 4.2.8 SEM microstructure images of the bottom surface of freeze-dried scaffolds at the same magnification: **(a)** pure chitosan scaffold (CS) **(b)** 10 wt.% pearl/chitosan composite scaffold **(c)** 10 wt.% HA/chitosan composite scaffold 10 wt.% **(d)** 10 wt.% 10pearl/90HA/chitosan scaffold **(e)** 10 wt.% 30pearl/70HA/chitosan scaffold **(f)** 10 wt.% 50pearl/50HA/chitosan scaffold. All images were captured at the x50 magnification and the scale bar at the bottom represented 100 μm105

Fig. 4.2.9 SEM microstructure images of the top surface of freeze-dried scaffolds at the same magnification: **(a)** pure chitosan scaffold (CS) **(b)** 10 wt.% pearl/chitosan composite scaffold **(c)** 10 wt.% HA/chitosan composite scaffold 10 wt.% **(d)** 10 wt.% 10pearl/90CaP_chitosan scaffold **(e)** 10 wt.% 30pearl/70CaP_chitosan scaffold **(f)** 10 wt.% 50pearl/50CaP_chitosan scaffold. Fig; other images were captured at the x300 magnification and the scale bar at the bottom represented 10 μm106

Fig. 4.2.10 SEM microstructure images of the top surface of freeze-dried scaffolds at different magnifications: **(a & b)** 30 wt.% HA/chitosan scaffold under x3,000 and x10,000 times magnifications, **(c & d)** 30 wt.% pearl/chitosan composite scaffold under x3,000 and x10,000 times magnifications, **(e & f)** 30 wt.% 30pearl/70CaP_chitosan scaffold under x3,000 and x10,000 times magnifications.107

Fig. 4.2.11 SEM microstructure images of the top surface of freeze-dried scaffolds at the same magnification: **(a & b)** 10 wt.% 30pearl/70CaP_chitosan scaffold under x70 and x1,000 times magnifications, **(c & d)** 30 wt.% 30pearl/70CaP_chitosan scaffold under x70 and x1,000 times magnifications, **(e & f)** 50 wt.% 30pearl/70CaP_chitosan scaffold under x70 and x1,000 times magnifications.108

Fig. 4.3.1 FTIR spectra of pearl, commercial HA and synthesized HA powders by three different methods (including chemical precipitation, sol-gel technique and hydrothermal method) attached with the typical peaks information.113

Fig. 4.3.2 FTIR-PAS spectra of commercial HA and synthesized HA powders by three different methods (including chemical precipitation, sol-gel technique, and hydrothermal method).115

Fig. 4.3.3. FTIR-PAS spectra of pearl, commercial HA and synthesized p/CaP composite powders by three different methods (including chemical precipitation, sol-gel technique and hydrothermal method) attached with the typical peaks information.117

Fig. 4.3.4 The stacked ATR spectra of sole CS, 50wt.% pearl/CS and 50wt.% HA/CS with the peak assignments of chemical functional groups.118

Fig. 4.3.5 The overlay and stack ATR spectra of 10, 30, 50 wt.% P1CaP9_CS, P3CaP7_CS and P5CaP5_CS. The overlay spectra are presented in **a.** with peak assignments of functional groups and **b.** with 3D stack spectra.120

Fig. 4.3.6 The comparison of ATR spectra for composite p/CaP CS scaffolds in different composition. Including **a.** 10, 30 and 50 wt.% P1CaP9_CS scaffolds; **b.** 10, 30 and 50 wt.% P3CaP7_CS scaffolds and **c.** 10, 30 and 50 wt.% P5CaP5_CS scaffolds.121

Fig. 4.3.7 The comparison of ATR spectra for composite CS scaffolds in different composition analysed from top and bottom surface. Including **a.** 50 wt.% pearl/CS scaffolds; **b.** 30 wt.% HA/CS scaffolds, **c.** 50 wt.% P3CaP7_CS scaffolds and **d.** 50 wt.% P5CaP5_CS scaffolds.123

Fig. 4.3.8 The comparison of Raman spectra for multi particle samples, including pearl platelets, commercial HA powder, sol-gel synthesized HA, precipitation synthesized HA and hydrothermal synthesized HA.	124
Fig. 4.3.9 Detailed peak fitting analysis of the sol-gel synthesized HA by Origin software between 1000 and 2000 cm^{-1} region.	126
Fig. 4.3.10 Detailed peak fitting analysis of the synthesized p/CaP composite particles by Origin software.	127
Fig. 4.3.11 X-Ray diffraction spectra of dried commercial pearl powders and the standard aragonite PDF card XRD (ICDD No. 01-071-2392) intensity pattern.	128
Fig. 4.3.12 X-Ray diffraction spectra of dried commercial and three different synthesized HA powders compared to the standard aragonite PDF card XRD (ICDD No. 01-074-0566) intensity pattern.	129
Fig. 4.3.13 The comparison XRD patterns of dried three different synthesized p/CaP powders compared to the spectra of commercial HA and pearl.	130
Figure 4.3.14 Representative XPS peaks of synthesized HA and the commercial pearl sample, with information of element positions and relative molar ratio (At%).	131
Figure 4.3.15 XPS survey spectra for synthesized pearl/CaP composite samples (3:7 and 4:6). Spectra showed that Ca, P, O and C were present in the samples.	132
Figure 4.3.16 XPS high-resolution results for C 1s and O 1s spectra of p/CaP 3:7 and 4:6 composite samples.	133
Figure 4.4.1 The compression test pictures of the sample specimens and the overall stress-strain curve of all samples plot with 4 times mean values up to 70% strain.	134

Figure 4.4.2 The compression test pictures of the sample specimens and the overall stress-strain curve of all samples plot with 4 times mean values up to 10% strain. This region is related to the elastic modulus region.135

Figure 4.4.3 The compression stress-strain curves performed to 70% strain in different scaffold samples. These scaffolds were obtained from the freeze-drying method in different compositions: **a.** the sole CS, **b.** pearl/CS composite (10, 30, 50 wt.%), **c.** HA/CS composite (10, 30, 50 wt.%), **d.** P1CaP9/CS (10, 30, 50 wt.%) **e.** P3CaP7/CS (10, 30, 50 wt.%), **f.** P5CaP5/CS (10, 30, 50 wt.%).137

Figure 5.2.1 The pH alteration of supernatant media taken at different time intervals of up to 28 days in the *in-vitro* degradation tests of different composite scaffolds in **a.** PBS and **b.** L-PBS. The involved scaffold specimens are CS, pearl_CS group (P1, P3 and P5), HA_CS group (H1, H3 and H5), pearl/CaP_CS group (P1CaP9_10/30/50, P3 CaP7_10/30/50 and P5 CaP5_10/30/50).151

Figure 5.2.2 The comparative results of *in-vitro* degradation weight analyses at different time intervals of dry weight remaining ratios up to 28 days in the *in-vitro* degradation tests of composite scaffolds in **a.** PBS and **b.** L-PBS (5 mg/mL) solution. The involved scaffold specimens are CS, pearl_CS group (P1, P3 and P5), HA_CS group (H1, H3 and H5), pearl/CaP_CS group (P1CaP9_10/30/50, P3CaP7_10/30/50 and P5CaP5_10/30/50).152

Figure 5.3.1 The cell proliferation and cytocompatibility analyzed by the AB assay up to 14 days of cultures. 6 groups of samples were tested including the sole CS, the pearl_CS group, the HA_CS group, pearl/CaP(10:90)_CS group (P1CaP9), pearl/CaP(30:70)_CS group (P3CaP7), and pearl/CaP(50:50)_CS group (P5CaP5), compared with control group, presented in a. and b. In Fig 5.3.1 a., relative fluorescent intensities were presented alongside the testing duration; the relative fluorescent intensities were presented in groups as shown in b independently.155

Figure 5.3.2 The cell proliferation and cytocompatibility analyzed by the AB assay up to 14 days of cultures. 6 groups of samples were tested including the sole CS, the pearl_CS group, the HA_CS group, p/CaP(10:90)_CS group (P1H9),

p/CaP(30:70)_CS group (P3CaP7), and p/CaP(50:50)_CS group (P5CaP5). Additionally, all composite scaffold groups had subgroups with same concentration in gradient (10, 30 ,50 wt.%) (*, **, and *** stands for $p < 0.01$, $p < 0.001$ and $p < 0.0001$, respectively).157

Figure 5.3.3 The comparative AB assay fluorescent intensity against day changes with 3 pearl/CaP_CS scaffold sample groups, including: P1CaP9_10, 30 ,50 wt.%, P3CaP7_10, 30 ,50 wt.% and P5CaP5_10, 30, 50 wt.% (*, **, and *** stands for $p < 0.01$, $p < 0.001$ and $p < 0.0001$, respectively).159

Figure 5.3.4 The comparative AB assay fluorescent intensity against day changes with P3CaP7_10, 30 ,50 wt.% and HA group samples (*, **, and *** stands for $p < 0.01$, $p < 0.001$ and $p < 0.0001$, respectively).160

Figure 5.3.5 The comparative SEM images of various scaffolds, including the H3, P3, P1CaP9_30 and P3CaP7_30 scaffold samples (a-d), respectively; and samples with grown MG-63 cells after 14 days incubation (e-h). All images are at x300 times magnifications.162

List of Abbreviations and Acronyms

3D:	3-Dimensional
AB:	AlamarBlue®
ACM:	Acid soluble matrix
ALP:	Alkaline Phosphatase
ATR:	Attenuated Total Reflectance
BET:	Brunauer-Emmett-Teller
CAM:	Chorioallantoic Membrane
CaP:	Calcium phosphate
CHA:	Carbonated HA
CS:	Chitosan
DDA:	Degree of deacetylation
DMEM:	Dulbecco's Modified Eagles' Medium
DMSO:	Dimethyl Sulfoxide
DSC:	Differential Scanning Calorimetry
DTA:	Differential Thermal Analysis
ECM:	Extracellular matrix
ELISA:	Enzyme-Linked Immunosorbent Assay
ELP:	Elastin-Like Polypeptides
EtOH:	Ethanol
FCS:	Fetal Calf Serum
FTIR:	Fourier Transform Infrared (IR) spectroscopy
HA:	Hydroxyapatite
HAc	Acetic acid
HMDS:	Hexamethyldisilane
MTT:	3-(4,5-Dimethylthiazolyl-2)-2,5-diphenyltetrazolium bromide

Mw:	Molecular Weight
pH:	Potentiometric hydrogen ion concentration
PAS:	Photo-Acoustic-Sampling
PBS:	Phosphate Buffer Solution
PES:	Polyethersulfone
SBF:	Simulated Body Fluid
SD:	Standard Deviation
SEM:	Scanning Electron Microscopy
TCP:	Tricalcium Phosphate
TGA:	Thermal Gravimetric Analysis
UTM:	Universal Test Machine
XRD:	X-Ray Diffraction
XPS:	X-Ray Photoelectron Spectroscopy

List of Appendices

Appendix A.	BET (Brunauer, Emmett and Teller) analysis	195
-------------	--	-----

1 Introduction

1.1 Introduction

This chapter includes an overall introduction of this project, which begins with a short background about the bone tissue, the related bone diseases, current treatment, and two materials involved in this research. It gives a brief description of the theme of the project, namely an investigation of the physiochemical and biological properties of the incorporation of pearl and calcium phosphate both as composite particles, as well as when loaded on porous chitosan scaffolds. Meanwhile, hypothesis, aims and objectives were also explained in this section, giving a fast illustration of the whole project.

1.2 Background

Bone is an intricate and highly specialized variant of connective tissue that plays a crucial role in forming the body's skeletal structure. This complex system not only provides a sturdy framework that supports the body and maintains its shape, but it also facilitates movement by serving as attachment points for muscles and tendons (Dimitriou et al., 2011; Petite et al., 2000). In addition to its structural role, bone has a vital function in the storage of essential minerals and

Innovative incorporation of pearl and calcium phosphate composite in bone regenerative scaffolds serves as a reservoir, particularly for calcium and phosphate. These minerals are critical for various bodily functions, including nerve transmission, muscle contraction, and blood clotting. The bone continuously releases these minerals into the bloodstream to maintain the body's mineral balance and meet metabolic needs (Dimitriou et al., 2011).

Indeed, bone is a dynamic tissue that exhibits remarkable regenerative capabilities. It possesses a distinctive capacity for self-repair and reconstruction, which continues to a certain degree throughout a person's life. This regenerative process is vital because bone tissues can be damaged due to a variety of factors, including diseases, injuries, or congenital anomalies. The dynamic nature of bone is demonstrated by the process of bone remodelling. This process involves the removal of old or damaged bone, known as resorption, and the creation of new bone, referred to as ossification (Dahlin et al., 1988). This continuous cycle not only helps in the repair of micro-damages or fractures but also plays a key role in adapting to physical stress and maintaining mineral homeostasis. However, it is important to note that while bones have a certain degree of self-healing capacity, severe or complex fractures, cancer, tumours and injury infections usually require medical intervention for proper healing (Peppas et al., 1994; Wang et al., 2017). Additionally, conditions like osteoporosis and aging can disrupt the balance of bone remodelling, leading to decreased bone density and increased fracture risk (Melton et al., 1996).

To repair and reconstruct the injured bone tissues, the grafting techniques including autografts, allografts and xenografts, are the most widely accepted strategy applied clinically for bone diseases treatment (Wang et al., 2017). However, the limitation of this technique is also obvious; the availability and donor sources of bone grafts, possibility of chronic pain, nerve injury, cosmetic defects, infections, immune rejection response and risk of secondary fractures (Langer et al., 2004; Lanza et al., 2020). In addition, with the increasing aging population worldwide, more people are suffering from the chronic degeneration of bone tissues, which is also associated with the disorder of other connective tissues, cartilage and tendon (Melton et al., 1996; Ager et al., 2006). All these above-mentioned limitations have been presented by researchers and scientists

for bringing more advanced techniques and materials into the personalized treatments for bone diseases, including the concept of tissue engineering (Langer et al., 2004).

Tissue engineering is an interdisciplinary field that applies principles of engineering and life sciences to develop biological substitutes that restore, maintain, or improve tissue function. It involves the design and fabrication of scaffolds, often using biocompatible materials, which support the growth and differentiation of cells to regenerate damaged or diseased tissues. This field's multifaceted nature, which includes the use of diverse materials and techniques, motivates researchers to explore and understand the regeneration process from various angles. Among the multitude of materials used, natural biomaterials have provided valuable insights. They reveal the scientific characteristics of the formation structure and performance of the organic-inorganic combination in the construction process based on inorganic materials within natural biological systems, where life processes occur. This natural strategy can be realized by studying biomimetic routes to control the synthesis of inorganic solids with an organic matrix, particularly in bone tissue engineering. Carbonate minerals, which are common and significant components of sediments and sedimentary rocks, also play a role. Furthermore, these minerals partially control the chemistry of the atmosphere and oceans through their reactions with natural waters.

Among all different kinds of carbonate minerals, calcium carbonate (CaCO_3) has been known as one of the most abundant minerals on earth and has long fascinated expectations because of its important implications in biomineralization, even with relatively poor mechanical strength (Meldrum, 2003). Over the history of the Earth, the primary source of marine carbonate minerals has shifted from abiotic precipitation to biogenic sources, and the simplest and most representative biominerals are pearls and shells (Morse et al., 2007). The nacre layer, which forms the primary structure of pearls and shells, possesses a remarkable assembly structure that contributes to the exceptional toughness of pearls. The shell is a complex composite of calcium carbonate and organic (polymer) materials, essentially comprising two layers: an outer layer of

Innovative incorporation of pearl and calcium phosphate composite in bone regenerative scaffolds

prismatic calcite that often resembles chalk, and an inner, pearly layer known as mother of pearl (Murr et al., 2012). This inner layer is predominantly composed of aragonite, but frequently contains mixed crystals of calcite.

Pearls are more complex, multilayered, concentric structures mimicking mother of pearl or the part of the mussel (mollusk) anatomy called the mantle. The mantle edge secretes the organic framework which controls the formation of the calcium carbonate crystals: their nucleation, growth, polymorphic structure, and even the positioning and elongation of crystal polygons within the concentric layers, and in the surface region which defines pearl quality (Murr et al., 2012). Not only considering the value of considering pearls as gemstone, but the ancient Chinese people also managed to apply pearl powders as a medicinal ingredient in traditional Chinese medicines for over thousands of years (Pei et al., 2021). Moreover, the *in vitro* study of nacre with the human osteoblast cells in 1992 represented the first utilization of nacre and pearl in bioengineering as the biomaterial in the research (Lopez et al., 1992).

Hydroxyapatite (HA) has been widely studied as one of the most representative bioceramics since 1950 (Kattimani et al., 2016; Koutsopoulos, 2002). It has very close association with the bony apatite structure and has been widely used as artificial bone substitutes because of many positive biological properties, including biocompatibility, bioactivity, osteoconduction, osteoinduction, and osteointegration (Kattimani et al., 2016; Koutsopoulos, 2002). However, the common commercial highly crystalized structure of HA has a lower biodegradation rate compared to some ion substituted, amorphous calcium phosphate (CaP), or poorly crystalline HA in both nano-scale and micro-scale, because of relatively low osteoblast adhesion and ions releasing rate (Maxian et al., 1993). Furthermore, the direct use of HA has presented drawbacks compared to the ion-substituted or modified HA based composite in different studies (Nagano et al., 1996; Nelson et al., 2006).

In recent years, pearl powders have been widely studied as an emerging natural biomaterials which has been proved to contribute to the antioxidant, anti-inflammatory, and osteogenic activity, and even induced the formation of HA

particles (Ni et al., 2003). The incorporation of pearl and HA has not been reported yet, which leaves a gap for further investigations. Therefore, the purpose of this study is to evaluate the physiochemical and biological effects about the incorporation of pearl and HA particles employed in bioactive scaffolds

1.3 Project Aim

The aim of this project is to obtain composite particles by incorporating pearl and CaP which are capable of improving and promoting the process of osteoblasts proliferation during bone regeneration.

1.4 Hypothesis

The hypothesis is based on the fact that pearl is able to induce the growth of HA particles when immersed in the stimulated body fluid (SBF) with a certain temperature and pH (Shen, 2011). Therefore, it is assumed that the incorporation of pearl with HA particles can be achieved by the chemical solutions and the binding of two particles is not simple mechanically contacted. Additionally, the composite particles obtained in this research are assumed to have enhanced compressive strength and can achieve the purpose of promoting osteoblasts when loaded on a porous bioactive scaffold.

1.5 Objectives

1 Preparation of pearl/CaP (p/CaP) composite powders

Preparation of stable composite particles incorporating pearls with HA via the synthesis process of HA by three different strategies, which includes the chemical precipitation method, sol-gel technique, and the hydrothermal process.

2 Characterization of the physiochemical properties of the obtained composite powders

Determining the physical, chemical and morphological characteristics of the obtained composite powders by using a series of evaluation techniques, including thermal gravimetric analysis (TGA), Fourier-transform infrared spectroscopy (FTIR), Raman spectroscopy, scanning electron microscopy (SEM), X-ray diffraction (XRD), Brunauer-Emmett-Teller (BET) surface area analysis, and X-ray photoelectron spectroscopy (XPS). Optimal p/CaP powders will be chosen and used in modified scaffold compositions.

3 Production of freeze-lyophilized scaffolds

Fabrication of stable scaffolds from chitosan (CS) and pearl, HA and p/CaP composite particles using a freeze-drying technique. The incorporation of three different particles aims to facilitate measurement of the compression strength and biological properties more comparatively.

4 Characterization of the obtained scaffolds

Similar to the characterization of the composite powders, several characterization processes including FTIR-attenuated total reflection (ATR) spectroscopy, SEM, and water absorption test for studying the chemical and morphological properties of the prepared scaffolds. Scaffolds loaded with the ideal components should exhibit an interconnected porous structure with homogeneous distributed powders. The mechanical analysis of scaffolds is conducted by compressive strength that also evaluates the compressive strength enhancement by the composite powders at the level of the scaffold.

5 Evaluation of biological properties

In-vitro degradation properties in the presence and absence of an enzyme (lysozyme) in the phosphate buffer solution (PBS) is designed to be assessed up to 4 weeks by measuring the changes of weight and pH. To observe the cytocompatibility, cytotoxicity and proliferation of cells, the analysis will be performed by employing the MG-63 osteosarcoma cells with the Alamar blue

(AB) assay protocol. Additionally, SEM scanning will be conducted for morphological study after the cell culture test.

1.6 Thesis Outline and Chapter Summary

The first chapter of this thesis gives a general overview and background of the project, whilst the second chapter focusses on a coherent review of current and relevant literature pertaining to this project. Chapter 3 is the materials and methodology chapter, describing the main materials used for composite powder preparation and scaffold preparation. Likewise, this chapter contains a stepwise description of the methodology followed to prepare the scaffolds as well as detailed information regarding the characterization methods used for the evaluation of powder samples and scaffold samples.

Chapter 4 is the first results chapter and focusses on identifying the physiochemical properties of composite powder samples successfully prepared by three different strategies in different concentrations. The effect of incorporating the pearl, HA and p/CaP particles into the chitosan based porous scaffolds fabricated by the freeze-drying technique is also examined. The hypothesis was that p/CaP would reinforce the mechanical properties of porous scaffolds compared to pearl chitosan (P/CS) scaffolds and HA chitosan (HA/CS) scaffolds at the same concentration of particles.

In chapter 5, which is the final results and discussion chapter in this thesis, the focus is primarily on developing and testing the biological properties of the obtained CS composite particles in different groups, including the *in-vitro* degradation test and the AB assay. Accordingly, in the last chapter, which is the final chapter in this thesis (chapter 6), the key findings of this PhD project are summarized and possible follow up experiments are discussed that evolved from this project but could not be undertaken due to time constraints.

2 Literature review

2.1 Introduction

This chapter offers a comprehensive background to the research conducted in this study, beginning with a detailed overview of bone structure, composition, restoration ability and diseases. It provides essential information pertinent to the research objectives, including an explanation of the healing process during bone regeneration, especially using biomaterials. Following a discussion on the composition of bone and its typical healing process, the chapter delves into HA and pearl, which are the two main materials studied in this research. The comprehensive background of both materials from various perspectives explained the physiochemical properties and the applications in recent research. Afterwards, the chapter discusses the natural bioactive materials which have been applied for the preparation of porous scaffolds in the bone regeneration process. Quantification methods used to analyse obtained particles and scaffolds are also reviewed, as well as the experimental procedures similar to tests for in vitro testing of bone regenerative scaffolds.

2.2 Bone


Bone tissue, a marvel of biological engineering, is a complex and dynamic substance that forms the skeletal framework of the vertebrate body (Rho et al., 1998). Not merely an inert structural component, bone is a vital, living tissue that fulfils multiple critical functions. It provides mechanical support, enabling movement and protecting internal organs. Furthermore, it serves as a reservoir for essential minerals, including calcium and phosphorus, vital for maintaining mineral homeostasis in the body. Bone tissue is also intrinsically involved in haematopoiesis, the process of blood cell formation, occurring within the bone marrow (Clarke, 2008). Its regenerative capacity ensures that bones can adapt to the ever-changing mechanical demands placed on them and recover from injuries.

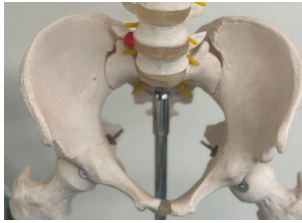
The fundamental building blocks of bone tissue are osteocytes, osteoblasts, and osteoclasts, each with unique roles. Osteoblasts are responsible for synthesizing the organic matrix, primarily composed of type I collagen, while osteocytes regulate the mineralization of this matrix. Osteoclasts, on the other hand, are involved in the breakdown of bone tissue during remodelling and repair processes. The balance between the activities of these cells, known as bone remodelling, ensures that bone remains a dynamic and adaptable tissue throughout an individual's life.

2.2.1 Bone classification

Anatomically, the initial 270 bones compose the skeletal system at the birth of a human, gradually the number decreases to 206 as a result of the fusion process when growing to adults. Based on their different functions and shapes, bone tissues are classified in 5 different classes which are flat bone, long bone, sesamoid bone, short bone, and irregular bone (table 1) (Clarke, 2008; Rho et al., 1998; Salinas et al., 2013; Steele, 1988).

Table 2.1 Characteristic, functions, and examples for different classifications of bones.

Classification of the bone	Characteristics	Functions	Examples	References
<p>Long bone</p> 	<p>Cylinder; longer with reduced width</p>	<p>Leverage</p>	<p>Femur, tibia, and ulna</p>	<p>Rho et al., 1998; Steele, 1988; Salinas et al., 2013</p>
<p>Short bone</p> 	<p>Cubical; equal length, width, and thickness</p>	<p>Balance; assist motion</p>	<p>in Carpals, tarsals</p>	<p>Rho et al., 1998; Steele, 1988; Salinas et al., 2013</p>
<p>Flat bone</p> 	<p>Thin curved and</p>	<p>Protection for internal organs</p>	<p>Ribs, sternum</p>	<p>Rho et al., 1998; Steele, 1988; Salinas et al., 2013</p>
<p>Irregular bone</p>	<p>Complicated irregular</p>	<p>Protection for internal</p>	<p>Facial bones, vertebrae</p>	<p>Rho et al., 1998; Steele, 1988; Salinas et al., 2013</p>



shapes

organs

et al., 2013

Sesamoid bone



Round
small

and Protections
for tendons

Patellae

Rho et al., 1998;
Steele, 1988; Salinas
et al., 2013

2.2.2 The structure of bone

As the rigid organ made up from both organic and inorganic components, which also known as the osseous tissue, bone has its unique functions and it is different from the other tissues in the body. Previous studies have already given an accurate and detailed description for the anatomical structure of bones (Katsimbri, 2017; Lerner, 2006; Salinas et al., 2013; Steele, 1988). For instance, a long bone is considered to be divided into three parts- epiphysis, metaphysis and diaphysis. Epiphysis situates at the end of both sides of a long bone with articular cartilage on the top, the diaphysis lies between the epiphysis, which is the main part of a long bone. Between the epiphysis and diaphysis, there is a narrow portion called metaphysis (see figure 2.1) (WikiJorunal of Medicine, 2014). The epiphysis is filled with bone marrow, in which red bone marrow is produced. In order to transfer erythrocytes, the epiphysis has a spongy structure filled with red marrow, which allows capillaries growing through (Katsimbri, 2017). Due to its unique structure, the osseous tissue is known as cancellous bone or spongy bone. Compared to the epiphysis, the diaphysis is cover by a denser outer layer, the cortical bone, which is filled with yellow marrow and medullary cavities inside (Katsimbri, 2017; Salinas et al., 2013). The metaphysis, the narrow

Innovative incorporation of pearl and calcium phosphate composite in bone regenerative scaffolds

portions in the mid of epiphysis and diaphysis, contains the cartilaginous epiphyseal plate (growth plate) that helps cartilage complete the process of chondrogenesis or osteogenesis.

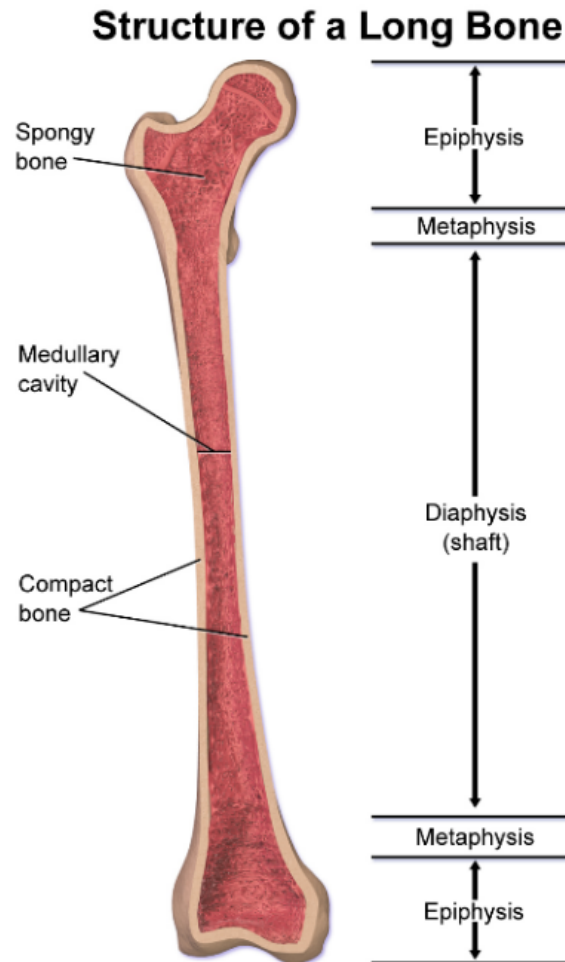


Fig 2.1 General structure of a long bone in 5 parts: Epiphysis (Top and bottom), metaphysis (between epiphysis and diaphysis), and diaphysis (WikiJournal of Medicine, 2014).

2.2.3 The remodelling process of bone

For human beings, from their birth to death, their bodies always keep undergoing the process of bone remodelling that about 10% of osseous tissue is renewed every year (Lerner, 2006). This cyclic process contains 5 stages, including activation, resorption, reversal, formation and termination (Katsimbri, 2017),

and different cells for example, osteoblast, osteoclast and osteocyte are involved in.

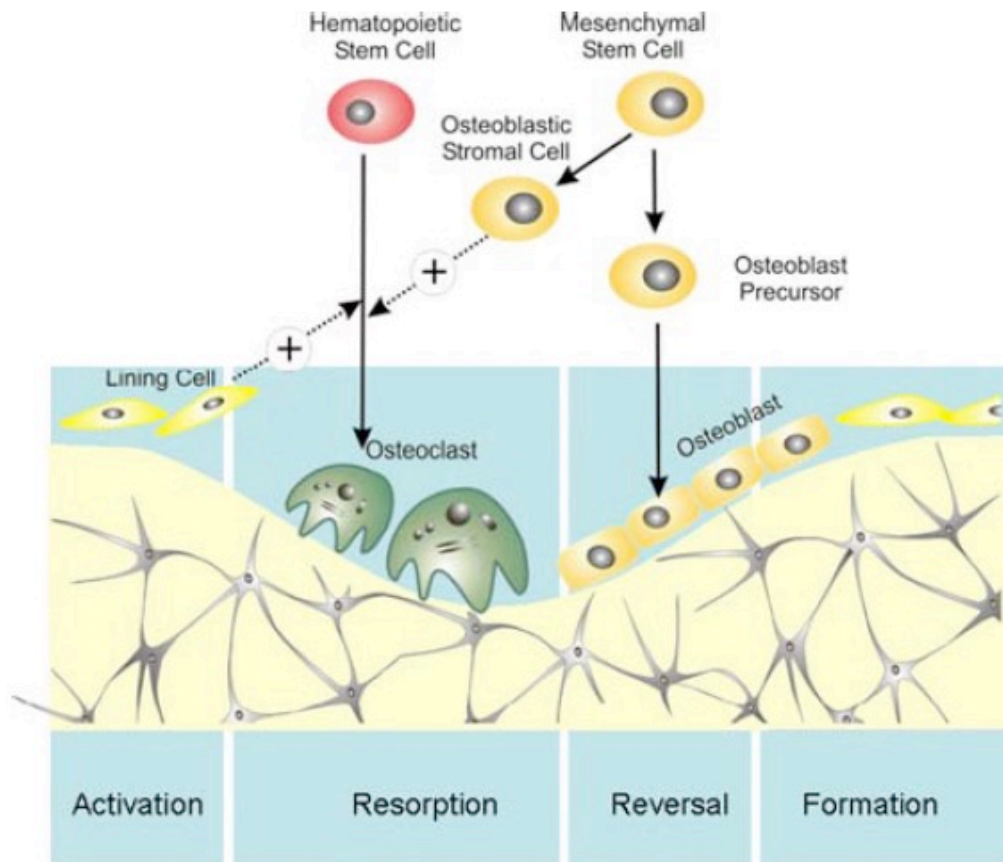


Fig 2.2 Overview of bone remodelling process with 4 process and cells included: Lining cells, Osteoclasts, Osteoblasts, Hematopoietic stem cells, Osteoblastic stromal cells, Mesenchymal stem cells, and Osteoblast precursor (Proff et al., 2009).

In bone remodelling process, three main species of cells have unreplaceable roles-osteoblasts, osteoclasts and osteocytes. As the only one originates from pluripotent mesenchymal stem cells (PMSCs), fibroblast-like osteoblasts secrete and synthesize type I collagen, which contributes as the major bone matrix protein (approximately 90%) (Katsimbri, 2017). Actively, osteoblasts are found on a bone surface in a cuboidal shape (Proff et al., 2009). With the help from microfilaments and enzymes (e.g. protein kinase), osteoblasts build a complex intracellular connection with other bone cells. Moreover, combined with calcium from extracellular fluid, osteoblasts also improve the mineralization process for fabricating HA crystals in bone remodelling process. Derived from macrophage-

monocyte cell lineage, the large multinucleated osteoclast is known as its capability of resorbing bones (Li et al., 2007).

Osteoclasts have capability to fuse existing multinucleate osteoclasts or with themselves to de novo multinucleate osteoclasts or remain as mononucleated cells to be served for further recruitment (Lerner, 2006). When osteoclasts are activated for commencing the bone resorption, they attach to the bone matrix and start to polarize, finally form podosomes and distinct membrane domains (Lerner, 2006). The ruffled border, sealing zone and the functional secretory domain consist of the membrane domains. Teitelbaum et al and Vaananen et al discovered that the ruffled border and sealing zone have great effect on the resorption process, whether one of them is disordered then the resorption is stopped (Mulari et al., 2003; Schlesinger et al., 1997). With the most number among the cell type in bone, which differentiated from osteoblasts, osteocytes have identically changed morphology compared to them. Its unique star shape helps attach to the bone matrix through the “channel” then forming the lacunar-canalicular network (Dimitriou et al., 2011; Mulari et al., 2003). The network produces signals for activating the remodelling process, as well as the metabolic signals that associated with increasing bone remodelling and decreasing bone mass (Dimitriou et al., 2011).

2.2.4 Bone related diseases

To date, it has been well established that different bone diseases are diagnosed and well categorized. In general, bone diseases are mainly caused by low bone density, poor nutrition and cancer. Commonly, bone diseases include bone spurs, chondroblastoma, bone fracture, bone defects, fibrous dysplasia, osteoarthritis and osteoporosis (Karsdal et al., 2016; Rodan et al., 2000; Westendorf et al., 2004). Clearly, the bone diseases are determined by multiple factors. Nonetheless, with the increase of ages, the self-bone regeneration process of skeletal system becomes weaker and leading to difficulties of treatments. Some typical bone diseases along with treatments are described below.

Osteoarthritis (OA). The primary symptoms of OA are joint pain and stiffness, which can be defined by joint symptoms and structural pathology. It is a muscular-skeletal disorder that initiated by micro- and macro-injury which leading to cell stress and extracellular matrix (ECM) degradation (Wieland et al., 2005). Hence, the over-adaptive repair responses are initiated and causing a series of tissue derangements which finally culminate in illness (Arden et al., 2006). From 1990s to 2017, as reported in the Osteoarthritis Research Society International (OARSI) White Paper, more than 10% of all adults aged over 60 have OA (Karsdal et al., 2016). Additionally, the economic burden of OA on patients and society has also increased with an incredible speed. The risk factors of obtaining OA are increasing which has been convinced by several studies. Obesity is considered to be the most critical factor related to OA that since 1980s till now, the number of overweight adults has more than doubled globally (over 1.9 billion adults) (Karsdal et al., 2016). The incidence of OA also can be expected because of the lack of physical activities, over/improper sports activities and other chronic diseases.

Currently OA is incurable that treatments only can provide relief the pain and improve the function of related joints. It has been reported that most patients take non-steroidal anti-inflammatory drugs (NSAIDs) as the main treatment; however, NSAIDs have significant adverse reactions followed by a number of studies (Glyn-Jones et al., 2015). Meanwhile, some of patients would rather take the joint replacement surgeries for the end-stage OA but results are not optimistic as reported.

Bone fractures. Bone fracture is the medical condition that describing the breaking of a complete bone. The main cause of bone fracture is the high force impact of stress from outside of the body. Additionally, some other factors which weaken the bone structure also results in bone fracture, which includes osteoporosis, bone cancers and osteogenesis imperfecta. Fracture healing involves a sequential set of stages to restore naturally which includes (1) hematoma formation, (2) fibrocartilaginous callus formation, (3) bony callus formation and (4) bone remodelling (Katsimbri et al., 2017; Langer et al., 2020; Proff et al., 2009). Although bone tissues undergo the regeneration process

Innovative incorporation of pearl and calcium phosphate composite in bone regenerative scaffolds continuously, with the increase of immortality and the mechanical movement, the healing process can be extended without other treatments. Clinically, according to the damage of fracture different materials and treatments were utilized for the stabilization and alignment of bones, surgeries are considered as well.

Nonetheless autografts remain the primary treatments for most bone repair procedures, the disadvantages of surgeries have promoted the development of tissue engineering and the utilization of biomaterials.

Osteoporosis. Osteoporosis, a prevalent systemic skeletal disorder, is characterized by reduced bone mineral density (BMD) and compromised bone microarchitecture (Rodan et al., 2000). It significantly elevates the risk of fragility fractures, particularly in the hip, spine, and wrist, making it a major public health concern (Karsdal et al., 2016). Osteoporosis is often considered a silent disease because it progresses without apparent symptoms until a fracture occurs. It is most common in postmenopausal women, although it can affect men and individuals of all ages. In the elderly, osteoporotic fractures are linked to high mortality rates and a substantial reduction in the quality of life. The cost of managing osteoporosis and its fractures is a considerable burden on healthcare systems worldwide.

In clinical practice, the assessment and management of osteoporosis primarily revolve around fracture risk evaluation and the prevention of fragility fractures. Dual-energy X-ray absorptiometry (DXA) is the gold standard for assessing BMD, and this measurement is utilized to identify individuals at risk of fractures (Karsdal et al., 2016). To date, several medications are available for the treatment of osteoporosis, with the aim of reducing the risk of fractures. These medications include bisphosphonates, denosumab, selective estrogen receptor modulators (SERMs) such as raloxifene, and anabolic agents like teriparatide and abaloparatide (Khosla et al., 2017). Additionally, lifestyle modifications, including weight-bearing exercise, dietary calcium and vitamin D intake, and smoking cessation, are recommended for all individuals with osteoporosis. The choice of treatment depends on multiple factors, including the individual's fracture risk,

age, sex, and comorbid conditions. The ever-evolving field of osteoporosis management continues to investigate new therapeutic approaches and preventative strategies to address this critical issue in public health.

2.2.5 Biomaterials applications for bone regeneration

In order to improve the natural regenerative capacity of bone tissue, different material types have been introduced and various biomaterials applications are designed. Since the early 20th century, the study of bone repair has been developed by generations of researchers. The essential milestones are illustrated with timeline in the figure 2.3 (Koons et al., 2020).

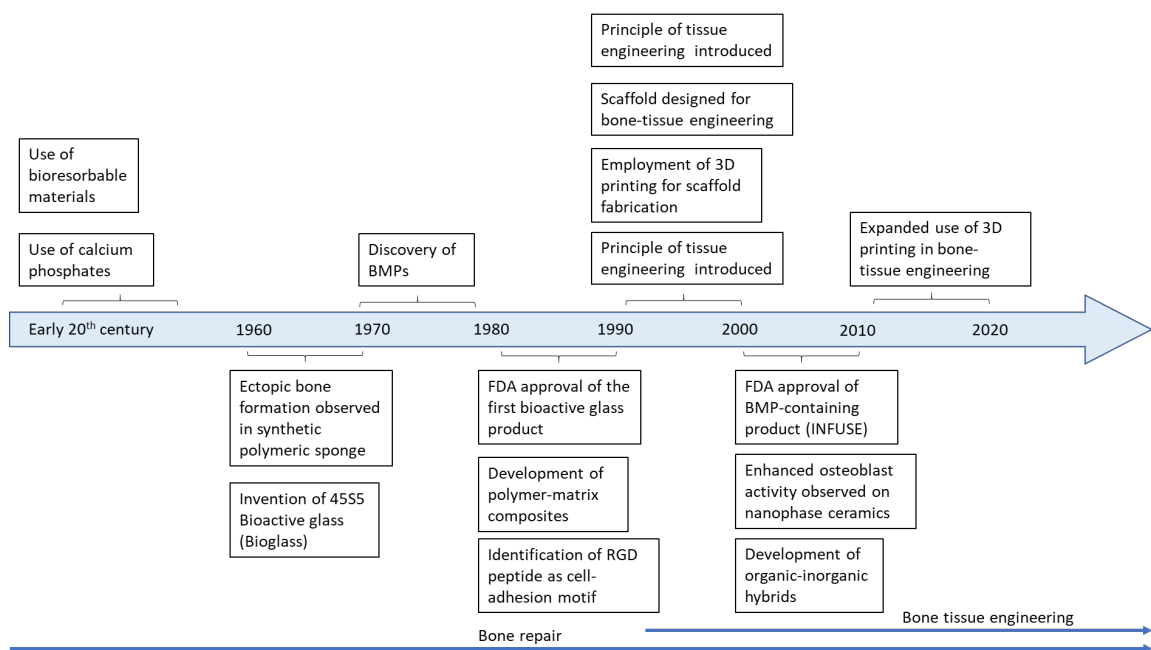


Fig 2.3 Major milestones of biomaterials application in timeline (modified, Koons et al., 2020).

It is well established that a large variety of materials have been proved to be promisingly employed for bone diseases treatment applications. Generally, multiple factors correlate to the choice of materials, including the strategy of surgeries and methods of fabrication. According to the type of materials, five

common materials have been utilized in bone tissue engineering which are natural polymers, synthetic polymers, bio-ceramics, biodegradable metals and carbon-based nanomaterials (Koons et al., 2020). Especially for bone regeneration, bio-ceramics are the most employed that traditionally play a critical role in clinical trials. Noticeably, the calcium phosphate derived ceramics, which also known as i.e. hydroxyapatite (HA), carbonated HA are the most common type for bone biomaterial applications.

Compared with other biomaterials, bio-ceramics provide a less expensive and potentially more compatible alternative to other biomaterials. As it contains a large number of bioactive ions, including Ca^{2+} , Mg^{2+} , Zn^{2+} and SiO_2 etc., the release of these ions from the bio-ceramics leading to the formation of a bioactive layer at the implants where osteoblasts can attach and grow. Thus, this bioactive layer can induce the biological interactions that contributes to the bone regeneration process. Meanwhile, the surface topography of these materials is of important that been reported by other reports (Gauthier et al., 2005; Matassi et al., 2011; Wang et al., 2012). It is also important to know that both topography and ion-release behaviour contribute to the deposition process of hyaluronic-acid-rich ECM.

Tissue engineering has been widely accepted in modern medical treatment aims at several diseases, which utilizes regenerative biomaterials with considerable biocompatibility to interact with cells/tissues of lesions (Kuchler-Bopp et al., 2017; Matassi et al., 2011; Wang et al., 2012). Those biomaterials could be synthetic or natural depend on their origin, which can provide numerous properties for purposes of treatments. According to those researches these years, developments and progress have been made including regenerative medicine, gene therapy, body implants and control of drug release (Guo et al., 2015; Khademhosseini et al., 2006; Langer et al., 2020; Muhammad et al., 2015). Therefore, it requires better biomaterials with multi-properties, which have a detailed understanding of biodegradability, particularly, the polymers. Moreover, as the material should be functional when implanted in vivo, it plays a crucial role for tissue regeneration through a series of pathways including cell to cell signalling, growth factor secretion, and the proliferation, differentiation and

formation of ECM [Rodan et al., 2000; Westendorf et al., 2004]. In these circumstances, biomaterials act as an artificial ECM containing specific biological and physical properties, which mimic the native bone tissue, as well as the function and structures.

Specifically, as mentioned above, calcium apatite based inorganic ceramics, different types of collagens and other organic components are incorporated in bone tissue which contributes bone into a bio-composite. In bone regeneration, therefore, bioactivity and biocompatibility have important roles in the properties of biomaterials. The biocompatibility, has been concerned with implantable biomaterial applications for a long period of time that those applications are supposed to be nontoxic and be able to perform the appropriate response to the host environment. It also has been well recognized that hydroxyapatite plays a critical role in bone tissue engineering because of the biocompatibility. Because of its composition and structure that highly close to natural bone mineral, HA has been considered as ideal material for bone regeneration. The release of Ca^{2+} and PO_4^{3-} promotes osteoblasts to form a bioactive mineral layer on the surface of hydroxyapatite which also demonstrates the bioactivity and osteoconductivity of hydroxyapatite. Thus, biocompatibility and bioactivity are considered to be the premier properties that will be studied in this project in two different biomaterials.

2.3 Hydroxyapatite

Hydroxyapatite, or hydroxylapatite (HA), is widely occurring in mines or act as a crucial component for many animals including humans. It has not been proved until 1970s that HA is the main inorganic component of human bones and teeth. As the key inorganic component of human bones and teeth, it has outstanding biocompatibility, bioactivity, osteoinductive capacity and osteoconductivity, which has been widely accepted in bone regeneration (Hing et al., 2004; Siddiqi et al., 2018; Wang et al., 1998).

The appeal of HA as a material for bone regeneration primarily stems from its structural and compositional resemblance to the human bone mineral phase. Its chemical formula, $\text{Ca}_{10}(\text{PO}_4)_6(\text{OH})_2$, closely mirrors the natural HA present in the extracellular matrix of bone tissue. This similarity fosters excellent biocompatibility, as the material is well-tolerated by the body without provoking adverse immune responses. Moreover, HA is osteoconductive, that provides a favourable environment for bone-forming cells, such as osteoblasts, to adhere, proliferate, and differentiate. Its biocompatibility and osteoconductive properties render HA an excellent substrate for promoting bone cell adhesion and growth, making it a valuable asset in the quest to engineer functional bone tissues for transplantation and repair.

2.3.1 Structure of nano and macro-HA

HA is an important bio-ceramic. Unlike other ceramics, HA is such one that reacts and forms chemical bonds with surrounding tissues, or gradually degrades to form new mineral components by osteoblasts for the process of bone remodelling. A number of publications have also demonstrated that CaP species alone (especially the HA) can promote (*in vitro*), cell proliferation, osteogenic differentiation, and promote desirable gene expression for bone regeneration (Hing et al., 2004; Wang et al., 1998; Urist et al., 1984; Wei et al., 2004). In bone regeneration, HA has been widely applied for hip, knee joints and teeth replacement, as well as the periodontal disease treatment, maxillofacial reconstruction and enhancement, patella fixation and spinal fusion. In addition, HA has also been used in the fields of catalysis, protein chromatography, and sewage treatment. However, the mechanical defects of HA severely limit its further application (Barralet et al., 1998; Landi et al., 2003; Urist et al., 1984).

Table 2.2 Physical and chemical properties of hydroxyapatite.

Material	HA, $\text{Ca}_{10}(\text{PO}_4)_6(\text{OH})_2$, Ca/P=1.667	References
Lattice parameter (Å)	a=9.42, c=6.87	Urist et al., 1984; Wei et al., 2004
Density (g/cm ³)	3.156	Urist et al., 1984; Wei et al., 2004
Hardness	5 (Mohr's scale), 343(Hv)	Urist et al., 1984; Wei et al., 2004
Elastic modulus (GPa)	80~120	Urist et al., 1984; Wei et al., 2004
Poisson's ratio	0.28	Urist et al., 1984; Wei et al., 2004
Thermal properties of densified sample	Thermal expansion coefficient= $11.8 \times 10^{-6}/K$ Melting point=1670°C Isostatic specific heat=0.739 J/gK	Urist et al., 1984; Wei et al., 2004
Chemical properties	$K_{sp} = 10^{-117.2}$, nearly soluble in water, pH=7~9 as weak alkali, easily dissolved in pH<3 environment	Urist et al., 1984; Wei et al., 2004

Nano-hydroxyapatite (n-HA) generally refers to those HAs which have at least one dimension in the three-dimensional space ranging from 1 to 100 nm, or those HAs self-assemble composed of as basic units (Siddiqi et al., 2018; Wei et al., 2004; Wei et al., 2004). N-HA also contains many types, including nanoparticles, nanofibers, nanoceramics, nano-self-assemblies, and nano-coatings etc. In histologic study, the HA which contains in bones of animals and humans, is also under nanoscale. The main components in natural bone tissues are inorganic bone mineral (60-70 wt.%) and water (10-20 wt.%) (Wang et al., 2012). Calcium phosphate is occurred in the bone tissue in an HA state or amorphous state, providing the necessary strength to the bone tissue. In

Innovative incorporation of pearl and calcium phosphate composite in bone regenerative scaffolds

addition, except collagens, bone also contains a small number of other substitutes including various proteins and inorganic salts (Liao et al., 2004). Collagen can be regarded as the skeleton of bone tissue, which exists in the form of microfibers in bone tissue. The length ranges of collagen are from 100 nm to 2000 nm, which builds up a woven network structure (Hing et al., 2004; Wei et al., 2004).

Distributed in collagen fibres, the HA crystals in the bone tissue are carbonated n-HA with plate or needle shapes, about 40-60 nm in length, 20 nm wide, and 1.5-5 nm thick (Urist et al., 1984). Those synthesized n-HA, which is designed parallel to the long axis of the collagen fibres, are proved optimistic for bone crystallization because they have a size close to original mineral crystals in natural bones. Studies have also shown that when the grain size of bioceramic materials reaches the nanometre level, it will have better mechanical properties, wear resistance and biological properties than conventional bio-ceramics (Fung, 2013; Liao et al., 2004; Rho et al., 1998; Sadat-Shojaj et al., 2013). Therefore, n-HA has great application prospects in the field of orthopaedics.

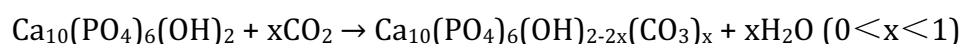
2.3.2 Carbonated hydroxyapatite

The significance is further underscored by the remarkable similarity between the chemical composition of HA and that of natural bone mineral. However, it's worth noting that while HA closely resembles bone mineral in terms of its basic components, bone mineral is not chemically identical to stoichiometric HA. Natural bone mineral incorporates additional elemental substituents into the HA lattice, with carbonate ions (CO_3^{2-}) being the predominant substitutes, accounting for about 4-8 wt.%. Importantly, this carbonate content in bone mineral varies with age (Barralet et al., 1998; Landi et al., 2003). Consequently, there is a compelling rationale for synthesizing carbonated-substituted bioceramics to closely mimic the chemical makeup of natural bone mineral. This endeavour aims to enhance the biocompatibility and biological response of HA when utilized in *in vivo* applications.

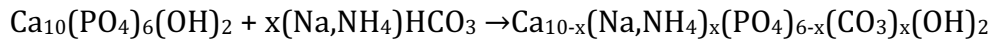
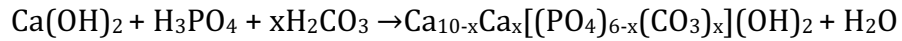
To date, several studies have investigated about the synthesis of carbonated hydroxyapatite (CHA) and it is well established that in the apatite structure, both hydroxyl and phosphate ions could be substituted by the carbonate ions, leading to A-type CHA, B-type CHA and AB type CHA (Hing et al., 2004; Rey et al., 1989). Moreover, among studies of different species of natural bone tissues, the ratio of A/B type is ranging between 0.7 and 0.9 (Sadat-Shojaj et al., 2013). Moreover, in the old tissue, the ratio was observed higher compared to younger ones. Several reports have shown that the presence of B-CHA in the apatite lattice could reduce the crystallinity and precipitate size, which means more soluble in vivo and in vitro (Barralet et al., 1998). Furthermore, A-CHA has been reported to demonstrate lower capacity of intersurface attachment with human trabecular osteoblastic cell, compared to stoichiometric HA (LeGeros, 1967).

At present, methods of the preparation of CHA mainly include co-precipitation, emulsification technique, sol-gel method, mechanochemical method, microwave method, and vapor diffusion microdrop method (Kannan et al., 2011). Saturated solutions of sodium bicarbonate (NaHCO_3), ammonium carbonate ($(\text{NH}_4)_2\text{CO}_3$), calcium carbonate (CaCO_3) or carbon dioxide (CO_2) can be used as the source of carbonate group introduction.

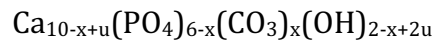
Since 1960s, various models have been proposed to describe the carbonate substitution as different techniques, sources of materials and parameters have great impact on the substitution process. The type-A CHA is generally obtained by thermal treatment in a CO_2 atmosphere or by ion exchange in a CO_2 saturated solution, which the principle is listed below (Rau et al., 2004).



The type-B CHA is generally prepared by the solution reaction of Ca^{2+} , PO_4^{3-} and CO_3^{2-} . Due to the difference in the electron's charges of carbonate and phosphate, the electricity price is not balanced after the same amount of replacement. Therefore, it is usually necessary to balance through cation vacancy structure defects or co-substitution of CO_3^- with monovalent ions such as Na^+ or NH_4^+ . The reaction formula is listed below.



On the premise of meeting the electricity price balance, many scholars have proposed different types of AB substitution by combining the analysis results of IR and XRD analysis of CHA (Lafon et al., 2003). Nebergal et al proposed a model for AB-CHA as:



where $0 < x < 2$, $0 < 2u < x$, x is the vacancy, u is the part of the vacancy to be filled (Kühl et al., 1963). It was assumed that when a CO_3^{2-} replaces a PO_4^{3-} , vacancy of Ca^{2+} and OH^- are generated accordingly. Vignoles et al believes that both CO_3^{2-} and OH^- are able to replace PO_4^{3-} , which would not leave a vacancy and hence the formula is $\text{Ca}_{10}(\text{PO}_4)_{6-x}(\text{CO}_3)_x(\text{OH})_2$ (Vignoles et al., 1988). According to the assumption that the constant value of Ca/P ratio 1.67 ($\text{Ca}/(\text{PO}_4^{3-} + \text{CO}_3^{2-})$) for AB-CHA, Gibson et al proposed another model that $\text{Ca}_{10}[(\text{PO}_4)_{6-x}(\text{CO}_3)_x](\text{OH})_{2-x}(\text{CO}_3)_x$ (Gibson et al., 2002).

The presence of carbonate groups greatly weakens the thermal stability of hydroxyapatite, which makes the decomposition temperature of apatite as low as 700 °C (Kannan et al., 2011). However, it also enhanced the sintering capability of calcium apatite compared to non-carbonate HA. Moreover, the incorporation of carbonate suppressed the growth of large crystal grains which caused the disorder of crystal lattice. Thus, the mechanical properties and hardness of CHA are much better than HA; the average strength of CHA is 210~250 % stronger than HA, three times that of cortical bone which is similar to dense alumina ceramics (Kannan et al., 2011; Martin et al., 1995).

Some reports have demonstrated that in the simulated body fluid (SBF) test, the surface of CHA is more likely to form the biomineralized layer compared to HA, which convinced CHA has better bioactivity (Barralet et al., 1998; Gibson et al., 2002; Landi et al., 2003; Martin et al., 1995). Moreover, cell culture assays have shown that the collagen synthesis of osteoblasts on CHA was increased, with had

better bone conduction capacity, faster biological resorption capacity and better binding capacity compared to non-carbonate HA (Barralet et al., 1998; Landi et al., 2003; Rey et al., 1989).

2.3.3 Methodologies for HA synthesis

The methodologies for synthesis of the HA are primarily important to design and construct the morphology and properties of the nano particles. Different techniques and methods for the preparation of HA are considered directly have impact on the assembly process of HA, the properties, structures, and biological capability. As mentioned above, HA has been widely studied in tissue engineering, for example, HA has been reported to be utilized as drug/GFs carriers and the main bioactivity components for bone regeneration treatment, even has been found having anticancer capacity (Aoki et al., 1993; Hong et al., 2010; Sokolova et al., 2007). Thus, in order to create or obtain the HA nanoparticles with desirable properties, structures, morphology, appropriate techniques and methodologies play an important role for the whole treatment.

To date, based on numerous studies, many methods have been created and developed for HA synthesis, which includes sol-gel processing, hydrothermal process, co-precipitation, emulsion method, mechano-chemical method, ultrasonic method, microwave processing, emulsion-hydrothermal combination and microwave-hydrothermal combination methodology (Chaudhry et al., 2006; Hong et al., 2010; Kuriakose et al., 2004; Lemos et al., 2006). Researchers observed that different methodologies with different pH, temperatures and react system causes nanoparticles demonstrate various morphologies, including nanorods, needle-like, spherical, wire-like nanocrystals, nanosheets and nanoplates (Han et al., 2006; He et al., 2007; Hong et al., 2010; Kuriakose et al., 2004; Yang et al., 2005; Zhang et al., 2007). All methods for HA synthesis have their own advantages and disadvantages that no one can be regarded as the best. The emulsion technique, for example, is a good method for the control of aggregation process and morphology and structure of products; however, it

Innovative incorporation of pearl and calcium phosphate composite in bone regenerative scaffolds requires much longer time and high energy cost to reach the high sintering temperature (Hong et al., 2010; Lemos et al., 2006). Chaudhry et al mentioned a continuous and rapid hydrothermal synthesis process that established a three-pump hydrothermal system (Chaudhry et al., 2006). As they described in the study, this method indeed promises nano-HA synthesized in nanorods structure within a short period of time. However, the yield of products might not reach the requirement of applications.

Thus, although a variety of techniques and methods have been created and attempted, a few of them can be considered as the promising methods. As Fratzl et al and Barralet et al mentioned in their study, the natural bone mineral components resemble the carbonated HA nanorods that organized in lamellae and connected by collagen (Barralet et al., 1998; Fratzl et al., 2004). Moreover, it has been reported that the morphology and structures of HA nano particles correlate to cell-specific cytotoxicity. Aoki et al discovered that the release of Ca^{2+} from HA and the intervention of intracellular Ca^{2+} homeostasis caused by the release process are the main reason of toxicity (Aoki et al., 1993). Zhao et al and Yuan et al also mentioned that the nanostructures and morphologies of HA highly correlate with the cell-specific cytotoxicity, specifically the nanorods and nano spherical like HA has less significant inflammation performance (Yuan et al., 2010; Zhao et al., 2013).

2.3.3.1 Precipitation technique

As the first and most widely studied method to synthesize HA, precipitation process of HA synthesis has been developed and modified into several derived methodologies including wet precipitation, co-precipitation, ultrasonic precipitation (Afshar et al., 2003; Cao et al., 2004; Hong et al., 2010). Differentiated from other methodologies, precipitation is characterized by using simple devices, low cost and easy to be employed in industrial production (Cao et al., 2004; Hong et al., 2010). Series of deep studies about the kinetic and react conditions of the synthesis process followed by the first report about the

intermediate states in the reaction pointed out that, the structures and properties of products have considerable connection with many parameters i.e. pH, temperature, the properties of precursors (Afshar et al., 2003; Liu et al., 2001; Motskin et al., 2009).

2.3.3.2 Sol-gel method

The synthesis of HA has been studied since the first clinical osteoceramic application in 1960s on dogs reported by Matin et al (1995). However, the most widely used methods at that age are precipitation-based techniques, which require high temperature and careful control of other parameters, e.g., pH control, slow titration and diluted solutions. To simplify the procedure and improve the homogeneity of products, sol-gel synthesis of HA attracted more attention from researchers (Han et al., 2006; Yang et al., 2005; Zhang et al., 2007). Sol-gel processing of HA is the method that requires calcium and phosphorus precursors, followed by over 24 hours stirring with controlled temperature conditions to get the gel. Heat treatment is employed after a long period of air-dry process in order to get the final products. As mentioned previously, sol-gel synthesis process indeed has its own advantages that affords molecular-level control of precursors, which increases the homogeneity of products with a milder react condition. Moreover, with the precise control the purity of crystal is also improved using simple devices. However, the remarkable time cost and following high temperature sintering still make the whole synthesis process difficult to be achieved.

2.3.3.3 Emulsion methodology

Compared with other sintering required techniques, significant benefits from emulsion technique attracted researchers to have several studies with it. The emulsion technique synthesis process is displayed below in Fig 2.4.

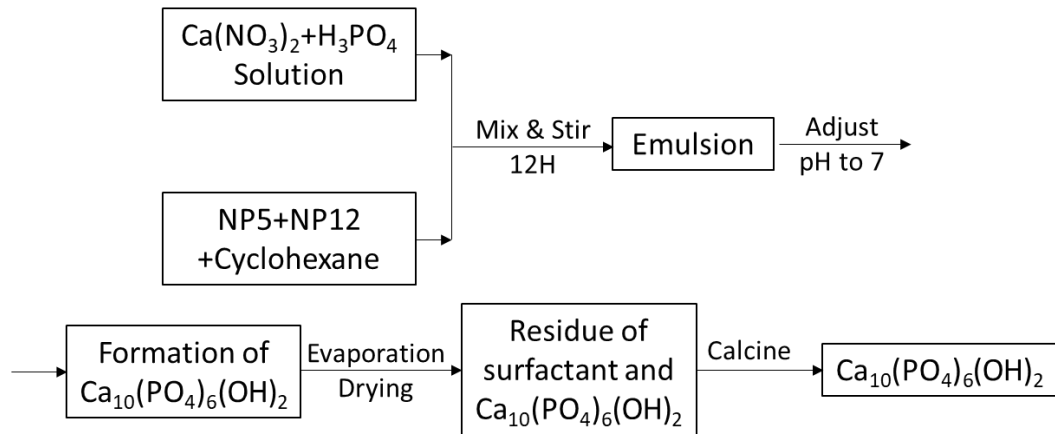


Fig 2.4 The flowchart diagram for HA synthesis using emulsion technique (Bose et al., 2003). Reprinted (adapted) with permission from {Bose, S. and Saha, S.K., 2003. Synthesis and characterization of hydroxyapatite nanopowders by emulsion technique. Chemistry of materials, 15(23), pp.4464-4469}. Copyright {2024} American Chemical Society.

As described in the flow chart, the emulsion technique is one of the few techniques which can provide nano-scale particle size under minimum agglomeration conditions (Bose et al., 2003). Microemulsion is a solution that stabilized thermodynamically, in which two immiscible liquids are stabilized by amphiphilic surfactants. Surfactants help to control the interfacial tension between two phases and stabilize the whole react system. Moreover, the emulsion technique provides an alternative method to get the fine HA particles with spherical morphology. However, it has also been reported that the physical properties of products such as particle size, density are not as expected (Jarudilokkul et al., 2007).

2.3.3.4 Hydrothermal processing

After employing the precipitation method for HA synthesis, researchers noticed that those commercial HA produced by the solid-state reactions to exhibit poor stability and mechanical properties. In order to improve the mechanical properties of dense HA particles, several wet chemical processes were invented

and in the contrast with other methodologies, hydrothermal process is proved to be one of the most practical routes for HANP synthesis. In detail, hydrothermal process provides a better performance for well dispersing nano particles and also helps to produce HANP with better mechanical and sintering properties (Afshar et al., 2003; Chaudhry et al., 2006; Cuneyt Tas et al., 1997). Moreover, the parameters of synthesis could be easily controlled with simple devices by changing temperature, flow rate and reaction duration, which leads to the formation of HANP with various of morphologies i.e. nanorods, needle-like and spheroid nanoparticles (Wang et al., 2010). Studies also reported that when conducted temperature between 60-150°C, the morphology of final HA products are mostly nanorods (Chaudhry et al., 2006; Wang et al., 2010). However, those products are usually agglomerated which may elicit and adverse response in vivo so that they are not able to be employed in biomedical applications. Moreover, the yield strength of the products is not strong enough that need further sintering treatment or ion-substitution modification in order to enhance the mechanical strength.

2.3.3.5 Mechano-chemical method

Since many other methods were devised to synthesise HA, it is more important to find a feasible and universal method or technique to improve the efficiency of commercializing process. Based on the dynamic grinding technique of preparing defective HA, mechano-chemical methods led these physiochemical conditions into one simple choice, which allow the crystallization process undertaken with the ~720°C to get β -tricalcium phosphate (β -TCP) directly (Choi et al., 2007). The basis of the mechano-chemical method is to deep squeeze and crush powders in the limited surface area with proper mill balls (i.e. Al_2O_3 , SiO_2) (Choi et al., 2007). No high temperature variation required during the mechano-chemical process, but high values of pressure is required to support the grinding process so that improve the fraction of powders.

Innovative incorporation of pearl and calcium phosphate composite in bone regenerative scaffolds

Since many other methods were devised to synthesise HA, it is more important to find a feasible and universal method or technique to improve the efficiency of commercializing process. Based on the dynamic grinding technique of preparing defective HA, mechano-chemical methods led these physiochemical conditions into one simple choice, which allow the crystallization process undertaken with the $\sim 720^{\circ}\text{C}$ to get β -tricalcium phosphate (β -TCP) directly (Choi et al., 2007). The basis of the mechano-chemical method is to deep squeeze and crush powders in the limited surface area with proper mill balls (i.e., Al_2O_3 , SiO_2) (Choi et al., 2007). No high temperature variation required during the mechano-chemical process, but high values of pressure is required to support the grinding process so that improve the fraction of powders.

2.3.3.6 Ultrasonic method

Sonochemistry and sonoluminescence have been tracking on the utilization of high-intensity ultrasound for more than 30 years, because the ultrasound provides a unique interaction between particles and energy through acoustic wave (Toriyama et al., 1996). Studies proved that during ultrasonic irradiation, the cavitation process could offer a superior temperature, that is the energy could be utilized in the chemical reactions in a very short scale of time (Cao et al., 2005). Hence, researchers came up with the idea of employing high-intense ultrasound in the preparation of HA powder, which is also known as the ultrasonic spray-pyrolysis technique. The involvement of ultrasound accelerates the heterogeneous reaction and assists to prepare the fine powders under a relative low temperature. However, the ultrasonic technique is not appropriate for factory production because of the high cost of equipment and the yield strength performance of final products is not as expected.

2.3.4 HA and HA based applications in bone regeneration

It has been well known that synthetic HA is exceedingly brittle that HA based applications has been considered that cannot be applied for load-bearing implants for a long period of time. Later, studies about incorporated HA into bioactive polymers provide researchers another strategy to solve the problem. Up to date, many biodegradable polymers including poly(lactic acid) (PLA), poly(-L-lactide acid) (PLLA), polyurethane (PU) and derived polymers have been employed in bone regeneration. Liu et al created a HA/PU scaffold that incorporated drug-loaded ethyl cellulose for bone regeneration, which proved the significant bioactivity of both HA and the loaded drug (Liu et al., 2010). The porous structure and the property of pores contributed to the establishment of extracellular bioactive membrane in a controlled and continuous way. Kim et al employed the study of nanocomposite fibres of HA/PLA for bone regeneration and characterized with comprehensive biological assays (Kim et al., 2006). It has been convinced that the biocompatibility and bioactivity of the bioactive ceramics demonstrated promising improvements for the bone regeneration process.

2.4 Pearl

Pearl, also called the nacreous pearl, which is produced by living shelled mollusks or other same species animals, is well known by its morphology and the worth of making jewellery after polishing and modification. Besides, as a natural biomaterial, pearl has more medical value including fabricate cosmetics, as an ingredient in traditional Chinese medicine as well as applied in tissue engineering. Recently, more researchers focused on the utilization of the pearl powder in biological fields, especially applied for bone regeneration. It has been well proved that these natural inorganic components indeed have beneficial effect on stimulating the differentiation of osteoblasts, as well as promoting the remodelling process of the bone (Bai et al., 2015; Kim et al., 2012).

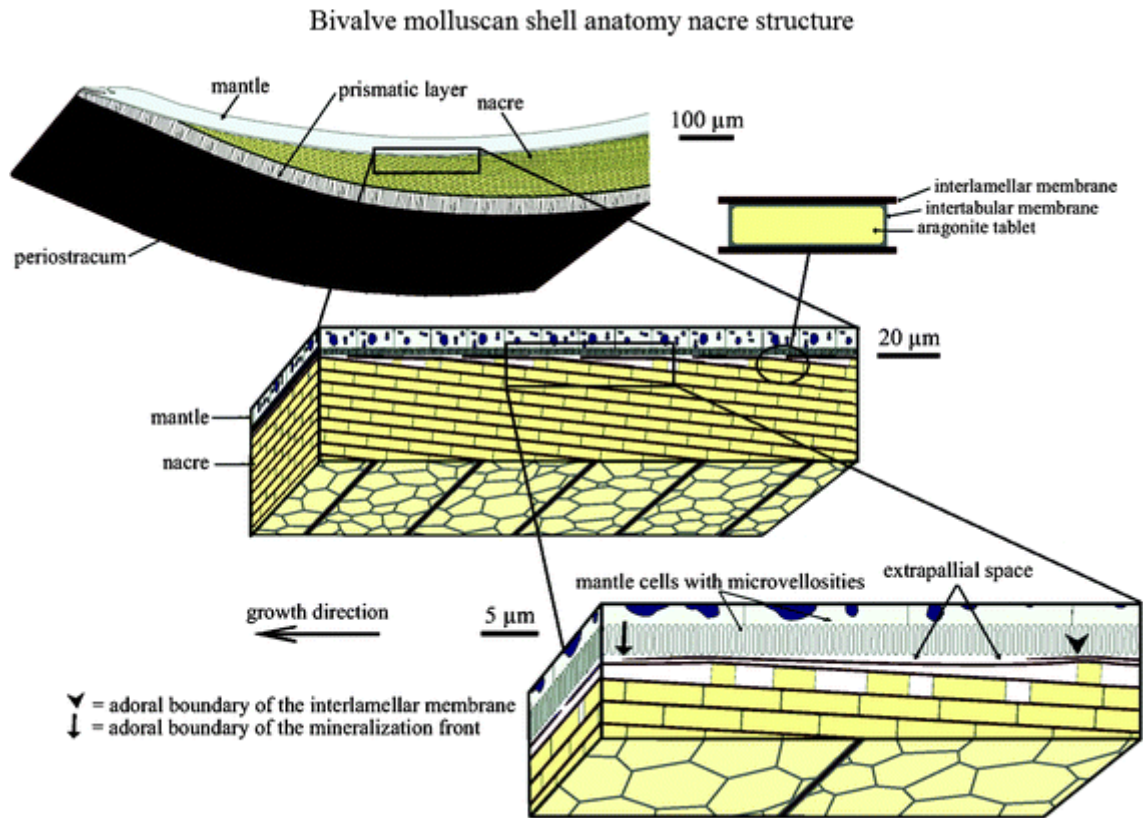


Figure 2.5 Schematic of the bivalve molluscan shell anatomy nacre structure (Sun and Bhushan, 2012).

Pearls usually exist in bivalve molluscs, including *pteriamarfenssi* (Dunker), *hyriopsis cumingii* (Lea) or *cristaria plicata* (Leach), which are lithiasis-like pathophysiological products formed in the mantle tissue where between the mantle cavity and the shell (Frank et al., 2019). Inorganic crystal precursors (mainly Ca^{2+} and CO_3^{2-} and trace metallic ions including Sr^{2+} , Na^+ , Ag^+ , Mg^{2+}) and amorphous CaCO_3 are secreted alongside the organic matrix molecules consisting of multiple polysaccharides, proteins and water by the mantle epithelial cells (Frank et al., 2019). The organic matrix fluid and inorganic crystal precursors wrap up the foreign body to form outer layer sheets in a "brick and mortar" arrangement, also known as the "brick and mortar" structure. The polysaccharides and protein fibres are incorporated into the mortar layer, and the flat aragonite tablets form the bricks layer aligning with each other.

Differences of pearls and shells can be distinguished from different aspects. For instance, metallic elements in nacreous layer of shells and pearls are different as reported by previous studies (Bai et al., 2015; Parker et al., 2010; Qiao et al., 2007) that more metallic elements, such as Mg^{2+} , Al^{3+} , Fe^{3+} , and Mn^{2+} can be characterized from the nacreous layer of shells. Different concentrations of metallic elements also have effect on the colour of shells. Moreover, the thickness of nacreous layers on pearls and shells also demonstrates significant morphological differences that more condensed crystal structure can be observed in pearl nacre layer compared to that of shells.

There are three main reasons for why researchers have extensively focused on the nacre. Firstly, it has a unique structure, “brick and mortar” structure which thanks to the organic matrix and the inorganic components ideally biomineralized by the nacre. Secondly, thanks to its unique structure, pearl demonstrates outstanding mechanical properties, which has markedly higher hardness and Young’s Modulus compared with bovine bone (Bai et al., 2015; Kim et al., 2012; Liao et al., 2002). More incredibly, pearl contains 95-98% ceramic components while the bone contains only 65%. Thirdly, it has been reported that pearl powder as a bone substitute material have better performance in bioactivity and osteoinductive capacity than HA, which has already been widely applied in applications for bone regeneration (Liao et al., 2002; Zhang et al., 2017).

“Brick and Mortar” Structure

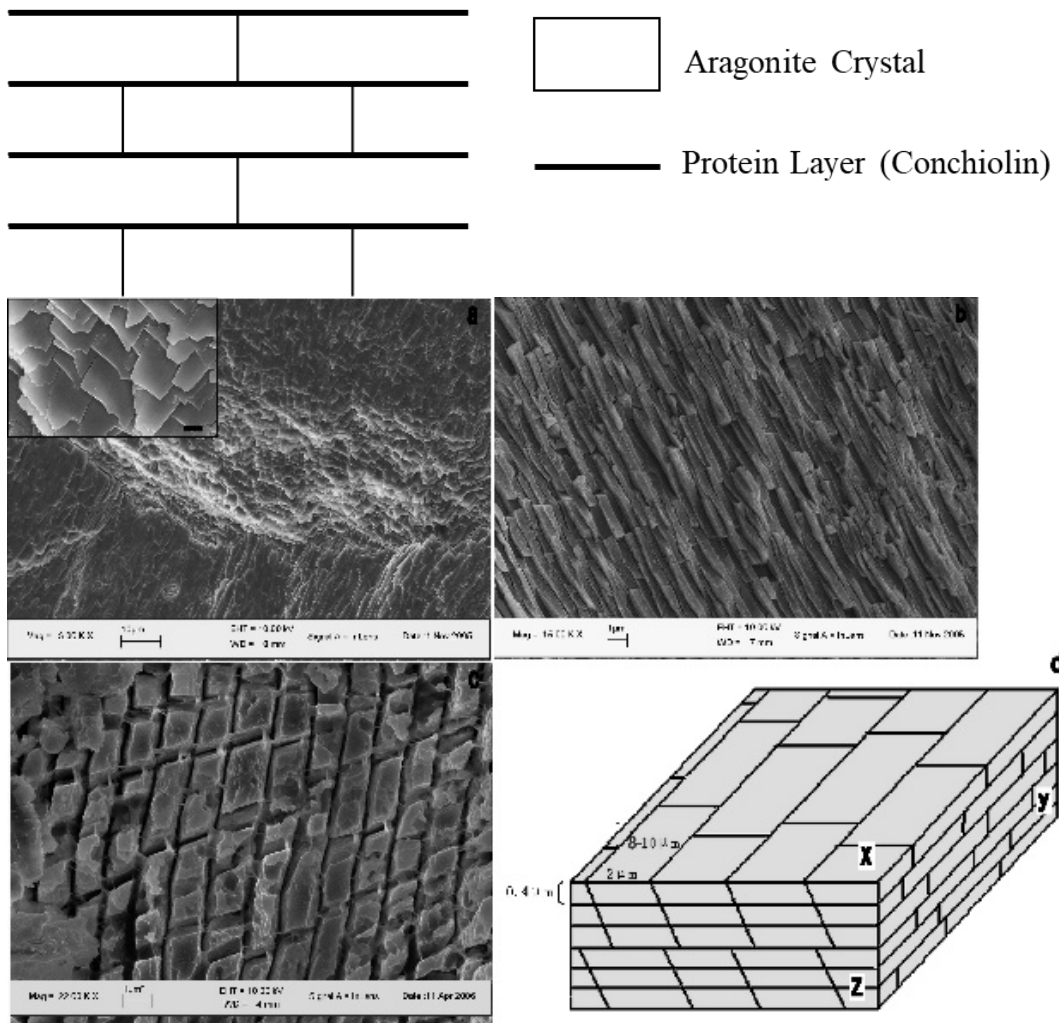


Fig. 2.6 “Brick and Mortar” structure of the pearl nacre layer: mainly consists of aragonite crystals and connected by protein layers between crystal layers. The upper scheme is the modified diagram for demonstration of the structure, and the bottom images are the SEM scans of lacklustre pearls (Parker et al., 2010; Qiao et al., 2007). Reprinted (adapted) with permission from { Qiao, L., Feng, Q.L. and Li, Z., 2007. Special vaterite found in freshwater lacklustre pearls. *Crystal growth & design*, 7(2), pp.275-279. }. Copyright {2024} American Chemical Society.

2.4.1 Inorganic components of pearl

Aragonite, also known as limestone, is a naturally carbonate mineral, with calcite and vaterite are the most three common crystal forms of calcium carbonate because of their different crystal structure. According to the study from Nora and Stephen, they mentioned that aragonite has an orthorhombic crystal structure with space group *Pinctada martensi* naturally (de Leeuw et al., 1988).

Saruwatari et al performed a deep investigation to comprehensively understand the initial nacre layer with focused ion beam (FIB) in scanning electron microscope (SEM) analyses (Saruwatari et al., 2009). According to their studies, aragonite crystallites are randomly orientated in the initial formation of nacreous layer, tangled with the organic matrix, which shaped like a horn. Parker et al performed another research via using Raman spectroscopy and SEM to analyse the aragonite-calcite transformation in mussel nacre, which demonstrates that the crystal morphology change process cannot be observed due to the degradation of the organic matrix; furthermore, the conclusion also showed nacre has considerable capability of thermal resistance as a biogenic material (Parker et al., 2010)

Previous studies have shown the possibility for tissue engineering of aragonite; Peretz et al demonstrated that 3-dimensional (3D) aragonite scaffolds have bioactivity for culturing both neurons and astrocytes as well as the neuronal tissue restoration (Peretz et al., 2007). Moreover, Kon et al. studied with crystalline aragonite bi-phasic scaffolds for chondral and osteochondral lesions that revealed a significant improvement in cylindrical implants (Kon et al., 2016)

Compared with aragonite, vaterite, also known as $\mu\text{-CaCO}_3$, is rare to be found in natural as an ore because it has less stable crystal system. It belongs to the hexagonal crystal system, $P6_3/mmc$. Naturally, the synthesis of vaterite is controlled by a gene, which exists only in two creatures: one marine creature from the class Ascidiacea, and the *Pomacea paludosa*, a freshwater snail (Lowenstam, 1975; Meenakshi et al., 1974). Due to its unstable structure, vaterite is more common to be found associated with other substances, for example

Innovative incorporation of pearl and calcium phosphate composite in bone regenerative scaffolds

organic tissue, gallstones, urinary calculi, as well as Chinese freshwater lackluster pearls which are cultured in the South of China. In that specie of pearl, vaterite is generally observed co-occurs with aragonite as formations of nacreous layer, or individually wraps the bead nucleus to compose a whole lacklustre pearl (Qiao et al., 2007)

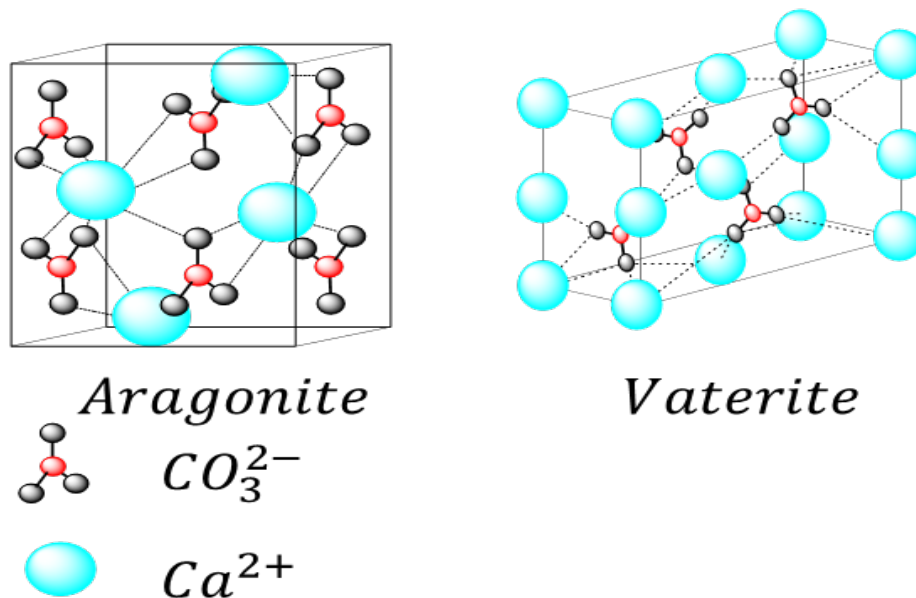


Fig. 2.7 Crystal structure of Aragonite (L, Face-centred orthorhombic system) and Vaterite (R, hexagonal crystal system).

2.4.2 Organic components of pearl

Pearls are categorized into seawater pearls and freshwater pearls because of the different water areas. According to their formation, they are divided into natural pearls and cultured pearls. The chemical composition of pearls varies slightly depending on their sources. According to studies from China, pearl contains a small amount of hard protein, which is conchiolin. Some researchers conducted amino acid analysis of this protein. After hydrolysing conchiolin with hydrochloric acid, it was found to contain 16 amino acids including glycine, tyrosine, alanine, valine, serine, and aspartic acid (Zhang et al., 1996). Moreover, some other Chinese researchers analysed the amino acid composition and content of Hepu pearl oyster and its pearl and found that it contains 22 kinds of

amino acids. Moreover, 5 kinds of those amino acids, such as taurine and ornithine, are newly discovered non-protein hydrolysates amino acids, and among these amino acids, the amount of taurine is the highest (Ripps et al., 2012; Zhang et al., 1996).

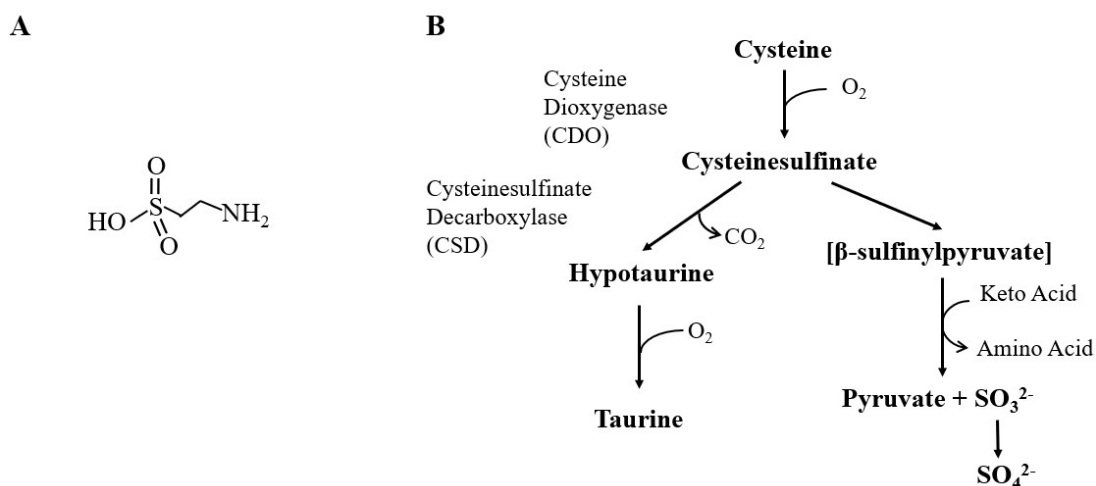


Fig. 2.8 Structure and formation of taurine. A: The chemical structure of taurine ($\text{NH}_2(\text{CH}_2)_2\text{SO}_2\text{OH}$). B: This diagram generally displays the main steps of the formation of taurine in the body. The enzyme cysteine dioxygenase (CDO) catalyses the conversion of L-cysteine to cysteine sulfinate, and the oxidation of hypotaurine (2-aminoethane sulfinate) results in taurine (modified) (Marcinkiewicz et al., 2014).

Taurine (2-aminoethanesulfonic acid) has an incredible amount inside the body of all animal species, plays an important role in many biological processes, which includes bile salts formation, modulation of intracellular free calcium concentration, maintenance of membrane balance and homeostasis (Greeb et al., 1991; Huxtable, 1992; Marcinkiewicz et al., 2014; Zulli, 2011). Inside the body of human, taurine is generally generated from methionine and cysteine metabolism via hypotaurine in hepatocytes (Marcinkiewicz et al., 2014; Zulli, 2011). Inside the plasma and extracellular fluid, the distribution of taurine tissue is found low concentrations (from 10 to 100 μM) while higher concentrations distribution are found inside cells, which up to 50 mM and related to the types of cell (Schaffer et al., 2009). This high distribution of taurine inside human bodies provides indications that taurine plays an important role in several intracellular reactions

Innovative incorporation of pearl and calcium phosphate composite in bone regenerative scaffolds and more ever-increasing evidence supports those. Therefore, the anti-inflammatory properties of taurine and taurine derivatives also have potential to be applied in biomaterials as an original material from pearl powders.

2.4.3 Pearls in bone regeneration

In recent years, an increasing number of studies had discussed the utilization of pearl powders in tissue engineering. Liu et al analysed both PLLA/aragonite and PLLA/vaterite scaffolds with their mechanical properties (Liu et al., 2013). In this study, pearl powder indeed strengthened the mechanical properties for scaffolds, and the yield strength of the pearl-based scaffold is positively related to the content of pearl. In another study, Liu et al fabricated both scaffolds and evaluated with rat bone marrow-derived mesenchymal stem cells (rBMSCs) (Liu et al., 2014). However, the PLLA/vaterite scaffolds decreased the proliferation of rBMSCs and the differentiation of osteogenic, which is remarkably questionable for utilizing the vaterite nacre.

Similarly, Dai et al. incorporated pearl powders (up to 20 wt.%) into PLA scaffolds by evaporation methodology and, following this research, innovatively utilized the electrospinning strategy to obtain the nanofibrous PLA/pearl scaffolds (Dai et al., 2015 & 2016). Results from *in vitro* tests indicated that pearl powder composite scaffolds have the potential to be considered as implantable devices for long-term bone tissue repairing. Li et al fabricated a composite scaffold of chitosan-hyaluronic acid (C-HA) and nano-pearl powder (NPP) by freeze-drying method (Li et al., 2020). According to the results of the biological assays from the research, the incorporation of pearl powders in the C-HA scaffolds can be used for the bone regeneration tissue engineering. More related information was listed in the table below.

Table 2.3 Various pearl/nacre biomedical applications in recent years.

Materials	Composites species	Applications	References
PLA	Scaffold-Nacre	Enhancement of mineralization and cell proliferation.	Dai et al., 2015 & 2016
PLLA	Scaffold-pearl/nacre	Improvement in mechanical strength, cell proliferation and ALP activity	Liu et al., 2013 & 2014
Poly (D, L-lactic acid) (PDLLA)	Scaffold-Nacre	High porosity and mechanical strength, suitable biocompatibility.	Xiao et al., 2012
Poly(lactic-co-glycolic acid) (PLGA)	Scaffold-Nano pearl powders	Better biocompatibility.	Xu et al., 2010; Yang et al., 2014
PCL	Scaffold-Pearl	Improved physicochemical and biological properties.	Zhang et al., 2018
Polyether ether ketone (PEEK)	Artificial implant-Pearl	A fourfold increase in cell density.	Shen et al., 2006
Poly(3-hydroxybutyrate-co-3-hydroxyvalerate (PHBV)	Powder blends with pearl powders	Improving mechanical strength, hydrophilicity, mineralization and biocompatibility	Bai et al., 2015
Ultra-high molecular weight polyethene (UHMWPE)	Powders composite with nacre powders	The incorporation of nacre performed the same wear durability compared with carbon nano-tube filler.	Liu et al., 2013
Chitosan-hyaluronic acid (C-HA)	Scaffold-Nano pearl powder	Enhanced cell adhesion, proliferation and osteogenic differentiation.	Li et al., 2020
Polypropylene (PP)	Monofilament s-Pearl	Cell proliferation was improved.	Deng et al., 2015
Polyaminoacid (PAA)	Scaffold-Pearl	Improved mechanical properties, bioactivity and osteogenic activity.	Wu et al., 2019
CaSO ₄	Scaffold-Pearl	Uniform intertwined macropores with	Du et al., 2018

high porosity, improved compressive strength, ideal bioactivity, and osteogenesis.

2.5 Bioactive scaffolds

From the perspective of biomaterials science, the organic, inorganic and cellular components of human bones made up to a balanced complex mechanism of bio-composite which has collective effect for bone remodelling. To date, the selected materials for bone regeneration has been developed to mimic and match the original bone tissue structure and function, which could promote the formation of new tissue, degrade over time and is of biocompatibility to the immune system. Currently, the common approach of using biodegradable scaffolds demonstrates desirable behaviour for clinical treatments. As the scaffolds could be regulated by specific parameters controlling, internal structure design (3D printing) and the selection of materials, it in turn matches the diverse and challenging requirements from clinic. In this project, two different bioactive scaffolds will be investigated.

2.5.1 Chitosan (CS) scaffolds

Chitin ($C_8H_{13}O_5N$)_n, a long chain copolymer of 2-acetamido-2-deoxy- β -D-glucose and 2-amino-2-deoxy- β -D-glucose, and *N*-acetyl-D-glucosamine (GlcNAc), was first discovered and isolated by the French chemist Henri Braconnot in 1811 (Park and Kim, 2010). Chitin consists of 2-acetamido-2-deoxy- β -D-glucose through a β (1→4) linkage, mainly occurring as a component of natural composite materials, such as in the exoskeleton of insect shells of marine crustaceans and as the primary component of cell walls in fungi (Yui et al., 1994). Dated back to the year 1951, the primary reference book written by the zoologist Richards (1951) first mentioned the existence of chitin in invertebrate insects and hoped later chemists to investigate its adequate chemical properties. With

developed techniques and knowledge of chitin, zoologists and chemists, including Muzzarelli, Hepburn and Neville, published the first book on chitin at the 1st International Conference on Chitin and Chitosan (Kumar et al., 2004; Muzzarelli et al., 1978). Since then, the burst of topic of chitosan and publications related to the development of chitin science has produced a more profound knowledge of chitosan in biological applications. However, few chitin-based applications or chitin derivatives are available to be applied for tissue regeneration. Several reasons have been concerned and mentioned in previous studies including the natural structures of chitin that its structural unit is considered to be the chitobiose (*O*-(2-amino-2-deoxy- β -*D*-glucopyranosyl) -(1-4)-2-amino-2-deoxy-*D*-glucose) which is not easy for processing, and the poor solubility of chitin compared with cellulose.

For decades, the natural biopolymer chitosan has been a subject of interest in tissue engineering. Chitosan is a linear polysaccharide usually obtained from the partial deacetylation of chitin. Since the ubiquitous enzymes degrade it in the human body, chitosan has been widely used in tissue engineering because of its unique advantages, including biocompatibility, biodegradability, hydrophilicity, non-antigenicity, non-toxicity, multi-functionality and more importantly it is the second most abundant biopolymer in nature after cellulose. Furthermore, chitosan is antimicrobial, hemostatic, and osteoconductive, thus promoting it for many biomedical applications.

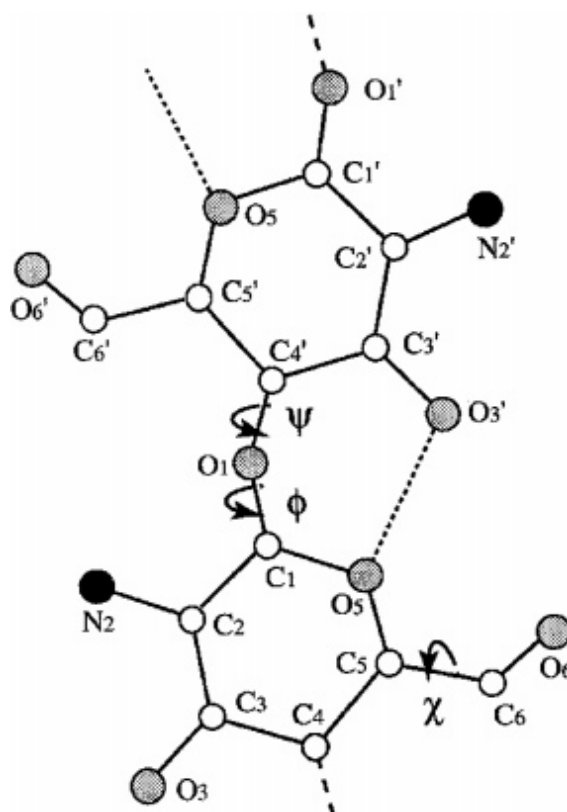


Figure 2.9 Chemical structure of a disaccharide segment of chitosan taken from the study by Kumar et al.(2004). Reprinted (adapted) with permission from { Kumar, M.R., Muzzarelli, R., Muzzarelli, C., Sashiwa, H. and Domb, A.J., 2004. Chitosan chemistry and pharmaceutical perspectives. Chemical reviews, 104(12), pp.6017-6084.}. Copyright {2024} American Chemical Society.

2.5.2 Properties of chitosan

In comparison to cellulose, chitosan shares a structural resemblance, with the key distinction being the replacement of the hydroxyl group at carbon-2 by acetamido or amino groups. What sets chitin and chitosan apart from other abundant polysaccharides is the inclusion of nitrogen, constituting approximately 6.89% of their composition. Notably, the presence of nitrogen, alongside the abundance of hydrogen groups in chitosan, confers cationic properties and remarkable film-forming capabilities, rendering it highly suitable for applications in drug delivery and various biomedical fields. Additionally, owing to its unique combination of hydrogen and amino groups, chitosan stands

as the sole occurring alkaline polysaccharide (Bakshi et al., 2020). Given its enzymatic hydrolysis into oligomers by egg-white and human lysozyme in vivo (Roman et al., 2020), chitosan exhibits excellent biocompatibility and biodegradability, making it an ideal choice for controlled drug delivery (Tomihata et al., 1997).

The chemical and physical attributes of chitosan are closely tied to a range of factors, including its molecular weight (MW), degree of deacetylation (DD), degree of crystallinity, and the distribution of amino, acetamido, and hydrogen groups, among others. The specific location and distribution of these three functional groups play a crucial role in shaping the intra- and intermolecular hydrogen bonding within chitosan, a factor that significantly influences its physical and chemical properties. Furthermore, modifications can be applied to the final chitosan products, where reacylation can lower the DD, and acidic or enzymatic depolymerization can decrease the molecular weight (MM). These modifications directly impact the physicochemical properties of chitosan, offering versatility in tailoring this material for various applications.

2.5.3 Molecular weight (MW)

The MW of chitosan is determined by the number of single glycosaminoglycan units, ranging from 50 to 2000 kDa. Many researchers have coincided that the physical and chemical properties including viscosity, solubility, elasticity and degradability are dependent on the MW, due to the length of the chitosan chains. According to previous research, there are a lot of reports discussing the relationship between various chitosan's properties and MW, such as the antimicrobial activity, hemostatic effect and antioxidant activity (Huang et al., 2004; Zheng & Zhu, 2003; Xing et al., 2005).

Mainly, with the increase of MW, chitosan exhibits lower crystallinity, degradation rate but enhanced mechanical strength and higher viscosity. The DD of chitosan can bring significant impact on the MW which plays an opposite effect on the degradation rate and also decrease the crystallinity.

2.5.4 Degree of deacetylation (DD)

Derived from chitin through the process of deacetylation, chitosan exhibits a greater solubility in acidic solvents when compared to chitin. The degree of deacetylation (DD) of chitosan plays a pivotal role in shaping its physicochemical and biological properties, which has prompted extensive research efforts aimed at manipulating this parameter to achieve specific desired characteristics. Typically, the deacetylation process is achieved through alkali treatment at specific temperatures ranging from 80 to 120°C. Mima et al. (1983) noted that during the initial 5 hours of alkali treatment, the DD of chitosan reached only 80%. Consequently, they developed a preparative method involving repeated cycles of alkali treatment and neutralization to maximize the level of deacetylation, ultimately reaching 100%.

As the deacetylation process unfolds, several significant changes occur. Firstly, an increase in amine content correlates with enhanced solubility and changes in crystallinity. Additionally, this process reduces the chain length of chitosan particles, resulting in heightened charge density and alterations in viscosity, driven by shifts in intermolecular hydrogen bonding. Higher DD leads to an increase in the flexibility of chitosan, although it may weaken the micro-mechanical properties of chitosan particles. Conversely, chitosan particles with lower DD have more extended chains and higher intra- and intermolecular bonding, making them particularly conducive to cell attachment and proliferation.

A study by Foster et al. (2015) explored the proliferation of olfactory epithelial cells on chitosan films with DD percentages of 72% and 85%. However, Huang et al. (2004) highlighted how a decrease in DD, from 88% to 46%, can influence the uptake efficiency by altering the ζ potential of nanoparticles. This change in ζ potential was associated with a certain level of cytotoxicity towards A549 cells. These findings underscore the intricate relationship between DD and the

biological responses and characteristics of chitosan, emphasizing the need for careful control and consideration of DD in various biomedical applications.

2.5.5 Processing of chitosan

Over the years, numerous studies have delved into the modification of chitosan to enhance its properties, primarily categorized into two main approaches: chemical grafting and enzymatic modification. In chemical modification, researchers have employed various reactions to achieve this enhancement. For instance, carboxymethylation of chitosan has been widely adopted for applications in wound healing, drug/gene delivery, and tissue engineering, as highlighted by Shariatinia (2018). This process has been shown to improve solubility and pH sensitivity, rendering it valuable in intestinal targeted drug delivery carriers. Acylation is often an intermediate step in carboxymethylation, as acylated chitosan contains more activated amino groups that can be utilized for amine group formation. Alkylation modification, conducted under alkaline conditions, involves the transformation of part of the hydroxyl or amino groups in chitosan through reactions with halogenated hydrocarbons or sulfates (Chen et al., 2022).

N-alkylated chitosan derivatives can be produced using either halogenated alkanes or the Schiff base method. Acylation modification is a well-established method to enhance chitosan, endowing it with good biocompatibility and the ability to carry and release drugs. This process induces hydroxyl groups to form esters and promotes the generation of acyl groups from amino groups, resulting in a combination of amino and hydroxyl products. Previous studies have explored other chemical modification methods, such as esterification modification (Negm et al., 2022), sulfonation modification (Dimassi et al., 2018), quaternary ammonium salt modification, graft copolymerization modification, and the Schiff base reaction (Shariatinia, 2018; Antony et al., 2019).

In contrast to chemical modification, enzymatic modification of chitosan offers precise control over the enhancement of macromolecular structure for specific

Innovative incorporation of pearl and calcium phosphate composite in bone regenerative scaffolds target chemical groups, with minimal environmental impact. Enzymatic modifications predominantly focus on grafting specific compounds to impart desired properties (Kumar et al., 1999; Mourya et al., 2008; Aljawish et al., 2016). For example, enzymatically modified quinone-chitosan composites have been deemed suitable materials for biomedical applications. This modification alters the surface hydrophobicity of chitosan, endowing it with physiological properties similar to vitamin K (Kumar et al., 2004).

Chitosan, along with its derivatives, possesses an array of properties that make it an attractive material for applications in wound healing, tissue regeneration, drug delivery, and gene delivery (Kumar et al., 2004; Park et al., 2010; Sarhan et al., 2016; Bano et al., 2017; Abd El-Hack et al., 2020). These biomedical applications can be broadly categorized into two major groups: hydrogels (scaffolds) and films. Chitosan hydrogels and scaffolds are prevalent in tissue engineering, serving as semi-synthetic or synthetic extracellular matrices. They provide an ideal environment for cell adhesion and cellular remodelling within three-dimensional structures that mimic the natural cellular environment. In the realm of tissue engineering, chitosan has been extensively utilized to produce porous scaffolds, hydrogels, films, membranes, and nanoparticles.

Various methods, including gelatin/chitosan scaffold prepared by freeze-drying (Alizadeh et al., 2013), porous scaffolds prepared by freeze-gelation (Ho et al., 2004), gelatin/chitosan scaffold prepared by electrospinning (Pezeshki-Modaress et al., 2018), gas foaming using CO₂ for scaffold preparation (Ji et al., 2011), and high-strength chitosan hydrogel prepared by 3D printing (Zhou et al., 2020), have been employed to achieve these applications. Additionally, recent research has underscored the significance of engineered gradient biomaterials in comparison to homogeneous structural materials, showcasing advancements in tissue grafts and tissue constructs.

2.6 Characterization techniques

2.6.1 Chemical characterization

Chemical characterization techniques play a pivotal role in academic research across a multitude of disciplines, from chemistry and materials science to biology. Chemical characterization techniques, in this study, including Fourier Transform Infrared Spectroscopy (FTIR), X-ray Diffraction (XRD), Raman Spectroscopy, and X-ray Photoelectron Spectroscopy (XPS), are extensively utilized in the research. These techniques provide critical insights into the composition, structure, and properties of biomaterials, contributing significantly to the development and understanding of these materials.

2.6.1.1 Fourier-transform infrared (FTIR) spectroscopy

FTIR spectroscopy is an infrared (IR) spectroscopy technique that utilizes the mathematical process, Fourier transform, to transfer raw data into visualized spectra. The IR spectrum commonly reveals the incident radiation is absorbed at a certain energy by the sample when an infrared radiation passed through. As an absorption spectroscopy, infrared spectroscopy identifies the interaction of incident light with the specimen by detecting the frequency changes and different vibrations of the absorbed radiation of molecules. The changes are detected and analysed in the detector and reflected as spectra for the structure characterization. Generally, different functional groups present at different wavelength ranging from 400 to 4000 cm^{-1} , the shape of peaks changes with different concentrations as well.

Previous research has already demonstrated the FTIR spectrum of hydroxyapatite and human bones and confirmed the components of human bones (Panda et al., 2003; Rehman et al., 1997; Ślósarczyk et al., 2005). Comparing the spectra of natural bones with synthetic HA, the significant chemical structure differences are told by the spectrum that prove the component of human bone.

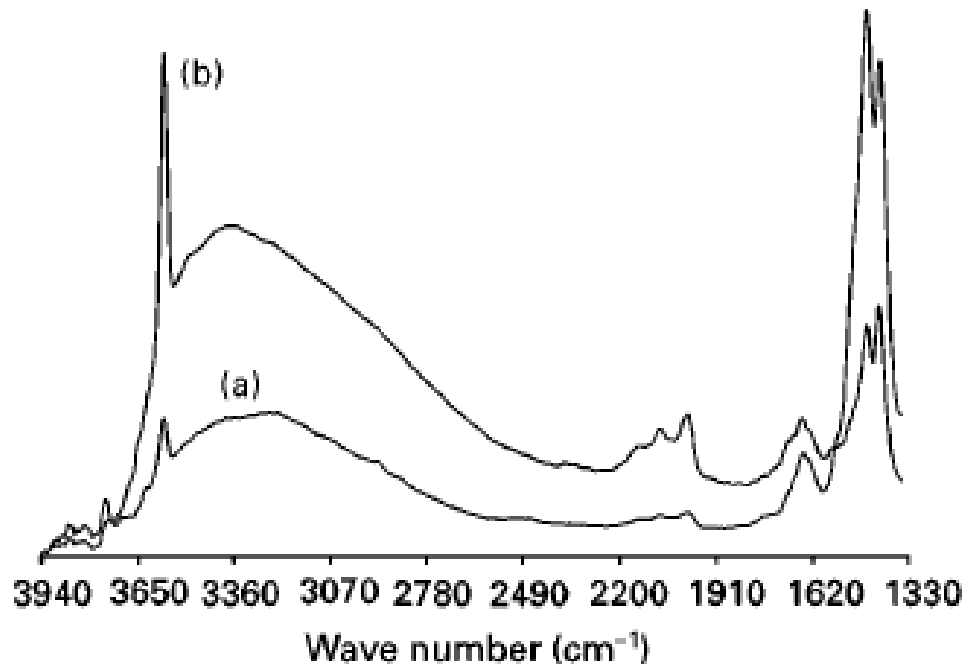


Fig. 2.10 Hydroxyl and carbonate bands of the carbonated (a) and hydroxyapatite (b) powders (Rehman et al., 1997).

2.6.1.2 FTIR-Attenuated Total Reflectance(ATR)

Attenuated Total Reflectance (ATR) is a sampling technique employed in tandem with Fourier Transform Infrared (FTIR) spectroscopy. This method involves the close contact analysis of a sample with a crystal surface, such as Zinc Selenide (ZnSe), Diamond, Germanium, and others, which have a higher refractive index than the sample itself. The process of total infrared light reflection through the crystal generates a unique wave that penetrates the sample. Consequently, the sample absorbs a minor portion of energy, leading to the attenuation of this evanescent wave. Thus, in this work, the FTIR-ATR technique is used for chemical characterizations to identify chemical compounds that distributed on the surface of the composite scaffolds.

2.6.1.3 FTIR-Photo-Acoustic Sampling (PAS)

The analysis of the chemical properties of opaque materials in the mid-infrared region can be challenging due to their high optical density. Traditional methods often require extensive sample preparation, including chemical treatment that may alter the specimen, and laborious size reduction processes. However, the Fourier Transform Infrared Photoacoustic Spectroscopy (FTIR-PAS) technique offers a more efficient approach. In this method, the infrared beam is absorbed by the specimen and converted into heat. This heat travels to the sample's surface, generating a gas that contributes to the formation of the PAS signal. This gas is produced as a result of thermal dilation affecting a thin layer of the surface, providing adequate optical density for absorbance spectrum measurement. Consequently, the FTIR-PAS technique proves to be an ideal method for characterising solid samples in the mid-IR region, with minimal or no sample preparation requirement (Rehman et al., 1997). Therefore, in this study, the FTIR-PAS technique has been employed to identify chemical composition of either synthesized or commercially acquired hydroxyapatite, pearl powders sponsored by the gNpearl Company (China), and the p/CaP composite particles.

2.6.1.4 Raman spectroscopy

Because of multidimensional analytical requirements from research, Raman spectroscopy, a vibrational spectroscopic technique has been emerged improved greatly in recent decades. Based on different types of monochromatic light scattering phenomenon, Rayleigh scattering or elastic scattering, Stokes Raman scattering and anti-stokes Raman scattering three different phenomena have been observed (Long, 1997; Rehman et al, 1997).

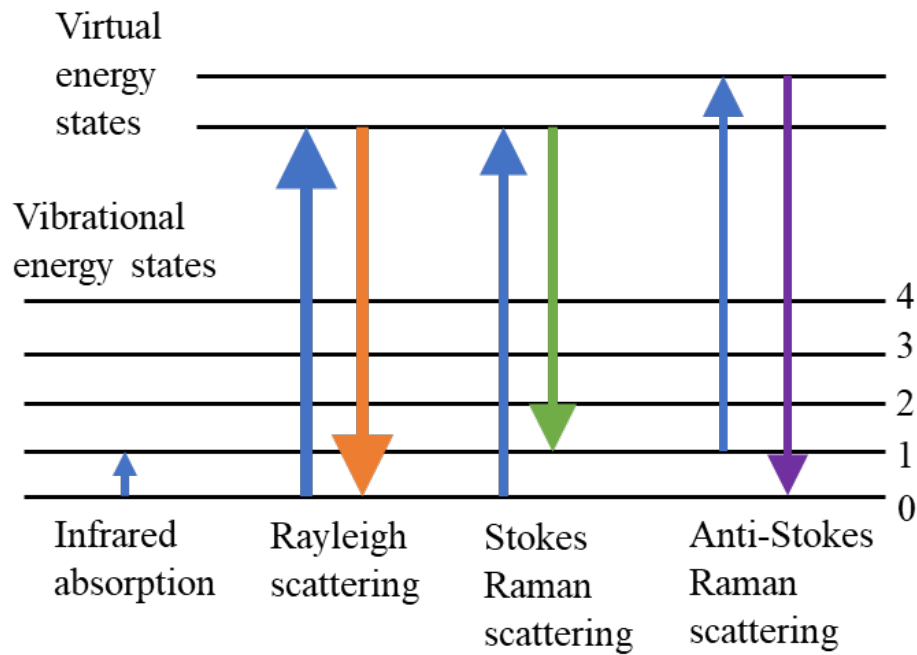


Figure 2.11 The energy level and different scattering phenomenon inside a Raman spectroscopy (modified).

Theoretically, when the laser beam hits a molecule, the photons will hit the electron cloud and bonds of that molecule. After hitting the molecule, those photons can cause the deformation of the electron cloud, in other words, it changes the vibration motion of bonds. In order to keep the whole system in a balance state, the molecule electrons release energy to photons, which cause the energy transfer leads to a frequency change of them. Those changes are captured by the spectroscopy to demonstrate the internal structures of different molecules. Based on different Raman scattering phenomenon and the usage of lasers, various types of Raman spectroscopy imaging modes such as spontaneous Raman imaging mode, including point-mapping Raman imaging, wide-field Raman imaging and fibre array Raman imaging; nonlinear Raman imaging mode which includes coherent anti-Stokes Raman scattering and stimulated Raman scattering microscopy; and emerging modes of imaging, for example surface-enhanced Raman scattering imaging, standoff Raman imaging and spatially offset Raman scattering imaging (Long, 1997; Rehman et al, 1997).

According to the report from large amount of research, Raman micro spectroscopy has been considered the most effective method to analyse the chemical internal structures, properties and even to predict the potential future chemical changes. Comparing to FTIR micro spectroscopy, (1) it requires less sample preparation or non-preparation required; (2) it is more sensitive in specific zones for sample characterizations where FTIR spectra shows only minor peaks. Therefore, two methods are both required for the characterization in order to get more detailed chemical properties of samples. In this study, the Raman spectroscopy was used to characterize the chemical groups in pearl and p/CaP composite samples as a complementary technique to the infrared results.

2.6.1.5 X-ray diffraction (XRD)

X-ray diffraction (XRD) has been well studied and utilized in chemical analysis for centuries. The principle of XRD is the application of the diffraction of the scattered light periodically. When the scattering X-rays pass through atoms, it can produce a diffraction pattern which includes the information about the atomic arrangement within the specimen. Specifically, XRD only uses for the observation of crystalline materials which have the periodic array with long-range order. As a non-destructive method, XRD offers an effective means to investigate a wide array of characteristics and properties in materials. This includes the assessment of their structural configuration, physical attributes, and crystallographic features. XRD excels at tasks such as phase and component analysis, determining crystallinity, measuring thickness, evaluating density and porosity, and elucidating atomic texture, among others. In tissue engineering, XRD is a commonly used method to study the crystalline structure of composite, especially to confirm the crystalline nature of composite scaffolds (Panda et al., 2003; Rey et al., 1989; Ślósarczyk et al., 2005).

In a recent study by Zeller-Plumhoff et al. (2019), they investigated bone formation at the interface of various implant materials, both biodegradable and non-biodegradable. Their approach involved quantitative analysis using two-

Innovative incorporation of pearl and calcium phosphate composite in bone regenerative scaffolds

dimensional X-ray diffraction (XRD) and small-angle X-ray scattering (SAXS) techniques. These analyses provided valuable insights into the ultrastructure of bone, specifically pertaining to the formation of its apatite layer, the measurement of its thickness, and the characterization of its texture. In this research, XRD analysis was performed on both raw and synthesized HA, the pearl and the p/CaP composite serving as a complementary chemical analysis method to augment the findings from FTIR and Raman techniques.

2.6.1.6 X-ray photoelectronic spectroscopy (XPS)

X-ray photoelectron spectroscopy (XPS) represents a significant advancement, as it enables the determination of the chemical composition within a thin surface layer of a solid material, as opposed to examining the bulk composition. In essence, it provides insights into chemical information perpendicular to the surface of materials. XPS takes the lead as the primary technique for surface chemical analysis due to its remarkable ability to strike a balance between offering qualitative data, facilitating quantification, and ensuring surface selectivity (Genet et al., 2008). Recently, Maachou et al (2013) has shown the investigation of chitosan-hydroxyapatite composite microparticles from the elemental perspective. In this study, this technique is considered to be a supplement characterization for studying the composite powder samples.

2.6.2 Physical characterization

Physical characterization techniques, including thermo gravimetric analysis/differential scanning calorimetry (TGA/DSC), surface area measurement - Brunauer-Emmett-Teller (BET), porosity estimation- water emission test, and morphology characterization with scanning electron microscope (SEM), are crucial in the field of biomaterials characterization. These physical characterization techniques provide comprehensive and valuable

information about the properties of biomaterials, contributing significantly to their design, synthesis, and application in various biomedical fields.

2.6.2.1 Thermal Analysis by TGA/DSC

The thermal analysis of materials encompasses several techniques, including thermal gravimetric analysis (TGA), differential thermal analysis (DTA), and differential scanning calorimetry (DSC). Each of these methods provides unique insights into the behaviour of materials under different temperature conditions. In TGA, samples are subjected to controlled heating within a specific atmosphere, such as argon, nitrogen, or air. During this process, any weight changes in the specimens are meticulously measured. TGA is a powerful tool for detecting temperature-dependent alterations in materials, which may include processes like dehydration, calcination, and disintegration.

DTA, on the other hand, involves heating both the material being tested and an inert reference sample simultaneously. By comparing the temperature-related responses of these two substances, DTA can pinpoint specific reaction temperatures, offering valuable information about events like oxidation, melting, and the formation of different phases (King, 2002). DSC is another essential technique used in thermal analysis. It quantifies the energy changes that occur within a sample as it is heated. This information is derived from measurements of heat capacity and enthalpy at increasing temperatures, collected through calorimetry. DSC is particularly informative as it reveals various characteristics of materials, such as the glass transition temperature, crystallization behaviour, and melting points. Similar to DTA, DSC is conducted by heating both the test sample and an inert reference sample for precise comparative analysis (Schick, 2009). These thermal analysis techniques collectively provide a wealth of information about material properties and behaviours under changing thermal conditions.

2.6.2.2 Surface Area Measurement - Brunauer-Emmett-Teller (BET)

The Brunauer-Emmett-Teller (BET) method is a pivotal technique in materials science, offering a sophisticated approach to characterizing surface areas. This method commences by placing a small sample within a carefully controlled vacuum environment. The sample is then subjected to a process known as outgassing, which involves the removal of adsorbed gases and other surface contaminants to ensure a pristine starting point.

Subsequently, a precise quantity of nitrogen gas (N_2) is introduced to the specimen's surface. This introduction of N_2 is controlled in such a way that it forms a single molecular layer on the sample's surface, a critical aspect of the method. The measurement is then meticulously recorded, focusing on the amount of nitrogen gas consumed in this process.

The significance of this measurement lies in its role as a reliable indicator of the specimen's surface area. By assessing the volume of N_2 gas adsorbed onto the sample, scientists gain valuable insights into the extent of available surface area. This quantitative analysis is instrumental in understanding the porosity, texture, and surface characteristics of materials, making the BET method an indispensable tool in scientific research (King, 2002).

2.6.2.3 Porosity estimation- water uptake test

The utilization of water uptake tests to estimate the porosity of bioactive scaffolds has gained considerable attention in the field of biomaterials and tissue engineering. Porosity is a critical parameter that influences the performance of scaffolds in regenerative medicine, affecting cell infiltration, nutrient transport, and overall tissue integration. Several studies have demonstrated the efficacy of water uptake tests in assessing the porosity of these scaffolds, offering a non-destructive and reliable means of characterization.

In a study by Smith et al. (2018), the researchers employed a water uptake test to determine the porosity of a novel chitosan-based scaffold designed for bone

tissue engineering. By monitoring the rate at which water permeated the scaffold and measuring the emitted water volume, they were able to calculate the scaffold's porosity accurately. This method provided a valuable tool for quality control and optimization of scaffold fabrication, ensuring the desired porosity for effective tissue regeneration.

Additionally, water uptake tests have been applied in evaluating the porosity of hydrogel-based scaffolds for cartilage tissue engineering. In a study by Chen et al. (2019), the researchers used this technique to quantify the scaffold's pore size and porosity, crucial factors in supporting chondrocyte growth and matrix production. The results from the water uptake test aided in the fine-tuning of scaffold parameters to achieve the optimal porosity, contributing to the success of cartilage regeneration strategies.

Moreover, water uptake tests have been utilized in combination with other analytical methods to comprehensively assess scaffold porosity. A study by Johnson et al. (2020) integrated micro-computed tomography (micro-CT) and water uptake testing to evaluate the porosity of composite scaffolds for bone tissue engineering. This multi-faceted approach allowed for detailed 3D porosity mapping, offering a deeper understanding of the scaffold's structural properties, thus enhancing the design and fabrication process.

2.6.2.4 Morphology characterization with scanning electron microscope (SEM)

In order to have a deep observation of the internal structure and morphology of materials in microns, it is necessary to utilize high-resolution microscope techniques or other methodologies. Therefore, as a type of electron microscope, scanning electron microscope (SEM) is ideal for the characterization especially in biological and chemical research.

It has been proven by sequences of studies using SEM to characterize the surface structures of materials especially for biomaterials. Li et al. (2005) utilized this

Innovative incorporation of pearl and calcium phosphate composite in bone regenerative scaffolds technique in studying the cell culturing assays and morphologies of chitosan-alginate hybrid scaffolds, which applied for bone tissue restoration. In that study, images from SEM evidently exhibit the related position of cells and scaffolds and provide the actual parameters of pores. Moreover, micrographs from SEM also detail impressive morphologies of individual osteoblasts and other different cells after cell culturing. Taboas et al. (2003) observed 3D polymer-ceramic scaffolds through SEM as well for evaluation of the composite product. Images created by SEM clearly display the morphology and the surface structure of scaffolds, which gives reasonable results for further discussion.

Therefore, as a method for characterization, it is necessary to apply SEM for morphology, internal structure, pore dimension, and cell culturing study. Moreover, this study aims at fabricating porous bioactive scaffolds which will design cell culture assays on samples, which undeniably need high resolution graph to prove the surface interactions between cells and scaffolds.

2.6.3 Mechanical characterization

Medical applications especially for bone regeneration, the mechanical properties of materials are generally considered as a key factor for design and production. Clinically, the mechanical properties of implants have huge impacts on different treatments, for example, dental applications require low density, good elastic modulus, toughness and fatigue strength while for chronic wound healing, which requires the scaffold with better elasticity and normal tensile strength. Bone as the most studied organ in the human body plays a very important role in motivation, protection and restoration as mentioned before. For bone regeneration, especially applied for hard bone repairing, implants are required to have reasonable mechanical behaviour such as tensile strength, yield strength and compressive strength.

Table 2.4 Key mechanical properties of human bone, HA, and pearl.

Mechanical	Human bone	HA	Pearl	References
------------	------------	----	-------	------------

properties				
Vertical elastic coefficient (E) (GPa)	3.5-22.1	60-130	62-83	Cuneyt et al., 1997; Fung, 2013; Klinkla et al., 2024; Shen et al., 2018
Tensile strength (MPa)	73-120	N/A	1300-1800	Cuneyt et al., 1997; Fung, 2013; Shen et al., 2018
Compressive strength (MPa)	200-4000	260-560	350-2500	Cuneyt et al., 1997; Fung, 2013; Klinkla et al., 2024
Strain (%)	1	0	N/A	Cuneyt et al., 1997; Fung, 2013; Klinkla et al., 2024
Porosity (%)	Inhomogeneous	Densified 0~4 Porous 20~40	N/A	Cuneyt et al., 1997; Fung, 2013; Klinkla et al., 2024

2.6.3.1 Mechanical strength

As aforementioned, the main constituents of bone are both organic and inorganic components and according to their chemical and physical structures, they play different roles in the whole composite. Organic components, i.e., collagens, proteins and polysaccharides behave as compliant materials with low modulus, high toughness which mostly related to the complexed fibrous system (Turner, 2006). Previous research about the stress-strain curve for bone demonstrated that although bone is a tough material under low strain rates, it is more brittle when under high strain rates (Burstein et al., 1976; Domrongkitchaiporn et al., 2002). Meanwhile, thanks to its hierarchical structure, crack propagation can be stopped in a short time, which appears a good toughness (under low strain rates) (Burstein et al., 1976). Moreover, both Young's modulus and compressive strength increase with increasing bone density and the degree of mineralization

Innovative incorporation of pearl and calcium phosphate composite in bone regenerative scaffolds

also contributes to strength and fracture strain. Finally, bone density, porosity, humidity, crystallization, and morphology all play a vital role for the mechanical property of bone.

Table 2.5 Critical mechanical properties of a compact human bone.

Test direction related to bone axis	Parallel	Normal	References
	Tensile strength (MPa)	124-174	49
Compressive strength (MPa)	170-193	133	Burstein et al., 1976; Turner, 2006
Bending strength (MPa)	160		Turner, 2006
Shear strength (MPa)	54		Turner, 2006
Young's modulus (GPa)	17.0-18.9	11.5	Burstein et al., 1976; Turner, 2006
	20-27(random)		Turner, 2006
Work of fracture (J/m ²)	6000 (low strain rate)		Turner, 2006
	98 (high strain rate)		Turner, 2006
K_{Ic} (MPa·m ⁻²)	2-12		Turner, 2006
Ultimate tensile strain (%)	1.4-3.1	0.7	Turner, 2006
Ultimate compressive strain (%)	1.85-2.6	2.8	Turner, 2006
Yield tensile strain (%)	0.7	0.4	Turner, 2006
Yield compressive strain (%)	1	1.1	Turner, 2006

2.6.3.2 Young's modulus

In tissue engineering, Young's modulus plays a relatively important role in the mechanical properties of biomaterials. The linear elasticity of scaffolds and implantations reflect the duration and strength of materials, so that to make sure the requirements of applications. The formula of calculation is listed below:

$$E = \frac{\sigma(\varepsilon)}{\varepsilon} = \frac{F/A}{\Delta L/L_0} = \frac{FL_0}{A\Delta L}$$

in this equations, E is Young's modulus, σ is the uniaxial stress, ε is the strain, F is the force exerted on an object under tension, A is the cross-sectional area, ΔL is the changes of length, L_0 is the original length (Wortman et al., 1965).

As aforementioned, the mechanical properties of biomaterials are required to reach the level of natural bone tissues which considering for the clinical treatments. Thus, in order to get the actual Young's modulus value, the length changes and the cross-section area are required to get various of data then calculate for the result.

2.6.4 Biological characterization

2.6.4.1 Cell culture

It was in the early 20th century that cell culture technique was developed to study the in vitro cell behaviour of animals (Thorpe, 2007). Through the following ages, cell culture has been defined as the cultivation of cells in vitro in an artificial environment that is suitable for their growth (Hudu et al., 2016; Wilmer, 2013). As one of the major tools used in cellular and molecular biology, cell culture provides a detailed model system to study the physiology and biochemistry of cells. Specifically, in biomaterials, cell culture has been considered as the primary tool that provides comprehensive understanding of the biological interactions between materials and cells. The biological actions of cells, including

Innovative incorporation of pearl and calcium phosphate composite in bone regenerative scaffolds proliferation, differentiation, and spatial arrangement, are essential for the formation of complete, normal tissue. Cell culture provides the biological environment that allow cells grow on biomaterials in a desirable condition, hence, being able to complete the gene expression and ultimately the process of differentiation *in vitro*.

2.6.4.2 Evaluation of Biodegradation

Various degradation mechanisms affect polymers, involving mechanical, thermal, photochemical, and chemical processes. Biodegradation of polymers primarily follows a chemical pathway, often with hydrolysis as the main process. This chemical breakdown can occur with or without the involvement of enzymes as catalysts. During hydrolysis, the polymer undergoes swelling due to water penetration, ultimately leading to the disintegration of the polymer network. This results in the formation of smaller molecules, including oligomers and monomers, as the polymer cleaves. The release of polymer components during degradation contributes to the development of cracks and porosity, affects the local pH, and results in a reduction in the polymer's overall mass. The speed of hydrolysis is influenced by various factors, including chemical bonding, molecular weight, pH, and crystallinity, and these parameters are often used to assess the extent of degradation. In natural-based polymers, enzymes play a significant role in accelerating biodegradation reactions (Göpferich, 1996).

Different types of polymers degrade at varying rates when exposed to different enzyme environments. For example, elastin-like polypeptides (ELP) are susceptible to degradation by enzymes such as trypsin, elastase, or collagenase (Li et al., 2012; Ong et al., 2006). Enzyme-crosslinked hyaluronic acid-based hydrogels may degrade when exposed to hyaluronidase enzymes (Lee et al., 2009), while fibrin gels break down through the action of activated plasmin (Li et al., 2012).

Chitosan degradation mechanisms involve hydrolytic, enzymatic, and oxidative processes. Hydrolysis reactions, although relatively slow and less efficient, break

down glycosidic linkages in chitosan. Hydrolytic degradation may be suitable for water-soluble chitosan derivatives, low molecular weight chitosan, or polyelectrolyte complexes with weak bonding (Jennings, 2017).

Enzymatic degradation of chitosan occurs through the action of enzymes such as lysozyme, chitinase β , or glucosidase in the body. Lysozyme is present in various body parts, with concentrations ranging from 1-14 $\mu\text{g/ml}$. Macrophages and neutrophils secrete lysozyme at tissue injury sites. Lysozyme-induced degradation leads to the cleavage of glycosidic linkages, a reduction in molecular weight, and dissolution. Chitosan fragments generated in this process include saccharides and glucosamine side-products, which may interact with proteoglycans or be eliminated from the body as metabolic by-products. Another enzyme involved in chitosan degradation is chitosanase or chitinase, which is specific to chitin. The human body has limited quantities of these enzymes, such as chitotriosidase and acid mammalian chitinase. Additionally, intestinal depolymerization of chitosan can occur due to β -glucosidase enzymes secreted by bacteria (Jennings, 2017).

Oxidative degradation, initiated by the formation of free radicals by macrophages, is relatively uncommon and leads to polymer breakdown, crosslinking, a decrease in molecular weight, and the opening of polymer rings. This degradation process can be induced by factors such as exposure to UV and gamma light. Alternatively, local oxidative degradation may occur at the interface between a biomaterial and tissue surface due to the generation of hydrogen peroxide and superoxide by phagocytic cells (Jennings, 2017).

For *in-vitro* degradation studies of biomaterials, including hydrogels, a common approach involves using lysozyme. In such studies, samples are weighed and immersed in a specific volume of lysozyme media prepared in PBS (phosphate-buffered saline) and incubated at 37°C (Jin et al., 2009; Qasim et al., 2017). Qasim et al. (2017) reported both *in-vitro* and *in-vivo* degradation studies for chitosan hydroxyapatite porous scaffolds. In the *in-vitro* degradation analysis, samples incubated in lysozyme media were evaluated through pH analyses and weight

Innovative incorporation of pearl and calcium phosphate composite in bone regenerative scaffolds measurements, while *in-vivo* degradation was assessed through histological examination.

2.6.4.3 Cell Cytotoxicity and Proliferation Assays

2.6.4.3.1 AlamarBlue® (Resazurin) assay

Similar to MTT, AlamarBlue® dye is employed for assessing cell viability and proliferation based on similar principles. Resazurin, a non-fluorescent dye, undergoes enzymatic reduction through cell metabolic activity, resulting in the formation of fluorescent pink-coloured resorufin. In contrast to MTT, the use of resazurin offers the advantage of cell reusability in subsequent experiments owing to its non-toxic nature. This not only promotes cost and time efficiency but is particularly beneficial when working with primary cells. To assess cell metabolic activity, resazurin is introduced into the cell culture media at a ratio of one to ten, and measurements can be taken using a fluorescent reader or a colorimeter (Brien et al., 2000).

In this project, the AB assay, recognized for its cytocompatibility that allows for the reuse of cells throughout the entire culture period, has been employed to analyse cell attachment, cytotoxicity, and proliferation

2.6.4.3.2 Cell proliferation and Morphology Imaging by SEM

SEM is a crucial technique for the analysis of cell morphology after proliferation. In SEM characterization, it's essential to fix and completely dehydrate wet cells and tissues before conducting electron microscopy imaging. As an example of the preparation process described by Braet et al. (1997), cells are initially fixed using a 2% glutaraldehyde solution overnight, preferably followed by a post-fixative treatment with 1% osmium. Subsequently, the samples undergo dehydration through a series of ethanol treatments (70%, 80%, 90%, 100%, 100%, 100%) at 10-minute intervals. The dehydration process is then finalized using HMDS

(hexamethyldisilane) chemicals for three minutes, followed by drying in a desiccator for approximately 25 minutes. Alternatively, increasing the HMDS immersion time to 5 minutes allows for drying in a fume cupboard, where the HMDS evaporates over a 30-minute period. Once dry, the samples are coated with gold and then imaged using SEM (Braet et al., 1997; Shively & Miller, 2009).

SEM is a highly effective and readily available technique for morphological analysis of cells and their adhesion to hydrogels. However, the presence of significant water content in hydrogels necessitates a thorough dehydration process before imaging. Given the often complex drying procedures for hydrogels or tissues, the use of HMDS as a chemical drying agent provides a simple yet efficient technique for sample preparation for SEM following incubation in this study.

2.6.4.3.3 Cell Differentiation Analyses

Osteoblast cells can originate from mesenchymal progenitor cells during intramembranous ossification or differentiate through osteochondral progenitor cells in endochondral ossification. This differentiation process is influenced by various stimuli, encompassing physical, mechanical, and biological signalling factors (Rutkovskiy et al., 2016). The entire differentiation process spans about a month. In the initial week of differentiation, we observe the downregulation of DNA and the initiation of processes like ALP secretion, the transformation of collagen types, and the production of extracellular matrix (ECM) components. Subsequently, in the following weeks, we witness the development of biomarkers like osteocalcin, osteonectin, osteopontin, and sialoprotein. The differentiation process culminates with the deposition of an apatite layer, which typically begins around the two-week mark.

To assess differentiation, one can detect various biomarkers, including ECM components like fibronectin, vitronectin, osteopontin, laminin, and osteonectin, alkaline phosphatase (ALP), collagen, and calcium phosphate. The determination of these markers can be achieved through different assays, such as Alizarin Red

Innovative incorporation of pearl and calcium phosphate composite in bone regenerative scaffolds for mineralization, Sirius Red for collagen detection, or enzyme-linked immunosorbent assay (ELISA) for quantifying the formation of ECM proteins (Hanna et al., 2018).

2.6.4.3.4 Alkaline Phosphatase (ALP) Assay

The alkaline phosphatase (ALP) enzyme plays a vital role as one of the osteogenic biomarkers by facilitating the hydrolysis process of phosphomonoesters, such as inorganic pyrophosphate, β -glycerol phosphate, and ATP. This hydrolysis results in the formation of inorganic phosphates and alcohols during mineralization. ALP significantly contributes to mineralization by breaking down inorganic pyrophosphate, a substance that inhibits the formation of hydroxyapatite (Balcerzak et al., 2003; Orriss et al., 2007).

To measure ALP enzyme activity in cells, a commercial kit can be employed, which is based on the transformation of the p-nitrophenyl phosphate substrate into a yellow chromogen called p-nitrophenyl by ALP. At different time points during a cell culture, the ALP activities can be determined by measuring the absorbance of ALP-treated cell media using a microplate reader at a wavelength of 405 nm (Cui et al., 2010). This approach allows for the quantitative assessment of ALP activity, providing valuable insights into the osteogenic potential of the cells under investigation.

2.6.4.4 Evaluation of Angiogenesis

Several *in-vitro* and *in-vivo* techniques are employed to investigate angiogenesis and assess proangiogenic and anti-angiogenic responses to various materials. These methods include *in-vivo* Matrigel assay, the chick Chorioallantoic Membrane (CAM) assay, *in-vitro* cellular tube formation assay, aorta ring assay, and newer techniques like the chick aortic arch assay and Matrigel sponge assay. Each of these techniques provides unique insights into the angiogenic potential of materials and their effects on blood vessel formation and growth.

The chick Chorioallantoic Membrane (CAM) is a specialized tissue enveloping the surface of chick embryos, known for its dense network of blood vessels and capillaries, and its role in providing gas exchange. The CAM assay is an invaluable *in-vivo* technique commonly employed to study angiogenesis, anti-angiogenesis, and the biocompatibility of tissue-engineered materials (Mangir et al., 2019; Ribatti et al., 1996). Using chick embryos as an *in-vivo* model for angiogenesis research offers numerous advantages over other animal models, including circumventing ethical constraints, reducing costs, expediting procedures, and avoiding invasive tests on animals.

The CAM assay can be conducted either *in-ovo* or using the more recent *ex-ovo* (shell-less) approach. In the *in-ovo* method, fertilized chick embryos are incubated in a humidified incubator at 37°C. After an incubation period of approximately 7 to 9 days, a square window is delicately cut in the eggshell's top. Then, one or two test materials are implanted onto the chorioallantoic membrane of the embryos. The embryos, having adhered to the shells, are carefully returned to the incubator. Over the course of up to 14 days, the development of microvasculature can be visualized and assessed using a microscope.

Despite the efficacy of *in-ovo* techniques, the *ex-ovo* (shell-less) CAM assay has emerged as a promising alternative. This method provides the advantage of real-time imaging and visualization of the entire CAM tissue at all stages of embryo development (Mangir et al., 2019). In the *ex-ovo* approach, fertilized chick embryos are incubated in a rotating humidified egg incubator at 37.5°C. After three days of incubation, the embryos are carefully extracted from their shells using a specialized cracking technique under sterile conditions. Once the embryo exhibits a well-established network, typically around day 7, sterile test materials are implanted on the shiny border of the CAM. In the subsequent days, the CAM region with the implant is imaged to assess the development of new blood vessels using a portable microscope. At day 14, the embryos are humanely sacrificed, and the retrieved implants can be subjected to further histological analyses. This *ex-ovo* approach offers distinct advantages in terms of real-time monitoring and visualization of angiogenic responses.

3 Materials and methodologies

3.1 Introduction

This chapter outlines materials and methods used to obtain results presented in this thesis's subsequent chapters. All experimental procedures were carried out with facilities available in Lancaster University, UK.

3.2 Hydroxyapatite and pearl/calcium phosphate composite

As a significant mineral constituent in bone tissue engineering, hydroxyapatite (HA) has been widely accepted in bone and dental applications due to its similarities to the mineral part of natural bone. Since the first process for the preparation of calcium-deficient HA was reported by Aikin (1807), the synthesis and research of calcium phosphate and its derivatives have been extensively developed. Since then, various techniques have been established to fabricate the

Innovative incorporation of pearl and calcium phosphate composite in bone regenerative scaffolds

HA, which has been classified into dry, wet, and high-temperature methods, such as chemical precipitation, sol-gel processing, hydrothermal process, co-precipitation, emulsion method, mechano-chemical method, ultrasonic method, microwave processing, emulsion-hydrothermal combination and microwave-hydrothermal combination methodology.

3.2.1 Synthesis of HA

In this research, the following reagents were used for hydroxyapatite synthesis: calcium nitrate tetrahydrate ($\text{Ca}(\text{NO}_3)_2 \cdot 4\text{H}_2\text{O}$, Acros Organics, Belgium); di-ammonium hydrogen phosphate ($(\text{NH}_4)_2\text{HPO}_4$, VWR-Prolabo Chemicals, Germany); ammonia solution ($\text{NH}_3 \cdot \text{H}_2\text{O}$, 35%, Thermo Fisher Scientific, UK); and ethanol (EtOH , $\geq 99.8\%$, AnalaR NORMAPUR[®], VWR-Prolabo Chemicals, France; 99.8%, ThermoScientific[™], UK). Commercial non-sintered HA particles (Plasma Biotol, CAPTAL[®], Buxton, UK) were used for comparison analysis. All solutions were dissolved and diluted in Milli-Q water (Milli-Q[®] Direct Water Purification System, Merck Millipore, Germany).

3.2.2 Chemical precipitation of HA

HA powders were obtained using a chemical precipitation method according to the protocol reported by Kumar et al. (2004). The chemical precipitation method took place in a two-neck, 2L round bottom glass flask placed in an oil bath (silicone oil), which was adjusted to and maintained at 75 °C for the whole reaction. To prevent evaporation and the potential over boiling of the solution, a glass condenser was fitted on the reactor's top neck to ensure the solution's refluxing and the cooling of ammonia gas (NH_3). The image of the reactor system during HA synthesis is shown below in Figure 3.1.

Calcium nitrate tetrahydrate ($\text{Ca}(\text{NO}_3)_2 \cdot 4\text{H}_2\text{O}$) solution and di-ammonium hydrogen phosphate ($(\text{NH}_4)_2\text{HPO}_4$) solution were prepared as the source of Ca^{2+}

and PO_4^{3-} , respectively. Ammonia solution ($\text{NH}_3\cdot\text{H}_2\text{O}$) was added dropwise to adjust the pH of the reaction solution. According to previous studies, the reactant solutions were prepared at a stoichiometric ratio of 0.1 M Ca^{2+} and 0.06 M PO_4^{3-} ions (equal to 1.67). For this, 0.1 M Ca^{2+} solution was prepared by dissolving the respective amount of $\text{Ca}(\text{NO}_3)_2\cdot\text{H}_2\text{O}$ in 200 mL of Milli-Q water; meanwhile, 0.06 M NH_4^+ solution was prepared in 200 mL Milli-Q water, respectively.

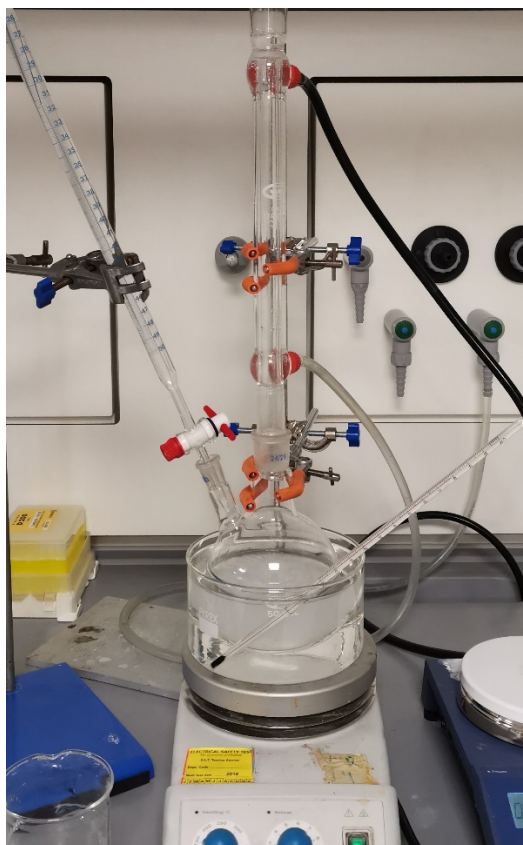


Figure 3.1 HA synthesis reaction set-up: A white HA solution formed during the reaction, which took place by the constant stirring of reagents in a round-bottom two-necked reactor placed in a silicone oil bath at 75 °C on a stirring heating plate. A glass condenser with water flow in the outer layer provides refluxing $\text{NH}_3\cdot\text{H}_2\text{O}$ and water, which was fitted on top neck of the reactor a dropping funnel for feeding reagent solution ($(\text{NH}_4)_2\text{HPO}_4$ solution), and a thermometer to monitor the temperature.

After dissolving to form the homogeneous solutions, the pH of both solutions was adjusted to 10.5 prior to starting the reaction by $\text{NH}_3\cdot\text{H}_2\text{O}$. Afterwards, the alkaline $(\text{NH}_4)_2\text{HPO}_4$ solution was added into the $\text{Ca}(\text{NO}_3)_2$ solution dropwise by

Innovative incorporation of pearl and calcium phosphate composite in bone regenerative scaffolds

maintaining constant stirring, the dropping speed was controlled strictly at 5 ml/min. When the addition of $(\text{NH}_4)_2\text{HPO}_4$ solution was finished, the pH of the reaction solution was measured and adjusted to 10 before adding the next round of NH_4^+ reagent solution. According to the total amount of NH_4^+ reagent solution and the speed of dropping, the pH adjustment process was repeated every hour to ensure the pH of the reaction solution was at 10 ± 0.3 . The stirring was stopped after a 4-hour reaction and then left the flask inside the silicone bath at 80 °C overnight to achieve an ageing effect. After the overnight ageing process, the solution was filtrated by using a vacuum filtration system with a 250 mm \emptyset filtration paper (Whatman™, Buckinghamshire, UK), a Büchner funnel, and a vacuum pump (Fisherbrand™, Leicestershire, UK).

During the filtration, HA precipitates were washed with Milli-Q water and repeated several (4-5) times until the final pH of the filtrated water reached below 8.0. Then, the neutralised precipitates were collected with the filtration paper inside a glass dish. Thereafter, the drying process was completed in a furnace (Carbolite® Gero, ELF 11/14B, Hope, Derbyshire, UK) at 80 °C for 48 h. The dried HA agglomerates were then crushed and ground in a mortar to obtain the fine HA powders.

3.2.3 Ethanol-based precipitation of hydroxyapatite

The equipment set-up for the synthesis of HA using the ethanol-based strategy was the same as aforementioned in the chemical precipitation method. The main difference in this strategy was the requirement to use the EtOH as the dissolving agent preparing the Ca^{2+} precursor. Similarly, two precursors were prepared separately at a stoichiometric ratio of 0.1 M Ca^{2+} and 0.06 M PO_4^{3-} ions (equal to 1.67). After dissolving to form the homogeneous solutions, the pH of both solutions were adjusted to 10.5 in prior, before starting the reaction by $\text{NH}_3 \cdot \text{H}_2\text{O}$. Afterwards, the alkaline $(\text{NH}_4)_2\text{HPO}_4$ solution was added into the $\text{Ca}(\text{NO}_3)_2/\text{EtOH}$ solution dropwise by maintaining constant stirring, and the dropping speed was controlled strictly at 5 ml/min.

When the addition of $(\text{NH}_4)_2\text{HPO}_4$ solution was finished, the pH of the reaction solution was measured and adjusted to 10 before adding the next round of NH_4^+ reagent solution. According to the total amount of NH_4^+ reagent solution and the speed of dropping, the pH adjustment process was repeated every hour to ensure the pH of the reaction solution was at 10 ± 0.3 . The stirring was stopped after a 4-hour reaction and then left the flask inside the silicone bath at 80 °C overnight to achieve an ageing effect. After the overnight ageing process, the solution was filtrated using a vacuum filtration system with a 250 mm \varnothing filtration paper, a Büchner funnel, and a vacuum pump. During the filtration, HA precipitates were washed with Milli-Q water and repeated several (4-5) times until the final pH of the filtrated water reached below 8.0. Then, the neutralised precipitates were collected with the filtration paper inside a glass dish. The drying process and vacuum filtration were employed for the final products, followed by the 48 h drying process.

3.2.4 Hydrothermal method synthesis of hydroxyapatite

In accordance with the research protocol from Wang et al. (2005), Neira et al. (2005) and previous related research about the hydrothermal synthesis of HA (Yan et al., 2001; Chaudhry et al., 2006; Khan et al., 2017), the low temperature (< 200 °C) hydrothermal synthesis of HA is more beneficial of controlling the crystal morphology of HA nanoparticles compared with other strategies. Previous reported hydrothermal syntheses of HA are generally conducted in a high-pressure long duration (over 16 h) system, in order to obtain the crystalline HA nanorods. In this research, based on the hydrothermal strategy modified and reported by the previous PhD student, further modifications were applied to the synthesis process.

Innovative incorporation of pearl and calcium phosphate composite in bone regenerative scaffolds

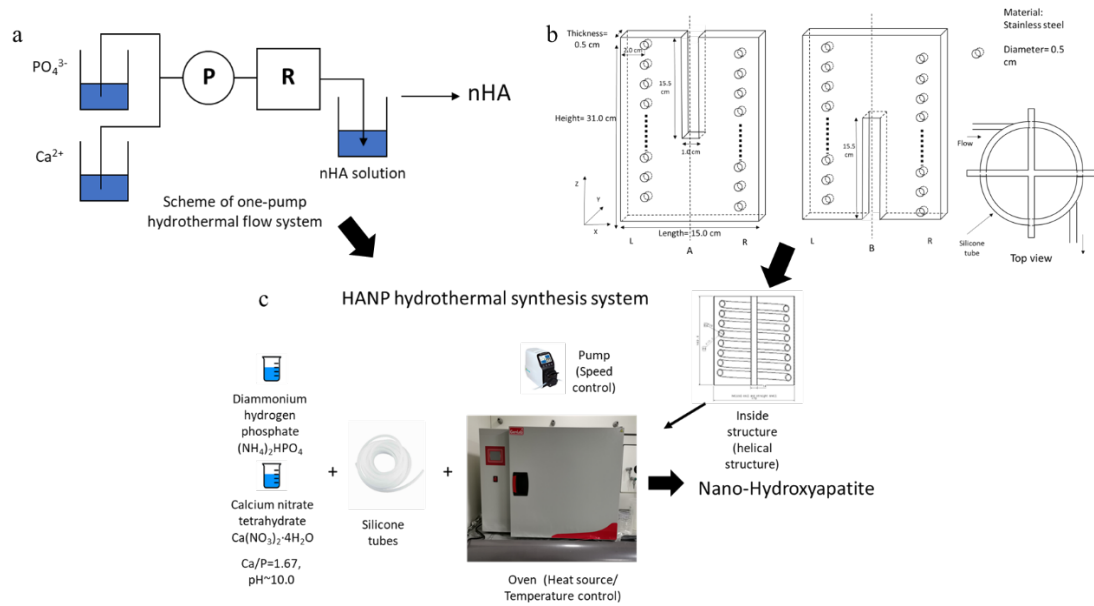


Figure 3.2 The flow chart of one-pump hydrothermal synthesis system (3.2a and 3.2c), and the helical stainless steel scaffold design (3.2b). The whole system used a peristaltic pump that can continuously drag both Ca^{2+} and PO_4^{2-} solutions into the heating oven with a constant speed. The helical scaffold with small holes inside the oven helped to increase the heat exchange area, in which the mixed solution flow through the reaction tubes, so that CaP/HA particles were generated along the reaction flow tube.

Similarly, the PO_4^{3-} and Ca^{2+} precursors were prepared by dissolving $\text{Ca}(\text{NO}_3)_2 \cdot 4\text{H}_2\text{O}$ and $(\text{NH}_4)_2\text{HPO}_4$ at the stoichiometric ratio in Milli-Q water, respectively. The oven was preheated to 150 °C before the start of reaction by adjusting the temperature control system. The pH of both solutions were adjusted above 10 before initiated the reaction. Afterwards, two solutions were mixed at a T-shape connector at the top of the oven at the same pace via a peristaltic pump as shown in Fig 3.2. After gathering all solution inside a round bottom flask, the product was immersed in the silicone oil at 150 °C overnight and then employed the vacuum filtration and drying process.

3.3 Synthesis of pearl/calcium phosphate (p/CaP) composite

According to the research presented by Ni and Ratner (2003), it has been noticed that nacre or pearl powders has the capability to transform to HA. The hypothetical formation mechanism of HA on the surface of pearl pellets was mentioned in the report that the pre-existed Ca^{2+} ions intend to bind with dissociated PO_4^{3-} to start a dissolution and precipitation reaction when soaked in phosphate buffer solution (PBS). This mechanism has also been applied to explain the formation of apatite coating layer on the surfaces of Bioglass® when implanted *in vivo*. Thus, in this research, the p/CaP composite particles were prepared by three different strategies based on the synthesis methods employed to obtain HA as aforementioned, including chemical precipitation, ethanol-based precipitation, and the hydrothermal method.

The experiment set-up was the same as mentioned in previous sections, that Ca^{2+} and PO_4^{3-} precursors were prepared in accordance with the stoichiometric ratio, respectively. However, to obtain the composite particles, pearl powders were weighted and pre-dispersed in Ca^{2+} solutions before starting the reaction. Other procedures including neutralisation and drying were following the same standard operations.

3.4 Scaffold fabrication

A bioactive polymeric scaffold plays a crucial role in facilitating the migration and differentiation of cells, both *in vivo* and *in vitro*. To be effective, the scaffold should possess a range of desirable properties, including cell attachment and migration, cell differentiation and proliferation, transport of biomolecules and nutrients, formation of extracellular matrix (ECM), and ultimately, the replacement and regeneration of functional tissues and organs. These properties

Innovative incorporation of pearl and calcium phosphate composite in bone regenerative scaffolds are essential for the scaffold to function as an artificial ECM that can support tissue growth and cell proliferation.

In designing a tuneable bioactive bone regenerative scaffold, several key features are necessary, including internal connectivity (at least >50%) (Mohammadi et al., 2021), pore sizes (100 to 600 μm) (Abbasi et al., 2020), mechanical strength (mimic the human bone tissue mechanical strength, as mentioned in Table 2.4 & 2.5), surface energy, biocompatibility, and biodegradability. These features not only support tissue growth and cell proliferation but also provide osteoinduction and osteogenic for this artificial ECM. osteoinduction refers to the ability of the scaffold to guide new bone growth, while osteoinductivity refers to the ability of the scaffold to stimulate stem cells to differentiate into preosteoblasts (Habibovic and de Groot, 2007). Osteogenic refers to the ability of the scaffold to promote the formation of new bone tissue.

In this study, the main fabrication methods used were freeze-drying and freeze-gelation. Sole chitosan (CS), HA/CS, pearl/CS, and p/CaP CS composite solutions were prepared and used to obtain the scaffolds. The synthesized p/CaP composites were evaluated for their physicochemical and biological properties. Chitosan, a natural polymer derived from chitin, is an excellent choice for scaffold fabrication due to its biocompatibility, biodegradability, and ability to promote cell attachment and proliferation. The addition of HA, a naturally occurring mineral that is a key component of bone tissue, can improve the mechanical properties of the scaffold and enhance its osteoinduction and osteogenesis. Pearl, another natural mineral, has also been shown to improve the mechanical strength of the scaffold.

The evaluation of the physicochemical and biological properties of the synthesized p/CaP composites is crucial in determining their effectiveness as a scaffold. Physicochemical properties such as surface area, pore size, and pore volume affect cell attachment, proliferation, and migration. Biological properties, such as cell viability, cell proliferation, and osteogenic differentiation, are critical for determining the scaffold's ability to support tissue growth and regeneration.

In conclusion, the design of a tuneable bioactive bone regenerative scaffold requires careful consideration of several key features, including internal connectivity, porosity, mechanical strength, surface energy, biocompatibility, and biodegradability. The use of chitosan, HA, and pearl in scaffold fabrication offers an effective approach for achieving these desirable properties. The evaluation of the physicochemical and biological properties of the synthesized p/CaP composites is crucial in determining their effectiveness as a scaffold for tissue growth and regeneration.

3.4.1 Freeze drying fabrication method

A common method to fabricate porous scaffolds with different pore sizes and interconnections is freeze drying or lyophilisation. This method is more ecofriendly than other methods such as particle leaching, emulsion templating, 3D printing and electrospinning, because it uses less organic solvents, shorter washing treatment and no etching procedure. Moreover, by changing variables during the freezing process, freeze drying can produce scaffolds with various porous morphologies and nanostructures. The addition of HA, pearl and pearl/CaP composite to chitosan scaffolds can enhance their mechanical and biological properties.

The fabrication of freeze-dried scaffolds involves four stages: solution formulation, unidirectional solidification of slurries, sublimation of ice crystals and subsequent thermal treatment. Four types of solutions were formulated in this study, namely pure chitosan solution, HA-chitosan solution, pearl-chitosan solution and pearl/CaP-chitosan composite solution, with varying component concentrations based on the weight fraction (10, 20, 30, 40 and 50 wt.%). The incorporation of HA, pearl or pearl and CaP into chitosan was intended to enhance the mechanical and biological performance of the scaffolds.

The chitosan solution was prepared by dissolving medium molecular weight chitosan powders (100 kDa to 300 kDa, Acros Organics, Germany) in 0.2 M acetic acid and heating and stirring at 50°C for 1 h, followed by cooling to room temperature for over 6 hours. Then, the ceramic components were added

Innovative incorporation of pearl and calcium phosphate composite in bone regenerative scaffolds

gradually to the solution and stirred overnight. The slurries were then poured into transparent plastic petri dishes ($\varnothing = 75$ mm) and degassed at room temperature for 2 hours to remove small bubbles. The samples were frozen in the freeze dryer from 0 °C to -20 °C (the gradient is -4 °C/h) for 24 h and then sublimated under a pressure of 0.7 mbar for over 24 h. Afterwards, the obtained scaffolds were processed a neutralization step that transferred the scaffolds from the original petri dishes by pressing the edges to larger petri dishes. The 3M EtOH/NaOH solution (90-95%) was applied for the neutralisation process that all scaffolds were immersed in the alkaline solution for another 12 h. Later, a series of wash and rinse steps were performed including, (1) 15 min in Milli-Q water, (2) 5 min in PBS solution, (3) 15 min in 80% EtOH solution, and (4) 15 min in 100 EtOH solution Thus, the scaffolds were left half covered in the hood to dry for 8-15 h.

3.5 Physical characterization

This section of the chapter outlines different physical characterisation methods performed in this project on both the scaffold samples and p/CaP composite particles to examine detailed morphological features. It consists of thermal gravity analysis (TGA) for the dynamic thermal properties of composite particles, scanning electron microscopy (SEM) to investigate the morphological properties of composite particles and composite scaffolds, porosity estimation by SEM, Brunauer-Emmett-Teller (BET) analysis and the liquid displacement method to measure the interconnectivity, pore size and porosity of scaffold samples.

3.5.1 TGA

The mass changes and thermal effects of pearl powders, HA powders and the p/CaP composite powders were measured using a simultaneous thermal analyser (NETZSCH STA 449 F3 Jupiter®) at the Engineering department of

Lancaster University. Powder samples were dried in an oven at 80 °C for 48 hours before being weighed (approximately 30.0 mg) and placed into aluminium crucibles for analysis. The temperature was set to increase from room temperature to 1100 °C at a rate of 10 °C/min in an air flow of 100 mL per minute. The software recorded the data in .csv files, which were analysed by plotting percentage of weight and derivative versus temperature in Origin 2021 software (OriginLab Corporation, Northampton, Massachusetts, USA).

3.5.2 SEM

Microstructure and morphology analysis of pearl, HA, p/CaP composite particles and bioactive scaffolds were performed by the JEOL JSM-7800F Scanning Electron Microscope (SEM) instrument (Field Emission SEM, JEOL Ltd., Tokyo, Japan). Prior to imaging, samples were mounted into 12.5 aluminium stubs using the double-sided carbon adhesive tabs (12 mm), and sputter-coated with gold powder (5 nm) once.

For particle samples, before imaging, powders were dried in oven at 80 °C for 48 hours in prior, the used a spatula to scoop a miniature portion of specimens on the carbon tabs. A aluminium stub was applied to tap a uniform distribution. For scaffold samples, all specimens were dried in oven at 40 °C for 48 hours in prior, then sectioned into cross-section, top surface and bottom surface specimens, respectively. Then, on each stub, three different surface scaffolds from the same sample were mounted horizontally in order to improve the electrical conductivity and facilitated detailed imaging.

3.5.3 Porosity estimation

In this study, the porosity of composite scaffold samples was analysed using the liquid displacement method, which is a commonly used technique in materials science research (Zhang et al., 1999; Hsu et al., 1997). Prior to analysis, all

Innovative incorporation of pearl and calcium phosphate composite in bone regenerative scaffolds scaffolds were dried in an oven for 48 hours under 40°C to ensure that they were completely dry. Three random circular scaffold specimens with a diameter of 10mm were then cut using a laser with a maximum power of 8% and a speed of 75mm/s.

To determine the porosity of the scaffold, the circular specimen of weight W was immersed in a graduated cylinder containing a known volume (V_0) of ethanol. Care was taken to ensure that no visible air bubbles emerged from the scaffold, and the cylinder was left for 5 minutes. The total volume of ethanol and ethanol-saturated scaffold was then recorded as V_1 . The volume difference ($V_1 - V_0$) represented the volume of the scaffold skeleton, while the residual ethanol volume after removing the scaffold from the cylinder was recorded as V_2 . The quantity ($V_0 - V_2$) was determined as the void volume of the foam. The total volume of the scaffold was then calculated as $V = (V_1 - V_0) + (V_0 - V_2) = V_1 - V_2$. The density of the scaffold (d) was expressed as $d = W / (V_1 - V_2)$, and the porosity of the scaffold (ϵ) was obtained by $\epsilon = (V_0 - V_2) / (V_1 - V_2)$.

In addition to porosity analysis, the SEM imaging of scaffolds was also analysed using ImageJ software (Version 1.53K). The results were calculated automatically by the distribution calculator from the software to attain an average distribution of pore size. It is worth noting that the standard deviation of 10% was obtained for all the measurements, indicating a reliable and consistent method for scaffold characterization. Overall, the combination of porosity analysis and SEM imaging provides valuable insights into the structural and morphological characteristics of the scaffold, which are crucial for optimizing its design and performance in bone tissue engineering applications.

3.5.4 BET

Surface area measurements of pearl, HA and p/CaP composite powders were recruited by the BET instrument (3 Flex Micromeritics® Instrument Corporation, Norcross, GA 30093 USA). Before analysing, powder samples were dried in the oven at 150 °C for 48 hours. 100 mg specimens were weighted and

then degassed inside the sample tubes at 200 °C for 2 hours. The BET analysis was set at 77K by using liquid nitrogen and using the nitrogen as the adsorptive gas. Measurement results were exported from the 3 Flex software (Version 6.01) as the .csv files and then imported into the Origin 2021 for data analysis.

3.6 Chemical characterization

The chemical structural properties of the powder samples and the composite scaffold samples were investigated by vibrational spectroscopy and X-ray diffraction (XRD) spectroscopy. Vibrational spectroscopy included Fourier Transform Infra Red (FTIR) spectroscopy and Raman spectroscopy. These techniques can provide information about the functional groups, molecular bonds and crystallinity of the materials. XRD spectroscopy was performed using a Single crystal and powder XRD-Rigaku SmartLab in the Department of Chemistry at Lancaster University. XRD can reveal the phase composition, crystal structure and lattice parameters of the materials.

3.6.1 FTIR spectroscopy

The FTIR spectra were collected from the Nicolet™ iN10 Infrared Microscope (Thermo Fisher Scientific Inc, Madison, WI, USA) and the results were by using the Thermo Nicolet OMINICTM Picta (Version 9.5.9, Thermo Fisher Scientific Inc, Madison, WI, USA) software then analysed by using Origin2021 (OriginLab Corporation, Northampton, Massachusetts, USA) software.

In this research, the FTIR-attenuated total reflectance (FTIR-ATR) was applied to analyse the chemical functional groups at the surface of the scaffold samples, which has been believed to be a fast and easy technique to be operated. The FTIR-photo acoustic sampling (FTIR-PAS) technique is another suitable method for the characterization of powder samples because of the heat conversion from the PAS signal that can convey to the surface of samples and then generates

Innovative incorporation of pearl and calcium phosphate composite in bone regenerative scaffolds

spectrum signals. Therefore, scaffold samples were analysed with the FTIR-ATR and powders were detected with the FTIR and FTIR-PAS spectroscopy. Powder samples powders were filled into metal sample holders ($\varnothing=10$ mm, x 2.5 mm depth) and the sample surface was flattened to level it with the top of the holder when using FTIR-PAS. Spectral data was acquired in the mid-infrared region ($4000-400\text{ cm}^{-1}$), at 4 cm^{-1} resolution, 200 spectrograph apertures accumulating 128 scans. Scaffold samples were cut into rectangular specimens ($10 \times 10\text{ mm}^2$, 6 mm in height) in prior, and the spectra was collected in the mid-infrared region by using an aperture of 150 with a resolution of 4 cm^{-1} accumulating 64 scans to acquire in FTIR-ATR mode. All background spectra were measured in prior and renewed every 2 hour. Both FTIR-ATR and FTIR-PAS spectra were collected by using the Nicolet™ iS50 spectrophotometer ((Thermo Fisher Scientific Inc, Madison, WI, USA)) in conjunction with the Thermo Nicolet OMNIC™ (Version 9.5.9, Thermo Fisher Scientific Inc, Madison, WI, USA) software, and then exported in .csv files then analysed by using the Origin2021 (OriginLab Corporation, Northampton, Massachusetts, USA) software.

3.6.2 Raman spectroscopy

The non-destructive vibrational spectroscopy technique, Raman spectroscopy, has been widely applied for analyzing the chemical structure, phase and polymorph, molecular structure and molecular interaction of non-biological and biological samples.

HA samples obtained by different synthesis strategies were analyzed via the dispersive Raman instrument (Thermo Scientific dxr™, Thermo Fisher Scientific Inc, Madison, WI, USA) and DXRxi Raman imaging microscope (Thermo Scientific dxr™xi, Thermo Fisher Scientific Inc, Madison, WI, USA). All spectra were collected with a 532 nm laser with the power of 10 mW, a pinhole aperture of 50 μm , an objective lens of x10 and 10 sec exposures for 30 scan times. Samples were mounted as a flat thin layer in the middle of a calcium fluoride slide. Spectra data was collected and analyzed by using the Thermo Nicolet OMNIC™ (Version

9.5.9, Thermo Fisher Scientific Inc, Madison, WI, USA) software, then plotted by using the Origin2021 (OriginLab Corporation, Northampton, Massachusetts, USA) software.

3.6.3 X-ray diffraction (XRD) spectroscopy

In this study, XRD was used to characterize various types of powders, including commercial and synthesized HA powders, pearl powders, and composite pearl powders. The measurements were performed using the SmartLab (Rigaku SmartLab®, Rigaku Co. Ltd., Japan) X-ray diffraction meter at the step size of $0.02^\circ 2\theta$ and the speed of $10^\circ 2\theta$ per min. A Cu K α tube operated at 40 kV and 80 mA was used for the generation of X-rays. The resulting spectra were analysed using the PDXL (Rigaku Co. Ltd., Japan) software, and .csv files were exported for further analysis in Origin2021 (OriginLab Corporation, Northampton, Massachusetts, USA) software.

To ensure the accuracy and reliability of the measurements, high-quality XRD pattern graphs acquired from the PDF-4 + 2021 (ICDD®, USA) software were used as standards. The use of standards is essential for ensuring that the peaks observed in the spectra correspond to the correct crystal structure and composition. The XRD analysis provided valuable information about the powders, including their crystal structure, phase purity, and composition. This information is essential for understanding the properties and potential applications of the powders in various fields, including materials science and biomedical engineering.

3.6.4 X-ray Photoelectron Spectroscopy (XPS)

In this study, the high resolution XPS spectra were obtained by the Kratos AXIS Supra (Kratos Analytical Ltd, Manchester, UK) XPS spectrometer. The detailed setup information was listed in the following results and discussions chapter.

3.7 Compressive strength characterization

Bone tissue regeneration involves scaffold design which has significant impact on the mechanical properties of bone. The goal is to repair, preserve or enhance damaged organs or tissues. The scaffolds must support cell function and growth by providing similar strength and structure as natural bones.

The mechanical strength of the fabricated scaffolds was analysed using a Universal Testing Machine (Instron® 3345, Norwood, MA, USA). The specimens for compression test were cut with a high-power laser processing workstation built by the School of Engineering of Lancaster University. A 100 kN load cell for compression tests to measure the deformation. The resultant data from the Bluehill® Universal Software (Version 4.06, Norwood, MA, USA) was imported into Origin2021 (OriginLab Corporation, Northampton, Massachusetts, USA) software for plotting. The Young's modulus was calculated based on the linear portion of the stress-strain curve.

The cylindrical porous composite scaffolds with an average diameter of 10 mm were tested in compression using a 100 kN load cell at a crosshead speed of 1 mm/min up to 70%, following the literature (Kathuria et al., 2009). Before testing, the sample was placed on the bottom compression plate and the upper compression plate was lowered until it touched the upper surface of the sample. The stress and strain in compression were calculated using the following equations:

$$\text{Stress} = \left(\frac{\text{Force}}{\pi \times (\text{radius of scaffold})^2} \right)$$

$$\text{Strain} = \left(\frac{\text{Deformation}}{\text{Original thickness of scaffold}} \right)$$



Figure 3.3 Image of the setup of compression testing of a composite porous scaffold specimen placed onto a lower compression plate in the Instron® UTM instrument in this experiment (Instron® 3345, Norwood, MA, USA).

3.8 Biological characterization

The scaffolds fabricated by the freeze drying technique were biologically evaluated to determine their suitability for bone tissue engineering applications and to optimize the regeneration parameters for creating an *in vitro* model. The evaluation involved using human osteoblasts from established cell lines and seeding them on the scaffolds. The cells were then cultured under physiological conditions for *in vitro* analysis of their viability, proliferation, adhesion and differentiation on the scaffolds.

The characterization in this research included the following aspects. The description of the cell culture methods and materials used in this study, such as the human osteoblast-like cell line MG-63 and the culture medium components. The evaluation of the swelling and in-vitro degradation properties of the

Innovative incorporation of pearl and calcium phosphate composite in bone regenerative scaffolds modified scaffolds before performing the cell culture experiments. These properties affect the mechanical stability and biodegradability of the scaffolds. The assessment of the biocompatibility and angiogenesis potential of the composite scaffolds with different compositions and formulations. The biocompatibility was measured by using AlamarBlue® (AB) assay and optical microscopy to examine the cell viability, proliferation, adhesion and differentiation on the scaffolds. The angiogenesis was investigated by using an ex-ovo Chick Chorioallantoic Membrane (CAM) assay to implant scaffold samples on chick embryo tissues at 37.5 °C. The microvascularization on CAM in contact with samples was imaged and quantified to compare angiogenesis among different specimens.

3.8.1 Cultured cells

The MG-63 cell line was selected as the primary focus of this study due to its widespread use in the field of bone tissue engineering research. This cell line, derived from osteosarcoma, shares similarities with other osteosarcoma-derived cell lines, including Saos-2 and U-2 OS, that offer advantages over non-cancerous osteoblast-like cells. Specifically, they exhibit a faster proliferation rate and superior adhesion to culture surfaces. However, it is important to note that these cancerous cells differ significantly from normal osteoblasts in terms of their ECM composition, collagen production, proliferation kinetics, and osteoid formation. These differences may be attributed to the fact that they originate from malignant bone tumours. Despite these differences, MG-63 is still considered a valuable model for studying osteoblast-like cell behaviour.

To ensure that an adequate number of MG-63 cells were available for this study, cell preservation and storage were necessary. Therefore, the cells were subjected to a process of thawing and freezing down to maintain them at identical passage numbers. This step was essential for maintaining consistency in the experimental conditions and reducing variability between samples. The preservation of MG-63

cells in this manner has been previously shown to be effective and has not been found to affect the behaviour or characteristics of the cells.

To freeze cells at a specific passage number after culturing, the initial step involved was to remove the old media from each T75 flasks. Afterward, the flask was washed with Dulbecco's Phosphate-Buffer Saline 1X (DPBS, Sigma Aldrich, USA) twice to eliminate any traces of remaining media. Next, 3 ml of trypsin-EDTA (Sigma Aldrich, USA) was added to each flask, and the flask was incubated for 5 minutes to assist in detaching cells from the bottom. The flask was then inspected under a microscope to ensure that all cells had detached completely.

To stop the action of trypsin-EDTA, 7 ml of fresh media was added to the flask, resulting in a total volume of 10 ml. The mixture was then centrifuged at 3500 rpm for 5 minutes, and the supernatant was discarded. The pellet was resuspended in media, and 15 μ l of cell suspension was placed in a hemocytometer, where the cells were counted under a light microscope. By estimating the total number of suspended cells in the media based on the average number of counted cells, the appropriate volume of cell suspension needed to achieve the closest million cells was determined, aspirated, and re-centrifuged. The next step involved adding freezing media consisting of 90% fetal calf serum (FCS, Sigma Aldrich, USA) and 10% dimethyl sulfoxide (DMSO, Sigma Aldrich, USA) to the cell pellet, and then resuspending the cell suspension. Finally, the cell suspension was aliquoted into cryovials and frozen in an isopropanol container at a concentration of 1 million cells/ml for 24 hours at -80°C , before being transferred to liquid nitrogen for long-term storage.

To revive or defrost frozen cells that had been stored in liquid nitrogen, a universal tube containing 20 ml of working media was first warmed in a 37°C water bath for 10 minutes. Subsequently, a cell vial containing roughly 1 ml of cell suspension was taken out of the liquid nitrogen and thawed in the water bath for approximately 4 minutes, or until only a small ball of ice remained in the vial. The vial and universal tube with media were then transferred to a tissue culture cabinet and mixed to achieve a total volume of 21 ml in the universal tube. The universal tube was centrifuged at 3500 rpm for 5 minutes, after which the

Innovative incorporation of pearl and calcium phosphate composite in bone regenerative scaffolds

supernatant was discarded. The remaining cell pellet was resuspended in 1 ml of working media and split into a 1:20 ratio for MG-63 cells. The resulting suspension was then transferred into a T75 flask containing around 14 ml of working media. After gently rocking the flask, it was placed in an incubator, and the media was changed every 2-3 days. All cells were monitored for proliferation and morphological changes, and when the cells reached 70-80% confluency, they were passaged into new T75 flasks for cell expansion, using trypsin-EDTA.

In conclusion, the selection of the MG-63 cell line for this study was based on its established role in bone tissue engineering research, as well as its advantages over non-cancerous osteoblast-like cells. Despite its cancerous origins, the use of this cell line provides valuable insight into osteoblast-like cell behaviour. Furthermore, preserving the cells through a process of thawing and freezing down allowed for consistency in the experimental conditions, reducing variability between samples.

3.8.2 *In-vitro* degradation tests

In tissue engineering, the rational design and fabrication of scaffolds play a pivotal role in determining the success of regenerative strategies (Mikos et al., 1993). A critical aspect of scaffold performance is its degradation behaviour, which necessitates comprehensive analyses to understand the intricate interplay between the scaffold and the surrounding biological milieu. Among the various analytical techniques employed, pH analysis and weight analysis emerge as a particularly crucial tool in unravelling the complexities of scaffold degradation processes.

In the degradation test, similar scaffold specimens were prepared using the same method as the swelling test and were placed in 3 mL of media solutions (PBS or lysozyme) in 7 mL vials at 37 °C for 1, 4, 7, 14, 21 and 28 days. The initial weight of specimens was recorded as w_i . The media solutions were changed every 2 days to maintain the conditions and ensure accurate results. The pH of the media solutions was measured using a pH-meter after every media change. After pH

measurements, samples were washed thrice with 1 mL of de-ionized water to remove surface ions, and weights were recorded as w_t after incubating the samples at 37 °C for 24 h to remove surface water without altering their original shape. The degree of in vitro degradation was calculated by the weight loss:

$$\text{Weight loss (\%)} = \frac{w_i - w_t}{w_i} \times 100\%$$

3.8.3 3-Dimensional cell culture

Three-dimensional (3D) cell culture on bioactive scaffolds is an emerging field in tissue engineering and regenerative medicine. Bioactive scaffolds provide a three-dimensional microenvironment that mimics the extracellular matrix (ECM) of tissues, which can guide cell behaviour and promote tissue regeneration. In 3D cell culture on bioactive scaffolds, cells are seeded onto or within the scaffold, where they can attach, proliferate, and differentiate in response to signals from the scaffold. This technique has the potential to revolutionize the field of tissue engineering by providing a more biomimetic platform for studying cellular behaviour and developing therapies for tissue repair and regeneration.

In this study, the viability and biocompatibility of the scaffolds were investigated using the osteoblast-like MG-63 cell lines. To prepare the scaffold samples obtained from the freeze-gelation, a cork borer was used. The samples were sterilized by immersing them in 70% ethanol for 2 hours in 48-well plates, followed by evaporating the ethanol for 24 hours in a Biological Safety Cabinet (Type-II) (BSC). After the sterilization process, the sterile samples were washed thrice with PBS, with 15 minutes of incubation between each wash to remove any residual ethanol.

Prior to cell seeding, the samples were conditioned with 200 μ L of serum-containing DMEM for 1 hour. Then, a suspension of MG-63 cells with a concentration of 2×10^5 cells/mL was seeded onto each scaffold sample using 100 μ L drops, achieving a final concentration of 2×10^4 cells/mL per sample. The cell-seeded samples were incubated in 1 mL of growth media. As a control, cells

Innovative incorporation of pearl and calcium phosphate composite in bone regenerative scaffolds with the same concentration were also seeded into empty wells of Tissue Culture Plastic (TCP). After cell seeding, the well plates were incubated overnight at 37.5 °C to allow for cell attachment.

3.8.4 Cell viability (AlamarBlue® assay)

To investigate the biocompatibility of the scaffolds and the proliferation of cells, MG-63 human cancerous osteoblast cell lines were defrosted and passaged in advance for the experiment. The cells were incubated in a Dulbecco's Modified Eagle Medium (DMEM, Gibco®, ThermoFisher™, Loughborough, UK) culture media supplemented with 10% of fetal calf serum (FCS, Sigma-Aldrich®, Dorset, UK), 1% penicillin/streptomycin (P/S, 10,000 U/mL, Gibco®, ThermoFisher™, Loughborough, UK). The adherent MG-63 cells were detached by using trypsin-EDTA (Gibco®, ThermoFisher™, Loughborough, UK) when they reached 90% confluency and passaged.

The AlamarBlue® (AB) assay was performed following the standard protocol which has been developed over 50 years (Bonnier et al., 2015; Mosmann, 1983). As a non-invasive indirect testing method, the AB assay utilized the diluted non-fluorescent resazurin sodium solution incubated with the samples then reduced to a fluorescent compound inside the media solutions. This reduction causes the colour change of the resazurin solution from dark blue to a pink colour then sent to the multiplate reader for fluorescence intensity or the absorption intensity detection. This indirect measurement could be considered as an indication of the viability or cytotoxicity for cell culture.

For preparing the resazurin solution, the procedure followed the standard protocol reported by Palomino and Portaels (1999). In general, the stock resazurin sodium solution was prepared in advance by dissolving the resazurin sodium salts in 1x PBS solutions to 0.26 g/L. The solution was then sterilized by filtering through a 0.20 µm polyethersulfone (PES) filter into a sterile glass bottle covering aluminium foil to prevent direct light exposure and storing at 4 °C. The

experimental resazurin solution was freshly prepared by diluting the stock solution with the DMEM media (1:9) and pre-warmed to 37 °C in advance.

All neutralized samples were cut by the cork borer with the diameters of 12 mm after soaking in 1% P/S-PBS solution overnight for rehydration. Following cutting three replicates from each sample groups, all specimens were placed into the 24-wells culture plates and then sterilized by immersing into 70% ethanol for 2 hour and then evaporated the ethanol for 24 hours in a Biological Safety Cabinet (Type-II) (BSC). Sterilized samples were then exposed under the UV light for 15 min for the extra sterilization. The cell contained media were seeded on the scaffolds after diluting cell media to a certain concentration (20,000 cells/mL in this study). After cell seeding, the well plates were incubated overnight at 37 °C for cell attachment and at the next day the AB assay was performed for cell attachment and cytotoxicity and the inflorescence intensities were recorded as the data of Day 1. In the rest of experiments, the AB assay were measured in different time intervals, including Day 1, Day 3, Day 6, Day 10 and Day 14.

At determined culture intervals, cultured samples were washed with 1 mL of PBS. Then, samples were immersed into 1 mL of resazurin solution in the wells of a 24 well-plate, which was covered with aluminium foil to prevent light contact, and incubated for 4 hours. After 4 h, the reduced resazurin media (resorufin), which transforms from blue towards pink tones, were taken in triplicate from each well as 200 µL aliquots, and poured into the wells of a 96-well plate with a zigzag pattern to prevent fluorescent interference of adjacent wells. The fluorescence values of the aliquot solutions were measured in a Infinite® 200 PRO microplate reader (TECAN®, Tecan Group Ltd., Männedorf, Switzerland) by using excitation and emission light wavelengths of 530 and 590 nm, respectively.

The AB assay results were expressed as a mean with standard deviations (SD) for repetitions. The statistical analyses were performed in GraphPad Prism (Version 8.0.2, San Diego, CA, USA) software by using Two-way ANOVA test. SEM scanning by using the Schottky Field Emission Scanning Electron Microscope (FESEM) (JEOL JSM-7800F, Tokyo, JAPAN) were performed for the morphological evaluation of visible cells attached on the scaffolds.

4 Physical and chemical studies of synthesized powders and composite scaffolds

4.1 Introduction

Bone tissue engineering is a rapidly growing field that aims to create functional bone tissue for the regeneration or repair of damaged bone. This process involves the use of various materials that can either stimulate the formation of bone from surrounding tissues or act as a template for the implanted bone cells. Four key components are required to achieve this, including a) a morphogenetic signal, b) responsive host cells, c) a suitable carrier for cells, and d) a viable and well-vascularised host bed (Burg et al., 2000; Croteau et al., 1999). Bioceramics are an important class of materials that have gained significant attention for their

Innovative incorporation of pearl and calcium phosphate composite in bone regenerative scaffolds potential applications in various fields of medicine, including bone tissue engineering, dental implants, and drug delivery. Hydroxyapatite (HA) and pearl are two of the most widely studied materials among these bioceramics due to their excellent biocompatibility and unique properties. HA is a natural mineral form of calcium apatite found in bones and teeth, and its chemical and physical similarity to the mineral component of natural bone makes it an attractive material for bone tissue engineering. On the other hand, pearl, a biogenic material, is composed of calcium carbonate and exhibits unique properties such as biocompatibility, biodegradability, and osteoinductivity. In recent years, significant progress has been made in the development of bioceramics and their use in various medical applications.

On the other hand, scaffolds also play an essential role in bone tissue engineering, which provides a 3D porous structure that facilitates cell attachment, growth, and matrix deposition. An ideal scaffold should have a suitable surface chemistry supporting cell attachment, proliferation, migration, and development. The surface chemistry can be tailored to control cellular behaviour and encourage the differentiation of mesenchymal stem cells into osteoblasts, which are responsible for bone formation. In addition, the scaffold should be biocompatible to avoid any adverse immune reactions or toxicity. Furthermore, the scaffold should support an extracellular matrix's production, organisation, and maintenance (Gogolewski, 2007; Gorna and Gogolewski, 2003). The extracellular matrix is a vital component in bone tissue engineering, providing the mechanical strength and structure required for bone regeneration.

In addition to being biocompatible and supporting the production of an extracellular matrix, scaffolds are required to be composed of highly interconnected porous networks to facilitate cell migration and nutrient distribution. These interconnected networks provide a pathway for delivering nutrients and oxygen to the cells and removing waste products. Furthermore, the pore size and distribution can be tailored to control cell behaviour and encourage the formation of new bone tissue.

This chapter demonstrates the physical and chemical characteristics of synthesized pearl, HA, p/CaP composite powders and composite chitosan scaffolds in diverse aspects, including TGA, SEM, porosity estimation, BET, FTIR, Raman spectroscopy, XRD spectroscopy, and mechanical characterisation. The physical and chemical characterisation of scaffold and composite pearl/calcium phosphate (p/CaP) powders is crucial in developing novel biomaterials for tissue engineering and regenerative medicine applications. Understanding the physical and chemical properties of these powders is essential to optimise their performance in vivo and ensure their safety and biocompatibility. By understanding the physical and chemical properties of synthesized particles, researchers can design more effective biomaterials that promote tissue regeneration and improve patient outcomes.

4.2 Physical study of powder and scaffold samples

4.2.1 TGA results and discussion of powders samples

Using the simultaneous thermal analysis technique, the thermal properties of pearl powders, HA powders, and pearl/calcium phosphate (p/CaP) composite powders were analyzed in the temperature range of 25 °C to 900 °C and 25 °C to 1100 °C, respectively. Figure 4.2.1 shows the weight loss of all the samples, while Figure 4.2.2, 4.2.3, and 4.2.4 depict the thermal stability analysis of each of the three samples individually. The weight loss observed in all the samples between 25 °C and approximately 150 °C is attributed to the removal of physical and chemically absorbed water. Between 200 °C and 700 °C, the second weight loss step was associated with the loss of both lattice water and organic content. From 700 °C onwards, significant differences in the thermal stability of the three different powder particles were observed which are discussed in detail below.

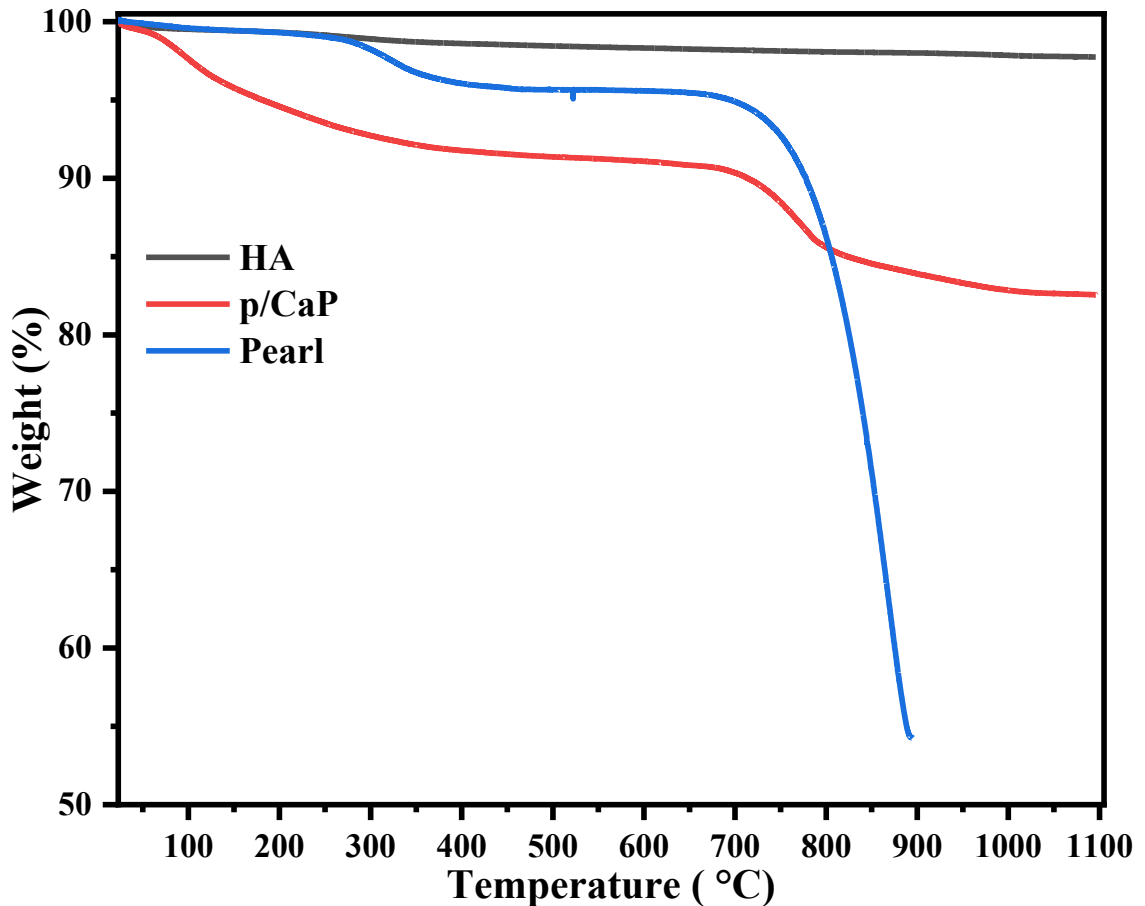


Fig 4.2.1 Thermal gravimetric analysis (TGA) data curves displaying the mass loss of hydroxyapatite (HA), pearl and pearl/CaP (p/CaP) composite powders. HA is in black line, pearl is in blue line and p/CaP is in red line.

In this research, the HA powder implemented in this TG analysis was synthesized in the lab. The thermal stability of HA has been extensively researched in the past, as reported in previous studies. Figure 4.2.2 illustrates the weight loss of the HA powder at temperatures ranging from 25 °C to 200 °C, which is attributed to the removal of absorbed water without any impact on lattice parameters, as observed by Zhou et al. (1993), Liao et al. (1999), and Mkukuma et al. (2004). Following this, there was a more rapid weight loss of approximately 0.66% between 210 °C and 400 °C, indicating the release of OH⁻ ions, leading to the contraction of α -lattice dimension, as noted by Liao et al (1999). Furthermore, a moderate broad exothermic peak observed at around 299 °C and a broad exothermic peak at 376 °C in the DTA curve confirmed the decomposition of

lattice water which is in agreement with the report by Ashok et al (2002). These findings indicate that the thermal behaviour of the synthesized HA powder is consistent with previous studies, and the TGA analysis results are reliable.

At higher temperatures, the weight of HA slowly decreased in the temperature range of 410 °C to 800 °C. Three exothermic peaks were obtained between 400 °C to 800 °C without any significant weight loss, at 459 °C, 559 °C and 671 °C, respectively. As reported in previous studies (Ashok et al., 2002; Liao et al., 1999; Mkukuma et al., 2004; Zhou et al., 1993), the constant dehydration of HA leads to the release of OH-1 during the heating. This causes the transform of HA into the oxyhydroxyapatite (OHA). The OHA can be presented by a formula: $Ca_{10}(PO_4)_6OH_{2-2x}O_x \square_x$, where \square stands for a vacancy (Zhou et al., 1993). In the range between 800 °C and 1100 °C, researchers pointed out the traces of β -tricalcium phosphate (β -TCP) and tetracalcium phosphate (TetCP) were observ-

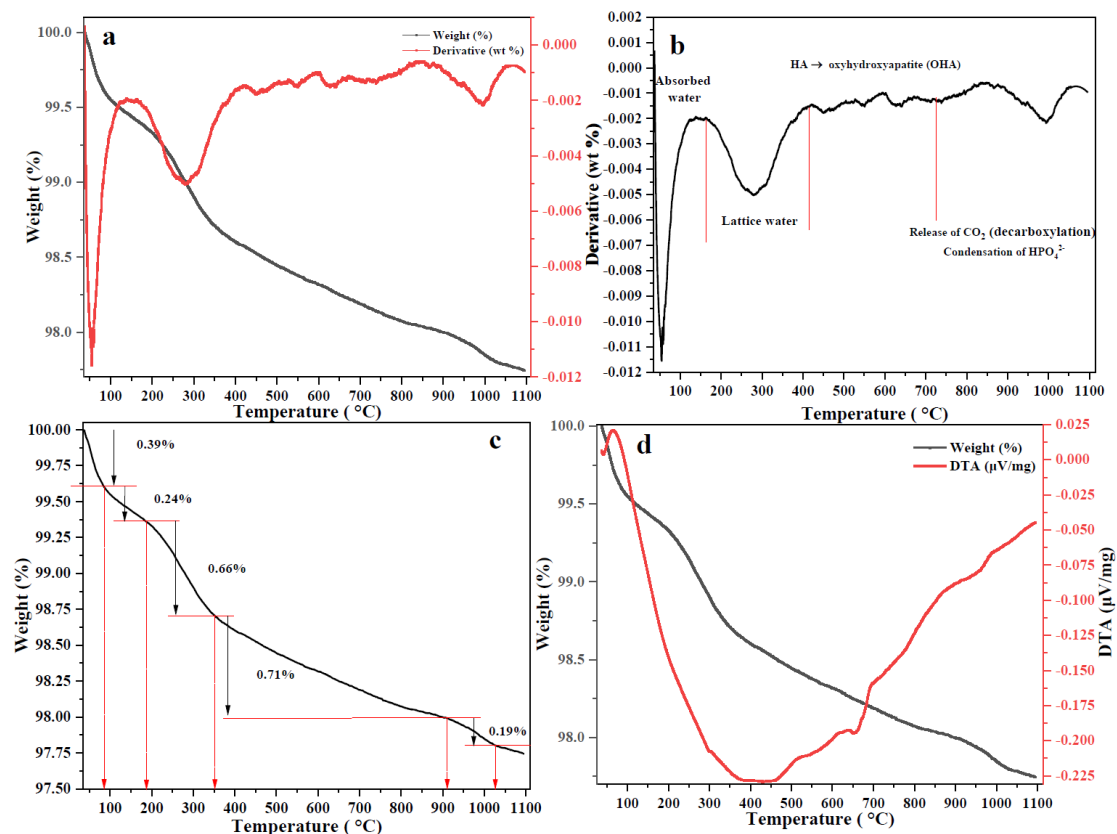


Fig. 4.2.2 TGA data curves demonstrating the weight loss versus temperature, including the 1st derivative of weight for the HA sample. (a) weight loss and derivative of weight against temperature. (b) 1st derivative of weight against temperature. (c) weight loss versus temperature curve. (d) DTA and weight loss against temperature curve.

Innovative incorporation of pearl and calcium phosphate composite in bone regenerative scaffolds

-ed in X-ray diffraction patterns in air, argon and CO₂ at 1000 °C, respectively (Liao et al., 1999; Zhou et al., 1993). In this research, the gas flow was composed of 20% N₂, 20% argon and 60% of air, thus an approximately 0.25% weight loss occurred the correlated with the further decomposition of OH⁻ and the decarboxylation eliminated the CO₂ resulting in transformation of the OHA into β-TCP. The 1st derivative curve also confirmed the endothermic behaviour due to the phase transition of HA crystals.

Fig 4.2.3 shows the thermalgravimetric curve of pearl powders heated at the same gas flow setup from room temperature to 900 °C. When the temperature was in the range from 25 °C to 250 °C, 0.9% absorbed water was eliminated. The second step in weight loss occurred between 250 °C to 480 °C and was attributed to the decomposition of organic compounds in pearl powders and the lattice water, also observed in the FTIR spectra (Bourrat et al., 2007; Guo et al., 2013; Ren et al., 2009). Two exothermic peaks at about 335 °C and 462 °C were observed from the DTA curve, respectively. The first moderate exothermic peak, scanned at 335 °C, was attributed to the decomposition of lattice water. As reported by Li et al. (2012), the weight loss (about 2.51 wt.%) up to 480 °C is mainly correlated with the disintegration of the organic components (Bourrat et al., 2007; Guo et al., 2013; Ren et al., 2009), which is in line with the reported related content of pearl or nacre powders in the previous section (2-5 wt.% organic components). It has been reported that the transformation temperature of the mineral matrix of nacre powders (aragonite, CaCO₃) is usually lower than that of natural aragonite (450-550 °C) due to the interaction of organic components (Guo et al., 2009). However, in this research, the phase transformation temperature ranges from 480 °C to 650 °C, which is attributed to the strong bonding of the organic matrix in pearl powders compared to nacre powders. A strong endothermic DTA peak obtained at 878 °C was associated with the decomposition of calcium carbonate (CaCO₃) as explained in the following reaction: $\text{CaCO}_3 \rightarrow \text{CaO} + \text{CO}_2$. The total weight loss in the endothermic stage is roughly 42.44%, which matches the molar weight percentage of CO₂ in CaCO₃.

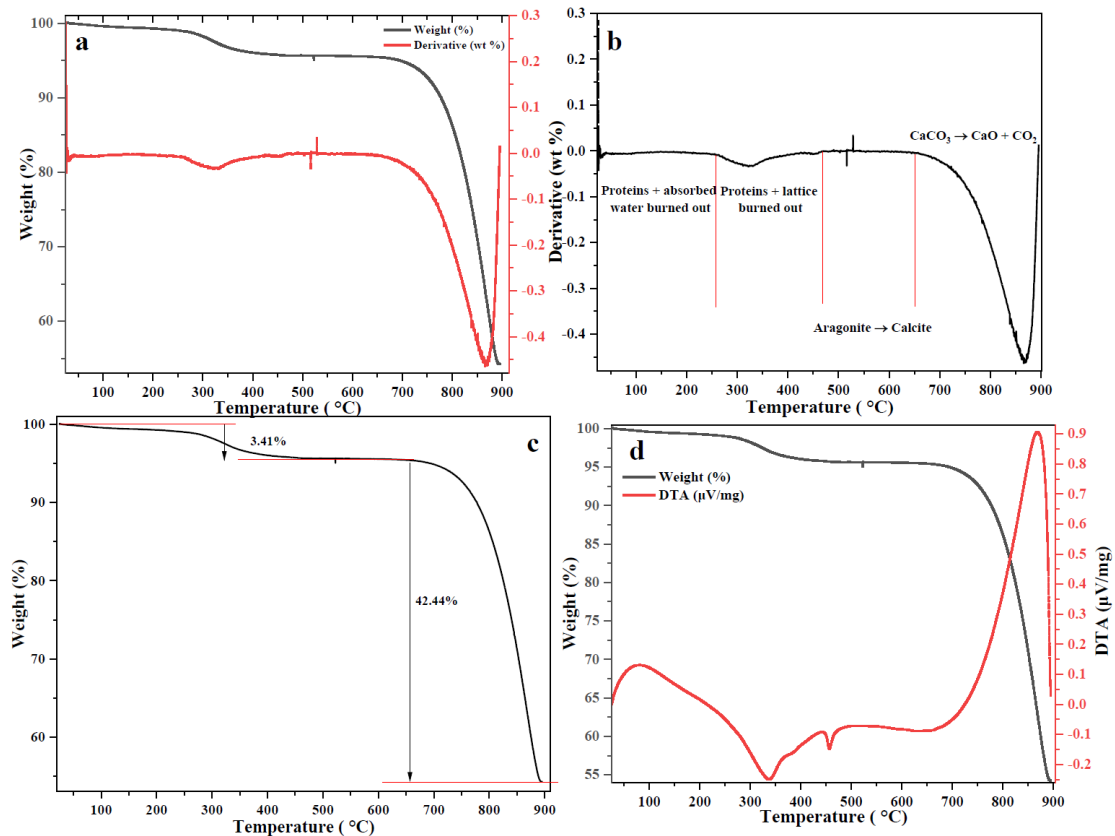


Fig. 4.2.3 TGA data curves demonstrating the weight loss versus temperature, including the 1st derivative of weight for the pearl sample. (a) weight loss and derivative of weight against temperature. (b) 1st derivative of weight against temperature curve. (c) weight loss versus temperature curve. (d) DTA and weight loss against temperature curve.

The TG analysis results of p/CaP composite samples are shown in Fig. 4.2.4. The overall weight loss is about 17.40 wt.%, which was attributed to two main stages. The initial 0.65 wt.% weight loss that occurred between 25 °C and 150 °C was considered due to the removal of absorbed water. An exothermic solid peak observed at approximately 339 °C was attributed to the decomposition of organic components in the pearl powder, compared with the DTA curve in Fig. 4.2.3 (d). However, direct calculation of the degradation of organic matrix according to the curve was not clear. Compared with the previous sole HA and sole pearl curves, two more exothermic peaks obtained between 380 °C and 620 °C probably represent the transformation of aragonite and HA, where a moderate weight loss (1.22 wt.%) occurred. Meanwhile, as in a previous study conducted by Raynaud et al (2002), it has been noticed that the CaP based particles including HA, β -TCP

Innovative incorporation of pearl and calcium phosphate composite in bone regenerative scaffolds and calcium-deficient HA (Ca-dHA) with different Ca/P ratio, especially between 1.50 and 1.667, that the hydrogenphosphate (HPO_4) groups in Ca-dHA have been observed to be condensed in the temperature range of 360-720 °C, which can be assigned to the TG curve (Fig 4.2.4).

Within the temperature region of 600 °C to 800 °C, a rapid weight loss was observed, as 5.20 wt.% components were decomposed. In comparison, in the DTA and TGA curves of pearl powder, the occurrence of weight loss was attributed to the decomposition of CaCO_3 ; however, the weight loss of composite particles is much less than that of the pure pearl powder, which probably correlated to the bonding between pearl and HA. The DTA curve also differed from those of pure pearl and pure HA, indicating that the endothermic reaction happened when the temperature was raised. Furthermore, the existence of phase transformation (exothermic signals) of the composite particles can also be detected.

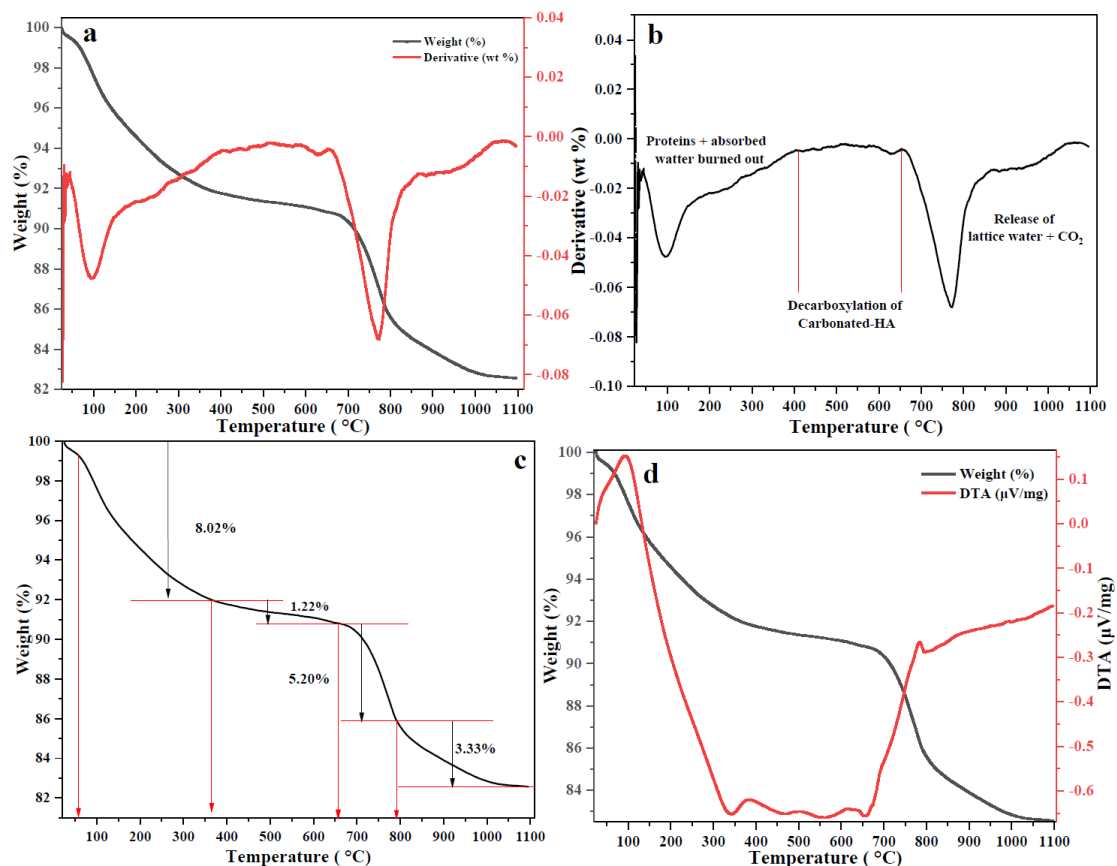


Fig. 4.2.4 TGA data curves demonstrating the weight loss versus temperature, including the 1st derivative of weight for the p/CaP composite sample. (a) weight loss and derivative of weight against temperature. (b) 1st derivative of weight against

temperature curve. (c) weight loss versus temperature curve. (d) DTA and weight loss against temperature curve.

The final heating stage was between 800 °C to 1100 °C, the weight loss in composite sample was 3.33 wt.%. The weight loss ratio slowed down from the previous state that closer to the endothermic transformation phase. Considering the components of the composite particles, the weight loss was more likely to be attributed to carbonate decomposition and the transformation of HA or OHA into β -TCP (Li et al., 2012). To draw a quick conclusion, p/CaP composite particles demonstrated thermal properties similar to both HA and pearl. More water-related contents were found as revealed from the TG curve at the temperature region from room temperature to approximately 360 °C. The decomposition of CaCO_3 was also observed from the spectra; however, the total weight loss was decreased compared to the sole pearl samples, which might indicate that the incorporation of CaP with pearl could enhance the thermal stability for the composite powders. Although the initial target was to synthesize the p/CaP composite particles; but the final product analysed by the thermal stability analysis suggested it is not the stoichiometric HA attached to the pearl platelets, which requires further characterizations like isothermal XRD analysis to study the actual chemical composition of the composite particles.

4.2.2 SEM analysis of powders and scaffold samples

4.2.2.1 SEM analysis of powders

The morphological analyses of pearl, HA and p/CaP composite samples obtained from 3 different synthetic methodologies, including the hydrothermal method, the precipitation method and the sol-gel technique, as well as the commercial HA samples were investigated by SEM.

Table 4.2.1 Details of porous chitosan scaffold composite samples prepared in this study. Pearl: CaP ratios indicate the mass ratio of pearl to CaP. Weight percentages (wt.%) are relative to chitosan.

Group of scaffolds	Abbreviation	Particles added to chitosan scaffold
Pure CS scaffolds	CS	-
	P1	10 wt.% pearl
Pearl/CS scaffolds	P3	30 wt.% pearl
	P5	50 wt.% pearl
	H1	10 wt.% HA
HA/CS scaffolds	H3	30 wt.% HA
	H5	50 wt.% HA
	P1CaP9_10	10 wt.% P1CaP9
Pearl: CaP (1:9)(P1CaP9)/CS scaffolds	P1CaP9_30	30 wt.% P1CaP9
	P1CaP9_50	50 wt.% P1CaP9
	P3CaP7_10	10 wt.% P3CaP7
P3CaP7/CS scaffolds	P3CaP7_30	30 wt.% P3CaP7
	P3CaP7_50	50 wt.% P3CaP7
	P5CaP5_10	10 wt.% P5CaP5
P5CaP5/CS scaffolds	P5CaP5_30	30 wt.% P5CaP5
	P5CaP5_50	50 wt.% P5CaP5

The SEM images of pearl powders in different magnifications are shown in Fig 4.2.5. Pearl powders utilized in this research were obtained commercially from southern China, the gN Pearl Group. The pearl platelets observed through the SEM were of independent, irregular, plate-like rectangular morphology. At higher magnifications, the individual rectangular morphology of small platelets can be seen more clearly. As displayed in Fig 4.2.5.d, the average diameter of the pearl

powder is around $0.54\ \mu\text{m}$ as calculated by the ImageJ 1.53K. The minimum diameter of the pearl powder is around $184\ \text{nm}$ and the maximum diameter is about $2.34\ \mu\text{m}$. The diameter distribution range of the pearl powders is between 0.18 and $2.34\ \mu\text{m}$. The distribution of the pearl powders diameter follows the left skewed distribution that the mode number of the diameter is around $1.08\ \mu\text{m}$ and the median number of the diameter is around $0.84\ \mu\text{m}$, with a standard deviation of 3.4312 and skewness of -4.3678 from the 1560 diameter samples.

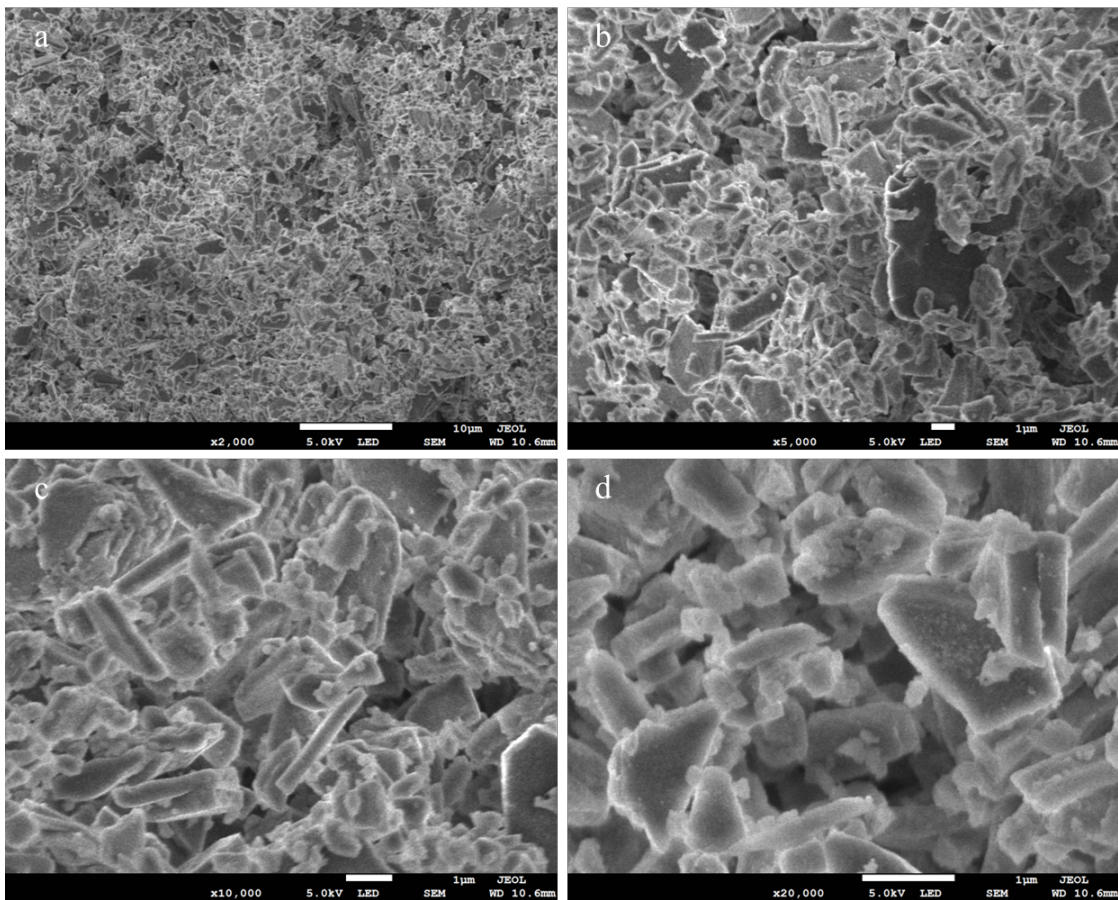


Fig. 4.2.5 SEM microstructure images of pearl powder samples with increasing magnifications. Magnifications increased from **a.** to **d.** by $\times 5,000$, $\times 10,000$, and $\times 20,000$, respectively. Scale bars at the bottom of images represent at **a.** is $10\ \mu\text{m}$ and at **b.** to **d.** are $1\ \mu\text{m}$.

The morphologies of the synthesized HA samples and the commercial HA samples were demonstrated in Fig 4.2.6. All HA samples synthesized by different methods exhibited rod-like agglomerated structures. Compared to the

Innovative incorporation of pearl and calcium phosphate composite in bone regenerative scaffolds commercial HA particles (Fig 4.2.6.d), HA samples obtained from the precipitation method (Fig 4.2.6.c) demonstrate more morphological similarity than the other two ones. More amorphous morphology was observed from the HA samples prepared by the hydrothermal technique (Fig 4.2.6.a) compared to the other HA samples, probably indicating a lower crystallinity compared with the samples prepared by the other two strategies.

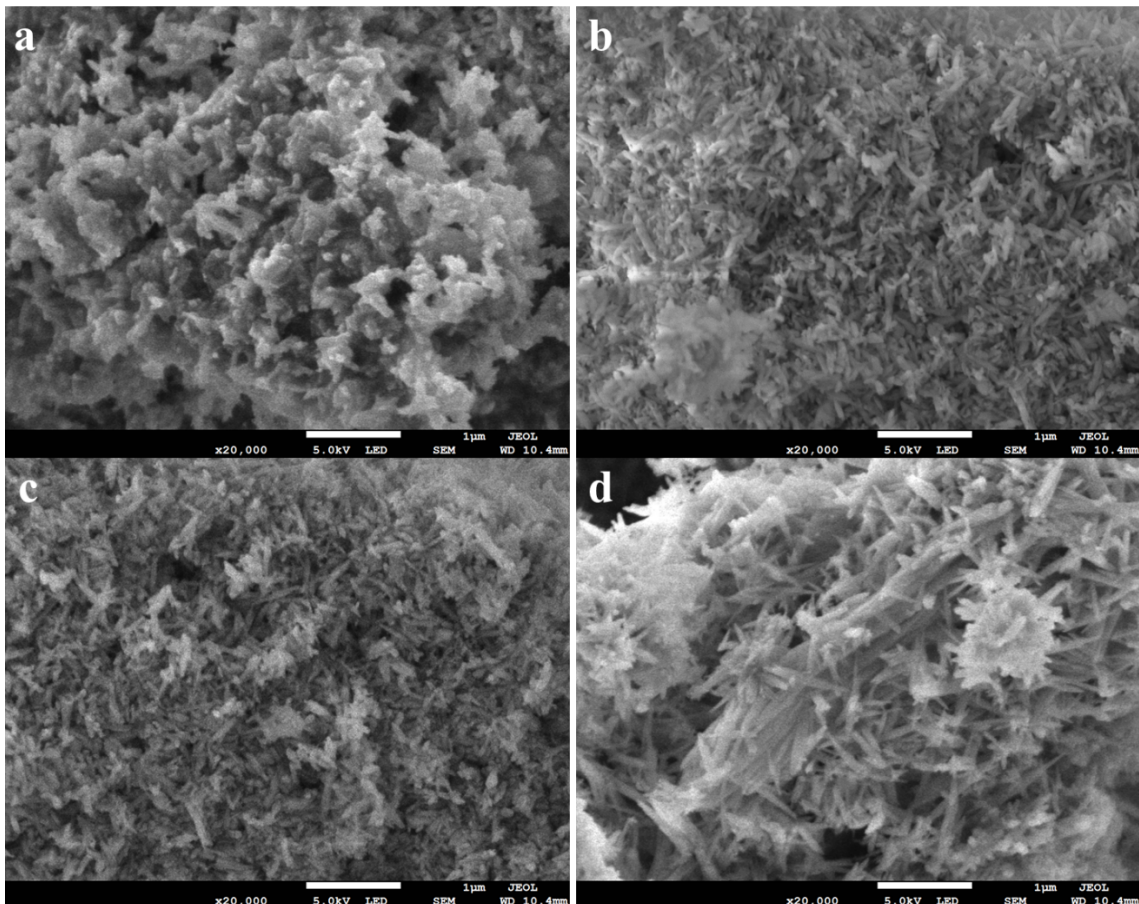


Fig. 4.2.6 SEM microstructure images of synthesized HA samples and commercial HA samples with the same x20,000 magnification. (a) HA samples synthesized by hydrothermal methodology, (b) HA samples obtained from the ethanol-based precipitation, (c) HA samples synthesized with the precipitation method, and (d) the HA commercial samples.

The morphology of the p/CaP composite samples was shown in Fig. 4.2.7. As shown in the figures, the embedded or attached crystals can be observed completely distributed through the pearl platelets. At lower magnifications

(x2,000 and x5,000), the synthesized amorphous CaP crystal agglomerates were easy to be recognized (Fig 4.2.7 **a**, **b**, **e** & **f**). At higher magnifications, the morphology of composite particles became more apparent, revealing crystals that exhibited an amorphous interconnected structure. Compared to the synthesized HA samples in Fig. 4.2.6 **b**, **c** & **d**, at the magnification of x20,000, the crystals attached to the pearl platelets represented a significant difference from those obtained by the ethanol-based precipitation and the precipitation technology; however, they exhibit morphological similarities with the HA prepared by the hydrothermal method. The morphology of the surface that pearl powder and synthesized crystals demonstrated clearly that those crystals were formed on a micron-scale; the entire surface appeared to be covered by the particles.

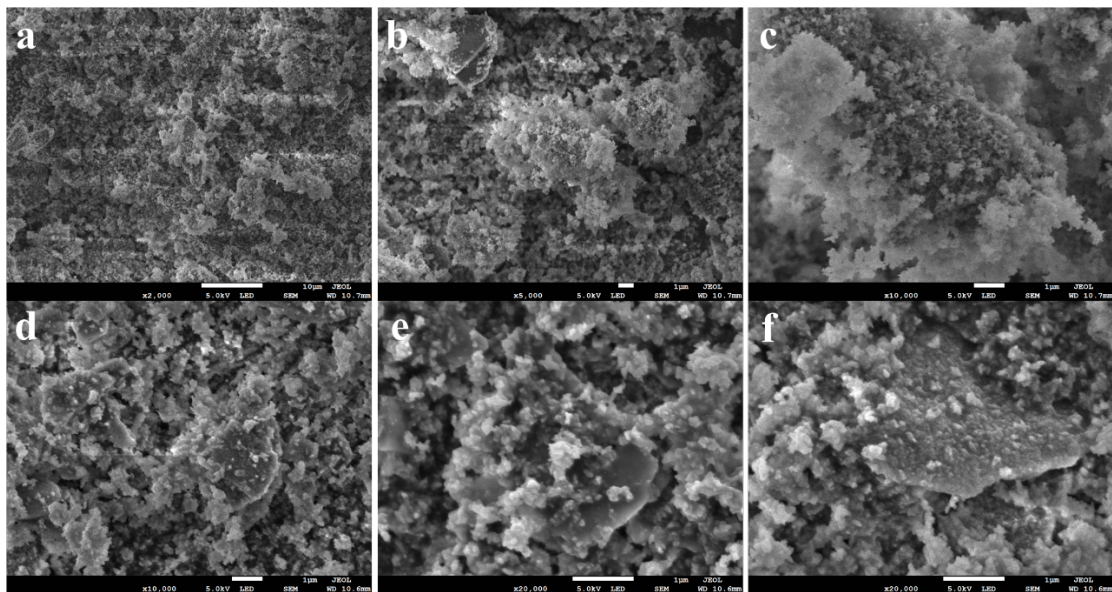


Fig. 4.2.7 SEM microstructure images of p/CaP samples with increasing magnifications, newly formed crystals are noticed attached to the pearl platelets. Magnifications increased from **a**. to **f**. by x2,000, x5,000, x10,000, and x20,000, respectively. Scale bars at the bottom of images represent at **a**. is 10 μm and at **b**. to **f**. are 1 μm.

The SEM analyses of particle samples showed the diverse morphological properties of composite powders as a result of different synthesis methods. Pearl powder samples exhibited significantly different morphology than the HA samples that is a typical platelet structure on the micro and nano scales. The commercial unsintered HA powders demonstrated the typical rod-like pin structures. Samples obtained from the precipitation method showed the more similar structure to that of the commercial sample. Samples synthesized from the hydrothermal technique showed a more amorphous structural morphology, which differs from the previous studies, suggesting that the design of the synthesis process by using the oven in this study, requires further improvements to increase the crystallinity. Furthermore, the attachment of CaP crystals and pearl platelets as demonstrated from the SEM images, indicated that the incorporation of pearl and CaP is feasible in this study. A recent study conducted by Lotsari et al (2018) pointed out that the existence of amorphous CaP clusters is beneficial for promoting the growth of bone apatites.

4.2.2.2 SEM analysis of composite scaffolds

The freeze-dried scaffold morphology was evaluated using SEM, as shown in the following figures. 16 samples, 32 specimens including the sole chitosan scaffolds, pearl/chitosan scaffolds (10, 30, 50 wt.%), HA/Chitosan scaffolds (10, 30, 50 wt.%), 10pearl/90CaP_chitosan scaffold (10, 30, 50 wt.%), 30pearl/70CaP_chitosan scaffold (10, 30, 50 wt.%), and 50pearl/50CaP_chitosan scaffold (10, 30, 50 wt.%) were measured and evaluated on both top and bottom surfaces.

All scaffolds exhibited interconnected porosity and it was possible to observe the distribution of ceramic crystals loaded onto the scaffold. As shown in Fig 4.2.8 a-f, the combination of different concentrations of ceramic crystals and the different kinds of components did not lead to visible changes in the structure of scaffolds.

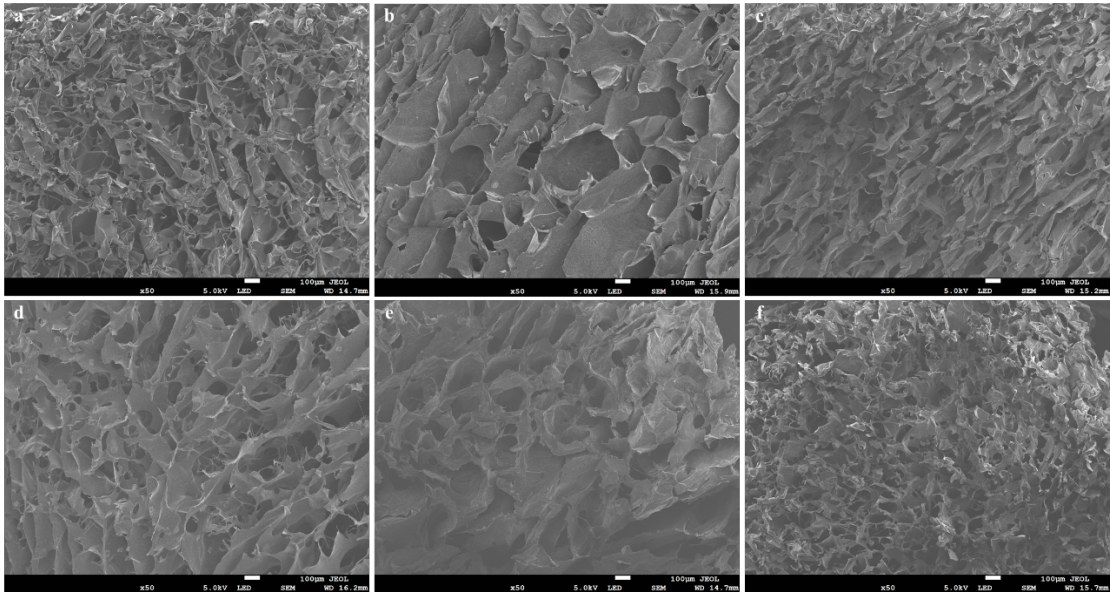


Fig. 4.2.8 SEM microstructure images of the bottom surface of freeze-dried scaffolds at the same magnification: **(a)** pure chitosan scaffold (CS) **(b)** 10 wt.% pearl/chitosan composite scaffold **(c)** 10 wt.% HA/chitosan composite scaffold **(d)** 10 wt.% 10pearl/90CaP_chitosan scaffold **(e)** 10 wt.% 30pearl/70CaP_chitosan scaffold **(f)** 10 wt.% 50pearl/50CaP_chitosan scaffold. All images were captured at the x50 magnification and the scale bar at the bottom represented 100 µm.

One significant difference that can be observed is that the top surface of scaffolds seems to be smoother than the bottom surface; the bottom surfaces exhibited a more porous morphology. A ceramic-rich side was found on the bottom surface of scaffolds, with more sedimentation of pearl particles, HA particles or the composite particles was found in the Fig. 4.2.8 **(c, d, e, f)**. The morphology of pearl/chitosan scaffolds were found to be different, as shown in Fig. 4.2.9 **(b and d)**; the platelets of crystals were embedded densely at the top surface of the scaffold, but could not be clearly observed on the bottom surface.

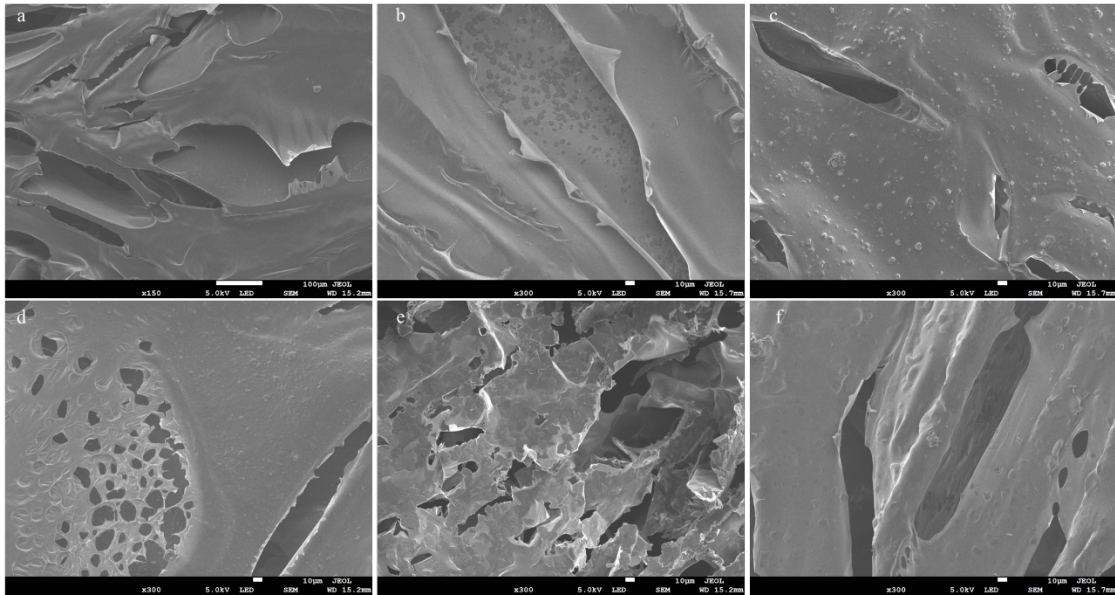


Fig. 4.2.9 SEM microstructure images of the top surface of freeze-dried scaffolds at the same magnification: **(a)** pure chitosan scaffold (CS) **(b)** 10 wt.% pearl/chitosan composite scaffold **(c)** 10 wt.% HA/chitosan composite scaffold **(d)** 10 wt.% 10pearl/90CaP_chitosan scaffold **(e)** 10 wt.% 30pearl/70CaP_chitosan scaffold **(f)** 10 wt.% 50pearl/50CaP_chitosan scaffold. Fig; other images were captured at the x300 magnification and the scale bar at the bottom represented 10 μ m.

The composite scaffolds containing p/CaP composite powders exhibited different morphologies compared with the sole HA/chitosan and pearl/chitosan scaffold as shown in Fig 4.2.10. The HA/chitosan composite scaffolds were prepared by the incorporation of commercial HA powders, thus, rod-like structure of HA powders was embedded packed on the matrix of chitosan scaffolds (Fig. 4.2.10 **a**, **b**). The pearl platelets were significantly observed through the SEM spectra in Fig 4.2.10 **c** and **d**, in which the typical platelets structures were arranged closely. The same platelet morphology was observed from the pearl/CaP_chitosan composite scaffold in Fig 4.2.10 **e** and **f**. Moreover, the amorphous particles were found embedded on the wall of chitosan scaffolds and attached on the pearl platelets.

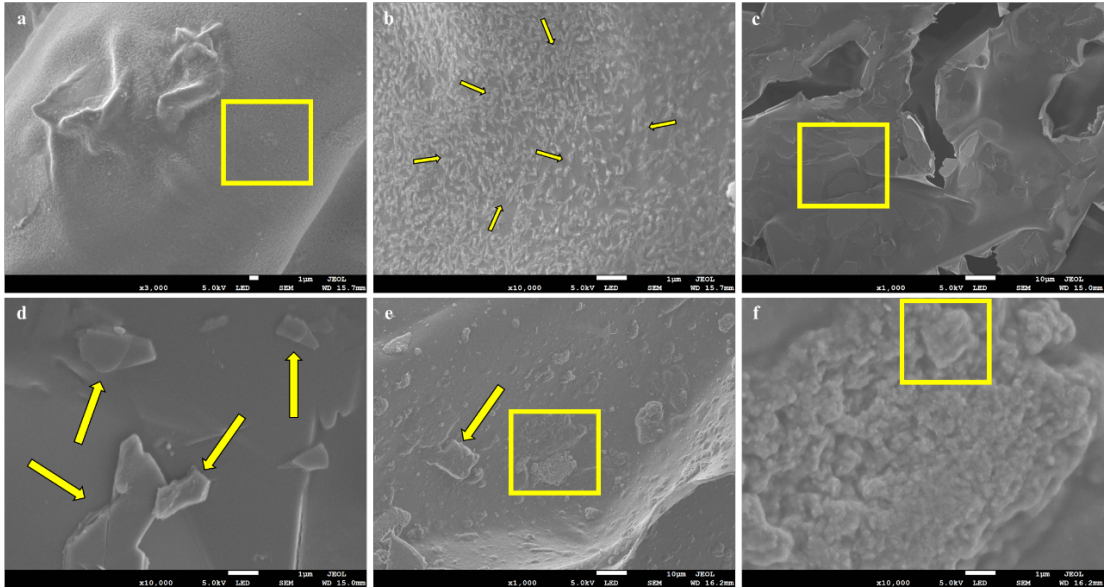


Fig. 4.2.10 SEM microstructure images of the top surface of freeze-dried scaffolds at different magnifications: (a & b) 30 wt.% HA/chitosan scaffold under x3,000 and x10,000 times magnifications, (c & d) 30 wt.% pearl/chitosan composite scaffold under x3,000 and x10,000 times magnifications, (e & f) 30 wt.% 30pearl/70CaP_chitosan scaffold under x3,000 and x10,000 times magnifications.

In Fig 4.2.11, scaffolds with the same components but with different weight concentrations exhibited similar porous morphological properties. With increasing concentration of composite powders, p/CaP particles covered the walls of chitosan scaffold more thoroughly and were dispersed on the surfaces more uniformly. Moreover, the increasing concentration of p/CaP particles also decreased the porosity of scaffolds which was confirmed later in the discussion of porosity estimation section. The change of pearl to CaP ratios also affected the porosity of scaffolds; with the higher concentration of pearl platelets, the porosity of scaffolds and the average pore size decreased slightly but the structure was not affected as demonstrated in table 4.2.2. The higher pearl to CaP ratio (from 10:90 to 50:50) additionally led to increased attachment of CaP onto the pearl surfaces, resulting in larger particle sizes and a subsequent decrease in the average pore size within the scaffold. This observation aligns with findings from previous studies (Januariyasa et al., 2020; Maji et al., 2015; Sari et al., 2021).

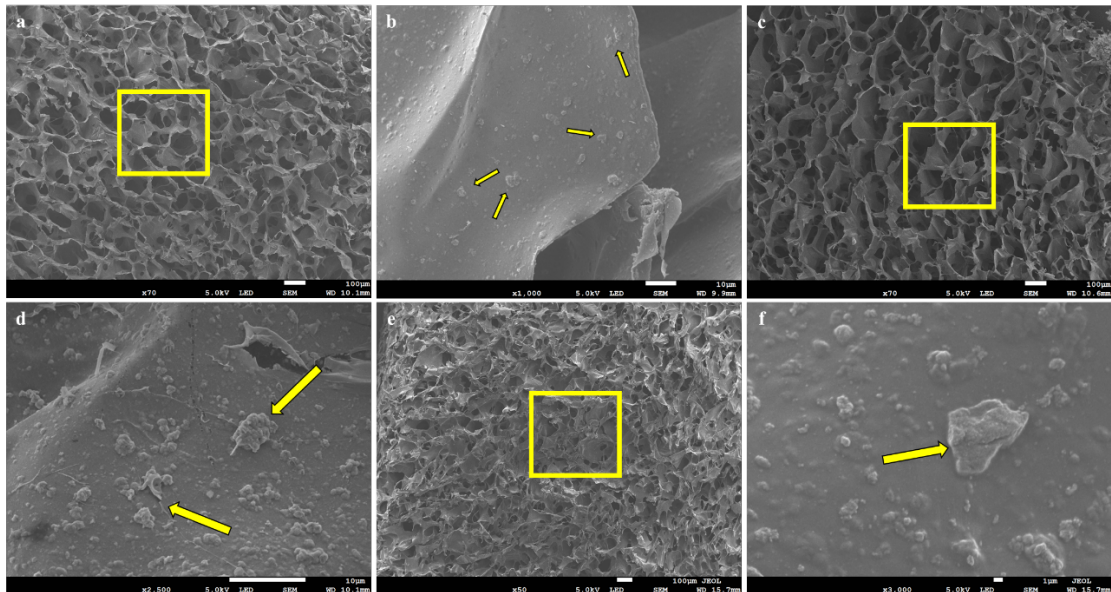


Fig. 4.2.11 SEM microstructure images of the top surface of freeze-dried scaffolds at the same magnification: **(a & b)** 10 wt.% 30pearl/70CaP_chitosan scaffold under x70 and x1,000 times magnifications, **(c & d)** 30 wt.% 30pearl/70CaP_chitosan scaffold under x70 and x1,000 times magnifications, **(e & f)** 50 wt.% 30pearl/70CaP_chitosan scaffold under x70 and x1,000 times magnifications.

Overall, SEM analyses showed that the scaffolds exhibited diverse morphological properties as a result of different compositions. Scaffolds prepared by the freeze-drying method demonstrated an interconnected and porous structural morphology that was respectively uniform. The HA/chitosan scaffold exhibited properties of rough amorphous particles dispersed over the CS matrix. In contrast, the pearl/chitosan scaffold demonstrated typical platelet particle characteristics when embedded in the CS matrix. The pearl/CaP_chitosan scaffold displayed an amorphous particle structure as well. Morphology of pores showed no significant difference when changed the type of crystal incorporation.

It has been seen that morphology of the composite scaffolds exhibited significant differences between the top surface and the bottom surface individually due to gravity. The amorphous composite p/CaP particles were embedded uniformly on the wall of chitosan scaffolds with increasing concentration. The porosity and the morphological structure of scaffolds did not exhibit much difference when the composition of mineral particles was changed. The statistical data of diameters of

pores from all scaffolds calculated by the ImageJ software are listed below in Table 4.2.2. As the table reveals, the average pore size of scaffolds were similar as

Table 4.2.2 Diameters of pores from the SEM images of all scaffolds.

Names	N total	Mean	Standard Deviation	Minimum	Median	Maximum	Median absolute deviation
		μm	μm	μm	μm	μm	μm
CS	351	110	104	32	99	590	12
P1	358	1210	115	32	99	596	22
P3	363	135	129	30	95	560	40
P5	373	115	109	30	83	559	22
H1	349	109	104	29	88	530	22
H3	388	119	114	29	91	529	27
H5	353	127	122	28	88	519	39
P1CaP9_10	347	122	116	29	83	545	29
P1CaP9_3	355	128	123	28	91	525	37
P1CaP9_50	358	129	123	31	108	583	20
P3CaP7_10	356	126	121	31	96	568	31
P3CaP7_30	362	138	132	31	107	578	21
P3CaP7_50	370	108	122	31	97	575	31
P5CaP5_10	349	111	116	26	100	486	34
P5CaP5_30	352	103	106	26	93	486	32
P5CaP5_50	355	100	104	29	89	532	28

observed from the SEM images. The maximum diameter of scaffolds was 596 μm and the minimum diameter was 26 μm . With the increasing composition of ceramic components, the trend of median diameter of scaffolds increased, which

Innovative incorporation of pearl and calcium phosphate composite in bone regenerative scaffolds also might be related to the increasing composition of pearl. Numerous studies reported the research related to the pore sizes for bone regeneration (Abbasi et al., 2020; Gross et al., 2014; Karageorgiou et al., 2005; Koons et al., 2020; Loh et al., 2013; Murphy et al., 2010; Oh et al., 2007; Petrie Aronin et al., 2009), it was mentioned that the larger pore sizes help to improve the formation of new bone when the interconnected pore size is larger than 100 μm .

4.2.3 Porosity estimation

The porosity estimation of all scaffold samples was conducted following a standard protocol of mentioned in Chapter 3. The results of the porosity test were calculated and are summarized below in table 4.2.3. Overall, the porosity of the scaffolds prepared in this research was relatively high, all over 60%, and the density of scaffolds increased as a result of incorporation of ceramic particles. In accordance with previous studies of porous scaffolds for bone regeneration (Abbasi et al., 2020; Hannink & Arts, 2011; Karageorgiou et al., 2005; Yavari et al., 2014), the porosity of scaffolds is an important parameter for the scaffolds but not the key factor. Higher porosity in scaffolds contributes to a greater surface area, favourable cell attachment and protein adhesion on the scaffold in vivo (Murphy et al., 2010; Abbasi et al., 2019). On the other hand, restricted pore size and lack of space for infiltration forces cells to differentiate instead of proliferating, thus, relative high porosity with optimal pore size may be more appropriate for encouraging bone formation in vivo (Oh et al., 2007; Loh et al., 2013; Gross et al., 2014).

Table 4.2.3 Densities and porosities of all sample scaffolds.

Composition	Density (g/cm ³)	Porosity
CS	0.061	80.33±10.37%
P1	0.065	81.77±3.76%

P3	0.071	79.00±4.49%
P5	0.076	76.23±5.42%
H1	0.079	81.35±3.42%
H3	0.082	79.23±4.17%
H5	0.089	75.10±7.27%
P1CaP9_10	0.067	78.64±1.08%
P1CaP9_30	0.072	75.83±5.40%
P1CaP9_50	0.075	69.25±5.42%
P3CaP7_10	0.065	78.17±1.18%
P3CaP7_30	0.068	76.13±1.70%
P3CaP7_50	0.074	70.90±6.79%
P5CaP5_10	0.064	69.73±8.62%
P5CaP5_30	0.068	67.73±4.62%
P5CaP5_50	0.071	63.73±3.92%

The density of all scaffolds was increased with the incorporation of ceramic particles. Compared with different compositions of pearl: CaP ratio, with the increasing concentration of pearl powders, the density of scaffolds decreased which might be related to the coating effect of CaP; the density of CaP is higher than pearl powders ($3.16 \text{ g/cm}^3 > 2.73 \text{ g/cm}^3$). The highest porosity among all scaffolds was 81.77% from the P1_CS scaffold whilst the lowest porosity of scaffolds was 67.73% from the P5CaP5_50 CS scaffold. Combined with the diameter data from the SEM results, the porosity and the geometry of pores might be independent and random of these two factors.

4.3 Chemical study of powder and scaffold samples

4.3.1 FTIR spectroscopy analysis

FTIR spectra of all powder samples, including commercial HA and pearl samples, and the synthesized HA and p/CaP samples were all characterized in Lancaster University FST B65, with the Nicolet™ iN10 Infrared Microscope and the iS50 Spectrophotometer.

4.3.1.1 FTIR analysis of powder sample

The FTIR spectra of the dried samples were presented in following figures which gave quick characterisations for chemical information. All tested samples were kept in an oven at 80 °C for 48 hours in prior for dehydration. In pearl powders, the broad region at 3000-3400 cm^{-1} was attributed to the hydroxyl stretch which is also marked by broad H_2O absorption. The peak at 2920 cm^{-1} was attributed to the $\nu(\text{C-H})$ in organic matrix of pearl; the peaks at 1430-1490 cm^{-1} are attributed to the amide I $\nu(\text{C-H})$ stretching. The triple peak at 2520-2650 cm^{-1} was assigned to bicarbonate (HCO_3^-) O-H stretching. Theoretically, carbonate ions have four vibrational modes but three of them are more active under the IR spectrometer, including ν_1 (1000-1100 cm^{-1}), ν_2 (840-910 cm^{-1}) and ν_3 (1350-1600 cm^{-1}) (Wang et al., 2019). In this study, the peak at 1787 cm^{-1} was attributed to the C=O groups in the carbonate ions and the strong board peak at 1656 cm^{-1} and the weak peak at 1414 cm^{-1} represented to the in-plane asymmetric bending of CO_3^{2-} (ν_3). The peaks at 1082, 845, 712 and 701 cm^{-1} are attributed to two other CO_3^{2-} vibrational modes. These identical IR peaks serve as distinctive markers for characterizing the samples as aragonite pearl (Ma & Lee, 2006).

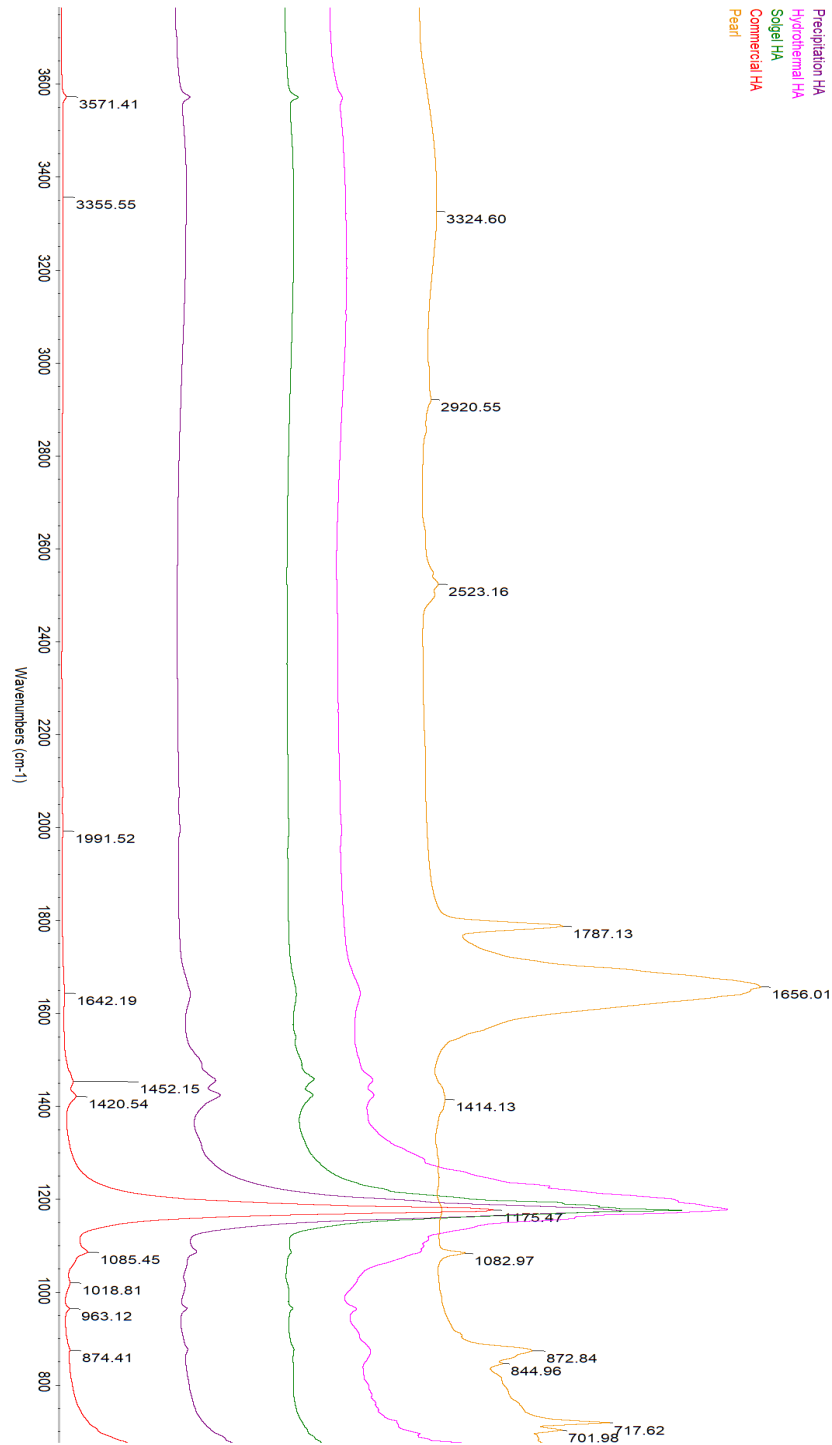


Fig. 4.3.1 FTIR spectra of pearl, commercial HA and synthesized HA powders by three different methods (including chemical precipitation, sol-gel technique and hydrothermal method) attached with the typical peaks information.

The FTIR spectrum of synthesized and commercial HA powders shown the similar peak chemical peaks characteristics as shown in Figure 4.3.1 and Figure

4.3.2. The peak at 3571 cm^{-1} is attributed to the stretching $\nu(\text{O-H})$, the broad peak at the region between $2800\text{-}3500\text{ cm}^{-1}$ is attributed to water absorption. Theoretically, four types of phosphate vibrational modes, including ν_1, ν_2, ν_3 and ν_4 , are infrared active which were observed from the spectrum of samples. Typical PO_4^{3-} (ν_3 and ν_1) stretching peaks were also observed between the region at $1030\text{-}1045\text{ cm}^{-1}$, $1060\text{-}1095\text{ cm}^{-1}$ and $959\text{-}962\text{ cm}^{-1}$ in all HA samples, respectively (Rehman & Bonfield, 1997).

Table 4.3.1 Typical FTIR peaks of pearl.

Peak (cm^{-1})	Assignment	Reference
3200-3500	O-H/N-H stretching	Shahzad et al., 2015
2800-3000	C-H (alkanes) stretching	Shahzad et al., 2015
2520-2650	O-H stretching (Bicarbonate group)	Alstadt et al., 2012
1792, 1786	C=O antisymmetric stretching	Alstadt et al., 2012
1630-1660	Carboxylate (COO^-) symmetrical stretching	Li et al., 2020
1490	In-plane asymmetric bending of CO_3^{2-} (ν_3)	Balmain et al., 1999
1430-1490	Bending vibration of CH_3	
844-1090	CO_3^{2-} out of plane bending / in-plane symmetric stretching (ν_2/ν_1)	Balmain et al., 1999
700-864	CO_3^{2-} in-plane bending (ν_4)	Ma and Lee, 2006
713	CO_3^{2-} in-plane stretching (ν_4)	Ma and Lee, 2006; Balmain et al., 1999

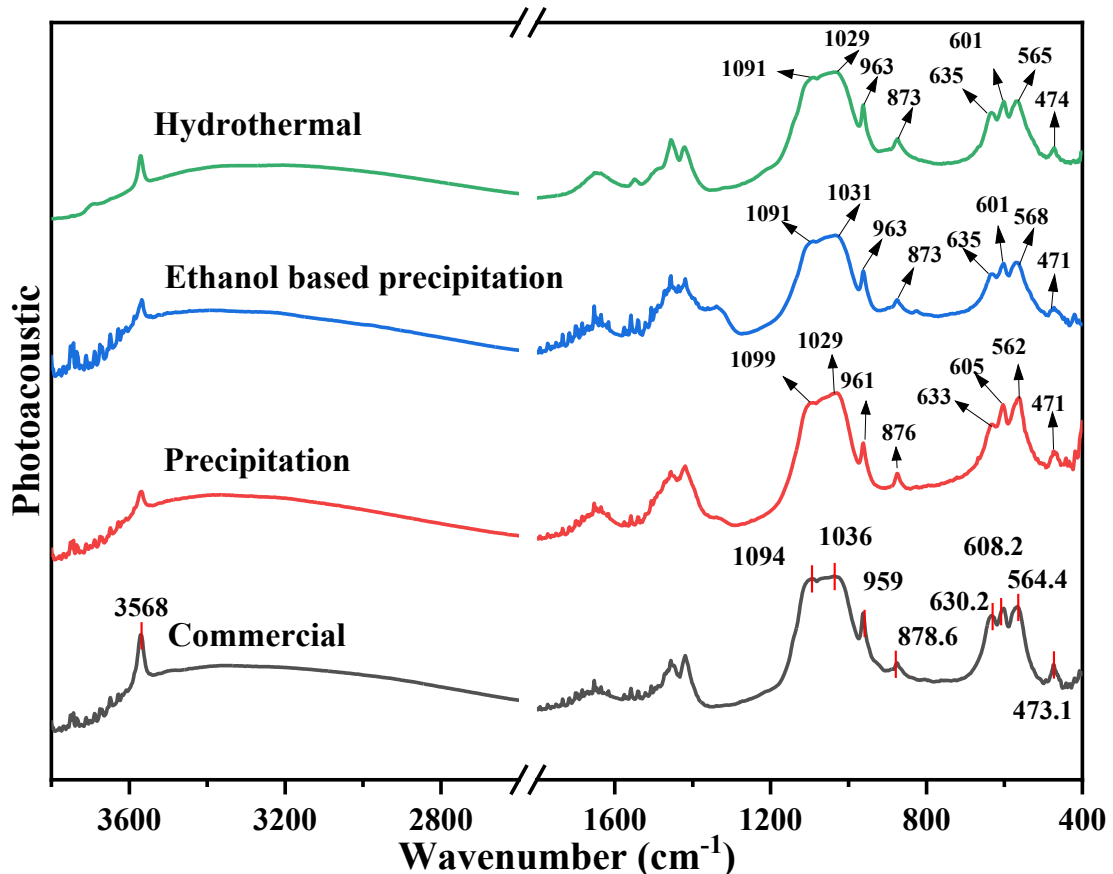


Fig. 4.3.2 FTIR-PAS spectra of commercial HA and synthesized HA powders by three different methods (including chemical precipitation, sol-gel technique and hydrothermal method).

The FTIR-PAS spectrum in Fig.4.3.3 provided further details of peak information at the region that wave number is below 700 cm^{-1} . As reported in the previous study (Rehman & Bonfield, 1997), bands at 630, 608 and 564 cm^{-1} are assigned to the PO_4^{3-} ν_4 stretching, and the band at 473 cm^{-1} is assigned to the PO_4^{3-} ν_2 stretching, respectively.

Table 4.3.2 Characteristic FTIR peaks of stoichiometric HA

Peaks (cm^{-1})	Assignment	Reference
3570	Hydroxyl O-H stretch	Berzina-Cimdina et al., 2012;

3420				Shahzad et al., 2015
1650	Carbonate	in-plane	asymmetric bending ν_3	Rehman & Bonfield, 1997; Shahzad et al., 2015
1000-1100, 1020-1120	Phosphate	in-plane	asymmetric bending ν_3	Berzina-Cimdina et al., 2012; Rehman & Bonfield, 1997
960	Phosphate	in-plane	symmetric stretching ν_1	Berzina-Cimdina et al., 2012; Rehman & Bonfield, 1997
870-877	Carbonate	out of plane	bending ν_2	Berzina-Cimdina et al., 2012; Rehman & Bonfield, 1997
630	OH ⁻		stretch	Berzina-Cimdina et al., 2012; Rehman & Bonfield, 1997
520-660	Phosphate	in-plane	stretching ν_4	Berzina-Cimdina et al., 2012; Rehman & Bonfield, 1997
440, 460, 475	Phosphate	in-plane	symmetric stretching ν_2	Berzina-Cimdina et al., 2012; Berzina-Cimdina et al., 2012; Rehman & Bonfield, 1997

The quantitative study of band area comparisons in this study was realised by using the Origin software that the relative peak area of O-H peak at 3560 cm^{-1} in commercial HA was 1842, while other composite samples are having much lower peak area; the sol-gel p/CaP was 956, the hydrothermal p/CaP was 944 and the precipitation one was 733. The results obtained indicate that the hydroxyl group decreased with increasing of the carbonate group, which agrees with the aforementioned previous studies about the replacement of carbonate groups with hydroxyl ions in CHA (Rey et al., 1989; Sadat-Shojaj et al., 2013; Saadat et al., 2018). The decreasing intensity of OH⁻ peak and the increasing intensity of carbonate peaks implies that the ion substitution process possibly exist during

the synthesis process of HA with the pearl powders, and the OH⁻ group in HA might be replaced by the carbonate group to obtain the type A CHA in accordance with research by Landi and Sønju (Landi et al., 2003; Sønju & Ruyrt, 1997).

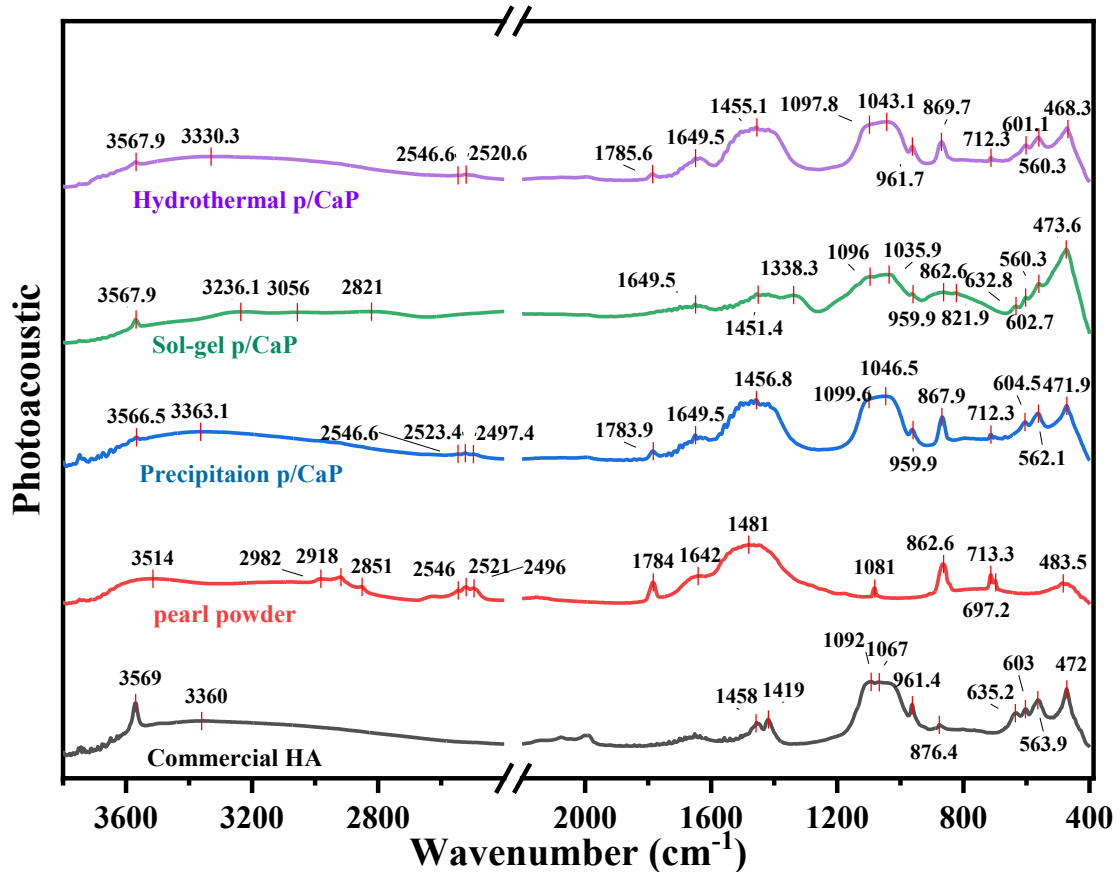


Fig. 4.3.3. FTIR-PAS spectra of pearl, commercial HA and synthesized p/CaP composite powders by three different methods (including chemical precipitation, sol-gel technique and hydrothermal method) attached with the typical peaks information.

4.3.1.2 FTIR analysis of scaffold samples

The ATR spectra of different scaffold samples including sole CS, 10, 30, 50 wt.% pearl/CS, 10, 30, 50 wt.% HA/CS, 10, 30, 50 wt.% pearl1_CaP9/CS (P1CaP9_CS), 10, 30, 50 wt.% P3CaP7_CS, and 10, 30, 50 wt.% P5CaP5_CS are given in the following figures.

The comparative ATR spectra of sole CS with pearl/CS and HA/CS were demonstrated in Figure 4.3.4. The overlapping of O-H and N-H stretching vibrations in the region between 3100 to 3500 cm⁻¹ were split into three weak

peaks. The intensity of those three bands shown in the figure from the composite scaffolds are higher than in the sole CS scaffold sample, which might be due to O-H peaks from the HA in the HA/CS scaffold and the stronger interaction of O-H groups with the organic components in pearl/CS scaffold. The amide I or C=O band and the amide II or N-H stretching were observed at 1620-1640 cm^{-1} and 1540-1550 cm^{-1} in scaffold samples, respectively. Bands shifted in composite samples compared to the sole CS samples as reported in the previous research (Han et al., 2010). However, the intensity of bands in the pearl/CS sample were relatively lower than in other samples, which might be due to the decomposition of pearl platelets when dissolving in the acetic acid (HAc) so that the 5% organic matrix could be decomposed at the same time. On the other hand, the peak located around 1545 cm^{-1} was attributed to symmetric deformation of NH_3^+ , whose intensity in sole CS was stronger than in the other two composite samples. This corresponds to the involvement of anion groups and the HA or pearl particles filled in the space between CS matrices.

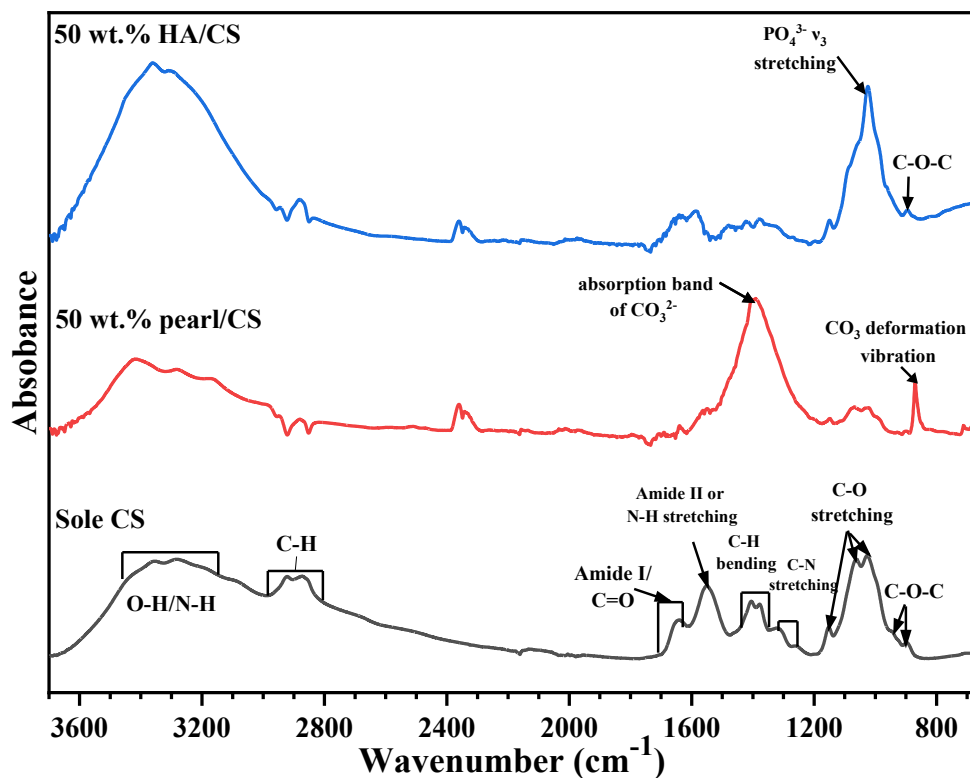


Fig. 4.3.4 The stacked ATR spectra of sole CS, 50wt.% pearl/CS and 50wt.% HA/CS with the peak assignments of chemical functional groups.

The weak C-H bending vibrations located in the region from 1380 to 1410 cm^{-1} were observed in HA/CS and sole CS samples. In HA/CS, the relative intensity of bands was weaker which may be related to the increase of the HA content, the C-O stretching vibration incorporated with P-O bands more. In pearl/CS sample, the C-H symmetrical vibration peak was covered by the absorption band of CO_3^{2-} which is because of the involvement of pearl platelets. Three scaffold samples demonstrated differences in the region between 1000 and 1200 cm^{-1} in which the sole CS exhibited moderate intensity peaks of C-O stretching, while the HA/CS exhibited the C-O stretching and a higher intensity peak at the region of 1020-1065 cm^{-1} due to asymmetric stretching (ν_3) of PO_4^{3-} band. However, the pearl/CS exhibited relatively weak peaks intensity in the region showing the peak of C-O stretching of the CS ring. This might be due to the pearl platelets taking up the gap in the CS matrix. Moreover, besides the CS saccharide C-O-C backbone stretching vibration at around 890-900 cm^{-1} , the characteristic carbonate deformation peak was observed from the pearl/CS scaffold at 869 cm^{-1} , in agreement with the data reported by Li et al. (2020).

For the p/CaP composite CS scaffolds, the comparative spectrum is given in Fig. 4.3.5. In comparison to sole CS, pearl/CS and HA/CS scaffolds, the p/CaP composite CS scaffolds exhibited the combined characteristic peaks of HA, pearl and CS. Due to the chemical properties of pearl platelets, CaCO_3 is dissolvable in acidic solution, and as the morphological images displayed in Fig. 4.2.3 show, the HA particles are separately located on the surface of the pearl platelets. Therefore, this morphological structure cannot allow HA to capsulize the pearl platelet resulting in the dissolvment of the CaCO_3 that results in different intensity of the CO_3^{2-} deformation peak at roughly 869 cm^{-1} . Band shift was observed in the spectra, at the region near 1020 cm^{-1} , which was assigned to the PO_4^{3-} asymmetric stretching. With the concentration of HA content decreasing, the P-O band shifted from (P1CaP9/CS 30 wt.%) 1017 cm^{-1} towards (P5CaP5/CS 50 wt.%) 1035 cm^{-1} . The intensity of the PO_4 band was also decreased in agreement with the decreasing trend in HA content. Moreover, the peak shift of the absorption carbonate band at around 1410 cm^{-1} towards 1360 cm^{-1} was observed in the spectra, and the intensity of band increased proportionally to the

Innovative incorporation of pearl and calcium phosphate composite in bone regenerative scaffolds increasing concentration of pearl powders. On the other hand, the crystallinity of composite particles decreased, as a result of decreasing intensity of characteristic phosphate and carbonate peaks.

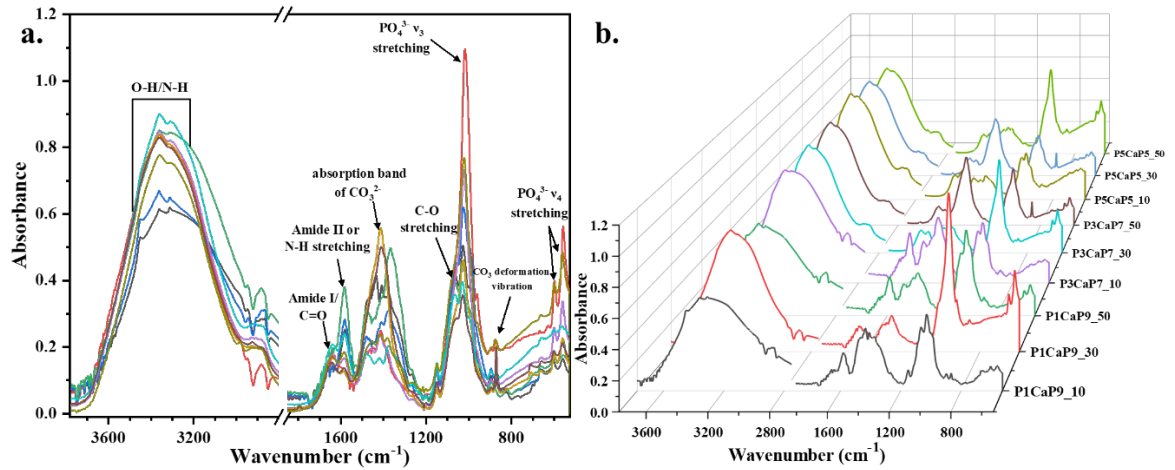


Fig. 4.3.5 The overlay and stack ATR spectra of 10, 30, 50 wt.% P1CaP9_CS, P3CaP7_CS and P5CaP5_CS. The overlay spectra are presented in **a.** with peak assignments of functional groups and **b.** with 3D stack spectra.

A comparative graph is presented below showing the different weight percentages of scaffolds possessing the same pearl/CaP ratio in Fig. 4.3.6. The comparative spectra were divided in accordance with the composition of composite particles, The results showed that when the weight percentages of mineral particles were increased, the intensity of the absorption carbonate peak at 1415 cm^{-1} increased, which covered the C-H bending peak and the C-N stretching peak existing in the chitosan matrix. This indicates that the dissolution of pearl powders released the free carbonated ions which were fixed by the cross-linked polymeric chitosan matrix. The phosphate ν_4 bands in the region of $520\text{-}660\text{ cm}^{-1}$ were detected by the infrared spectroscopy. Only peaks centred at 601 and 558 cm^{-1} showed well-defined sharp bands, which was in agreement with the previous study (Rehman and Bonfield, 1997). This result suggested that although part of the p/CaP composite particles can be dissolved by the HAc, but a certain amount of CHA might also exist on the surface of the scaffold. In addition, it has been noticed that in P1CaP9 and P3CaP7 composite

CS scaffolds, 30 wt.% samples possessed slightly more intensity of the phosphate peak at around 1017-1025 cm^{-1} , but differently in the p5h5 sample. This result might correspond with the detailed structural properties of p/CaP composites requiring further investigations.

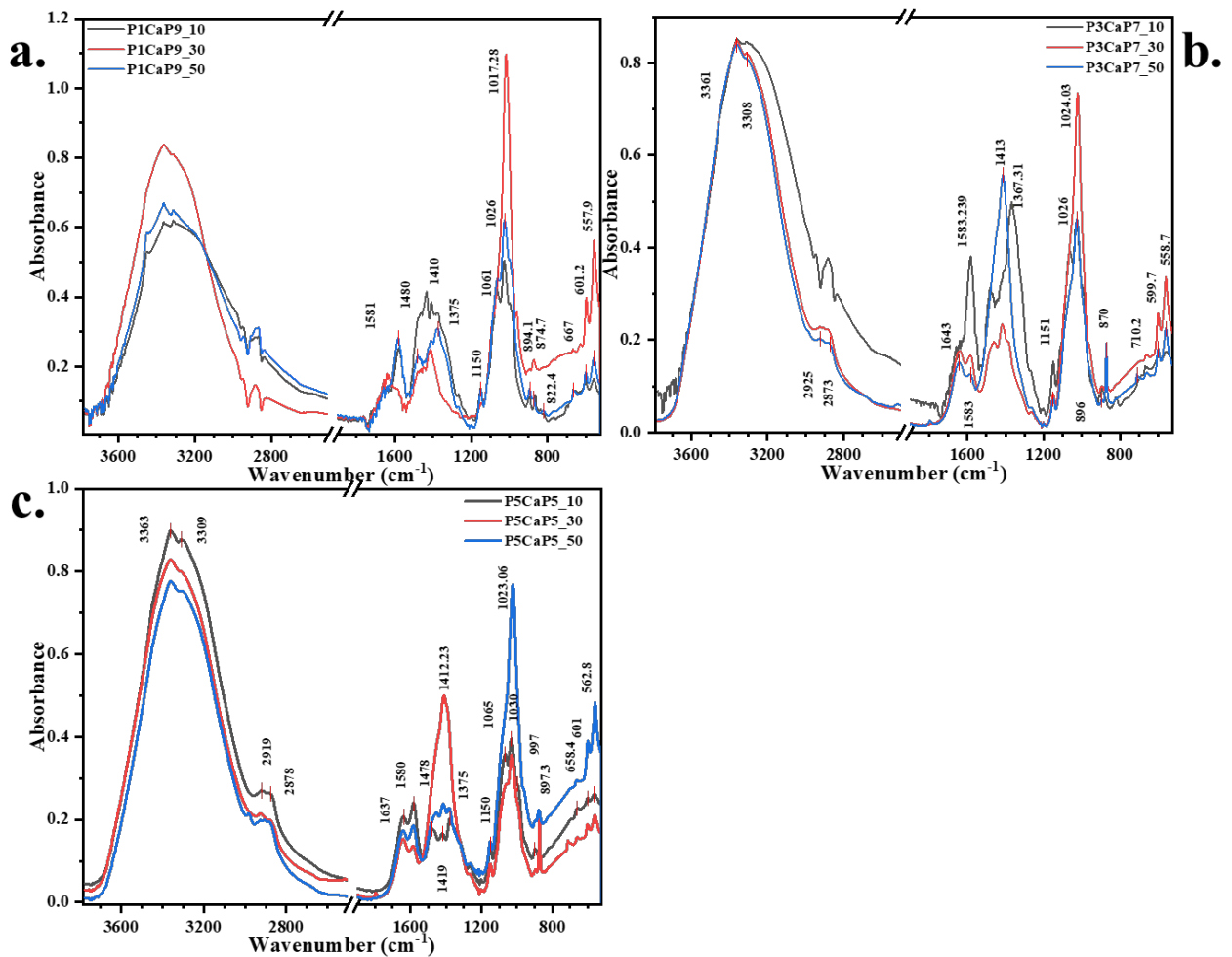


Fig. 4.3.6 The comparison of ATR spectra for composite p/CaP CS scaffolds in different composition. Including **a.** 10, 30 and 50 wt.% P1CaP9_CS scaffolds; **b.** 10, 30 and 50 wt.% P3CaP7_CS scaffolds and **c.** 10, 30 and 50 wt.% P5CaP5_CS scaffolds.

On the other hand, the effect of gravity is also a critical parameter in the preparation of homogeneous scaffolds, contributing to the differences of the bioactive behaviour between top and bottom surfaces. As displayed in Fig. 4.3.7, the ATR spectra of composite scaffolds, including top and bottom surface analysis, demonstrating comparatively for different compositions. The ATR

spectra of top surfaces of all composite scaffolds demonstrated slightly lower peak intensities of functional groups than in their bottom surfaces. The broad O-H/N-H band and the C-H stretching peak positioned around 3355 cm^{-1} and 3301 cm^{-1} , and 2925 cm^{-1} and 2875 cm^{-1} had higher peak intensity in the bottom surfaces. Differently from other samples, the top and bottom surfaces of pearl/CS scaffold were observed displaying more significant intensity differences that characteristic bands of top surfaces was relatively higher than the bottom surfaces displayed in Fig.4.3.7.a because of the y-axis scale.

The O-H/N-H band demonstrated larger intensity differences which was possibly due to the structural morphological differences caused by the freeze-drying method between top and bottom layers in agreement with the study performed by Lv and Feng (2006). The N-H band and CO_3^{2-} stretching band positioned at around 1549 and 1411 cm^{-1} presented strong peak intensities in the bottom surface sample. This might be due to the interaction between carbonate compounds from the pearl and the chitosan matrix which was affected by the gravity that made them enriched at the bottom layers. With the increasing amount of pearl content, the characteristic peaks of CS were observed overlapped by the C-O stretching peaks in pearl/CS samples; however, in other samples containing low or no pearl, those peaks which represented the CS matrix were observed and only small peak intensity differences were observed, which might prove the interaction between carbonate compounds and chitosan matrix.

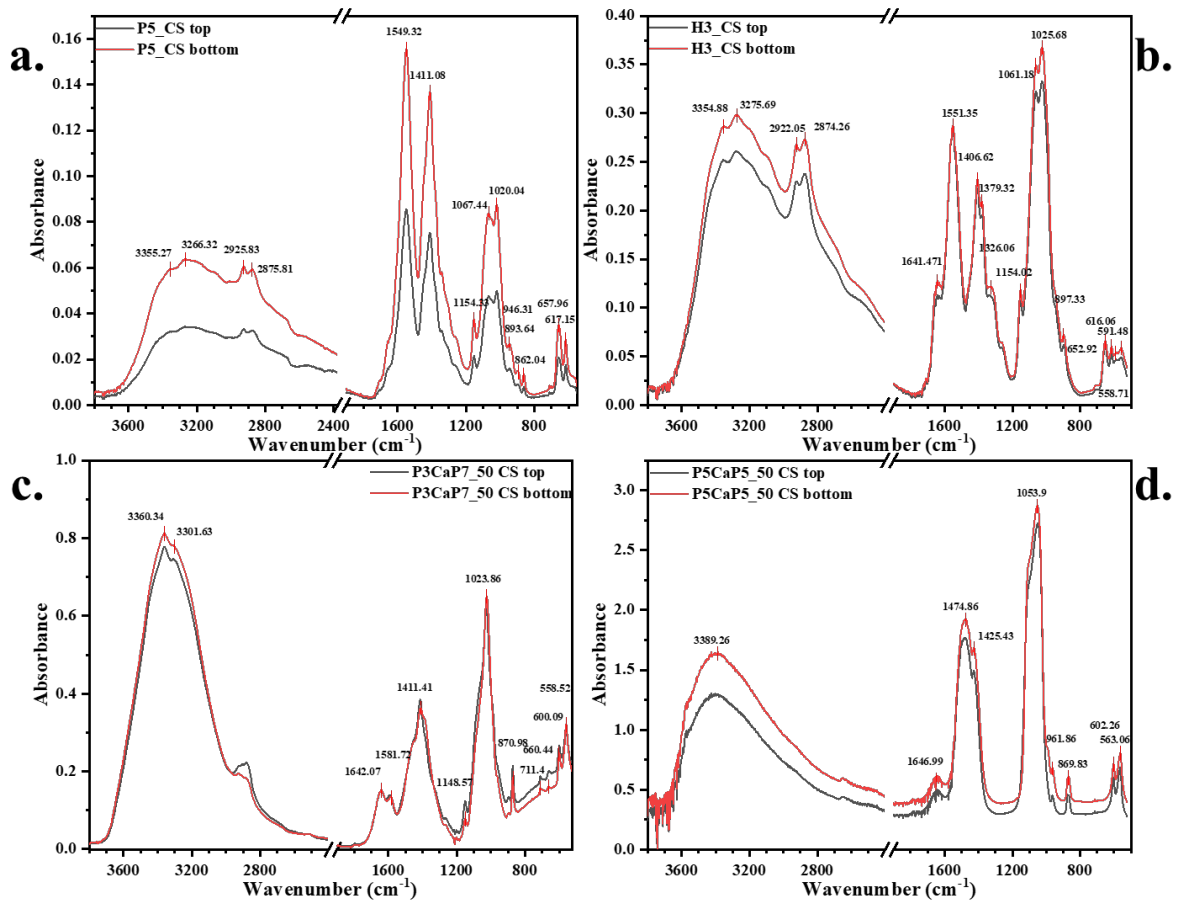


Fig. 4.3.7 The comparison of ATR spectra for composite CS scaffolds in different composition analysed from top and bottom surface. Including **a.** 50 wt.% pearl/CS scaffolds; **b.** 30 wt.% HA/CS scaffolds, **c.** 50 wt.% P3CaP7_CS scaffolds and **d.** 50 wt.% P5CaP5_CS scaffolds.

4.3.2 Raman spectroscopy analysis of powder samples

Raman spectroscopy analysis performed by point characterization and mapping characterization was demonstrated in the following figures. The Raman analysis of pearl, commercial HA and synthesized HA is shown in Fig. 4.3.8. In comparison with the FTIR spectra mentioned in the previous section, the Raman spectra of pearl powders demonstrated three significant vibrational carbonate peaks and the characteristic aragonite lattice peaks. As reported, aragonite pearls and vaterite pearl platelets are hard to distinguish visually, the Raman spectra displayed detailed difference in the lattice modes region of 100 to 300 cm^{-1}

Innovative incorporation of pearl and calcium phosphate composite in bone regenerative scaffolds (Wehrmeister et al., 2010). Furthermore, the region between 1070 and 1090 cm^{-1} also shows different peak structures; the vaterite displays a triplet peak but aragonite and pearl have a single sharp symmetric stretching peak. The spectra gave no information of the ν_2 carbonate out-of-plane vibration signal that is in agreement with the previous study about the differences between cultured and natural pearl powders (Urmos et al., 1991; Zakaria et al., 2008).

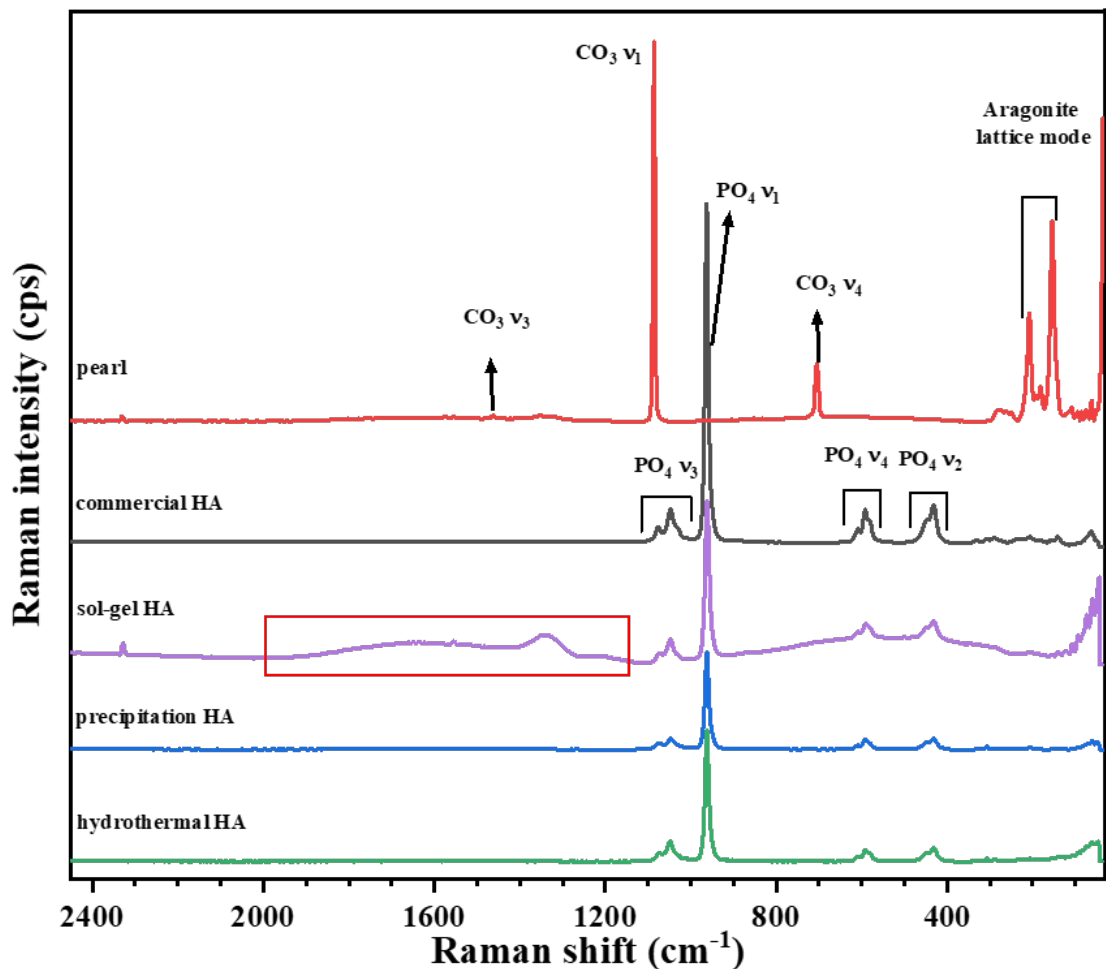


Fig. 4.3.8 The comparison of Raman spectrum for multi particle samples, including pearl platelets, commercial HA powder, sol-gel synthesized HA, precipitation synthesized HA and hydrothermal synthesized HA.

The spectra of the synthesized HA samples provided additional information for characterization. All four vibrational modes of phosphate including ν_1 , ν_2 , ν_3 and ν_4 , were observed from the spectra as Rehman and Bonfield (1997) stated. However, the intensity of peaks from synthesized samples were lower than those

in the commercial HA. The sharpest peak detected at 962 cm^{-1} is the active ν_1 phosphate symmetric stretching band for all samples, but the sol-gel synthesized HA had more significant intensity than the others. The ν_3 , ν_4 and ν_2 region also showed the same intensive results for all synthesized samples, which indicated the crystallinity differences between each sample obtained from the different methodologies.

Differences between samples were observed in the ν_3 phosphate region ($1000\text{-}1100\text{ cm}^{-1}$). Commercial HA samples demonstrated a broad band with three explicit peaks at 1030 , 1046 and 1076 cm^{-1} , whereas in the sol-gel HA showed the corresponding peaks at 1046 and 1072 cm^{-1} , in the precipitation HA showed the peaks at 1046 and 1074 cm^{-1} , and in the hydrothermal HA peaks at 1048 and 1074 cm^{-1} were seen. The observation of the differences of peak shifts indicated that the obtained HA particles from three synthesis processes were more likely to be assigned to tri-calcium phosphate (TCP) phase HA according to Koutsopoulos (2002). The ν_4 phosphate region ($568\text{-}624\text{ cm}^{-1}$) also demonstrated significant differences in 4 samples; the O-P-O bond in commercial HA were assigned to 582 , 592 and 608 cm^{-1} , respectively; whilst in sol-gel HA peaks were seen at 591 and 608 cm^{-1} accompanying overlapping shoulder, in the precipitation HA peaks were seen at 593 and 613 cm^{-1} and in the hydrothermal HA at 579 , 591 and 610 cm^{-1} . The doubly degenerate bending mode (ν_2) of the phosphate group were seen at 431 and 449 cm^{-1} in the commercial sample showing no morphological differences with the synthesized HA samples.

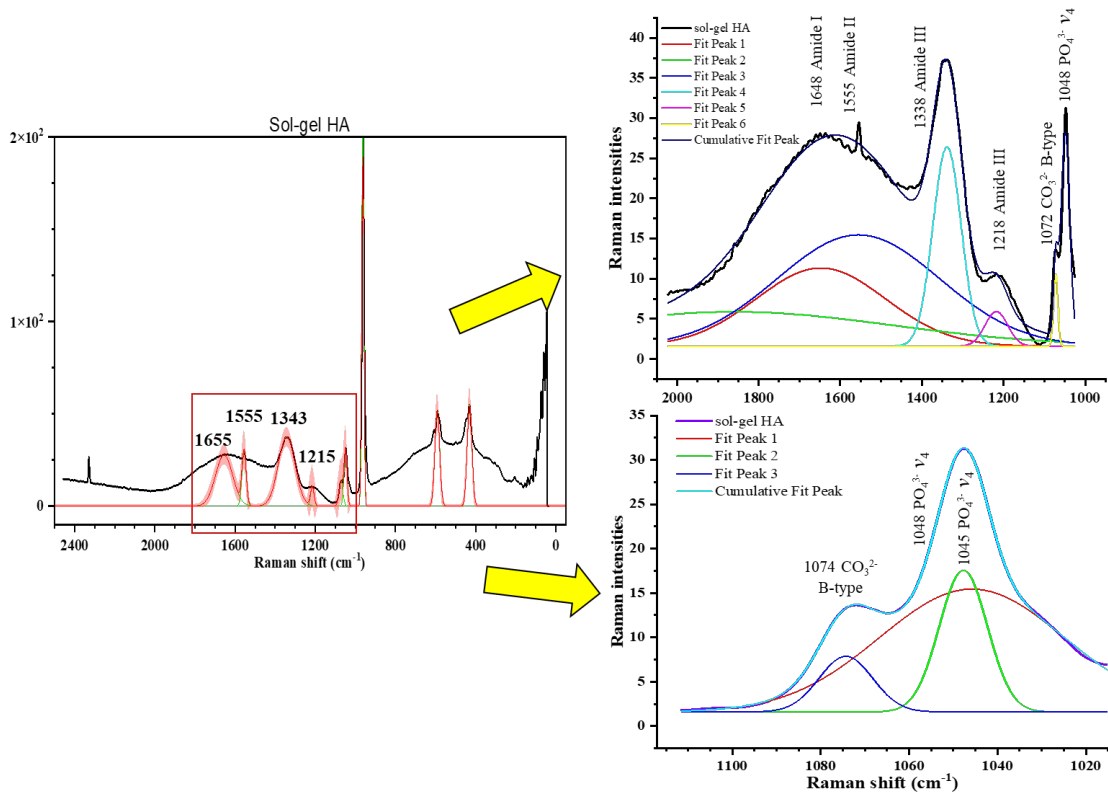


Fig. 4.3.9 Detailed peak fitting analysis of the sol-gel synthesized HA by Origin software between 1000 and 2000 cm^{-1} region.

Moreover, in the spectrum of sol-gel synthesized HA, organic peaks positioned between 1200 and 1800 cm^{-1} and the overlapping vibration at the region from 300 to 900 cm^{-1} were observed. The detailed peaks analysis was shown below in Figure 4.3.9 by using Origin software. By using Gaussian function of regression analysis of the region between 1000 and 2000 cm^{-1} , the non-linear cumulative fit peaks matched well with the original spectra signals and the decomposition spectral peaks as mentioned in the research by Timchenko et al (2018). At the $\text{PO}_4 \nu_4$ mode region (1020 to 1090 cm^{-1}) displayed in the fitting spectrum in Figure 4.3.9, more detailed information was provided that the peak at 1030 cm^{-1} in commercial HA samples could be attributed to the overlapping effect of two PO_4 peaks, and the peak positioned at 1072 cm^{-1} could be related to the overlapping effect by the broad PO_4 peak and the B-type CO_3 , which explained the observation of CO_3^{2-} signal in FTIR spectra.

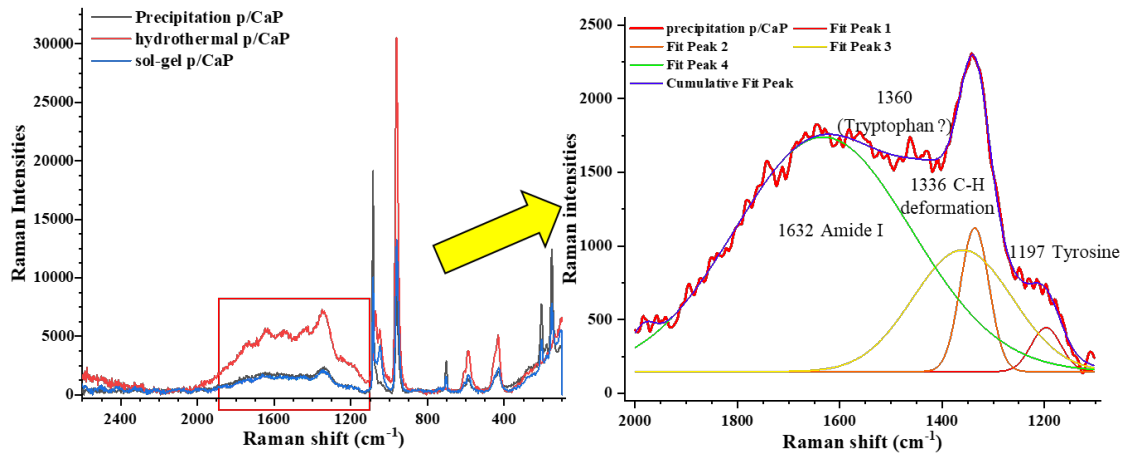


Fig. 4.3.10 Detailed peak fitting analysis of the synthesized p/CaP composite particles by Origin software.

The effects of different synthesis strategies on p/CaP composite particles were investigated via Raman spectroscopy as shown in Figure 4.3.9. The intensity of the type-B carbonate peak at 1074 cm^{-1} was higher than that in the synthetic HA samples, indicating the increasing concentration of carbonate contents in the composite particles. The detailed analysis of the region between 1100 and 2000 cm^{-1} were shown in this figure. The vibrational peaks of organic compounds including Amide-I peaks, Tyrosine and potential Tryptophan were observed by fitting the spectrum. Previous research has discussed the involvement of Tyrosine and Tryptophan in controlling the metabolism of osteoblast-osteocyte and the regulation of bone formation (Pallu et al., 2012; Shah et al., 2016).

4.3.3 XRD spectroscopy analysis of powder samples

The X-ray diffraction analysis of particle samples were performed to evaluate the crystallinity characteristics from different synthetic parameters for preparation of the samples. HA samples and pearl samples were compared with high quality ranked standard PDF card from the ICSD Fiz database. The standard HA sample chosen is PDF no. 01-074-0566 and the standard aragonite sample is with the PDF no. 01-071-2392 for comparison. The multiple XRD patterns were plotted via the Origin software as shown in the following figures.

The XRD pattern of pearl powder sample matched well to the standard aragonite as shown in Figure 4.3.10, although the overall peak intensities were slightly different, indicating the differences of crystallinity between pearl and natural aragonite. The characteristic CaCO_3 peaks were standard positioned at the following 2θ angles and corresponding planes: 26° (111), 27° (102), 31° (200), 33° (112), 33° (201), 36° (210, 020), 37° (103), 38° (013), 42° (121), 43° (022), 45° (004), 46° (122), 48° (104), 50° (213), 52° (311) and 53° (302) (De Villiers, 1971).

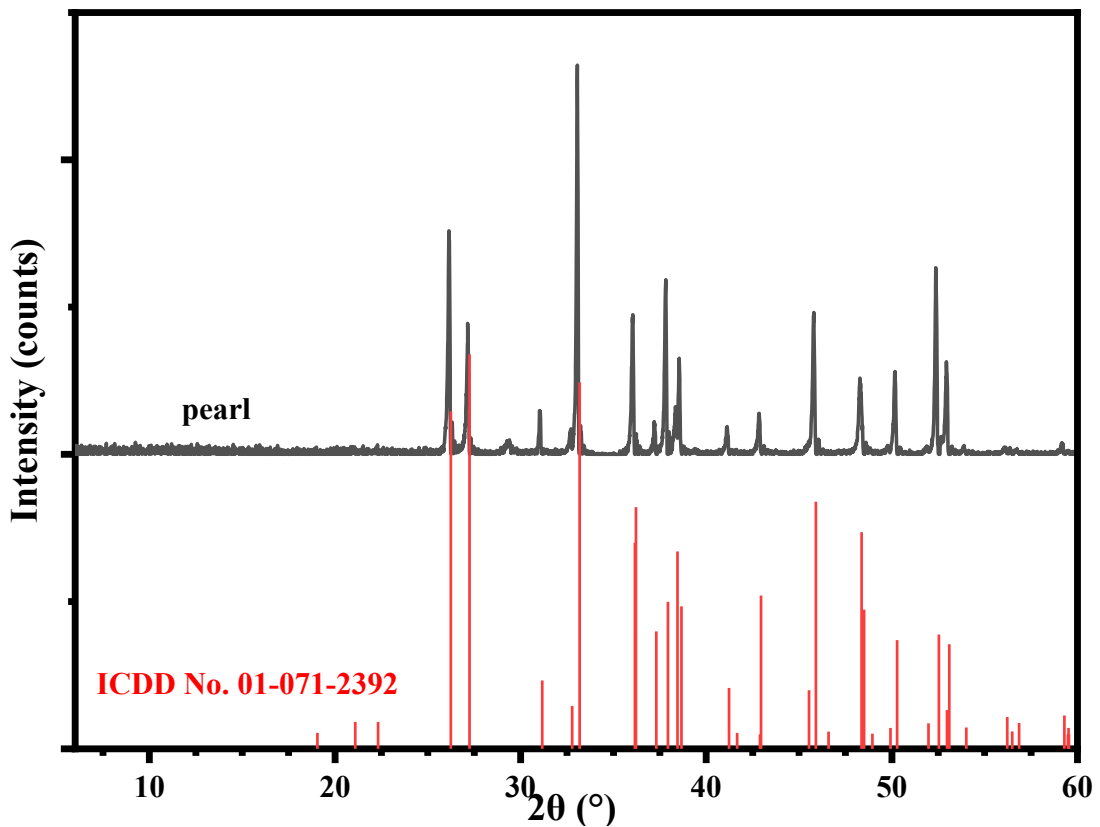


Fig. 4.3.11 X-Ray diffraction spectra of dried commercial pearl powders and the standard aragonite PDF card XRD (ICDD No. 01-071-2392) intensity pattern.

Comparing the commercial and synthetic HA sample with the standard HA XRD patterns, the spectra are shown in Figure 4.3.11. The main HA peaks positioned at the 2θ angle region between 20° and 56° were observed from all samples but the morphology and peak intensities including: 26° (002), 29° (120), 32° (211, 112), 33° (300), 34° (202), 40° (310), 47° (222), 50° (213, 321), 51° (410), 52°

(402) and 53° (004) (Sudarsanan and Young, 1969). At the region of $32-34^\circ$, the typical three shoulder peaks rose adjacent in all synthetic samples; however, the notable intensity and structural differences of peaks indicating the different crystallinity of three synthesis strategies. The precipitation HA matched better with the standard HA and commercial XRD intensity pattern, demonstrating relatively higher crystallinity while the HA samples prepared by the hydrothermal method appeared to be less crystallized. According to the previous report, it has been noticed that the hydrothermal process is not ideal to control the morphology and crystallinity of synthesized HA; although sol-gel method is notable for its low-temperature formation, larger surface area and the potential generation of the secondary product (usually calcium oxide, CaO), could decrease the crystallinity of products (Sadat-Shojai et al., 2013). In addition, at the 2θ region of $39-42^\circ$, the two shoulder peaks observed in other samples were overlapped in one broad peak as shown in HA synthesized by hydrothermal HA sample. More noises and spurious peaks were observed from the spectra of the sample prepared by the hydrothermal methodology comparing with the other two synthesized HA samples.

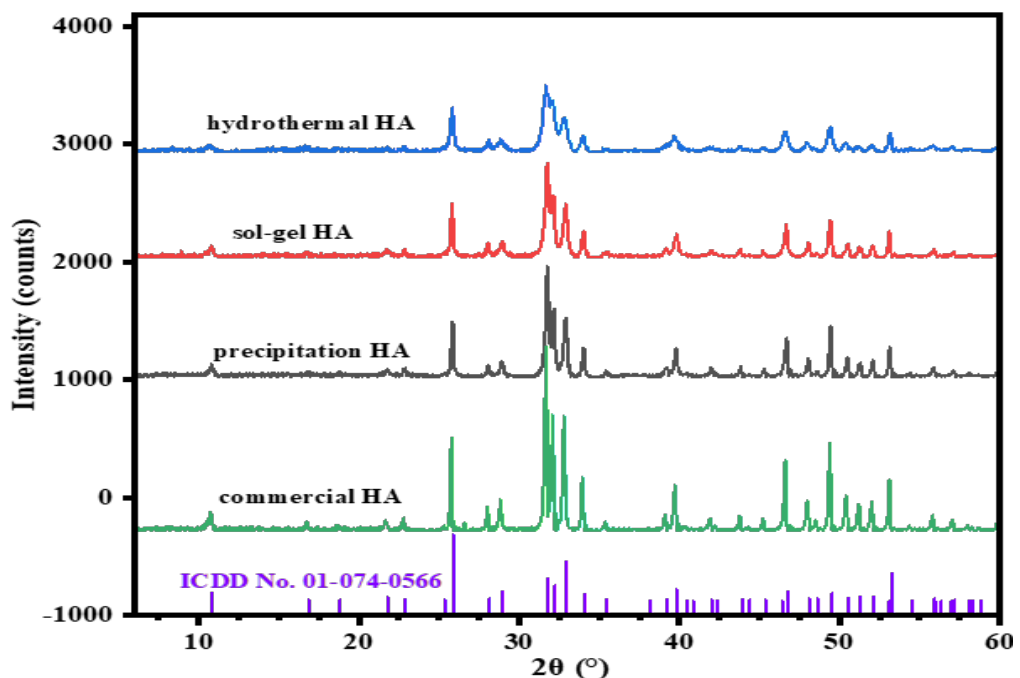


Fig. 4.3.12 X-Ray diffraction spectrum of dried commercial and three different synthesized HA powders compared to the standard aragonite PDF card XRD (ICDD No. 01-074-0566) intensity pattern.

In the diffraction pattern of the p/CaP samples, the main characteristic HA peak positions remained the same as the synthesized HA samples, indicating that the HA surrounded the surface of the pearl, but the crystallinity of the synthesized HA was not of significance as the stoichiometric HA. As mentioned in the previous section about the SEM analysis of the composite samples, the observation confirmed the attachment of HA on the pearl platelets in an amorphous morphology which is in agreement with the relative weak peak intensities of all synthesized particles. Moreover, the sharp peak at the 2θ angle of 32.8° in the spectra of sole HA, shifted slightly to around $33.0^\circ (\pm 0.03^\circ)$ which is closer to the characteristic CO_3^{2-} peak at 33.05° . This peak shift indicated that the attachment of synthesized HA on pearl surface were connected by the chemical reaction, which also was in agreement with the results of the FTIR-PAS results. As shown in Figure 4.3.12, the diffraction pattern of three composite samples demonstrated significant crystallinity differences the CaP coatings adhered on the surfaces of pearl platelets synthesized by precipitation method were more crystal than samples obtained from other methods.

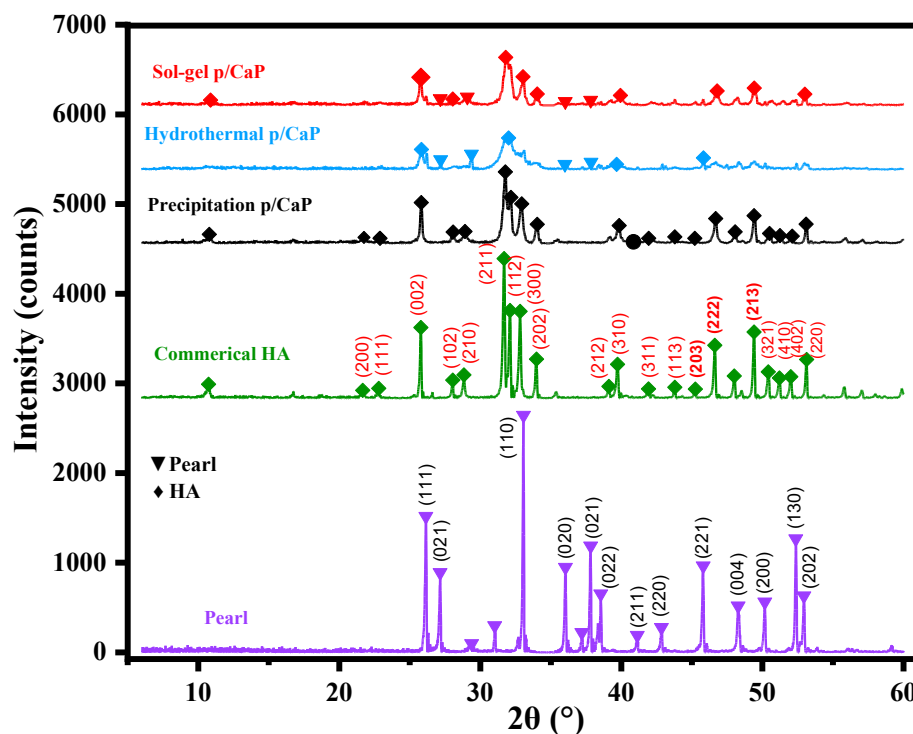


Fig. 4.3.13 The comparison XRD patterns of dried three different synthesized p/CaP powders compared to the spectra of commercial HA and pearl.

As Raynaud et al (2002) reported in the previous research, the XRD patterns of the unsintered or non-thermal treatment CaP composite could be overlapped by the HA peaks, for instance, the CaO peak is stable at room temperature but only can be detected at 750 °C. However, the single phased CaP apatites could be performed by the precipitation method, which in this study, matched the observed more crystalized XRD pattern shown in the p/CaP composite particles.

4.3.4 XPS analysis of powder samples

The XPS analysis was performed using the Kratos AXIS Supra XPS spectrometer (Kratos Analytical Ltd, Manchester, UK) equipped with a monochromatized aluminium X-ray source accelerated to the voltage of 15 keV at 225 W output power. The pass energy of survey spectra was set at 160 eV and the high-resolution spectra was collected at the set of 20 eV pass energy. The binding energy scale was set by fixing the C 1s component due to carbon bound only to carbon and hydrogen at 285.0 eV. The data analysis was performed with the CasaXPS program (Casa Software, Teignmouth, UK). Samples including synthesized HA by precipitation method, p/CaP (30:70, 40:60) composite particles by precipitation method and commercial pearl powders were dried in an oven at 120 °C over 48 hours before the evaluation.

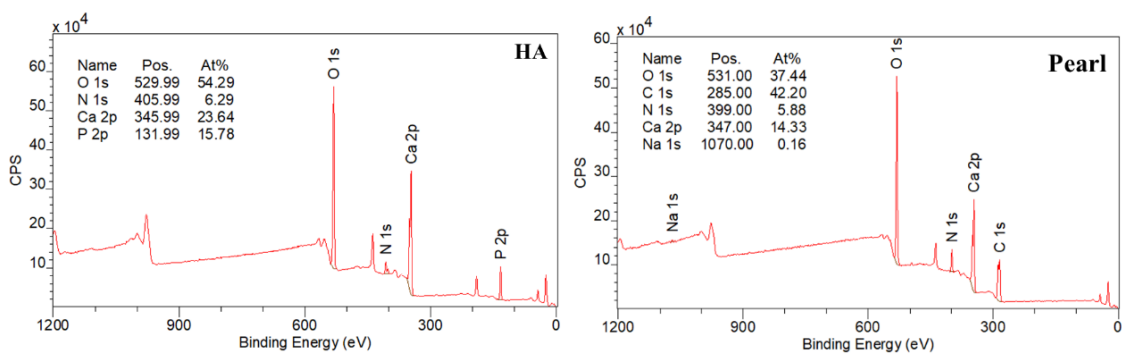


Figure 4.3.14 Representative XPS peaks of synthesized HA and the commercial pearl sample, with information of element positions and relative molar ratio (At%).

The elemental surface composition of HA and pearl are shown in Figure 4.3.13 which expected to display the Ca, P, O peaks in HA spectra and O, C, N, Na, Ca in pearl spectra, respectively. Besides those expected typical elemental peaks, a minor peak of N was observed in the HA spectra which was different from the typical spectrum of standard HA or β -TCP as previously studied (Lu et al., 2000). According to the content mentioned in the chapter of methodologies, this N peak might be assigned to the nitrate (NO_3) from the $\text{CaNO}_3 \cdot 4\text{H}_2\text{O}$. The Ca/P ratio was calculated in correlated with the atomic percent (At%) and the relative sensitive factor (RSF) provided by the equipment, that obtained a relative smaller surface Ca/P molar ratio of 1.50 (compared with the theoretical bulk HA sample) was in agreement with the previous catalyst study of standard HA by Tsuchida et al (2008). The typical XPS pattern of pearl showed no detection of phosphorus, but nitrogen was present on the surface, which is assigned to the existence of organic compounds of the peptide $-\text{NH}_2$ group.

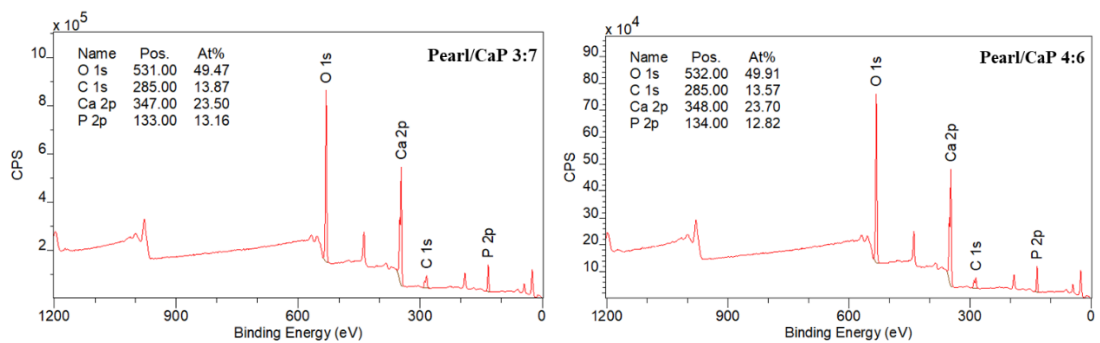


Figure 4.3.15 XPS survey spectra for synthesized pearl/CaP composite samples (3:7 and 4:6). Spectra showed that Ca, P, O and C were present in the samples.

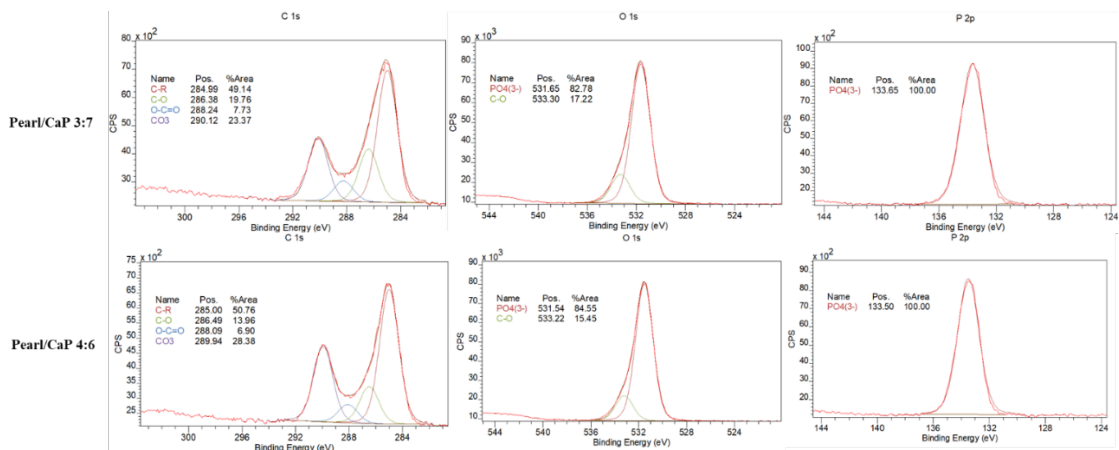


Figure 4.3.13 XPS high-resolution results for C 1s and O 1s spectra of p/CaP 3:7 and 4:6 composite samples.

The XPS spectrum of pearl/CaP 3:7 and pearl/CaP 4:6 is shown in the following figures. Besides the expected Ca, C and O peaks, a small P (2p) peak was observed in all composite samples examined. Compared with the sole pearl sample, the phosphorus had atomic percentages raising from 0 to 13.16% and 12.82%, respectively. The carbonate-type carbon was observed in pearl and p/CaP composite samples at the same binding energy.

4.4 Mechanical studies of composite scaffolds

The mechanical studies of composite scaffolds under compression stress were measured up to a certain percent of strain which was 70% for all sample groups. Figure 4.4.1 demonstrated the compression testing setup and the overall compression stress-strain curve for all scaffolds samples tested by a Universal Test Machine.

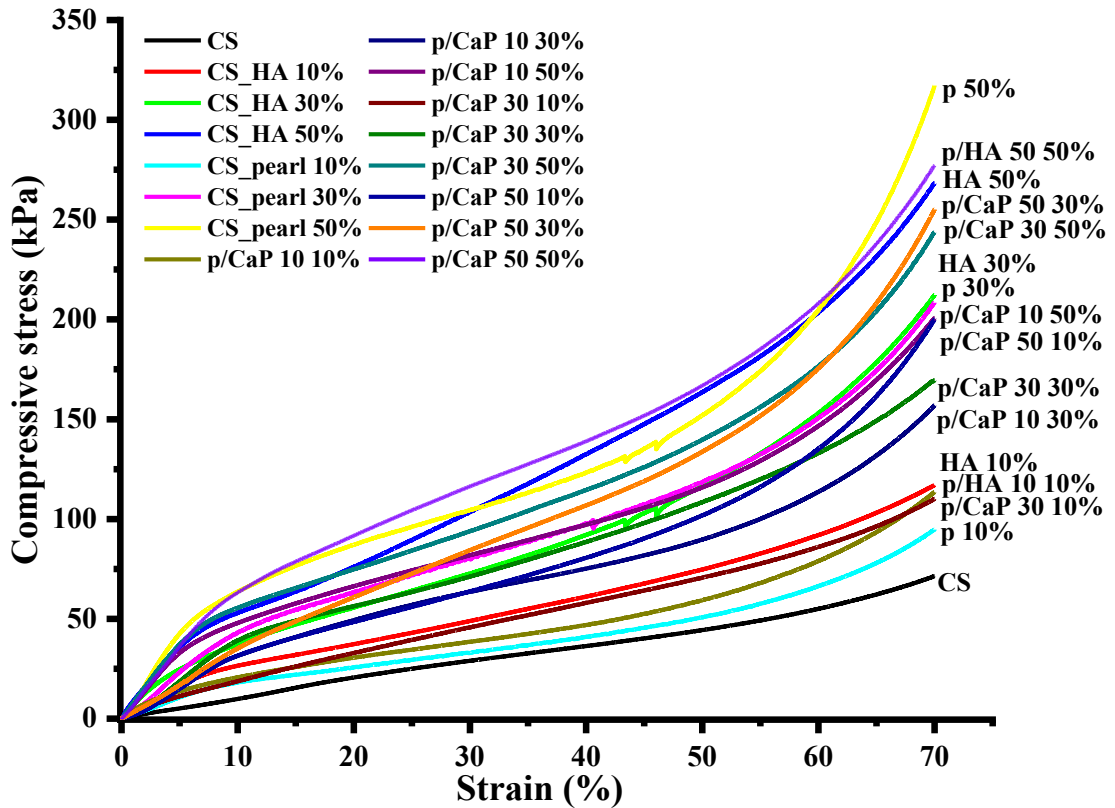


Figure 4.4.1 The compression test pictures of the sample specimens and the overall stress-strain curve of all samples plot with 4 replicates up to 70% strain.

All stress-strain curves comprise analogous multi-stage deformation, including the linear elastic deformation and flexural deformation region at small strain (0-8%), a plateau region at more larger strain (10-45%), followed by solidifying region in which the stress sharply increases at very large strain (45-70%) (Liu and Wang, 2023; Wan et al., 2008). During the elastic and flexural deformation stage, the onset of a series of minor cracks can be more obviously observed from the Fig 4.4.2, were corresponded to the maximum applied stress. The residual load-bearing capacity was provided by the collapsed interconnected pores, in which the chitosan polymer provided the necessary link and more polymer infiltration at the plateau region.

The individual compression stress-strain curves for different chitosan composite scaffolds were exhibited in Figure 4.4.2. All scaffold samples exhibited an elastic-plastic-elastic property as shown in the curve, which might be assigned to their porous structure. A significant increase in compression strength and elastic modulus were observed in comparison with the mean value between sole CS scaffold and composite CS scaffolds. At the 70% strain point, the pure CS scaffold

possessed the lowest mechanical strength reaching approximately 74 kPa while the pearl/CS 50 wt.% sample exhibited the highest strength at around 330 kPa.

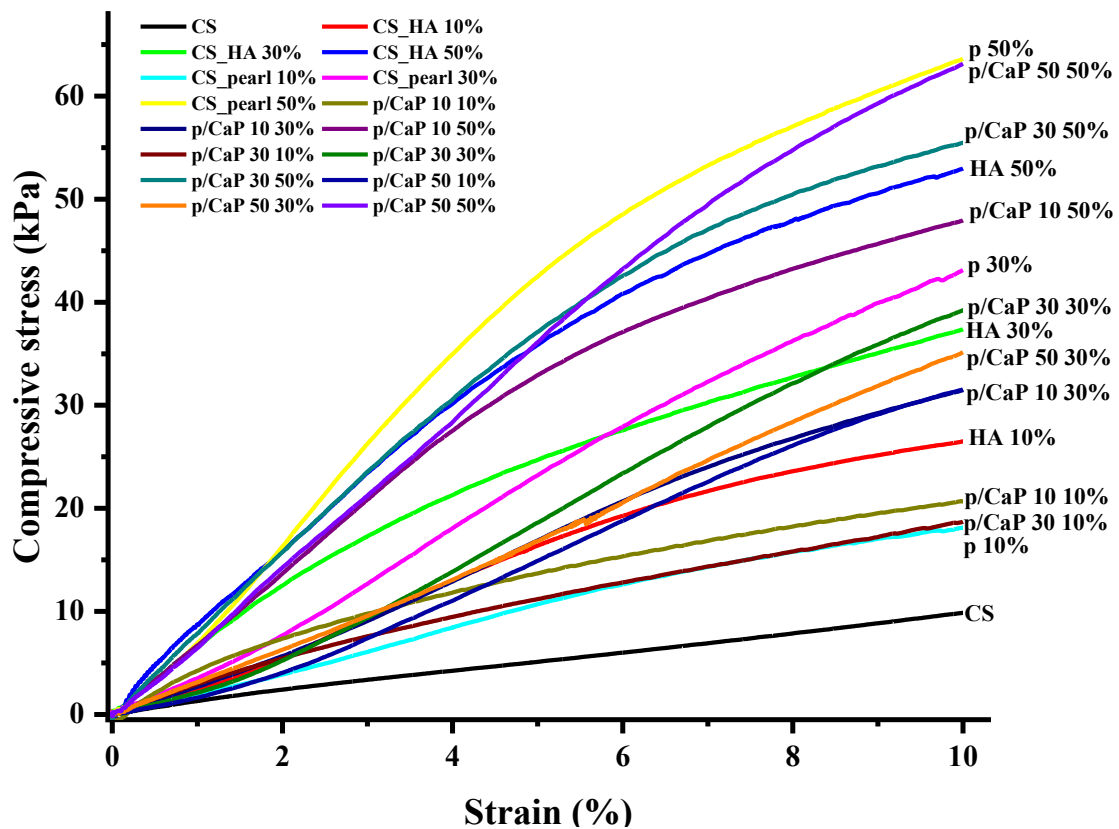


Figure 4.4.2 The compression test pictures of the sample specimens and the overall stress-strain curve of all samples plot with 4 times mean values up to 10% strain. This region is related to the elastic modulus region.

The elastic modulus was calculated according to the stress-strain linear regression of the lower elastic region of all samples and the R^2 were all ≥ 0.998 as listed in the table 4.4.1 below. The elastic modulus of the composite CS scaffolds was within the region of those articular cartilage tissues reported to be in the range of 0.5 and 1.0 MPa (Guilak et al., 1999; Mow et al., 1980). But comparing to the Young's modulus of human trabecular bone tissues which was reported previously to be in the range of 0.9 GPa to 2.0 GPa (Odgaard et al., 1991; Rho et al., 1993), the tested results revealed that the chitosan based porous scaffolds might not be ideal compared to other hard tissue engineering scaffolds. This improvement might be thought to result from the increasing Ca^{2+} and carbonate

groups from the pearl or pearl/CaP components interacted with the amino groups in the CS (Kim et al., 2015; Venkatesan et al., 2010).

Table 4.4.1 Elastic modulus of all CS and CS composite scaffolds.

Type of scaffolds	Elastic modulus (MPa)	R ² value
CS	0.13±0.009	0.9993
H1	0.34±0.008	0.9994
H3	0.59±0.019	0.9981
H5	0.74±0.014	0.9991
P1	0.46±0.013	0.9988
P3	0.48±0.005	0.9994
P5	0.87±0.015	0.9986
P1CaP9_1	0.22±0.008	0.9993
P1CaP9_3	0.30±0.012	0.9987
P1CaP9_5	0.70±0.010	0.9982
P3CaP7_1	0.29±0.003	0.9997
P3CaP7_3	0.42±0.016	0.9986
P3CaP7_5	0.76±0.003	0.9995
P5CaP5_1	0.35±0.007	0.9991
P5CaP5_3	0.36±0.018	0.9983
P5CaP5_5	0.73±0.012	0.9988

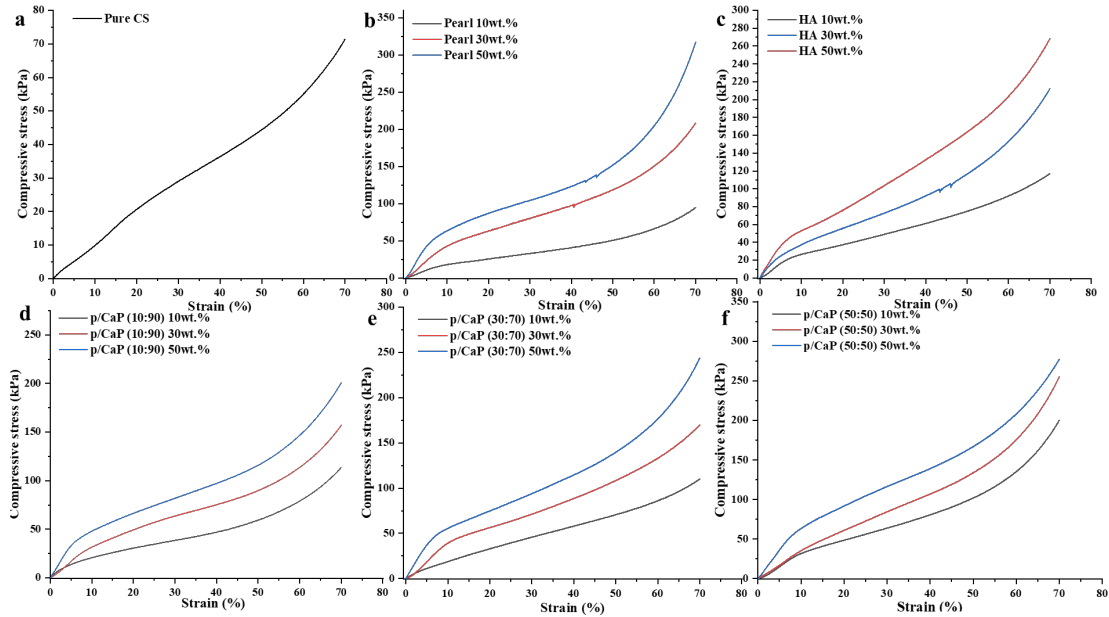


Figure 4.4.3 The compression stress-strain curves performed to 70% strain in different scaffold samples. These scaffolds were obtained from the freeze-drying method in different compositions: **a.** the sole CS, **b.** pearl/CS composite (10, 30, 50 wt.%), **c.** HA/CS composite (10, 30, 50 wt.%), **d.** P1CaP9/CS (10, 30, 50 wt.%) **e.** P3CaP7/CS (10, 30, 50 wt.%) **f.** P5CaP5/CS (10, 30, 50 wt.%).

Overall, compared with the pure chitosan scaffolds, the Young's modulus of p/CaP scaffolds was significantly enhanced due to the incorporation of hard particles. When increased the pearl to CaP ratio from 10:90 to 30:70, a significant Young's modulus increase was observed, which might be because the formation of carbonated CaP components increased the compressive strength. However, a slight decrease in Young's modulus was observed when increasing the pearl to CaP ratio to 50:50, possibly linked to agglomerates of composite particles leading to pore clogging, as discussed in section 4.2.2. In the present case, it was observed in Table 4.4.1 and Fig 4.4.2 that the compressive modulus and the stress at 10% strain of pearl chitosan combined scaffolds have relatively better strength and higher dimensional stability, compared with the HA chitosan combined scaffolds. However, the mechanical strength of the p/CaP chitosan scaffolds presented a low strength and poor dimensional stability, indicating the larger deformation of the internal structure of the composite scaffolds. On the

other hand, the addition of p/CaP composite particles allowed the scaffolds to have the enhancement in the compressive strength compared to the pure chitosan scaffolds.

4.5 Discussions

The synthesis of composite powders involving pearl and calcium phosphate (p/CaP) through three distinct methods, stemming from hydroxyapatite (HA) synthesis, represents an innovative approach. Amorphous CaP has garnered increasing attention in comparison to stoichiometric HA due to its crucial role in bone apatite nucleation and the mineralization process within the bone remodelling cycle. Previous studies, such as Raynaud's (2002), have suggested that amorphous calcium phosphate (ACP) may be sequestered and deposited via intracellular and vesicular mechanisms in the gap zones of the collagen matrix. This proposed role positions ACP as a transient phase, acting as a precursor for subsequent apatite growth. Complementary in-vitro investigations, employing collagen as the organic scaffold, further substantiate the presence of ACPs at the gap zones of collagen, serving as a precursor stage before transforming into apatite. Earlier studies by Boonrungsiman et al. (2012), Omelon et al. (2009), and Rustom et al. (2019) have provided additional insights into the growth mechanism associated with the transformation of amorphous CaP to apatite. Consequently, the anticipated outcome for p/CaP composite particles is an enhancement in biocompatibility and osteogenesis properties.

In this research, we employed three distinct synthesis methods to fabricate p/CaP powders through a relatively straightforward process. We systematically investigated the impact of these different synthesis approaches on the thermal stability, morphology, and chemical structure of the resulting composite. Notably, all three methods involved an additional aging process, possibly accounting for the observed similar morphological properties in the scanning electron microscopy (SEM) analysis. Following a 24-hour aging period at 85 °C, the

resultant products underwent filtration using a vacuum filtration system and subsequent drying.

Thermogravimetric analysis (TGA) was conducted to assess the thermal stability of the composite produced by the three methods. Strikingly, our findings revealed that the various synthesis approaches had no significant influence on the thermal stability of the composite. This intriguing result suggests that the incorporation of amorphous CaP particles played a role in reducing the deformation of carbonate compounds in pearl, contributing to the overall thermal stability of the composite material.

The SEM analysis of p/CaP composite samples uncovered a compelling integration of embedded or attached crystals intricately distributed throughout the pearl platelets. Even at lower magnifications, the synthesized amorphous CaP crystal agglomerates exhibited clear visibility, while at higher magnifications, an intricate, amorphous interconnected structure emerged. This unique amalgamation of pearl and CaP imparted distinctive morphological characteristics, particularly at higher magnifications, setting it apart from HA samples obtained through alternative synthesis methods. Significantly, the SEM images provided compelling evidence supporting the feasibility of incorporating both pearl and CaP in this study.

The attachment of CaP crystals and pearl platelets showcased promising interactions, substantiating the notion that amorphous CaP clusters, as observed in this study, play a pivotal role in fostering the growth of bone apatites. This observation aligns with the findings of Lotsari et al. (2018), underlining the critical importance of amorphous CaP clusters in the autocatalytic nucleation of HA and the formation of Ponsner's clusters. The SEM results offer valuable morphological insights, laying the foundation for further explorations into the potential applications of the pearl/CaP composite in the realm of bone regeneration and related fields.

The chemical analyses conducted through Fourier-transform infrared spectroscopy with photoacoustic detection (FTIR-PAS), Raman spectroscopy, X-

Innovative incorporation of pearl and calcium phosphate composite in bone regenerative scaffolds

ray diffraction (XRD), and X-ray photoelectron spectroscopy (XPS) have furnished additional insights into the properties of p/CaP particles. The XRD results revealed pronounced distinctions in the composite derived from three distinct methods, with the crystallinity of p/CaP originating from the precipitation method surpassing that obtained through the other two strategies. Notably, the suboptimal control over morphology and crystallinity in the synthesized HA could be attributed to constraints in the hydrothermal process.

The hydrothermal method, while recognized for its capability for low-temperature formation and the generation of secondary products (typically calcium oxide, CaO), appears to be associated with limitations in achieving higher crystallinity compared to the other composite scaffolds that of other two methods. The ethanol-based precipitation method, celebrated for its capacity to operate at lower temperatures and provide larger surface areas, also led to a reduction in the final product's crystallinity. Only the traditional chemical precipitation method of synthesizing p/CaP products exhibited higher crystallinity of the final products, proved by the SEM, XRD and FTIR spectra.

The results obtained from FTIR and Raman spectroscopy contribute to a comprehensive understanding of the chemical properties inherent in the pearl/CaP (p/CaP) composite and its individual constituents. In the FTIR spectra, distinctive chemical features unique to pearl powder were discerned, encompassing hydroxyl stretches, organic matrix vibrations, and carbonate groups. The presence of carbonate ions in the pearl powder was substantiated by the carbonate peaks observed at 1787 cm^{-1} , 1656 cm^{-1} , and 1414 cm^{-1} , unequivocally identifying it as aragonite pearl.

Furthermore, both commercial and synthesized HA samples manifested characteristic peaks corresponding to phosphate vibrations in the FTIR spectra. Variations in peak intensity across these samples hinted at differences in crystallinity. The FTIR-PAS spectra further elucidated phosphate vibrations, offering nuanced insights into the lower wave number region.

This multifaceted spectroscopic analysis underscores the unique chemical signatures of pearl powder and HA, elucidating the distinctiveness of the p/CaP composite. The identification of aragonite pearl and the characterization of phosphate vibrations provide a foundation for understanding the intricacies of the composite's chemical composition, crucial for applications in bone regeneration and related fields.

The quantitative analysis of band areas yielded insightful information, indicating a discernible decrease in hydroxyl group intensity and a concomitant increase in carbonate group intensity within the p/CaP composite when compared to HA. This observation aligns harmoniously with previous studies that have postulated the substitution of hydroxyl ions with carbonate groups in calcium hydroxyapatite (CHA). The ion substitution process, intrinsic to the synthesis of HA with pearl powders, is likely underpinned by the replacement of OH⁻ groups with carbonate groups. This transformative process culminates in the development of type-A CHA, elucidating the chemical dynamics and structural modifications occurring during the synthesis of the p/CaP composite.

Raman spectroscopy provided additional insights into the chemical composition. The pearl powder exhibited vibrational carbonate peaks and distinctive lattice modes, allowing for differentiation between aragonite and vaterite structures. Synthesized HA samples showed lower intensity in phosphate peaks compared to commercial HA, indicating variations in crystallinity. Differences in the ν_3 and ν_4 phosphate regions suggested the presence of tri-calcium phosphate (TCP) phase HA in the synthesized samples. The Raman analysis of p/CaP composite particles indicated an increased concentration of carbonate contents, particularly in the type-B carbonate peak at 1074 cm^{-1} . The spectrum also revealed organic compound peaks, including Amide-I peaks, Tyrosine, and potential Tryptophan. The involvement of Tyrosine and Tryptophan in bone metabolism and regulation of bone formation aligns with the potential bioactive properties of the p/CaP composite.

The freeze-dried composite scaffolds in this investigation showcased interconnected and porous structures with homogeneity. SEM characterization of

the porous morphologies across all scaffolds revealed dimensions ranging from 26 to 600 μm , aligning with the requisites for cell migration and proliferation in bone tissue engineering. The surface morphologies of the pearl, HA, and p/CaP composite scaffolds exhibited distinctive rough structures. The HA/CS scaffold displayed a pin-like morphology attributed to the unique crystal structure of commercial HA. Conversely, pearl/CS scaffolds showcased platelet crystal distribution on scaffold walls. The p/CaP-CS scaffolds presented a morphology combining pearl platelets and HA, but SEM revealed more dispersed amorphous crystal agglomerations. This dispersion contributed to a decrease in porosity, as discussed in the preceding section (4.2.2.2).

FTIR-ATR spectroscopy was employed to characterize the chemical properties of the scaffolds. Limited differences in peak intensity between the bottom and top layers of all scaffold samples indicated a relatively homogeneous distribution of pearl, HA, and p/CaP composite, promising for their bioactive performance.

The mechanical properties of different scaffold groups demonstrated enhancements when comparing HA scaffold groups with the p/CaP scaffold groups. None of the scaffolds experienced breakage at 70% strain, and all specimens rebounded close to their initial state after testing. The highest mean compression strength at 70% in the composite chitosan scaffolds was noted at 330 kPa, specifically from the pearl 50 wt.% CS scaffold. Additionally, the highest elastic modulus reached up to 0.87 MPa. This compressive test result is associated with the distinct morphological structures of pearl, HA, and p/CaP. As previously discussed, the platelet structure of pearl was more embedded on the chitosan matrix wall, while p/CaP scaffolds demonstrated larger agglomerations attached to the surface. Research by Zeng and Zhang (2013) proposed that the incorporation of pearl can significantly enhance the mechanical properties of composite chitosan microspheres, with cationic compounds from chitosan particles actively interacting with the organic matrix of pearl shell powders. This perspective provides insight into the mechanical strength enhancement of p/CaP chitosan scaffolds. However, increasing the pearl to CaP ratio to 50:50 resulted in larger particle sizes, causing clotting of internal pores, as indicated by decreased

porosity in the porosity estimation section, as well as changes in the elastic modulus.

In conclusion, the synthesis of p/CaP composite through precipitation, sol-gel, and hydrothermal methods has been successfully demonstrated. The physiochemical assessments of the composite particles have revealed a strong chemical binding between pearl and amorphous CaP particles. This binding holds significant promise for advancing our understanding of the mineralization process and the intricate chemical structure of this composite material.

The choice of the freeze-drying technique emerged as a reasonable strategy for fabricating composite chitosan scaffolds in this study. Notably, the enhancement in compressive strength was observed, and it is suggested that this improvement may be attributed to the chemical properties inherent in p/CaP composite powders.

5 Biological studies of composite scaffolds

5.1 Introduction

This chapter describes the biochemical and biological characterizations of composite CS scaffolds in diverse aspects, including the *in-vitro* degradation and cell viability/cytotoxicity assays. The swelling capacity of the composite scaffolds were determined by weight loss and pH changes during the incubation of specimens in a phosphate buffer saline (PBS), in the presence or absence of lysozyme enzymes. The gradual weight loss of scaffold was obtained for both PBS and lysozyme-PBS (L-PBS) media. Cell cytocompatibility, proliferation and differentiation were investigated by utilizing MG-63 osteoblast-like cell lines. The cytotoxicity and proliferation were evaluated by employing the repeatable indirect AlamarBlue® (AB) assay, and cell adhesion was observed by employing SEM.

5.2 *In-vitro* degradation tests

In the realm of tissue engineering, the meticulous investigation of scaffold degradation is paramount for the success of regenerative strategies (Mikos et al, 1993). A nuanced understanding of scaffold degradation necessitates comprehensive analyses, with pH and weight analyses emerging as pivotal tools to unravel the intricate dynamics of scaffold interactions within the biological milieu.

The degradation of scaffolds is a multifaceted process influenced by diverse factors, including cellular activity, enzymatic processes, and the inherent properties of the scaffold material (Place et al., 2009). As scaffolds undergo degradation, they release byproducts that can modulate the local pH environment. Simultaneously, changes in weight offer tangible insights into the physical integrity of the scaffold. These dual analyses become critical for comprehending the kinetics and mechanisms of degradation.

The pH analysis assumes significance due to its ability to provide real-time, quantitative information about the acidity or alkalinity of the microenvironment surrounding the scaffold. This information is crucial for understanding the potential impact of pH fluctuations on cellular behaviour, including proliferation, differentiation, and overall tissue regeneration (Li et al., 2017). Moreover, pH variations can influence the solubility of scaffold materials, directly impacting their mechanical integrity and structural support during tissue regeneration.

Weight analysis, on the other hand, complements pH studies by offering tangible evidence of scaffold degradation. Changes in weight over time provide valuable data on the mass loss associated with degradation processes. This quantitative metric becomes instrumental in evaluating the durability and stability of scaffolds under physiological conditions, guiding the optimization of scaffold designs for specific tissue engineering applications.

The integration of pH and weight analyses in scaffold degradation studies represents a holistic approach that captures both the chemical and physical

Innovative incorporation of pearl and calcium phosphate composite in bone regenerative scaffolds aspects of the process. This comprehensive understanding is essential for tailoring scaffold designs, ensuring they meet the demands of specific tissue environments. Through these analyses, researchers can fine-tune degradation rates, optimize material properties, and advance the development of scaffolds with tailored profiles for regenerative therapies.

In summary, pH and weight analyses stand as cornerstones in the systematic characterization of scaffold degradation in tissue engineering (Agrawal et al., 2001). Their synergistic role in deciphering the complex interplay between scaffolds and biological systems is pivotal for advancing the field towards the development of regenerative therapies with enhanced precision and efficacy.

Degradation is paramount for the success of regenerative strategies (Mikos et al., 1993). A nuanced understanding of scaffold degradation necessitates comprehensive analyses, with pH and weight analyses emerging as pivotal tools to unravel the intricate dynamics of scaffold interactions within the biological milieu.

The degradation of scaffolds is a multifaceted process influenced by diverse factors, including cellular activity, enzymatic processes, and the inherent properties of the scaffold material (Place et al., 2009). As scaffolds undergo degradation, they release byproducts that can modulate the local pH environment. Simultaneously, changes in weight offer tangible insights into the physical integrity of the scaffold. These dual analyses become critical for comprehending the kinetics and mechanisms of degradation.

The pH analysis assumes significance due to its ability to provide real-time, quantitative information about the acidity or alkalinity of the microenvironment surrounding the scaffold. This information is crucial for understanding the potential impact of pH fluctuations on cellular behaviour, including proliferation, differentiation, and overall tissue regeneration (Li et al., 2017). Moreover, pH variations can influence the solubility of scaffold materials, directly impacting their mechanical integrity and structural support during tissue regeneration.

Weight analysis, on the other hand, complements pH studies by offering tangible evidence of scaffold degradation. Changes in weight over time provide valuable data on the mass loss associated with degradation processes. This quantitative metric becomes instrumental in evaluating the durability and stability of scaffolds under physiological conditions, guiding the optimization of scaffold designs for specific tissue engineering applications.

The integration of pH and weight analyses in scaffold degradation studies represents a holistic approach that captures both the chemical and physical aspects of the process. This comprehensive understanding is essential for tailoring scaffold designs, ensuring they meet the demands of specific tissue environments. Through these analyses, researchers can fine-tune degradation rates, optimize material properties, and advance the development of scaffolds with tailored profiles for regenerative therapies.

In summary, pH and weight analyses stand as cornerstones in the systematic characterization of scaffold degradation in tissue engineering (Agrawal et al., 2001). Their synergistic role in deciphering the complex interplay between scaffolds and biological systems is pivotal for advancing the field towards the development of regenerative therapies with enhanced precision and efficacy.

5.2.1 Preparation of test samples and degradation media

Cylindrical scaffold specimens were prepared by utilizing the cork borer (5/16 inch) and four sample replicates from each sample group were prepared for the experiment. All specimens were sanitized by exposed under UV light for 1 h before starting the experiment. Samples were prepared under the same conditions for both PBS and L-PBS media test groups. Each sample was weighted to a similar mass of 0.2 ± 0.05 g and recorded as W_i .

Two different degradation media were prepared for this study, the PBS and lysozyme-PBS solutions. The PBS media was prepared by dissolving one PBS tablet in 200 ml Milli-Q water (pH \approx 7.4) and autoclaved at 132 °C in an automatic

Innovative incorporation of pearl and calcium phosphate composite in bone regenerative scaffolds autoclave for 20 min, including heating, ventilation and cooling time of 1 h in total. Then, PBS solutions were stored in a fridge at 4 °C until needed for the *in-vitro* degradation studies. The lysozyme-PBS solution was prepared by dissolving an amount of lysozyme from hen egg white (≤ 20.000 U/mg, Thermo Fisher Scientific™, MP Medical™, Loughborough, UK) in the PBS media and stored at 4 °C.

The scaffold specimens including 3 ml of PBS/L-PBS solution were placed into 7 ml vials and incubated at 37 °C for the tests at different time intervals: 1, 4, 7, 14, 21 and 28 days. All sample tubes were manually swirled twice daily, and the sample media were replaced every 48 hours.

5.2.2 pH analysis

During the degradation test, pH alteration in media was determined by measuring the pH of the solution via a pH-meter, at each designed time intervals (1, 4, 7, 14, 21, 28).

5.2.3 Weight analysis

After pH measurements, samples were placed into the wells of a 24 well-plate and rinsed with 1 ml of de-ionized water thrice to remove any ions absorbed on the surface. Then, all samples were placed into new vials with slightly loosened lids and incubated at 37 °C for 24 h for the removal of surface water while still maintaining their scaffold form rather than as dried film. After 24 h incubation, scaffolds were weighted which were recorded as (W_t). Weight loss was expressed as the dry weight remaining ratio or weight loss percentage at following equations, respectively.

$$\text{Dry weight remaining ratio} = \frac{W_t}{W_i} \times 100\%$$

$$\text{Weight loss (\%)} = \frac{W_i - W_t}{W_i} \times 100\%$$

5.2.4 Results and discussion

The comparative pH alteration plots of the degradation of samples in both PBS and lysozyme media specimens are given in Figure 5.2.1. The pH range over the whole degradation period was lower in L-PBS media specimens (~6.9-7.3) while sole PBS media specimens were higher (~7.0-7.4). During the first 7 days, the pH of most scaffold supernatants in both media showed an increase that could be associated with swelling of the scaffold samples. Samples in sole L-PBS media showed a more significant pH changes might be assigned to the effect of lysozyme that accelerated the deformation of CS matrix. A sudden decrease in the pH was observed between day-7 and day-14, which indicates the start of deswelling and weight loss. Between day-14 and day-28, the pH of the supernatants of samples in PBS became more stable than those in L-PBS media, however, the final pH at day-28 of all samples returned to around the same level of two different media. Overall, the minor pH difference of all samples after the 28-day in-vitro degradation test, indicated the relative pH stability of all scaffold samples. In comparison with the study presented by Wei et al (2008), this pH stability could be correlated with the released fragments and oligomers from the chitosan cannot be largely accumulated.

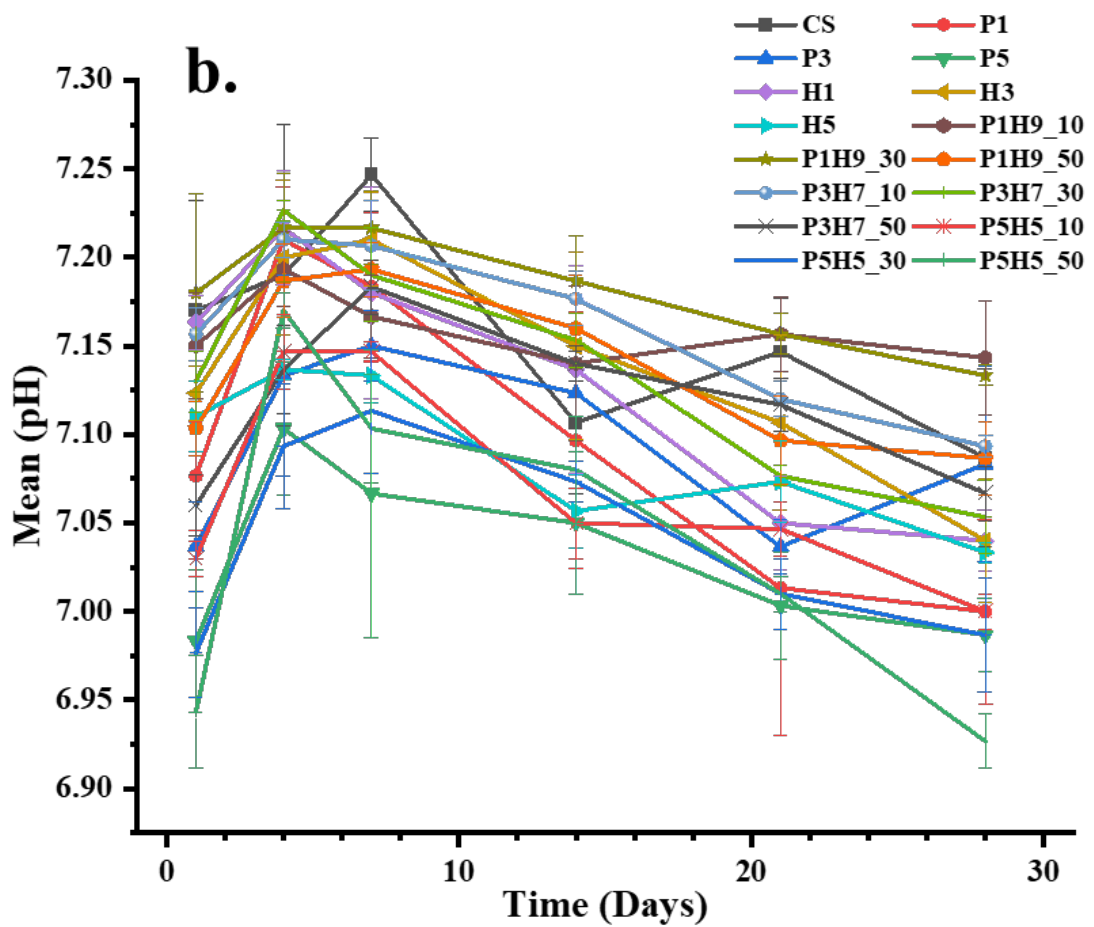
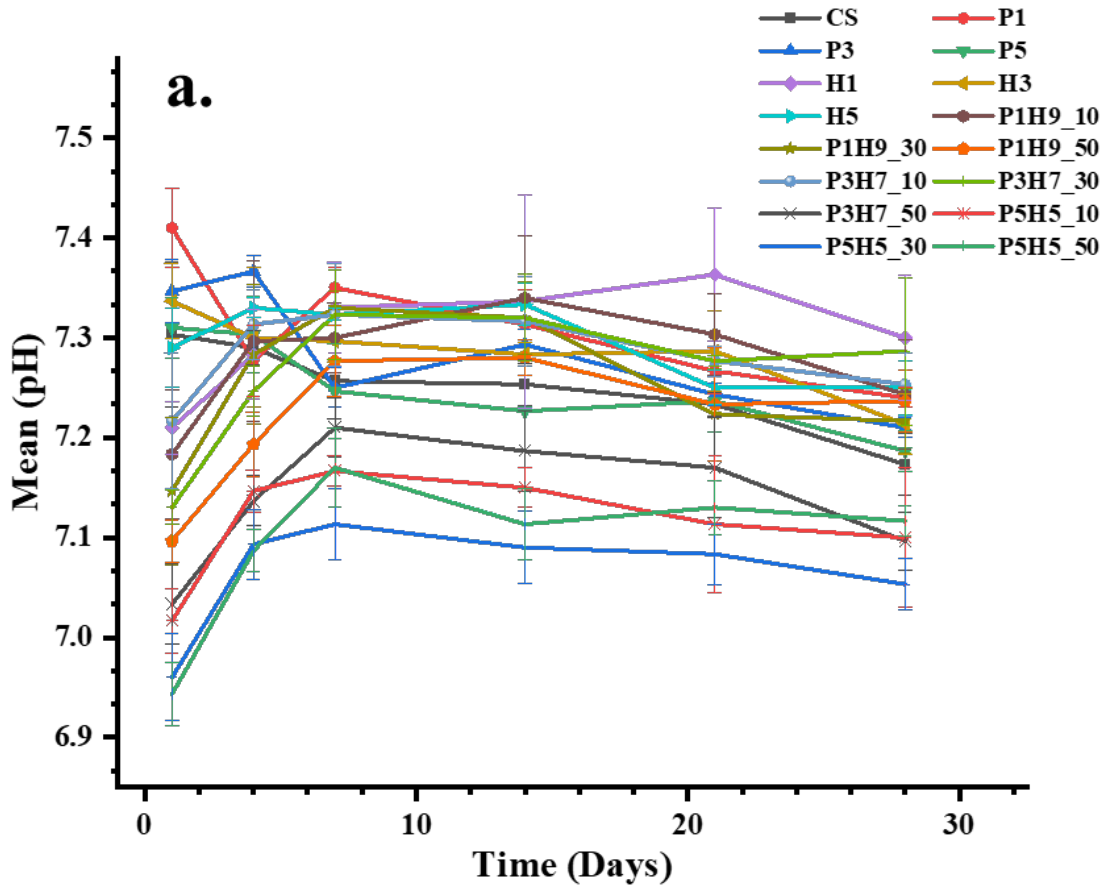


Figure 5.2.1 The pH alteration of supernatant media taken at different time intervals of up to 28 days in the *in-vitro* degradation tests of different composite scaffolds in **a.** PBS and **b.** L-PBS. The scaffold specimens are CS, pearl_CS group (P1, P3 and P5), HA_CS group (H1, H3 and H5), pearl/CaP_CS group (P1CaP9_10/30/50, P3 CaP7_10/30/50 and P5 CaP5_10/30/50).

The *in-vitro* degradation was based on weight decrease of the samples in media during the incubation of samples in both the presence and absence of the lysozyme enzyme (5 mg/ml) in PBS in 28 days. During the first day of incubation in both media, scaffold specimens lost almost 8 to 10% of their weight. This part of weight loss at the beginning could be associated with water lost due to further gelation at 37 °C during drying for 24 h. From day-4 to day-28, the degradation ratio of all samples in the PBS following almost the same linear trend. A multi-stage degradation was found in samples soaked in L-PBS. More significant weight changes can be observed from the second test, indicated the degradation rate was accelerated by the lysozyme, which increased the hydrolysis reaction of the chitosan particles. The degradation speed of scaffolds incubated in the presence of L-PBS media was faster in comparison to sole PBS media specimens as shown in figure 5.2.2.

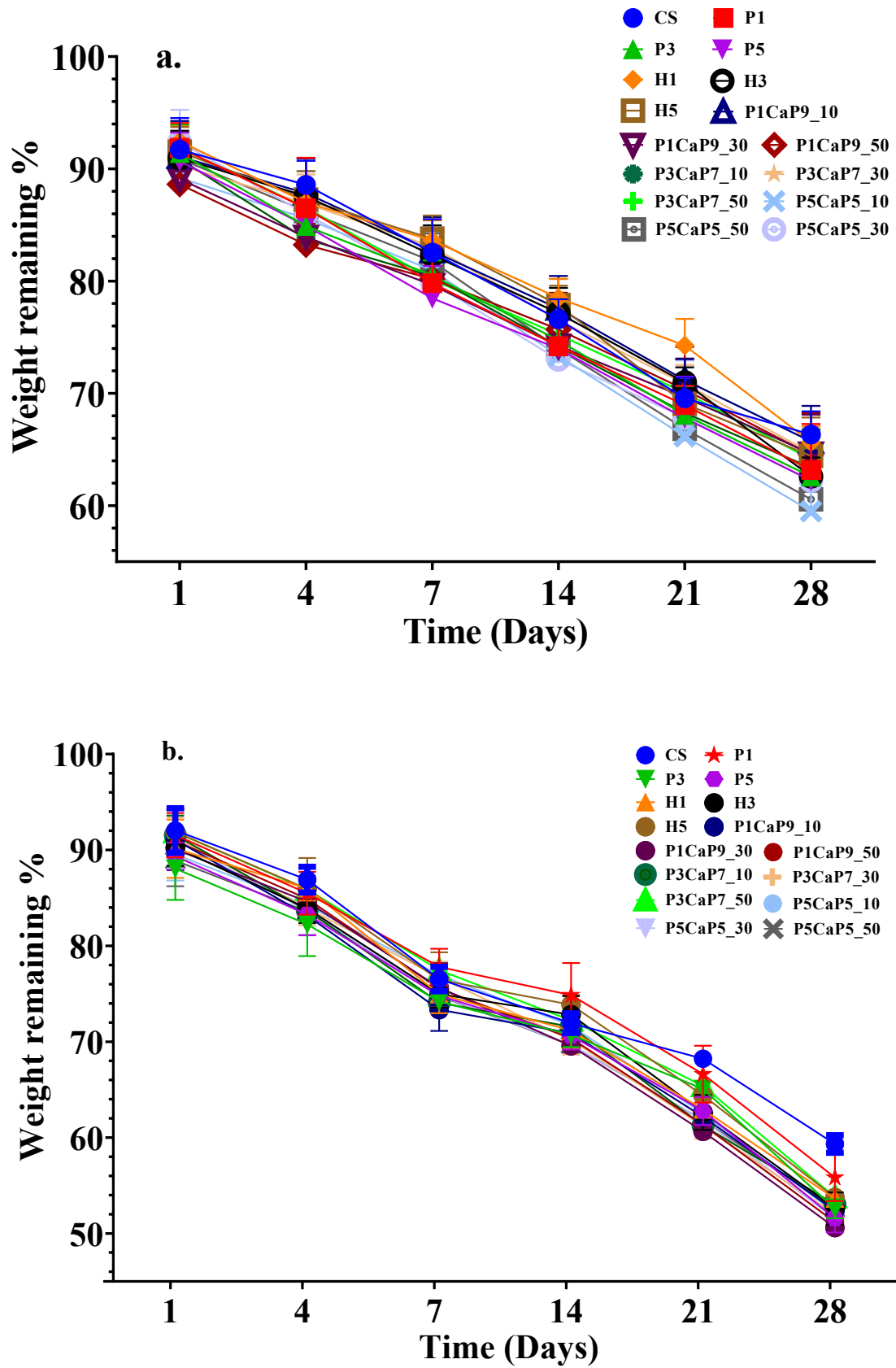


Figure 5.2.2 The comparative results of *in-vitro* degradation weight analyses at different time intervals of dry weight remaining ratios up to 28 days in the *in-vitro* degradation

tests of composite scaffolds in **a.** PBS and **b.** L-PBS (5 mg/mL) solution. The scaffold specimens are CS, pearl_CS group (P1, P3 and P5), HA_CS group (H1, H3 and H5), pearl/CaP_CS group (P1CaP9_10/30/50, P3CaP7_10/30/50 and P5CaP5_10/30/50).

In comparison between specimens degraded in PBS and L-PBS media, the degradation rate after 28-days in two different medias showed a little difference, specimens immersed in PBS showed a relatively linear degradation rate continuously throughout the whole experiment; on the other hand, in L-PBS media, specimens had a noticeably slower degradation between day 7 and day 14. Moreover, the total weight loss of all samples in PBS was up to 40%, while in the L-PBS the total degradation rate was increased to nearly 50%. According to the two-way ANOVA test programmed by the GraphPad Prism (Version 8.0.2, San Diego, CA, USA), the results of this *in-vitro* degradation test and pH alteration were not statistically significant when compared between different samples (the adjusted p value > 0.9999); however, significant differences were observed while comparing along the time intervals ($p < 0.0001$).

5.3 Cell viability-AlamarBlue[®] (AB) assay

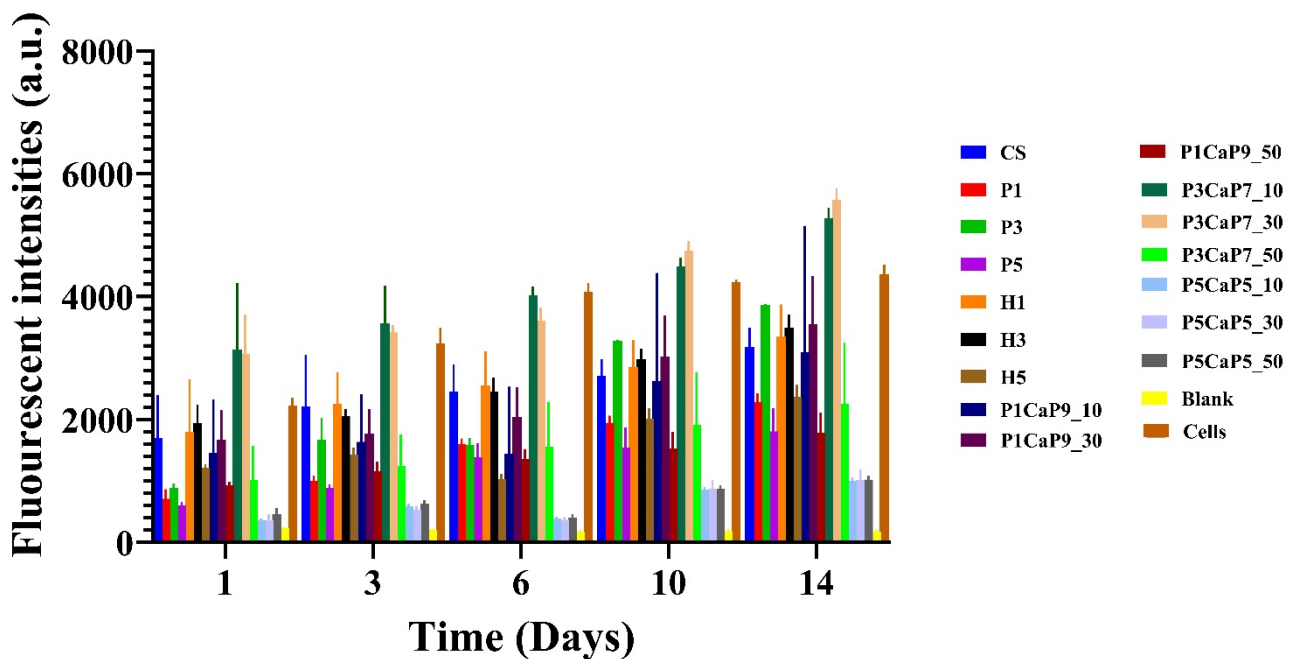
To investigate the biocompatibility of the scaffolds and the proliferation of cells, MG-63 human cancerous osteoblast cell lines were defrosted and passaged in advance for the experiment. The cells were incubated in a Dulbecco's Modified Eagle Medium (DMEM, Gibco[®], ThermoFisher[™], Loughborough, UK) culture media supplemented with 10% of fetal calf serum (FCS, Sigma-Aldrich[®], Dorset, UK), 1% penicillin/streptomycin (P/S, 10,000 U/mL, Gibco[®], ThermoFisher[™], Loughborough, UK). The adherent MG-63 cells were detached by using trypsin-EDTA (Gibco[®], ThermoFisher[™], Loughborough, UK) when they reached 90% confluency and passaged.

As aforementioned, at determined culture intervals, the fluorescence values of the aliquot solutions were measured in an Infinite[®] 200 PRO microplate reader

(TECAN®, Tecan Group Ltd., Männedorf, Switzerland) by using excitation and emission light wavelengths of 530 and 590 nm, respectively. The AB assay results were expressed as a mean with standard deviations (SD) for repetitions. The statistical analyses were performed in GraphPad Prism (Version 8.0.2, San Diego, CA, USA) software by using Two-way ANOVA test. SEM scanning by using the Schottky Field Emission Scanning Electron Microscope (FESEM) (JEOL JSM-7800F, Tokyo, JAPAN) were performed for the morphological evaluation of visible cells attached on the scaffolds.

5.3.1 AB assay results and discussion

Figure 5.3.1. shows the measurements of cell metabolic activities as indicators of cell viability via AB assay by fluorescent reading at 5 time intervals. The results of the AB experiment were performed on the scaffolds with a cell concentration of 20,000 cells/sample. The cell cytocompatibility of the scaffolds and the cell viability results can be revealed from the fluorescent intensity changes throughout the 14-day incubation period. More detailed comparative statistical studies are displayed in Figure 5.3.2, Figure 5.3.3 and Figure 5.3.4.



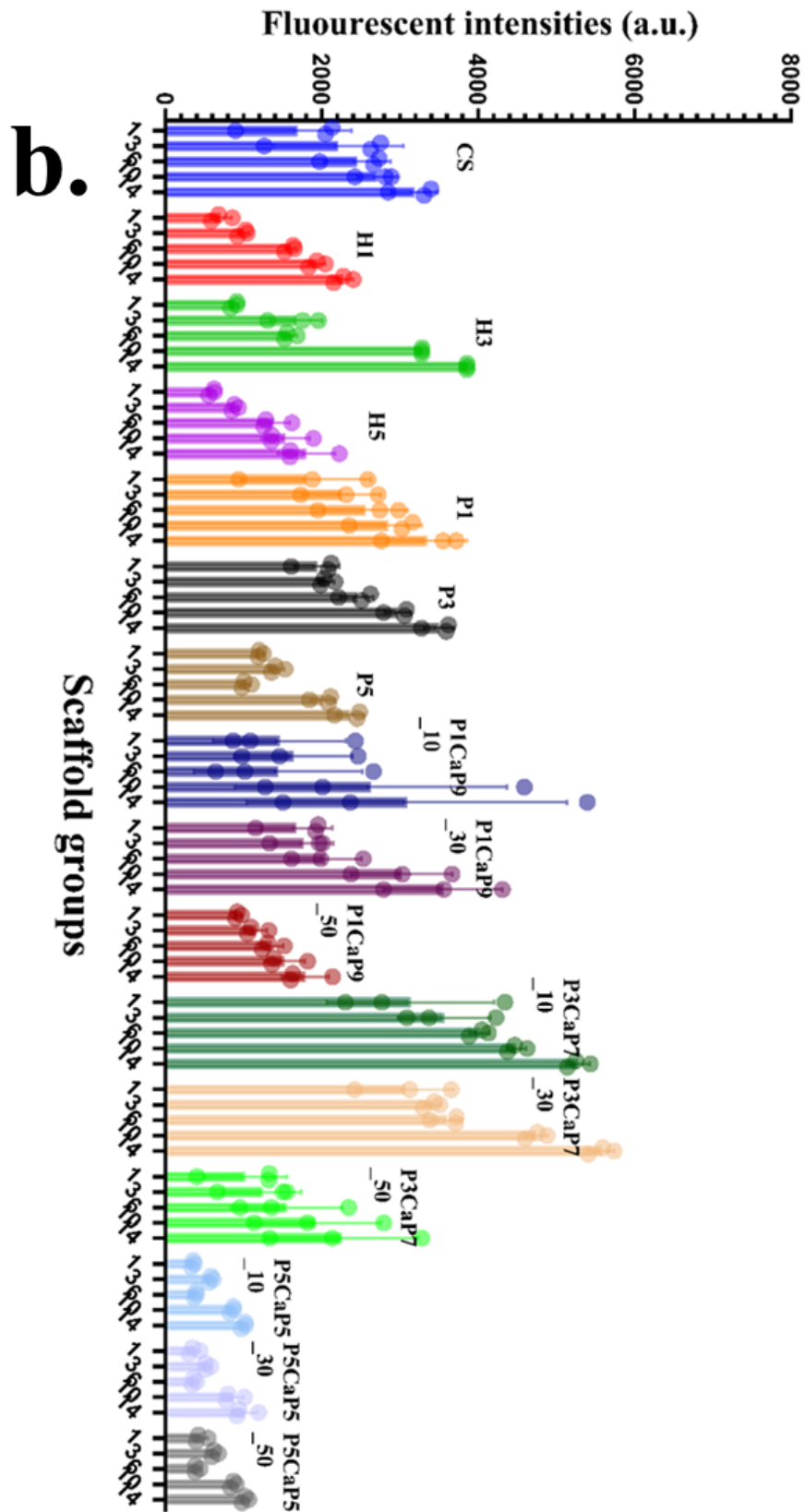


Figure 5.3.1 The cell proliferation and cytocompatibility analyzed by the AB assay up to 14 days of cultures. 6 groups of samples were tested including the sole CS, the pearl_CS group, the HA_CS group, pearl/CaP(10:90)_CS group (P1CaP9), pearl/CaP(30:70)_CS

Innovative incorporation of pearl and calcium phosphate composite in bone regenerative scaffolds group (P3CaP7), and pearl/CaP(50:50)_CS group (P5CaP5), compared with control group, presented in **a.** and **b.** In Fig 5.3.1 **a.**, relative fluorescent intensities were presented alongside the testing duration; the relative fluorescent intensities were presented in groups as shown in **b** independently.

Additionally, all composite scaffold groups had subgroups with the same concentration in gradient (10, 30, 50 wt.%). The experiments were performed with 3 sample replicas and 1 control group and 1 blank group, and the results were expressed as the mean \pm SD.

The fluorescent intensities of samples between different groups were in the vicinity of 500 to 3,000 in day 1 and most samples showed a slight increase during the first week of culture. The reason for the different initial fluorescent intensities from different sample groups are probably due to the affinity between cells and the scaffolds that the migration and attachment process on different samples might be influenced by different factors, including the surface energy, porosity of scaffolds. Obviously, the P5CaP5 group showed the worst cytocompatibility at each time point compared to other p/CaP composite group, HA group and the pearl group. The observed correlation could be attributed to the concentration of CO₃²⁻ contents, as discussed in a related study that demonstrated poor cytocompatibility when incorporating high concentrations of calcium carbonate with chitosan scaffolds, along with lower porosity and average pore size (Liu and Wang, 2023). Moreover, studies of the chitosan CaCO₃ composite scaffolds provided agreements of that the incorporation of CO₃²⁻ contents that at a small amount of concentration (0.5 μ M to 30wt. %) exhibits good biocompatibility and osteogenic differentiation potential (Chen et al., 2018; Huang et al., 2020; Januariyasa et al., 2020; Kumar et al., 2013; Sambudi et al., 2015); however, no previous study mentioned high concentration (over 30wt. %) incorporation of CO₃²⁻ with chitosan scaffolds.

As time increases, MG-63 cells on all scaffolds proliferated obviously. During the first week of incubation, all samples show increasing proliferation of MG-63 cells except the P5CaP5 group samples. Moreover, cells proliferation on composite

scaffolds in H1, H3, P3CaP7_10 and P3CaP7_30 groups were observed to be more significant than on the sole CS scaffold group, which indicates good cytocompatibility and promotion of the proliferation of MG-63. From day 6 to day 14, compared with the first incubation interval, a slightly higher proliferation of cell metabolic activities was observed, especially the P5CaP5 group samples show a significantly increased fluorescent intensity at day 10. The highest cell viability was obtained with the P3CaP7_30 sample at day 14 which is similar to the P3CaP7_10 sample. To have more detailed analysis, according to the overall fluorescent intensity change throughout the 2-week experiment, three groups of samples were analysed and studied below.

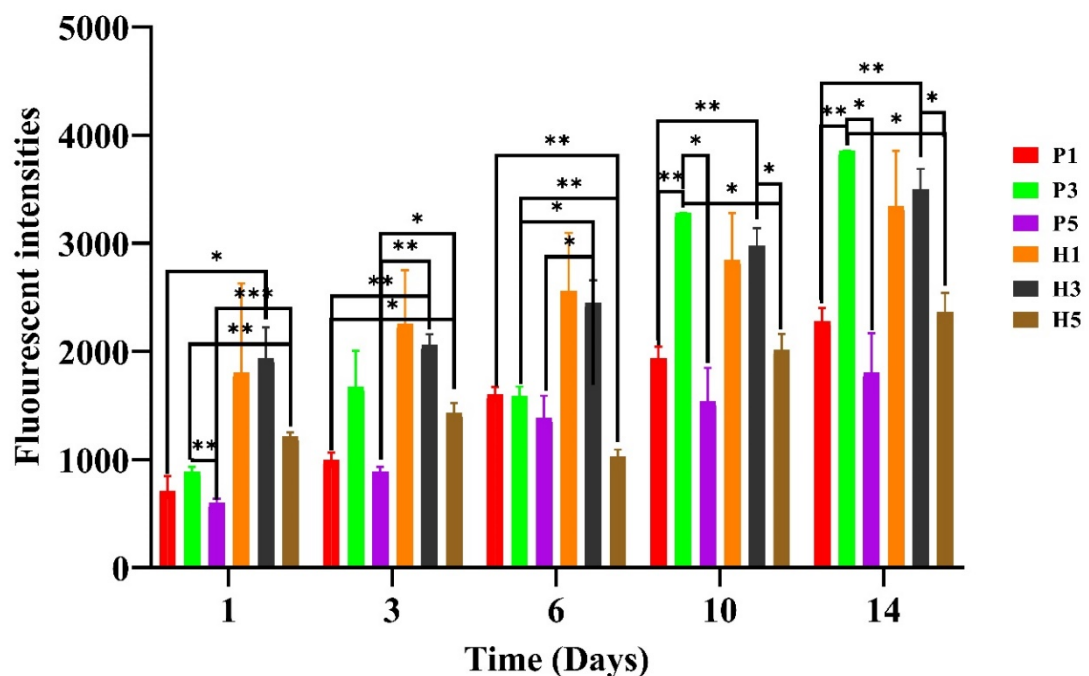


Figure 5.3.2 The cell proliferation and cytocompatibility analyzed by the AB assay up to 14 days of culture. 6 groups of samples were tested including the sole CS, the pearl_CS group, the HA_CS group, p/CaP(10:90)_CS group (P1H9), p/CaP(30:70)_CS group (P3CaP7), and p/CaP(50:50)_CS group (P5CaP5). Additionally, all composite scaffold groups had subgroups with the same concentration in gradient (10, 30, 50 wt.%) (*, **, and *** stands for $p < 0.01$, $p < 0.001$ and $p < 0.0001$, respectively).

Figure 5.3.2 demonstrates the comparative fluorescent intensity changes between the HA group and the pearl group; all samples could promote the proliferation of MG-63 cells. According to the results of the two-way ANOVA test and the linear regression study for the proliferation rate of all samples in Table 5.1, the proliferation rate of MG-63 on P3 samples is the highest among all other composite scaffolds. This trend of proliferation indicated that 30 wt.% of pearl powders could promote the proliferation of cells faster than HA. The low initial fluorescent intensities of pearl group samples at day 1 compared to the results of HA groups can be related to the low cell attachment and cell metabolic activity after 24 hours. Noticeably, the P5 samples showed overall a low fluorescent intensity and relatively low proliferation rate after 14 days incubation, which might be correlated with the too high CaCO_3 concentration. The results of increased pearl contents from 10 to 30 wt.%, which showed soaring proliferation are in agreement with the study by Li et al. (2020); with a greater proportion of pearl particles, the composite scaffolds could show better cell proliferation ability.

Table 5.1 One factor linear regression study of the 14-day AB assay fluorescent intensity changes for cell proliferation on different samples.

Sample name	Proliferation rate (a.u.)	R ²
CS	102.56±15.27	0.5272
P1	121.02±2.31	0.943
P3	230.02±5.32	0.9231
P5	89.82±10.32	0.7814
H1	109.34±14.88	0.5344
H3	123.41±5.85	0.9229
H5	91.84±9.56	0.7157
P1CaP9_10	133.59±30.78	0.2262
P1CaP9_30	154.86±13.45	0.6996

P1CaP9_50	82.17±12.98	0.7484
P3CaP7_10	157.02±13.18	0.7214
P3CaP7_30	196.01±6.89	0.9041
P3CaP7_50	84.48±20.15	0.3551
P5CaP5_10	48.71±11.02	0.7936
P5CaP5_30	50.98±13.00	0.7471
P5CaP5_50	43.27±13.85	0.7091

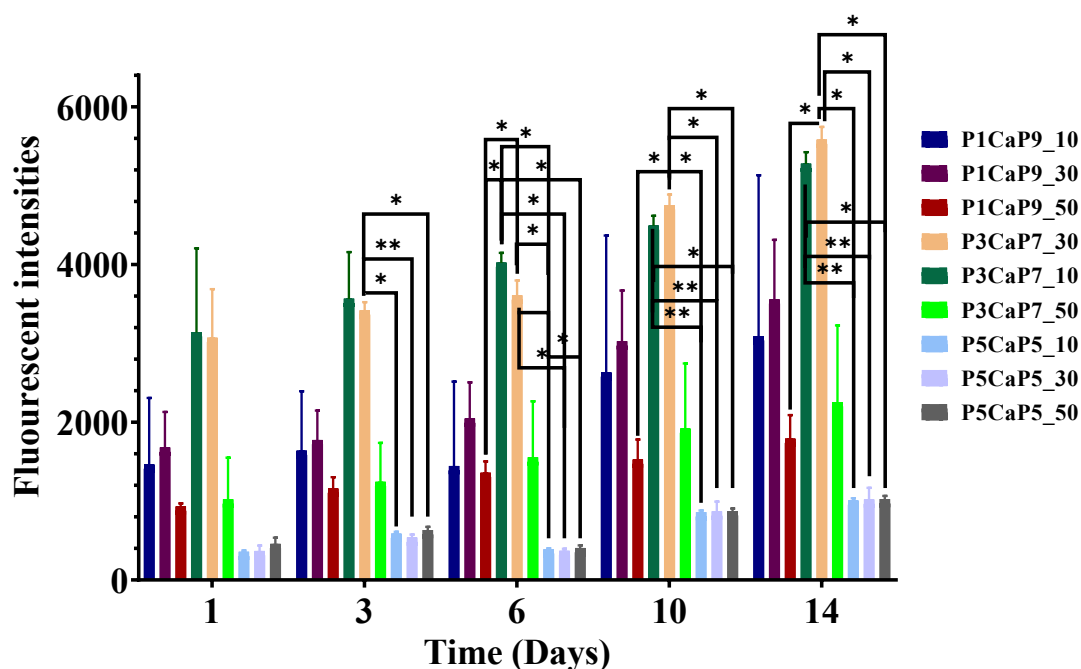


Figure 5.3.3 The comparative AB assay fluorescent intensity against day changes with 3 pearl/CaP_CS scaffold sample groups, including: P1CaP9_10, 30, 50 wt.%, P3CaP7_10, 30, 50 wt.% and P5CaP5_10, 30, 50 wt.% (*, **, and *** stands for $p < 0.01$, $p < 0.001$ and $p < 0.0001$, respectively).

Similar results were also observed from the p/CaP composite scaffolds group as shown in Figure 5.2.3. The increasing proportion of pearl contents exhibited higher and better cell metabolic activity when p/CaP ratio increased from 10:90 to 30:70. Combined with the proliferation ratio obtained by the linear regression

study in table 5.1, the highest proportion of bioactive particles incorporated with chitosan (50 wt.%) might not be able to offer a better cell proliferation rate compared to 10 and 30 wt.%. On the other hand, comparing the composite p/CaP_CS scaffolds with HA scaffolds in this study, as shown in figure 5.2.1 and 5.2.4, the obvious enchantment of biocompatibility and cell proliferation ability were observed that at day 14, the fluorescent intensity of H3 samples is lower than the results of P1CaP9_30 and P3CaP7_30. Thus, the existence of p/CaP composite particles did not show obvious toxicity with cells, and p/CaP incorporated CS porous scaffolds could offer a better cell proliferation rate compared to the HA_CS scaffolds.

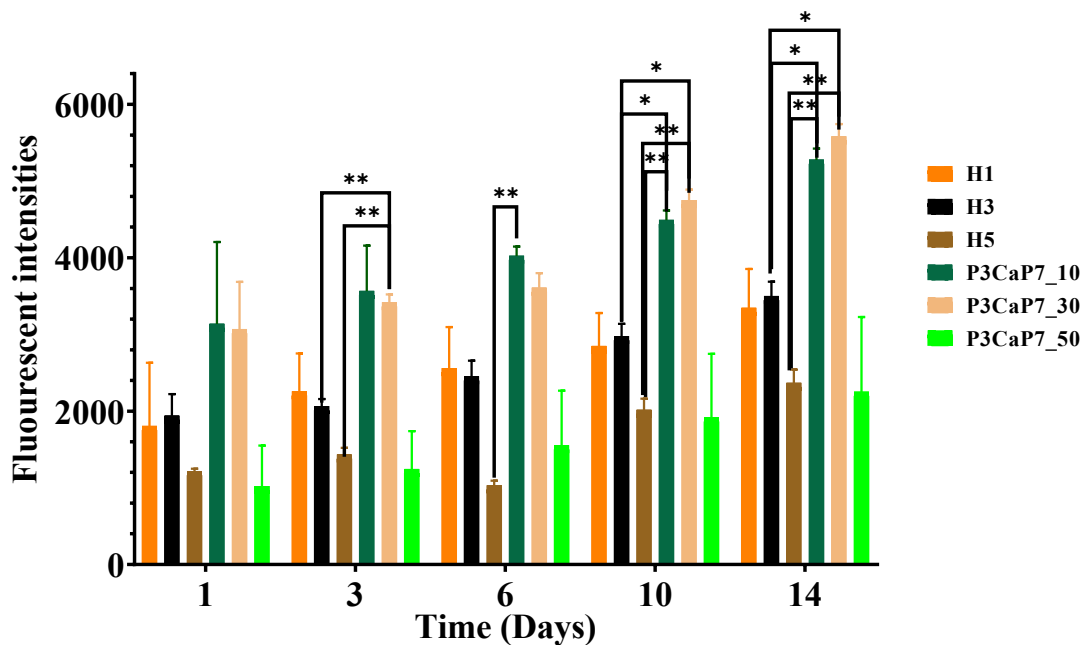


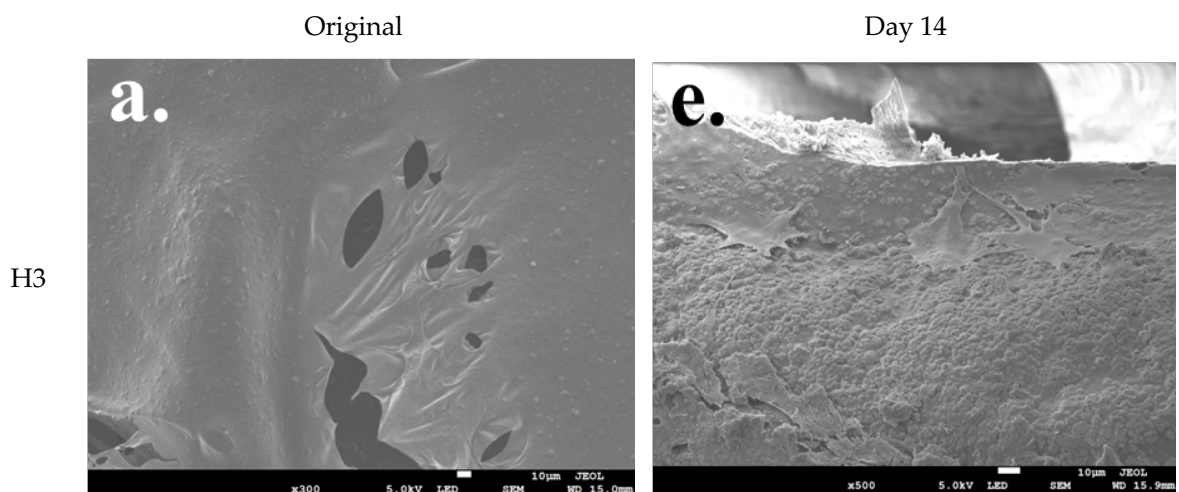
Figure 5.3.4 The comparative AB assay fluorescent intensity against day changes with P3CaP7_10, 30, 50 wt.% and HA group samples (*, **, and *** stands for $p < 0.01$, $p < 0.001$ and $p < 0.0001$, respectively).

Overall, the scaffolds did not lead to cell cytotoxicity, and gradual cell proliferation was observed in all culture experiments. The best initial cell attachment was mostly observed in the P3CaP7_10 scaffold and the highest cell proliferation rate was observed on the P3 scaffolds. Compared to the results of HA_CS scaffolds and the sole chitosan scaffold, cell proliferation differences were

significantly noticed in this experiment. Besides the cell experiment data, the compressive property and the porosity of the p/CaP composite CS scaffolds could also effectively modulate the osteogenic differentiation of cells. The higher CaCO_3 content scaffolds, including the P5, P5CaP5 groups and P3CaP7_50 samples, while their cell proliferation performance was even worse than the sole CS scaffolds, which could be explained by the smaller average pore size and low compressive modulus as mentioned in the previous chapter. It was planned to do further cellular work to make a better comparison between different groups of samples, including the MTT assay and the alkaline phosphatase (ALP) activity test. However, due to the limitation of project time and contamination, these were not possible to be finished.

5.3.2 Cell proliferation/migration observation by SEM

The visible cell proliferation and attachments morphologies on the scaffold samples were observed by SEM at day 14, which would be a supportive method to confirm the results obtained from the AB assay that could prove whether bacterial contaminations were present on the scaffolds. According to the AB assay results on day 14, four different samples from 3 different groups including the H3, P3, P1CaP9_30 and P3CaP7_30 scaffolds were chosen for characterization.



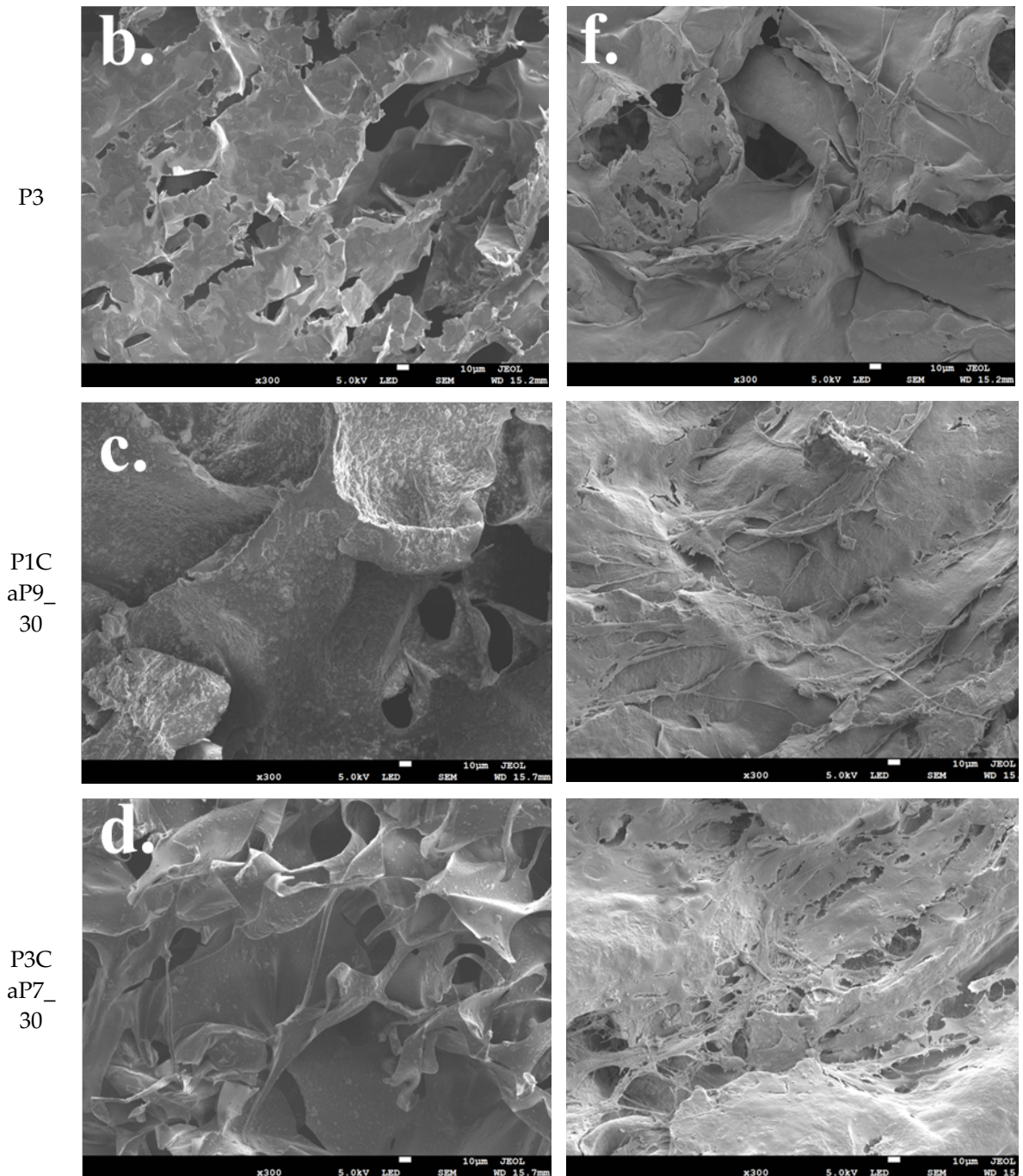


Figure 5.3.5 The comparative SEM images of various scaffolds, including the H3, P3, P1CaP9_30 and P3CaP7_30 scaffold samples (a-d), respectively; and samples with grown MG-63 cells after 14 days incubation (e-h). All images are at x300 times magnifications.

As shown in Figure 5.3.5, all composite scaffolds exhibited a similar microstructure, with particles distributed on the chitosan matrix. On day 14, cells were observed successfully attached to the surface of each sample with

extending morphology. Firstly, compared between P3 and H3 samples, cells were successfully distributed on the top surface on both scaffolds; obvious difference were visible between H3 and P3; namely that more external cellular cross-linking morphologies could be observed from the P3 samples. It is revealing that pearl powder indeed affect the cell morphology on the scaffold surfaces. However, cell numbers on P3 scaffold were slightly reduced compared to the H3 scaffold, which corresponded to the result of AB assay results. In addition, the P1CaP9_30 and P3CaP7_30 scaffold samples showed a higher number of cell attachments compared to the P3 scaffold samples, and the cellular cross-linking structure could be more clearly identified from the SEM images. Thus, the existence of the p/CaP composite particles not only showed cell proliferation ability, furthermore, the ability of promoting fibroblasts migration was also approved from this research.

5.4 Discussion

In the investigation of in-vitro degradation of composite scaffolds, the scaffolds exhibited a gradual degradation process in both PBS and L-PBS media. The presence of lysozymes slightly accelerated the degradation speed when compared to the degradation in sole PBS media. The total degradation after 4 weeks reached up to 40% and 50% in lysozyme and PBS media, respectively.

A comparison with previous research (Chesnutt et al., 2009; Liu et al., 2014; Zhang and Zhang, 2001; Zhang and Zhang, 2002) revealed interesting insights. Notably, the pH changes observed in the in-vitro degradation tests indicated a more significant shift in the sole pearl scaffold compared to the p/CaP scaffold. This observation can be attributed to the presence of CaP, as reported by Zhang and Zhang (2002). Although the exact mechanism is not thoroughly studied, chemical interactions, including covalent bonding, ion-dipole interactions, and complexation of Ca^{2+} ions with the chitosan polymer matrix, are believed to play a role in limiting the release of chitosan-acetate. This mechanism could effectively control the pH changes during the degradation process of the scaffold.

In this study, around a 10% more degradation difference contributed by L-PBS is considered due to the chosen higher concentration of lysozyme used. As Chesnutt et al (2009) reported, the sole chitosan scaffold degraded significantly faster than the chitosan scaffolds with CaP incorporated, which is different from what has been observed from this study. Noticeably, the reported chitosan-CaP composite scaffolds were prepared by a co-precipitation method. This technique also improved the mechanical strength of the composite scaffolds as reported in the study, which provided another potential of the fabrication of p/CaP chitosan scaffolds.

In cell culture studies, scaffold compositions did not show much cytotoxicity effect on the cells, except those P5CaP5_CS scaffolds, and cells gradually proliferated during the culturing of up to 14 days. In the experiment group, the cell seeding density of 20,000 cells per scaffolds (\varnothing :12 mm x 5 mm) cultured in 24-well plate by using 1 mL growth media was found to be the optimal seeding condition, in accordance with previous studies (Chesnutt et al., 2009; Liu et al., 2014; Zhang and Zhang, 2001; Zhang and Zhang, 2002). In this experiment, the initial cell attachment after 24 h was very different; the pearl chitosan groups demonstrated the worst cell attachment but the composite p/CaP group significantly had better cell activity. After 14-days, the beneficial effect of pearl, HA and CaP individually at increasing cell compatibility is reported by different studies (Liu et al., 2014; Zhao et al., 2013; Zhang and Zhang, 2002). The effect of HA in contributing to absorption of serum proteins including fibronectins and vitronectins leading to the attachment of integrins and hence providing attachment of osteoblast precursor cells has been reported (Wei and Ma, 2004).

In the present study, the cell viability of samples exhibited variations between test intervals, and the cell proliferation performance with all compositions showed distinct patterns. The p/CaP group scaffolds, particularly the P3CaP7_30 scaffold, demonstrated the highest terminal fluorescent intensity after the 14-day incubation period. This finding suggests robust cell proliferation and activity in this specific composition. However, it is noteworthy that the P5CaP5 group exhibited the lowest fluorescent intensity, indicating comparatively lower cell proliferation.

Relevant studies by Zhang and Zhang (2001), Zhang et al. (2018), and Li et al. (2020) provide insights into the impact of varying concentrations of CaP and pearl on cellular activity and proliferation. Zhang and Zhang (2001) focused on the uptake of macroporous chitosan/calcium phosphate composite scaffolds, revealing that increasing the concentration of CaP led to enhanced cellular activity and proliferation, supporting the formation of apatite. Zhang et al. (2018) explored the incorporation of pearl powder content with PCL scaffolds, demonstrating that higher pearl contents, up to 80 wt.%, facilitated increased proliferation and osteogenesis. Li et al. (2020) studied nano-pearl powder/chitosan-hyaluronic acid porous composite scaffolds and concluded that higher pearl concentrations (0 to 25 wt.%) promoted cell proliferation and osteogenesis.

However, the observed poor cell proliferation reaction in the present study with a 50:50 ratio of pearl to CaP suggests a unique response that might be related to an unknown mechanism. This anomaly emphasizes the need for further in-depth investigation into the specific conditions and interactions at this particular composition ratio. Understanding the underlying factors influencing cell behaviour in response to different material compositions is crucial for optimizing scaffold design and enhancing their effectiveness in applications.

6 Conclusions and future works

6.1 Introduction

This final concluding chapter encapsulates the principal discoveries of this thesis project and explores potential subsequent experiments that arose from it but cannot be pursued due to time limitations and external circumstances beyond our control.

6.2 Conclusions

The aim of this study was to synthesize pearl/calcium phosphate (p/CaP) composite particles that can promote the proliferation and differentiation of osteoblasts during bone regeneration process. This study focused on the synthesis of the p/CaP composite particles using three different methods based on the strategies for HA fabrications, by incorporation the bioactive chitosan

scaffolds to facilitate evaluation of the osteogenesis activity of the composite scaffolds.

The p/CaP composite powders were synthesized by the three different methods in this study. The physiochemical results showed that the chosen three strategies for the incorporation of pearl and HA are feasible for obtaining the p/CaP composite, that three strategies influence the final product composite particles for the crystallinity and the actual CaP components. The FTIR spectra demonstrated the presence of CaP in the bulky synthesized composite particles, combined with the organic compounds originated from the pearl platelets. Individually, composites obtained from different methods showed different FTIR spectra as discussed in chapter 4. This chemical compound difference was also observed by the XRD diffractograms; hence, the crystal structures of the composite particles are influenced by the synthesis process.

Likewise, this study compared the p/CaP composites in three different composition groups, that is 10:90, 30:70 and 50:50. TGA analysis revealed that the incorporation of CaP components improved the thermal stability of the composite particles compared to the pearl. The existence of attached CaP contents that covered the surface of pearl platelets resulted in the reduction of the crystal polymorph transformation of calcium (CaCO_3) (from aragonite to calcite) contents as revealed from the TG curve. The SEM characterization confirmed that the CaP covered the surface of pearl platelets, showing the amorphous morphology of the CaP; on the other hand, HA particles were observed surrounding the composite particles. These findings confirmed the ability of pearl to promote the generation of CaP components during the synthesis process of HA and that the carbonate groups played an important role. The attachment of CaP and surrounding HA particles to pearl platelets reveals a positive contribution to the biomineralization process.

The chitosan composite scaffolds were obtained with the freeze—drying technique, which provide the porous structure that would provide sufficient surface for bone tissue and cells to grow and develop. Through SEM characterization and porosity estimation analysis, it has been confirmed that the

Innovative incorporation of pearl and calcium phosphate composite in bone regenerative scaffolds produced scaffolds possessed the necessary porous structure and distribution of composite particles which is expected to enable and promote osteogenesis. Moreover, the FTIR-ATR analysis proved the distribution of p/CaP particles throughout the chitosan matrix quantitatively, which will provide a highly bioactive surface for bone tissue engineering purposes.

Compressive mechanical analysis showed the incorporation of pearl with CaP composite into the chitosan matrix would enhance the compressive strength compared to the pure chitosan matrix. This also showed the incorporation of p/CaP composite could enhance the mechanical strength of the scaffold vertically.

In-vitro degradation study showed that the presence of p/CaP composites in the scaffold play a major role on its degradation profile. Comparing to the pH change and weight loss results of pearl_CS and HA_CS scaffolds, p/CaP_CS scaffolds demonstrated the higher degradation ratio than the HA groups and lower than the pearl groups, indicating the existence of CO₃ compounds and amorphous CaP composite controlled the degradation process of the scaffold, which provides potential for long-term bone regeneration requirements.

Furthermore, the biological response to the fabricated porous p/CaP scaffolds was thoroughly evaluated, revealing their non-cytotoxic nature in the presence of MG-63 osteoblast cells. This widely recognized cell line provided valuable insights into the osteoblast-like features, reflecting the expected behaviour of the scaffolds during interactions with osteoblasts. The 14-day cell culture results highlighted the optimal performance of scaffolds with a 30:70 pearl: CaP ratio, demonstrating enhanced proliferation and differentiation of osteoblasts. SEM analysis corroborated the positive crosslinking and osteogenesis performance of these scaffolds, emphasizing their potential in bone tissue engineering. However, scaffolds with a high pearl: CaP ratio (50:50) and elevated p/CaP concentrations (50 wt.%) exhibited poor or non-osteogenic behaviour, underscoring the importance of carefully balanced pearl: CaP ratios and p/CaP concentrations for effective osteogenesis. This research offers crucial insights into achieving the desired osteogenic effects while avoiding potential toxic outcomes.

In conclusion, this study demonstrated the feasibility of preparing the p/CaP composite, incorporation of p/CaP into chitosan scaffolds, and demonstration of the non-cytotoxicity and the proliferation capability of the scaffold using the MG-63 cell lines involve *in-vitro* biological test. The idea of involving natural CaCO₃ components in bone tissue regeneration is easy and low cost; in this research, which only used relatively simple and inexpensive technology was used to exhibit the potential of the scaffold for clinical applications.

6.3 Future work

During this research, an exceptional pandemic event took place which thwarted the potential of complementing some of the evaluations to be presented in this thesis. Therefore, some future work would be considered beneficial to improve the research.

- As discussed in chapter 2, the organic matrix of pearl or nacre can be categorized into water soluble matrix (WSM), acid soluble matrix (ASM) and acid insoluble matrix (AIM). However, the discussion about the interaction between the extracellular receptors and low molecular weight WSM has not been well studied. Kim et al (2012) reported that WSM plays an important role in the signalling pathways during the development process of bone tissue, but the effect of WSM is different from that of the bone morphogenetic protein-2 (BMP-2). Further exploration is needed to understand the differences between these two proteins.
- It would be useful to comprehensively characterise the attachment of pearl and CaP composite components, and especially to identify the composition of the CaP composite. Previous studies have reported several biomimetic “pearl-like” or “nacre-like” ceramic composite particles in the biomineralization process of CaCO₃ (Barthelat et al., 2007; Corni et al., 2012; Liu et al., 2019). Investigating the mineralization process happening during the synthesis

process of HA might contribute to understanding of the biomineralization process of p/CaP.

- The porosity of scaffold samples was estimated by using SEM and water absorption test, these results were inconclusive. It would have been useful to use a more advanced technique, such as the micro-computed tomography for more precise porosity analysis.
- Although cell toxicity and proliferation were investigated via the alamar blue (AB) assay, cell differentiation tests were not conducted due to multiple limitations. Therefore, the calcium and collagen deposition assay and the alkaline phosphatase (ALP) assay should be considered in future work.
- It was intend to perform the chorioallantoic membrane (CAM) assay initially, as the angiogenesis of new blood vessels plays an important role in bone regeneration processes. However, due to the long processing time and lab contamination, it was not possible to be perform this before the end of this research. Thus, it is suggested in the future work.
- This research used chitosan as the scaffold material support to evaluate the biological properties of the p/CaP composite. However, the acidic solution for dissolving chitosan powders also dissolved the p/CaP composite which may influence the physiochemical and biological results. Therefore, an innovative alkaline chitosan hydrogel/scaffold can be considered as an alternative. Furthermore, other bioactive scaffolds including the polycaprolactone (PCL), poly-(L-lactic) acid (PLLA), and the polyether ether ketone (PEEK) can be considered as carrier matrices for future study.

7 Bibliography

Abbasi, N., Hamlet, S., Love, R.M. and Nguyen, N.T., 2020. Porous scaffolds for bone regeneration. *Journal of science: advanced materials and devices*, 5(1), pp.1-9.

Abd El-Hack, M.E., El-Saadony, M.T., Shafi, M.E., Zabermawi, N.M., Arif, M., Batiha, G.E., Khafaga, A.F., Abd El-Hakim, Y.M. and Al-Sagheer, A.A., 2020. Antimicrobial and antioxidant properties of chitosan and its derivatives and their applications: A review. *International Journal of Biological Macromolecules*, 164, pp.2726-2744.

Afshar, A., Ghorbani, M., Ehsani, N., Saeri, M.R. and Sorrell, C.C., 2003. Some important factors in the wet precipitation process of hydroxyapatite. *Materials & Design*, 24(3), pp.197-202.

Ager, J.W., Balooch, G. and Ritchie, R.O., 2006. Fracture, aging, and disease in bone. *Journal of Materials Research*, 21(8), pp.1878-1892.

Agrawal, C.M. and Ray, R.B., 2001. Biodegradable polymeric scaffolds for musculoskeletal tissue engineering. *Journal of Biomedical Materials Research: An Official Journal of The Society for Biomaterials, The Japanese Society for Biomaterials, and The Australian Society for Biomaterials and the Korean Society for Biomaterials*, 55(2), pp.141-150.

Aikin, A. and Aikin, C.R., 1807. *A Dictionary of Chemistry and Mineralogy, with an Account of the Processes Employed in Many of the Most Important Chemical Manufactures: To which are Added a Description of Chemical Apparatus, and Various Useful Tables of Weights and Measures, Chemical Instruments.* (Vol. 1). Arch.

Alizadeh, M., Abbasi, F., Khoshfetrat, A.B. and Ghaleh, H.J.M.S., 2013. Microstructure and characteristic properties of gelatin/chitosan scaffold prepared by a combined freeze-drying/leaching method. *Materials Science and Engineering: C*, 33(7), pp.3958-3967.

- Aljawish, A., Muniglia, L., Klouj, A., Jasniewski, J., Scher, J. and Desobry, S., 2016. Characterization of films based on enzymatically modified chitosan derivatives with phenol compounds. *Food Hydrocolloids*, 60, pp.551-558.
- Alstadt, K.N., Katti, D.R. and Katti, K.S., 2012. An in situ FTIR step-scan photoacoustic investigation of kerogen and minerals in oil shale. *Spectrochimica Acta Part A: Molecular and Biomolecular Spectroscopy*, 89, pp.105-113.
- Aoki, A., Yoseph, S., Pasolli, H.A. and Torres, A.I., 1993. Stability of pituitary weight after multiple reproductive cycles. *Experimental and Toxicologic Pathology: Official Journal of the Gesellschaft fur Toxikologische Pathologie*, 45(1), pp.39-40.
- Antony, R., Arun, T. and Manickam, S.T.D., 2019. A review on applications of chitosan-based Schiff bases. *International journal of biological macromolecules*, 129, pp.615-633.
- Arden, N. and Nevitt, M.C., 2006. Osteoarthritis: epidemiology. *Best practice & research Clinical rheumatology*, 20(1), pp.3-25.
- Ashok, M., Sundaram, N.M. and Kalkura, S.N., 2003. Crystallization of hydroxyapatite at physiological temperature. *Materials Letters*, 57(13-14), pp.2066-2070.
- Bai, J., Dai, J. and Li, G., 2015. Electrospun composites of PHBV/pearl powder for bone repairing. *Progress in natural science: materials international*, 25(4), pp.327-333.
- Bakshi, P.S., Selvakumar, D., Kadirvelu, K. and Kumar, N.S., 2020. Chitosan as an environment friendly biomaterial—a review on recent modifications and applications. *International journal of biological macromolecules*, 150, pp.1072-1083.
- Balmain, J., Hannoyer, B. and Lopez, E., 1999. Fourier transform infrared spectroscopy (FTIR) and x-ray diffraction analyses of mineral and organic matrix during heating of mother of pearl (nacre) from the shell of the mollusc *Pinctada maxima*. *Journal of Biomedical Materials Research: An Official Journal of The Society for Biomaterials, The Japanese Society for Biomaterials, and The Australian Society for Biomaterials and the Korean Society for Biomaterials*, 48(5), pp.749-754.
- Bano, I., Arshad, M., Yasin, T., Ghauri, M.A. and Younus, M., 2017. Chitosan: A potential biopolymer for wound management. *International journal of biological macromolecules*, 102, pp.380-383.
- Barralet, J., Best, S. and Bonfield, W., 1998. Carbonate substitution in precipitated hydroxyapatite: an investigation into the effects of reaction temperature and bicarbonate ion concentration. *Journal of Biomedical Materials Research: An Official Journal of The Society for Biomaterials, The Japanese Society for Biomaterials, and the Australian Society for Biomaterials*, 41(1), pp.79-86.

- Barthelat, F., Tang, H., Zavattieri, P.D., Li, C.M. and Espinosa, H.D., 2007. On the mechanics of mother-of-pearl: a key feature in the material hierarchical structure. *Journal of the Mechanics and Physics of Solids*, 55(2), pp.306-337.
- Berzina-Cimdina, L. and Borodajenko, N., 2012. Research of calcium phosphates using Fourier transform infrared spectroscopy. *Infrared spectroscopy-materials science, engineering and technology*, 12(7), pp.251-263.
- Boonrungsiman, S., Gentleman, E., Carzaniga, R., Evans, N.D., McComb, D.W., Porter, A.E. and Stevens, M.M., 2012. The role of intracellular calcium phosphate in osteoblast-mediated bone apatite formation. *Proceedings of the National Academy of Sciences*, 109(35), pp.14170-14175.
- Bonnier, F., Keating, M.E., Wrobel, T.P., Majzner, K., Baranska, M., Garcia-Munoz, A., Blanco, A. and Byrne, H.J., 2015. Cell viability assessment using the Alamar blue assay: a comparison of 2D and 3D cell culture models. *Toxicology in vitro*, 29(1), pp.124-131.
- Bose, S. and Saha, S.K., 2003. Synthesis and characterization of hydroxyapatite nanopowders by emulsion technique. *Chemistry of materials*, 15(23), pp.4464-4469.
- Bourrat, X., Francke, L., Lopez, E., Rousseau, M., Stempflé, P., Angellier, M. and Albéric, P., 2007. Nacre biocrystal thermal behaviour. *CrystEngCo*
- Braet, F., De Zanger, R. and Wisse, E., 1997. Drying cells for SEM, AFM and TEM by hexamethyldisilazane: a study on hepatic endothelial cells. *Journal of microscopy*, 186(1), pp.84-87.
- Burstein, A.H., Reilly, D.T. and Martens, M., 1976. Aging of bone tissue: mechanical properties. *JBJS*, 58(1), pp.82-86.
- Cao, M.H., Wang, Y.H., Guo, C.X., Qi, Y.J. and Hu, C.W., 2004. Preparation of ultrahigh-aspect-ratio hydroxyapatite nanofibers in reverse micelles under hydrothermal conditions. *Langmuir*, 20(11), pp.4784-4786.
- Cao, L.Y., Zhang, C.B. and Huang, J.F., 2005. Synthesis of hydroxyapatite nanoparticles in ultrasonic precipitation. *Ceramics International*, 31(8), pp.1041-1044.
- Chaudhry, A.A., Haque, S., Kellici, S., Boldrin, P., Rehman, I., Khalid, F.A. and Darr, J.A., 2006. Instant nano-hydroxyapatite: a continuous and rapid hydrothermal synthesis. *Chemical communications*, (21), pp.2286-2288.
- Chen, Y., Yu, J., Ke, Q., Gao, Y., Zhang, C. and Guo, Y., 2018. Bioinspired fabrication of carbonated hydroxyapatite/chitosan nanohybrid scaffolds loaded with TWS119 for bone regeneration. *Chemical Engineering Journal*, 341, pp.112-125.
- Chen, Q., Qi, Y., Jiang, Y., Quan, W., Luo, H., Wu, K., Li, S. and Ouyang, Q., 2022. Progress in Research of Chitosan Chemical Modification Technologies and Their Applications. *Marine Drugs*, 20(8), p.536.

- Chesnutt, B.M., Viano, A.M., Yuan, Y., Yang, Y., Guda, T., Appleford, M.R., Ong, J.L., Haggard, W.O. and Bumgardner, J.D., 2009. Design and characterization of a novel chitosan/nanocrystalline calcium phosphate composite scaffold for bone regeneration. *Journal of Biomedical Materials Research Part A: An Official Journal of The Society for Biomaterials, The Japanese Society for Biomaterials, and The Australian Society for Biomaterials and the Korean Society for Biomaterials*, 88(2), pp.491-502.
- Chien, R.C., Yen, M.T. and Mau, J.L., 2016. Antimicrobial and antitumor activities of chitosan from shiitake stipes, compared to commercial chitosan from crab shells. *Carbohydrate polymers*, 138, pp.259-264.
- Choi, D. and Kumta, P.N., 2007. Mechano-chemical synthesis and characterization of nanostructured β -TCP powder. *Materials Science and Engineering: C*, 27(3), pp.377-381.
- Clarke, B., 2008. Normal bone anatomy and physiology. *Clinical journal of the American Society of Nephrology: CJASN*, 3(Suppl 3), p.S131.
- Corni, I., Harvey, T.J., Wharton, J.A., Stokes, K.R., Walsh, F.C. and Wood, R.J.K., 2012. A review of experimental techniques to produce a nacre-like structure. *Bioinspiration & biomimetics*, 7(3), p.031001.
- Cui, G., Li, J., Lei, W., Bi, L., Tang, P., Liang, Y., Tao, S. and Wang, Y., 2010. The mechanical and biological properties of an injectable calcium phosphate cement-fibrin glue composite for bone regeneration. *Journal of Biomedical Materials Research Part B: Applied Biomaterials: An Official Journal of The Society for Biomaterials, The Japanese Society for Biomaterials, and The Australian Society for Biomaterials and the Korean Society for Biomaterials*, 92(2), pp.377-385.
- Cuneyt Tas, A., Korkusuz, F.E.Z.A., Timucin, M. and Akkas, N., 1997. An investigation of the chemical synthesis and high-temperature sintering behaviour of calcium hydroxyapatite (HA) and tricalcium phosphate (TCP) bioceramics. *Journal of Materials Science: Materials in Medicine*, 8, pp.91-96.
- Dahlin, C., Linde, A., Gottlow, J. and Nyman, S., 1988. Healing of bone defects by guided tissue regeneration. *Plastic and reconstructive surgery*, 81(5), pp.672-676.
- Dai, J., Bai, J., Jin, J., Yang, S. and Li, G., 2015. Stimulation by pearl of mineralization and biocompatibility of PLA. *Advanced Engineering Materials*, 17(11), pp.1691-1697.
- Dai, J., Yang, S., Jin, J. and Li, G., 2016. Electrospinning of PLA/pearl powder nanofibrous scaffold for bone tissue engineering. *RSC advances*, 6(108), pp.106798-106805.
- de Leeuw, N.H. and Parker, S.C., 1998. Surface structure and morphology of calcium carbonate polymorphs calcite, aragonite, and vaterite: an atomistic approach. *The Journal of Physical Chemistry B*, 102(16), pp.2914-2922.

De Villiers, J.P., 1971. Crystal structures of aragonite, strontianite, and witherite. *American Mineralogist: Journal of Earth and Planetary Materials*, 56(5-6), pp.758-767.

Dimassi, S., Tabary, N., Chai, F., Blanchemain, N. and Martel, B., 2018. Sulfonated and sulfated chitosan derivatives for biomedical applications: A review. *Carbohydrate polymers*, 202, pp.382-396.

Dimitriou, R., Jones, E., McGonagle, D. and Giannoudis, P.V., 2011. Bone regeneration: current concepts and future directions. *BMC medicine*, 9(1), pp.1-10.

Dimitriou, R., Jones, E., McGonagle, D. and Giannoudis, P.V., 2011. Bone regeneration: current concepts and future directions. *BMC medicine*, 9(1), pp.1-10.

Domrongkitchaiporn, S., Pongskul, C., Sirikulchayanonta, V., Stitchantrakul, W., Leeprasert, V., Ongphiphadhanakul, B., Radinahamed, P. and Rajatanavin, R., 2002. Bone histology and bone mineral density after correction of acidosis in distal renal tubular acidosis. *Kidney international*, 62(6), pp.2160-2166.

Du, X., Yu, B., Pei, P., Ding, H., Yu, B. and Zhu, Y., 2018. 3D printing of pearl/CaSO₄ composite scaffolds for bone regeneration. *Journal of materials chemistry B*, 6(3), pp.499-509.

Engelhard, M.H., Droubay, T.C. and Du, Y., 2017. *X-ray photoelectron spectroscopy applications* (No. PNNL-SA-111274). Pacific Northwest National Lab.(PNNL), Richland, WA (United States). Environmental Molecular Sciences Lab.(EMSL).

FRANK, W., PONDER, L., DAVID, R.P. and JULIET, M., 2019. *BIOLOGY AND EVOLUTION OF THE MOLLUSCA*. CRC PRESS.

Fratzl, P., Gupta, H.S., Paschalis, E.P. and Roschger, P., 2004. Structure and mechanical quality of the collagen-mineral nano-composite in bone. *Journal of materials chemistry*, 14(14), pp.2115-2123.

Fung, Y.C., 2013. *Biomechanics: mechanical properties of living tissues*. Springer Science & Business Media.

Gauthier, O., Müller, R., von Stechow, D., Lamy, B., Weiss, P., Bouler, J.M., Aguado, E. and Daculsi, G., 2005. In vivo bone regeneration with injectable calcium phosphate biomaterial: a three-dimensional micro-computed tomographic, biomechanical and SEM study. *Biomaterials*, 26(27), pp.5444-5453.

Genet, Michel J., Christine C. Dupont-Gillain, and Paul G. Rouxhet. "XPS analysis of biosystems and biomaterials." *Medical Applications of Colloids* 177 (2008).

Gibson, I.R. and Bonfield, W., 2002. Novel synthesis and characterization of an AB-type carbonate-substituted hydroxyapatite. *Journal of Biomedical Materials Research: An Official Journal of The Society for Biomaterials, The Japanese Society*

Innovative incorporation of pearl and calcium phosphate composite in bone regenerative scaffolds

for *Biomaterials*, and *The Australian Society for Biomaterials and the Korean Society for Biomaterials*, 59(4), pp.697-708.

Glyn-Jones, S. and Palmer, A.J., 2015. Agricola, R.; Price, A.J.; Vincent, T.L.; Weinans, H.; Carr. *AJ Osteoarthritis. Lancet*, 386(9991), pp.376-387.

Göpferich, A., 1996. Mechanisms of polymer degradation and erosion. *The biomaterials: silver jubilee compendium*, pp.117-128.

Green, T.R., Fellman, J.H., Eicher, A.L. and Pratt, K.L., 1991. Antioxidant role and subcellular location of hypotaurine and taurine in human neutrophils. *Biochimica et Biophysica Acta (BBA)-General Subjects*, 1073(1), pp.91-97.

Gross, B.C., Erkal, J.L., Lockwood, S.Y., Chen, C. and Spence, D.M., 2014. Evaluation of 3D printing and its potential impact on biotechnology and the chemical sciences.

Guilak, F., Jones, W.R., Ting-Beall, H.P. and Lee, G.M., 1999. The deformation behavior and mechanical properties of chondrocytes in articular cartilage. *Osteoarthritis and cartilage*, 7(1), pp.59-70.

Guo, B., Lei, B., Li, P. and Ma, P.X., 2015. Functionalized scaffolds to enhance tissue regeneration. *Regenerative biomaterials*, 2(1), pp.47-57.

Habibovic, P. and de Groot, K., 2007. Osteoinductive biomaterials—properties and relevance in bone repair. *Journal of tissue engineering and regenerative medicine*, 1(1), pp.25-32.

Han, J.K., Song, H.Y., Saito, F. and Lee, B.T., 2006. Synthesis of high purity nano-sized hydroxyapatite powder by microwave-hydrothermal method. *Materials chemistry and physics*, 99(2-3), pp.235-239.

Han, J., Zhou, Z., Yin, R., Yang, D. and Nie, J., 2010. Alginate-chitosan/hydroxyapatite polyelectrolyte complex porous scaffolds: Preparation and characterization. *International journal of biological macromolecules*, 46(2), pp.199-205.

Hanna, H., Mir, L.M. and Andre, F.M., 2018. In vitro osteoblastic differentiation of mesenchymal stem cells generates cell layers with distinct properties. *Stem cell research & therapy*, 9(1), pp.1-11.

Hannink, G. and Arts, J.C., 2011. Bioresorbability, porosity and mechanical strength of bone substitutes: what is optimal for bone regeneration? *Injury*, 42, 22-25.

He, Q., Huang, Z., Liu, Y., Chen, W. and Xu, T., 2007. Template-directed one-step synthesis of flowerlike porous carbonated hydroxyapatite spheres. *Materials Letters*, 61(1), pp.141-143.

Hing, K.A., Best, S.M., Tanner, K.E., Bonfield, W. and Revell, P.A., 2004. Mediation of bone ingrowth in porous hydroxyapatite bone graft substitutes. *Journal of*

Biomedical Materials Research Part A: An Official Journal of The Society for Biomaterials, The Japanese Society for Biomaterials, and The Australian Society for Biomaterials and the Korean Society for Biomaterials, 68(1), pp.187-200.

Ho, M.H., Kuo, P.Y., Hsieh, H.J., Hsien, T.Y., Hou, L.T., Lai, J.Y. and Wang, D.M., 2004. Preparation of porous scaffolds by using freeze-extraction and freeze-gelation methods. *Biomaterials*, 25(1), pp.129-138.

Hong, Y., Fan, H., Li, B., Guo, B., Liu, M. and Zhang, X., 2010. Fabrication, biological effects, and medical applications of calcium phosphate nanoceramics. *Materials Science and Engineering: R: Reports*, 70(3-6), pp.225-242.

Hsu, Y.Y., Gresser, J.D., Trantolo, D.J., Lyons, C.M., Gangadharam, P.R. and Wise, DL, 1997. Effect of polymer foam morphology and density on kinetics of in vitro controlled release of isoniazid from compressed foam matrices. *Journal of Biomedical Materials Research: An Official Journal of The Society for Biomaterials and The Japanese Society for Biomaterials*, 35(1), 107-116.

Hudu, S.A., Alshrari, A.S., Syahida, A. and Sekawi, Z., 2016. Cell culture, technology: enhancing the culture of diagnosing human diseases. *Journal of clinical and diagnostic research: JCDR*, 10(3), p.DE01.

Huang, M., Khor, E. and Lim, L.Y., 2004. Uptake and cytotoxicity of chitosan molecules and nanoparticles: effects of molecular weight and degree of deacetylation. *Pharmaceutical research*, 21(2), pp.344-353.

Huang, Y.Z., Ji, Y.R., Kang, Z.W., Li, F., Ge, S.F., Yang, D.P., Ruan, J. and Fan, X.Q., 2020. Integrating eggshell-derived CaCO₃/MgO nanocomposites and chitosan into a biomimetic scaffold for bone regeneration. *Chemical Engineering Journal*, 395, p.125098.

Huxtable, R.J., 1992. Physiological actions of taurine. *Physiological reviews*, 72(1), pp.101-163.

Januariyasa, I.K., Ana, I.D. and Yusuf, Y., 2020. Nanofibrous poly (vinyl alcohol)/chitosan contained carbonated hydroxyapatite nanoparticles scaffold for bone tissue engineering. *Materials Science and Engineering: C*, 107, p.110347.

Jarudilokkul, S., Tanthapanichakoon, W. and Boonamnuayvittaya, V., 2007. Synthesis of hydroxyapatite nanoparticles using an emulsion liquid membrane system. *Colloids and Surfaces A: Physicochemical and Engineering Aspects*, 296(1-3), pp.149-153.

Jennings, J.A., 2017. Controlling chitosan degradation properties in vitro and in vivo. In *Chitosan Based Biomaterials Volume 1* (pp. 159-182). Woodhead Publishing.

Ji, C., Annabi, N., Khademhosseini, A. and Dehghani, F., 2011. Fabrication of porous chitosan scaffolds for soft tissue engineering using dense gas CO₂. *Acta Biomaterialia*, 7(4), pp.1653-1664.

Kannan, S., Vieira, S.I., Olhero, S.M., Pina, S., e Silva, O.D.C. and Ferreira, J.M.F., 2011. Synthesis, mechanical and biological characterization of ionic doped carbonated hydroxyapatite/ β -tricalcium phosphate mixtures. *Acta Biomaterialia*, 7(4), pp.1835-1843.

Karageorgiou, V. and Kaplan, D., 2005. Porosity of 3D biomaterial scaffolds and osteogenesis. *Biomaterials*, 26(27), pp.5474-5491.

Karsdal, M.A., Michaelis, M., Ladel, C., Siebuhr, A.S., Bihlet, A.R., Andersen, J.R., Guehring, H., Christiansen, C., Bay-Jensen, A.C. and Kraus, V.B., 2016. Disease-modifying treatments for osteoarthritis (DMOADs) of the knee and hip: lessons learned from failures and opportunities for the future. *Osteoarthritis and cartilage*, 24(12), pp.2013-2021.

Kathuria, N., Tripathi, A., Kar, K.K. and Kumar, A., 2009. Synthesis and characterization of elastic and macroporous chitosan-gelatin cryogels for tissue engineering. *Acta biomaterialia*, 5(1), pp.406-418.

Katsimbri, P., 2017. The biology of normal bone remodelling. *European journal of cancer care*, 26(6), p.e12740.

Kattimani, V.S., Kondaka, S. and Lingamaneni, K.P., 2016. Hydroxyapatite--Past, present, and future in bone regeneration. *Bone and Tissue Regeneration Insights*, 7, pp.BTRI-S36138.

Khademhosseini, A., Langer, R., Borenstein, J. and Vacanti, J.P., 2006. Microscale technologies for tissue engineering and biology. *Proceedings of the National Academy of Sciences*, 103(8), pp.2480-2487.

Khan, T.A., Peh, K.K. and Ch'ng, H.S., 2002. Reporting degree of deacetylation values of chitosan: the influence of analytical methods. *J Pharm Pharmaceut Sci*, 5(3), pp.205-212.

Khan, A.S., Hussain, A.N., Sidra, L., Sarfraz, Z., Khalid, H., Khan, M., Manzoor, F., Shahzadi, L., Yar, M. and Rehman, I.U., 2017. Fabrication and in vivo evaluation of hydroxyapatite/carbon nanotube electrospun fibers for biomedical/dental application. *Materials Science and Engineering: C*, 80, pp.387-396.

Khosla, S. and Hofbauer, L.C., 2017. Osteoporosis treatment: recent developments and ongoing challenges. *The lancet Diabetes & endocrinology*, 5(11), pp.898-907.

Kim, H.W., Lee, H.H. and Knowles, J.C., 2006. Electrospinning biomedical nanocomposite fibers of hydroxyapatite/poly (lactic acid) for bone regeneration. *Journal of Biomedical Materials Research Part A: An Official Journal of The Society for Biomaterials, The Japanese Society for Biomaterials, and The Australian Society for Biomaterials and the Korean Society for Biomaterials*, 79(3), pp.643-649.

Kim, H., Lee, K., Ko, C.Y., Kim, H.S., Shin, H.I., Kim, T., Lee, S.H. and Jeong, D., 2012. The role of nacreous factors in preventing osteoporotic bone loss through both

osteoblast activation and osteoclast inactivation. *Biomaterials*, 33(30), pp.7489-7496.

Kim, H.L., Jung, G.Y., Yoon, J.H., Han, J.S., Park, Y.J., Kim, D.G., Zhang, M. and Kim, D.J., 2015. Preparation and characterization of nano-sized hydroxyapatite/alginate/chitosan composite scaffolds for bone tissue engineering. *Materials Science and Engineering: C*, 54, pp.20-25.

King, A.G., 2001. *Ceramic technology and processing: a practical working guide*. William Andrew.

Klinkla, R., Kaewmaraya, T., Bootchanon, A., Saisopa, T., Fongkaew, I., Yimnirun, R., Khamkongkao, A., Rattanachai, Y. and Sailuam, W., 2024. Effects of Sr and Mg doping on elastic, mechanical, and optical properties of hydroxyapatite: A first-principles study. *Results in Physics*, 57, p.107352.

Kon, E., Robinson, D., Verdonk, P., Drobnic, M., Patrascu, J.M., Dulic, O., Gavrilovic, G. and Filardo, G., 2016. A novel aragonite-based scaffold for osteochondral regeneration: early experience on human implants and technical developments. *Injury*, 47, pp.S27-S32.

Koons, G.L., Diba, M. and Mikos, A.G., 2020. Materials design for bone-tissue engineering. *Nature Reviews Materials*, 5(8), pp.584-603.

Koutsopoulos, S., 2002. Synthesis and characterization of hydroxyapatite crystals: a review study on the analytical methods. *Journal of Biomedical Materials Research: An Official Journal of The Society for Biomaterials, The Japanese Society for Biomaterials, and The Australian Society for Biomaterials and the Korean Society for Biomaterials*, 62(4), pp.600-612.

Kuchler-Bopp, S., Larrea, A., Petry, L., Idoux-Gillet, Y., Sebastian, V., Ferrandon, A., Schwinté, P., Arruebo, M. and Benkirane-Jessel, N., 2017. Promoting bioengineered tooth innervation using nanostructured and hybrid scaffolds. *Acta Biomaterialia*, 50, pp.493-501.

Kühl, G. and Nebergall, W.H., 1963. Hydrogenphosphat-und carbonatapatite. *Zeitschrift für anorganische und allgemeine Chemie*, 324(5-6), pp.313-320.

Kumar, G., Smith, P.J. and Payne, G.F., 1999. Enzymatic grafting of a natural product onto chitosan to confer water solubility under basic conditions. *Biotechnology and bioengineering*, 63(2), pp.154-165.

Kumar, R., Prakash, K.H., Cheang, P. and Khor, K.A., 2004. Temperature driven morphological changes of chemically precipitated hydroxyapatite nanoparticles. *Langmuir*, 20(13), pp.5196-5200.

Kumar, M.R., Muzzarelli, R., Muzzarelli, C., Sashiwa, H. and Domb, A.J., 2004. Chitosan chemistry and pharmaceutical perspectives. *Chemical Reviews*, 104(12), pp.6017-6084.

- Kumar, P.S., Ramya, C., Jayakumar, R. and Lakshmanan, V.K., 2013. Drug delivery and tissue engineering applications of biocompatible pectin–chitin/nano CaCO₃ composite scaffolds. *Colloids and Surfaces B: Biointerfaces*, 106, pp.109-116.
- Kuriakose, T.A., Kalkura, S.N., Palanichamy, M., Arivuoli, D., Dierks, K., Bocelli, G. and Betzel, C., 2004. Synthesis of stoichiometric nano crystalline hydroxyapatite by ethanol-based sol–gel technique at low temperature. *Journal of Crystal Growth*, 263(1-4), pp.517-523.
- Lafon, J., Champion, E., Bernache-Assollant, D., Gibert, R. and Danna, A., 2003. Thermal decomposition of carbonated calcium phosphate apatites. *Journal of thermal analysis and calorimetry*, 72(3), pp.1127-1134.
- Landi, E., Celotti, G., Logroscino, G. and Tampieri, A., 2003. Carbonated hydroxyapatite as bone substitute. *Journal of the European Ceramic Society*, 23(15), pp.2931-2937.
- Langer, R. and Tirrell, D.A., 2004. Designing materials for biology and medicine. *Nature*, 428(6982), pp.487-492.
- Lanza, R., Langer, R., Vacanti, J.P. and Atala, A. eds., 2020. *Principles of tissue engineering*. Academic press.
- Lee, F., Chung, J.E. and Kurisawa, M., 2009. An injectable hyaluronic acid–tyramine hydrogel system for protein delivery. *Journal of Controlled Release*, 134(3), pp.186-193.
- LeGeros, R.Z., 1967. *Crystallographic studies of the carbonate substitution in the apatite structure*. New York University.
- Lemos, A.F., Rocha, J.H.G., Quaresma, S.S.F., Kannan, S., Oktar, F.N., Agathopoulos, S. and Ferreira, J.M.F., 2006. Hydroxyapatite nano-powders produced hydrothermally from nacreous material. *Journal of the European Ceramic Society*, 26(16), pp.3639-3646.
- Lerner, U.H., 2006. Bone remodeling in post-menopausal osteoporosis. *Journal of dental research*, 85(7), pp.584-595.
- Li, Z., Ramay, H.R., Hauch, K.D., Xiao, D. and Zhang, M., 2005. Chitosan–alginate hybrid scaffolds for bone tissue engineering. *biomaterials*, 26(18), pp.3919-3928.
- Li, J., Li, H., Shi, L., Fok, A.S., Ucer, C., Devlin, H., Horner, K. and Silikas, N., 2007. A mathematical model for simulating the bone remodeling process under mechanical stimulus. *Dental materials*, 23(9), pp.1073-1078.
- Li, H.Y., Tan, Y.Q., Zhang, L., Zhang, Y.X., Song, Y.H., Ye, Y. and Xia, M.S., 2012. Bio-filler from waste shellfish shell: preparation, characterisation, and its effect on the mechanical properties on polypropylene composites. *Journal of hazardous materials*, 217, pp.256-262.

- Li, Y., Rodrigues, J. and Tomás, H., 2012. Injectable and biodegradable hydrogels: gelation, biodegradation and biomedical applications. *Chemical Society Reviews*, 41(6), pp.2193-2221.
- Li, J., Wu, C., Chu, P.K. and Gelinsky, M., 2020. 3D printing of hydrogels: Rational design strategies and emerging biomedical applications. *Materials Science and Engineering: R: Reports*, 140, p.100543.
- Li, X., Xu, P., Cheng, Y., Zhang, W., Zheng, B. and Wang, Q., 2020. Nano-pearl powder/chitosan-hyaluronic acid porous composite scaffold and preliminary study of its osteogenesis mechanism. *Materials Science and Engineering: C*, 111, p.110749.
- Liao, C.J., Lin, F.H., Chen, K.S. and Sun, J.S., 1999. Thermal decomposition and reconstitution of hydroxyapatite in air atmosphere. *Biomaterials*, 20(19), pp.1807-1813.
- Liao, H., Mutvei, H., Hammarström, L., Wurtz, T. and Li, J., 2002. Tissue responses to nacreous implants in rat femur: an in situ hybridization and histochemical study. *Biomaterials*, 23(13), pp.2693-2701.
- Liao, S.S., Cui, F.Z., Zhang, W. and Feng, Q.L., 2004. Hierarchically biomimetic bone scaffold materials: nano-HA/collagen/PLA composite. *Journal of Biomedical Materials Research Part B: Applied Biomaterials: An Official Journal of The Society for Biomaterials, The Japanese Society for Biomaterials, and The Australian Society for Biomaterials and the Korean Society for Biomaterials*, 69(2), pp.158-165.
- Liu, H., Zhang, L., Shi, P., Zou, Q., Zuo, Y. and Li, Y., 2010. Hydroxyapatite/polyurethane scaffold incorporated with drug-loaded ethyl cellulose microspheres for bone regeneration. *Journal of Biomedical Materials Research Part B: Applied Biomaterials*, 95(1), pp.36-46.
- Liu, Y.S., Huang, Q.L., Feng, Q.L., Hu, N.M. and Albert, O., 2013. Structural features and mechanical properties of PLLA/pearl powder scaffolds. *Journal of Mechanics in Medicine and Biology*, 13(01), p.1350020.
- Liu, Y. and Sinha, S.K., 2013. Wear performances and wear mechanism study of bulk UHMWPE composites with nacre and CNT fillers and PFPE overcoat. *Wear*, 300(1-2), pp.44-54.
- Liu, Y.S., Huang, Q.L., Kienzle, A., Müller, W.E.G. and Feng, Q.L., 2014. In vitro degradation of porous PLLA/pearl powder composite scaffolds. *Materials Science and Engineering: C*, 38, pp.227-234.
- Liu, X., Li, K., Wu, C., Li, Z., Wu, B., Duan, X., Zhou, Y. and Pei, C., 2019. Influence of copper (II) on biomineralization of CaCO₃ and preparation of micron pearl-like biomimetic CaCO₃. *Ceramics International*, 45(11), pp.14354-14359.

- Liu, X. and Wang, Z., 2023. Chitosan-calcium carbonate scaffold with high mineral content and hierarchical structure for bone regeneration. *Smart Materials in Medicine*, 4, pp.552-561.
- Loh, Q.L. and Choong, C., 2013. Three-dimensional scaffolds for tissue engineering applications: role of porosity and pore size.
- Long, D.A., 1977. Raman spectroscopy. *New York*, 1.
- Lopez, E., Vidal, B., Berland, S., Camprasse, S., Camprasse, G. and Silve, C., 1992. Demonstration of the capacity of nacre to induce bone formation by human osteoblasts maintained in vitro. *Tissue and Cell*, 24(5), pp.667-679.
- Lotsari, A., Rajasekharan, A.K., Halvarsson, M. and Andersson, M., 2018. Transformation of amorphous calcium phosphate to bone-like apatite. *Nature communications*, 9(1), p.4170.
- Lowenstam, H.A. and Abbott, D.P., 1975. Vaterite: a mineralization product of the hard tissues of a marine organism (Ascidacea). *Science*, 188(4186), pp.363-365.
- Lu, H.B., Campbell, C.T., Graham, D.J. and Ratner, B.D., 2000. Surface characterization of hydroxyapatite and related calcium phosphates by XPS and TOF-SIMS. *Analytical chemistry*, 72(13), pp.2886-2894.
- Lv, Q. and Feng, Q., 2006. Preparation of 3-D regenerated fibroin scaffolds with freeze drying method and freeze drying/foaming technique. *Journal of Materials Science: Materials in Medicine*, 17, pp.1349-1356.
- Ma, H.Y. and Lee, I.S., 2006. Characterization of vaterite in low quality freshwater-cultured pearls. *Materials Science and Engineering: C*, 26(4), pp.721-723.
- Ma, Z., Mao, Z. and Gao, C., 2007. Surface modification and property analysis of biomedical polymers used for tissue engineering. *Colloids and Surfaces B: Biointerfaces*, 60(2), pp.137-157.
- Maachou, H., Genet, M.J., Aliouche, D., Dupont-Gillain, C.C. and Rouxhet, P.G., 2013. XPS analysis of chitosan-hydroxyapatite biomaterials: from elements to compounds. *Surface and interface analysis*, 45(7), pp.1088-1097.
- Martin, R.I. and Brown, P.W., 1995. Mechanical properties of hydroxyapatite formed at physiological temperature. *Journal of Materials Science: Materials in Medicine*, 6, pp.138-143.
- Maji, K., Dasgupta, S., Kundu, B. and Bissoyi, A., 2015. Development of gelatin-chitosan-hydroxyapatite based bioactive bone scaffold with controlled pore size and mechanical strength. *Journal of Biomaterials Science, Polymer Edition*, 26(16), pp.1190-1209.
- Mangir, N., Dikici, S., Claeysens, F. and MacNeil, S., 2019. Using ex ovo chick chorioallantoic membrane (CAM) assay to evaluate the biocompatibility and angiogenic response to biomaterials. *ACS Biomaterials Science & Engineering*, 5(7), pp.3190-3200.

Matassi, F., Nistri, L., Paez, D.C. and Innocenti, M., 2011. New biomaterials for bone regeneration. *Clinical cases in mineral and bone metabolism*, 8(1), p.21.

Marcinkiewicz, J. and Kontny, E., 2014. Taurine and inflammatory diseases. *Amino acids*, 46, pp.7-20.

Maxian, S.H., Zawadsky, J.P. and Dunn, M.G., 1993. In vitro evaluation of amorphous calcium phosphate and poorly crystallized hydroxyapatite coatings on titanium implants. *Journal of biomedical materials research*, 27(1), pp.111-117.

Meenakshi, V.R., Blackwelder, P.L. and Watabe, N., 1974. Studies on the formation of calcified egg-capsules of ampullarid snails: I. Vaterite crystals in the reproductive system and the egg capsules of *Pomacea paludosa*. *Calcified Tissue Research*, 16, pp.283-291.

Meldrum, F.C., 2003. Calcium carbonate in biomineralisation and biomimetic chemistry. *International Materials Reviews*, 48(3), pp.187-224.

Melton Iii, L.J., 1996. Epidemiology of hip fractures: implications of the exponential increase with age. *Bone*, 18(3), pp.S121-S125.

Mikos, A.G., Bao, Y., Cima, L.G., Ingber, D.E., Vacanti, J.P. and Langer, R., 1993. Preparation of poly (glycolic acid) bonded fiber structures for cell attachment and transplantation. *Journal of biomedical materials research*, 27(2), pp.183-189.

Mima, S., Miya, M., Iwamoto, R. and Yoshikawa, S., 1983. Highly deacetylated chitosan and its properties. *Journal of Applied Polymer Science*, 28(6), pp.1909-1917.

Mkukuma, L.D., Skakle, J.M.S., Gibson, I.R., Imrie, C.T., Aspden, R.M. and Hukins, D.W.L., 2004. Effect of the proportion of organic material in bone on thermal decomposition of bone mineral: an investigation of a variety of bones from different species using thermogravimetric analysis coupled to mass spectrometry, high-temperature X-ray diffraction, and Fourier transform infrared spectroscopy. *Calcified tissue international*, 75, pp.321-328.

Mohammadi, H., Sepantafar, M., Muhamad, N. and Bakar Sulong, A., 2021. How does scaffold porosity conduct bone tissue regeneration?. *Advanced Engineering Materials*, 23(10), p.2100463.

Morse, J.W., Arvidson, R.S. and Lüttge, A., 2007. Calcium carbonate formation and dissolution. *Chemical reviews*, 107(2), pp.342-381.

Mosmann, T., 1983. Rapid colorimetric assay for cellular growth and survival: application to proliferation and cytotoxicity assays. *Journal of immunological methods*, 65(1-2), pp.55-63.

Motskin, M., Wright, D.M., Muller, K., Kyle, N., Gard, T.G., Porter, A.E. and Skepper, J.N., 2009. Hydroxyapatite nano and microparticles: correlation of particle properties with cytotoxicity and biostability. *Biomaterials*, 30(19), pp.3307-3317.

- Mourya, V.K. and Inamdar, N.N., 2008. Chitosan-modifications and applications: Opportunities galore. *Reactive and Functional polymers*, 68(6), pp.1013-1051.
- Mow, V.C., Kuei, S.C., Lai, W.M. and Armstrong, C.G., 1980. Biphasic creep and stress relaxation of articular cartilage in compression: theory and experiments.
- Mulari, M.T., Zhao, H., Lakkakorpi, P.T. and Väänänen, H.K., 2003. Osteoclast ruffled border has distinct subdomains for secretion and degraded matrix uptake. *Traffic*, 4(2), pp.113-125.
- Murphy, C.M., Haugh, M.G. and O'brien, F.J., 2010. The effect of mean pore size on cell attachment, proliferation and migration in collagen-glycosaminoglycan scaffolds for bone tissue engineering. *Biomaterials*, 31(3), pp.461-466.
- Murr, L.E. and Ramirez, D.A., 2012. The microstructure of the cultured freshwater pearl. *JOM*, 64, pp.469-474.
- Muzzarelli, R.R.A., Praiser, E.R., et al., 1978. *Proceedings of the 1st International Conference on Chitin Chitosan*. MIT Press.
- Nagano, M., Nakamura, T., Kokubo, T., Tanahashi, M. and Ogawa, M., 1996. Differences of bone bonding ability and degradation behaviour in vivo between amorphous calcium phosphate and highly crystalline hydroxyapatite coating. *Biomaterials*, 17(18), pp.1771-1777.
- Negm, N.A., Hefni, H.H., Abd-Elaal, A.A., Badr, E.A. and Abou Kana, M.T., 2020. Advancement on modification of chitosan biopolymer and its potential applications. *International journal of biological macromolecules*, 152, pp.681-702.
- Neira, I.S., Kolen'ko, Y.V., Lebedev, O.I., Van Tendeloo, G., Gupta, H.S., Guitián, F. and Yoshimura, M., 2009. An effective morphology control of hydroxyapatite crystals via hydrothermal synthesis. *crystal growth and design*, 9(1), pp.466-474.
- Nelson, M., Balasundaram, G. and Webster, T.J., 2006. Increased osteoblast adhesion on nanoparticulate crystalline hydroxyapatite functionalized with KRSR. *International journal of nanomedicine*, 1(3), p.339.
- Ni, M. and Ratner, B.D., 2003. Nacre surface transformation to hydroxyapatite in a phosphate buffer solution. *Biomaterials*, 24(23), pp.4323-4331.
- Odgaard, A. and Linde, F., 1991. The underestimation of Young's modulus in compressive testing of cancellous bone specimens. *Journal of biomechanics*, 24(8), pp.691-698.
- Oh, S.H., Park, I.K., Kim, J.M. and Lee, J.H., 2007. In vitro and in vivo characteristics of PCL scaffolds with pore size gradient fabricated by a centrifugation method. *Biomaterials*, 28(9), pp.1664-1671.
- Omelson, S., Georgiou, J., Henneman, Z.J., Wise, L.M., Sukhu, B., Hunt, T., Wynnyckyj, C., Holmyard, D., Bielecki, R. and Grynpas, M.D., 2009. Control of vertebrate skeletal mineralization by polyphosphates. *PLoS One*, 4(5), p.e5634.

Ong, S.R., Trabbic-Carlson, K.A., Nettles, D.L., Lim, D.W., Chilkoti, A. and Setton, L.A., 2006. Epitope tagging for tracking elastin-like polypeptides. *Biomaterials*, 27(9), pp.1930-1935.

Orriss, I.R., Utting, J.C., Brandao-Burch, A., Colston, K., Grubb, B.R., Burnstock, G. and Arnett, T.R., 2007. Extracellular nucleotides block bone mineralization in vitro: evidence for dual inhibitory mechanisms involving both P2Y2 receptors and pyrophosphate. *Endocrinology*, 148(9), pp.4208-4216.

Pallu, S., Rochefort, G.Y., Jaffre, C., Refregiers, M., Maurel, D.B., Benaitreau, D., Lespessailles, E., Jamme, F., Chappard, C. and Benhamou, C.L., 2012. Synchrotron ultraviolet microspectroscopy on rat cortical bone: involvement of tyrosine and tryptophan in the osteocyte and its environment.

Palomino, J.C. and Portaels, F., 1999. Simple procedure for drug susceptibility testing of *Mycobacterium tuberculosis* using a commercial colorimetric assay. *European Journal of Clinical Microbiology and Infectious Diseases*, 18, pp.380-383.

Park, B.K. and Kim, M.M., 2010. Applications of chitin and its derivatives in biological medicine. *International journal of molecular sciences*, 11(12), pp.5152-5164.

Parker, J.E., Thompson, S.P., Lennie, A.R., Potter, J. and Tang, C.C., 2010. A study of the aragonite-calcite transformation using Raman spectroscopy, synchrotron powder diffraction and scanning electron microscopy. *CrystEngComm*, 12(5), pp.1590-1599.

Pei, J., Wang, Y., Zou, X., Ruan, H., Tang, C., Liao, J., Si, G. and Sun, P., 2021. Extraction, purification, bioactivities and application of matrix proteins from pearl powder and nacre powder: a review. *Frontiers in Bioengineering and Biotechnology*, 9, p.649665.

Peppas, N.A. and Langer, R., 1994. New challenges in biomaterials. *Science*, 263(5154), pp.1715-1720.

Peretz, H., Talpalar, A.E., Vago, R. and Baranes, D., 2007. Superior survival and durability of neurons and astrocytes on 3-dimensional aragonite biomatrices. *Tissue engineering*, 13(3), pp.461-472.

Petite, H., Viateau, V., Bensaid, W., Meunier, A., de Pollak, C., Bourguignon, M., Oudina, K., Sedel, L. and Guillemain, G., 2000. Tissue-engineered bone regeneration. *Nature biotechnology*, 18(9), pp.959-963.

Petrie Aronin, C.E., Sadik, K.W., Lay, A.L., Rion, D.B., Tholpady, S.S., Ogle, R.C. and Botchwey, E.A., 2009. Comparative effects of scaffold pore size, pore volume, and total void volume on cranial bone healing patterns using microsphere-based scaffolds. *Journal of Biomedical Materials Research Part A: An Official Journal of The Society for Biomaterials, The Japanese Society for Biomaterials, and The*

Australian Society for Biomaterials and the Korean Society for Biomaterials, 89(3), pp.632-641.

Pezeshki-Modaress, M., Zandi, M. and Rajabi, S., 2018. Tailoring the gelatin/chitosan electrospun scaffold for application in skin tissue engineering: an in vitro study. *Progress in biomaterials*, 7, pp.207-218.

Place, E.S., Evans, N.D. and Stevens, M.M., 2009. Complexity in biomaterials for tissue engineering. *Nature materials*, 8(6), pp.457-470.

Posner, A.S. and Betts, F., 1975. Synthetic amorphous calcium phosphate and its relation to bone mineral structure. *Accounts of Chemical Research*, 8(8), pp.273-281.

Proff, P. and Römer, P., 2009. The molecular mechanism behind bone remodelling: a review. *Clinical oral investigations*, 13, pp.355-362.

Qasim, S.B., Delaine-Smith, R.M., Fey, T., Rawlinson, A. and Rehman, I.U., 2015. Freeze gelled porous membranes for periodontal tissue regeneration. *Acta biomaterialia*, 23, pp.317-328.

Qiao, L., Feng, Q.L. and Li, Z., 2007. Special vaterite found in freshwater lackluster pearls. *Crystal growth & design*, 7(2), pp.275-279.

Raafat, D., Von Bargaen, K., Haas, A. and Sahl, H.G., 2008. Insights into the mode of action of chitosan as an antibacterial compound. *Applied and environmental microbiology*, 74(12), pp.3764-3773.

Rau, J.V., Cesaro, S.N., Ferro, D., Barinov, S.M. and Fadeeva, I.V., 2004. FTIR study of carbonate loss from carbonated apatites in the wide temperature range. *Journal of Biomedical Materials Research Part B: Applied Biomaterials: An Official Journal of The Society for Biomaterials, The Japanese Society for Biomaterials, and The Australian Society for Biomaterials and the Korean Society for Biomaterials*, 71(2), pp.441-447.

Raynaud, S., Champion, E., Bernache-Assollant, D. and Thomas, P., 2002. Calcium phosphate apatites with variable Ca/P atomic ratio I. Synthesis, characterisation and thermal stability of powders. *Biomaterials*, 23(4), pp.1065-1072.

Rehman, I. and Bonfield, W.J.J., 1997. Characterization of hydroxyapatite and carbonated apatite by photo acoustic FTIR spectroscopy. *Journal of Materials Science: Materials in Medicine*, 8, pp.1-4.

Ren, F., Wan, X., Ma, Z. and Su, J., 2009. Study on microstructure and thermodynamics of nacre in mussel shell. *Materials chemistry and physics*, 114(1), pp.367-370.

Rey, C., Collins, B., Goehl, T., Dickson, I.R. and Glimcher, M.J., 1989. The carbonate environment in bone mineral: a resolution-enhanced Fourier transform infrared spectroscopy study. *Calcified tissue international*, 45, pp.157-164.

- Rho, J.Y., Ashman, R.B. and Turner, C.H., 1993. Young's modulus of trabecular and cortical bone material: ultrasonic and microtensile measurements. *Journal of biomechanics*, 26(2), pp.111-119.
- Rho, J.Y., Kuhn-Spearing, L. and Zioupos, P., 1998. Mechanical properties and the hierarchical structure of bone. *Medical engineering & physics*, 20(2), pp.92-102.
- Ribatti, D., Vacca, A., Roncali, L. and Dammacco, F., 2004. The chick embryo chorioallantoic membrane as a model for in vivo research on angiogenesis. *International Journal of Developmental Biology*, 40(6), pp.1189-1197.
- Richards, L., 1951. *Integument of arthropods*. U of Minnesota Press.
- Ripps, H. and Shen, W., 2012. taurine: a “very essential” amino acid. *Molecular vision*, 18, p.2673.
- Rodan, G.A. and Martin, T.J., 2000. Therapeutic approaches to bone diseases. *Science*, 289(5484), pp.1508-1514.
- Roman, D.L., Ostafe, V. and Isvoran, A., 2020. Deeper inside the specificity of lysozyme when degrading chitosan. A structural bioinformatics study. *Journal of Molecular Graphics and Modelling*, 100, p.107676.
- Roohani, I., Cheong, S. and Wang, A., 2021. How to build a bone?-Hydroxyapatite or Posner’s clusters as bone minerals. *Open Ceramics*, 6, p.100092.
- Rustom, L.E., Poellmann, M.J. and Johnson, A.J.W., 2019. Mineralization in micropores of calcium phosphate scaffolds. *Acta Biomaterialia*, 83, pp.435-455.
- Rutkovskiy, A., Stensløkken, K.O. and Vaage, I.J., 2016. Osteoblast differentiation at a glance. *Medical science monitor basic research*, 22, p.95.
- Sadat-Shojai, M., Khorasani, M.T., Dinpanah-Khoshdargi, E. and Jamshidi, A., 2013. Synthesis methods for nanosized hydroxyapatite with diverse structures. *Acta biomaterialia*, 9(8), pp.7591-7621.
- Sambudi, N.S., Sathyamurthy, M., Lee, G.M. and Park, S.B., 2015. Electrospun chitosan/poly (vinyl alcohol) reinforced with CaCO₃ nanoparticles with enhanced mechanical properties and biocompatibility for cartilage tissue engineering. *Composites Science and Technology*, 106, pp.76-84.
- Sarhan, W.A., Azzazy, H.M. and El-Sherbiny, I.M., 2016. Honey/chitosan nanofiber wound dressing enriched with *Allium sativum* and *Cleome droserifolia*: enhanced antimicrobial and wound healing activity. *ACS applied materials & interfaces*, 8(10), pp.6379-6390.
- Sari, M., Hening, P., Ana, I.D. and Yusuf, Y., 2021. Porous structure of bioceramics carbonated hydroxyapatite-based honeycomb scaffold for bone tissue engineering. *Materials Today Communications*, 26, p.102135.

- Saruwatari, K., Matsui, T., Mukai, H., Nagasawa, H. and Kogure, T., 2009. Nucleation and growth of aragonite crystals at the growth front of nacles in pearl oyster, *Pinctada fucata*. *Biomaterials*, 30(16), pp.3028-3034.
- Salinas, A.J., Esbrit, P. and Vallet-Regí, M., 2013. A tissue engineering approach based on the use of bioceramics for bone repair. *Biomaterials Science*, 1(1), pp.40-51.
- Schaffer, S.W., Azuma, J. and Mozaffari, M., 2009. Role of antioxidant activity of taurine in diabetes. *Canadian journal of physiology and pharmacology*, 87(2), pp.91-99.
- Schick, C., 2009. Differential scanning calorimetry (DSC) of semicrystalline polymers. *Analytical and bioanalytical chemistry*, 395, pp.1589-1611.
- Schlesinger, P.H., Blair, H.C., Teitelbaum, S.L. and Edwards, J.C., 1997. Characterization of the osteoclast ruffled border chloride channel and its role in bone resorption. *Journal of Biological Chemistry*, 272(30), pp.18636-18643.
- Schreiber, S.B., Bozell, J.J., Hayes, D.G. and Zivanovic, S., 2013. Introduction of primary antioxidant activity to chitosan for application as a multifunctional food packaging material. *Food Hydrocolloids*, 33(2), pp.207-214.
- Shah, F.A., Snis, A., Matic, A., Thomsen, P. and Palmquist, A., 2016. 3D printed Ti6Al4V implant surface promotes bone maturation and retains a higher density of less aged osteocytes at the bone-implant interface. *Acta biomaterialia*, 30, pp.357-367.
- Shariatnia, Z., 2018. Carboxymethyl chitosan: Properties and biomedical applications. *International journal of biological macromolecules*, 120, pp.1406-1419.
- Shen, S., 2011. *Preparation method of nano pearl powder-modified nano hydroxyapatite*. China National Intellectual Property Administration Patent no. CN2011103987492A. Available at: <https://patents.google.com/patent/CN102416199A/en> (Accessed at: 17 June 2020)
- Shen, Y., et al., 2018. *The composite material of pearl powder/PEEK quasi natural bone, its preparation method and applications*. China National Intellectual Property Administration Patent no. CN200610114415. Available at: <https://patents.google.com/patent/CN1943800A/en> (Accessed at: 1 June 2022)
- Shively, S. and Miller, W.R., 2009. The use of HMDS (hexamethyldisilazane) to replace critical point drying (CPD) in the preparation of tardigrades for SEM (scanning electron microscope) imaging. *Transactions of the Kansas Academy of Science*, 112(4), pp.198-200.
- Siddiqi, S.A., Azhar, U., Manzoor, F., Jamal, A., Tariq, M., Saleem, M., Chaudhry, A.A. and Rehman, I.U., 2018. FABRICATION OF BIOCOMPATIBLE NANO-

CARBONATED HYDROXYAPATITE/POLYMER SPONGY SCAFFOLDS. *Digest Journal of Nanomaterials & Biostructures (DJNB)*, 13(2).

Ślósarczyk, A., Paszkiewicz, Z. and Paluszkiewicz, C., 2005. FTIR and XRD evaluation of carbonated hydroxyapatite powders synthesized by wet methods. *Journal of Molecular Structure*, 744, pp.657-661.

Sokolova, V., Kovtun, A., Prymak, O., Meyer-Zaika, W., Kubareva, E.A., Romanova, E.A., Oretskaya, T.S., Heumann, R. and Epple, M., 2007. Functionalisation of calcium phosphate nanoparticles by oligonucleotides and their application for gene silencing. *Journal of Materials Chemistry*, 17(8), pp.721-727.

Sønju Clasen, A.B. and Ruyter, I.E., 1997. Quantitative determination of type A and type B carbonate in human deciduous and permanent enamel by means of Fourier transform infrared spectrometry. *Advances in Dental Research*, 11(4), pp.523-527.

Steele, D.G. and Bramblett, C.A., 1988. *The anatomy and biology of the human skeleton*. Texas A&M University Press.

Sudarsanan, K.T. and Young, R.A., 1969. Significant precision in crystal structural details. Holly Springs hydroxyapatite. *Acta Crystallographica Section B: Structural Crystallography and Crystal Chemistry*, 25(8), pp.1534-1543.

Sun, T., Zhou, D., Mao, F. and Zhu, Y., 2007. Preparation of low-molecular-weight carboxymethyl chitosan and their superoxide anion scavenging activity. *European polymer journal*, 43(2), pp.652-656.

Sun, J. and Bhushan, B., 2012. Hierarchical structure and mechanical properties of nacre: a review. *Rsc Advances*, 2(20), pp.7617-7632.

Taboas, J.M., Maddox, R.D., Krebsbach, P.H. and Hollister, S.J., 2003. Indirect solid free form fabrication of local and global porous, biomimetic and composite 3D polymer-ceramic scaffolds. *Biomaterials*, 24(1), pp.181-194.

Thorpe, T.A., 2007. History of plant tissue culture. *Molecular biotechnology*, 37, pp.169-180.

Timchenko, P.E., Timchenko, E.V., Frolov, O.O., Volova, L.T. and Pisareva, E.V., 2018, October. Detailed Analysis of Raman Spectra for Express Assessment of the Hydroxyapatite Quality. In *2018 IEEE International Conference on Electrical Engineering and Photonics (EExPolytech)* (pp. 233-235). IEEE.

Tomihata, K. and Ikada, Y., 1997. In vitro and in vivo degradation of films of chitin and its deacetylated derivatives. *Biomaterials*, 18(7), pp.567-575.

Toriyama, M., Ravaglioli, A., Krajewski, A., Celotti, G. and Piancastelli, A., 1996. Synthesis of hydroxyapatite-based powders by mechano-chemical method and their sintering. *Journal of the European Ceramic society*, 16(4), pp.429-436.

- Tsuchida, T., Kubo, J., Yoshioka, T., Sakuma, S., Takeguchi, T. and Ueda, W., 2008. Reaction of ethanol over hydroxyapatite affected by Ca/P ratio of catalyst. *Journal of Catalysis*, 259(2), pp.183-189.
- Turnbull, G., Clarke, J., Picard, F., Riches, P., Jia, L., Han, F., Li, B. and Shu, W., 2018. 3D bioactive composite scaffolds for bone tissue engineering. *Bioactive materials*, 3(3), pp.278-314.
- Turner, C.H., 2006. Bone strength: current concepts. *Annals of the New York Academy of Sciences*, 1068(1), pp.429-446.
- Urist, M.R., Huo, Y.K., Brownell, A.G., Hohl, W.M., Buyske, J., Lietze, A., Tempst, P., Hunkapiller, M. and DeLange, R.J., 1984. Purification of bovine bone morphogenetic protein by hydroxyapatite chromatography. *Proceedings of the National Academy of Sciences*, 81(2), pp.371-375.
- Urmos, J., Sharma, S.K. and Mackenzie, F.T., 1991. Characterization of some biogenic carbonates with Raman spectroscopy. *American Mineralogist*, 76(3-4), pp.641-646.
- Venkatesan, J. and Kim, S.K., 2010. Chitosan composites for bone tissue engineering—an overview. *Marine drugs*, 8(8), pp.2252-2266.
- Vignoles, M., Bonel, G., Holcomb, D.W. and Young, R.A., 1988. Influence of preparation conditions on the composition of type B carbonated hydroxyapatite and on the localization of the carbonate ions. *Calcified Tissue International*, 43, pp.33-40.
- Wan, Y., Wu, H., Cao, X. and Dalai, S., 2008. Compressive mechanical properties and biodegradability of porous poly (caprolactone)/chitosan scaffolds. *Polymer Degradation and Stability*, 93(10), pp.1736-1741.
- Wang, M., Joseph, R. and Bonfield, W., 1998. Hydroxyapatite-polyethylene composites for bone substitution: effects of ceramic particle size and morphology. *Biomaterials*, 19(24), pp.2357-2366.
- Wang, Y., Zhang, S., Wei, K., Zhao, N., Chen, J. and Wang, X., 2006. Hydrothermal synthesis of hydroxyapatite nanopowders using cationic surfactant as a template. *Materials Letters*, 60(12), pp.1484-1487.
- Wang, W., Zhao, L., Ma, Q., Wang, Q., Chu, P.K. and Zhang, Y., 2012. The role of the Wnt/ β -catenin pathway in the effect of implant topography on MG63 differentiation. *Biomaterials*, 33(32), pp.7993-8002.
- Wang, W. and Yeung, K.W., 2017. Bone grafts and biomaterials substitutes for bone defect repair: A review. *Bioactive materials*, 2(4), pp.224-247.
- Wang, X., Ye, Y., Wu, X., Smyth, J.R., Yang, Y., Zhang, Z. and Wang, Z., 2019. High-temperature Raman and FTIR study of aragonite-group carbonates. *Physics and Chemistry of Minerals*, 46, pp.51-62.

Wehrmeister, U., Soldati, A.L., Jacob, D.E., Häger, T. and Hofmeister, W., 2010. Raman spectroscopy of synthetic, geological and biological vaterite: a Raman spectroscopic study. *Journal of Raman Spectroscopy: An International Journal for Original Work in all Aspects of Raman Spectroscopy, Including Higher Order Processes, and also Brillouin and Rayleigh Scattering*, 41(2), pp.193-201.

Wei, G. and Ma, P.X., 2004. Structure and properties of nano-hydroxyapatite/polymer composite scaffolds for bone tissue engineering. *Biomaterials*, 25(19), pp.4749-4757.

Westendorf, J.J., Kahler, R.A. and Schroeder, T.M., 2004. Wnt signaling in osteoblasts and bone diseases. *Gene*, 341, pp.19-39.

Wieland, H.A., Michaelis, M., Kirschbaum, B.J. and Rudolphi, K.A., 2005. Osteoarthritis—an untreatable disease?. *Nature reviews Drug discovery*, 4(4), pp.331-344.

WikiJournal of Medicine. 2014. *Anatomy of a long bone*. Available at: https://en.wikiversity.org/wiki/WikiJournal_of_Medicine/Medical_gallery_of_Blausen_Medical_2014 (Accessed: 12 May 2020).

Willmer, E.N. ed., 2015. *Cells and tissues in culture: methods, biology and physiology*. Elsevier.

Wisniak, J., 2012. Antoine Alexandre Brutus Bussy. *Revista CENIC. Ciencias Químicas*, 43.

Woranuch, S. and Yoksan, R., 2013. Preparation, characterization and antioxidant property of water-soluble ferulic acid grafted chitosan. *Carbohydrate polymers*, 96(2), pp.495-502.

Wortman, J.J. and Evans, R.A., 1965. Young's modulus, shear modulus, and Poisson's ratio in silicon and germanium. *Journal of applied physics*, 36(1), pp.153-156.

Wu, D., Isaksson, P., Ferguson, S.J. and Persson, C., 2018. Young's modulus of trabecular bone at the tissue level: A review. *Acta biomaterialia*, 78, pp.1-12.

Wu, Y., Ding, Z., Ren, H., Ji, M. and Yan, Y., 2019. Preparation, characterization and in vitro biological evaluation of a novel pearl powder/poly-amino acid composite as a potential substitute for bone repair and reconstruction. *Polymers*, 11(5), p.831.

Xiao, W.D., Zhong, Z.M., Tang, Y.Z., Xu, Z.X., Xu, Z. and Chen, J.T., 2012. Repair of critical size bone defects with porous poly (D, L-lactide)/nacre nanocomposite hollow scaffold. *Saudi medical journal*, 33(6), pp.601-607.

Xing, R., Liu, S., Guo, Z., Yu, H., Wang, P., Li, C., Li, Z. and Li, P., 2005. Relevance of molecular weight of chitosan and its derivatives and their antioxidant activities in vitro. *Bioorganic & medicinal chemistry*, 13(5), pp.1573-1577.

Yan, L., Li, Y., Deng, Z.X., Zhuang, J. and Sun, X., 2001. Surfactant-assisted hydrothermal synthesis of hydroxyapatite nanorods. *International Journal of Inorganic Materials*, 3(7), pp.633-637.

Xu, M., Li, Y., Suo, H., Yan, Y., Liu, L., Wang, Q., Ge, Y. and Xu, Y., 2010. Fabricating a pearl/PLGA composite scaffold by the low-temperature deposition manufacturing technique for bone tissue engineering. *Biofabrication*, 2(2), p.025002.

Yang, Z., Huang, Y., Chen, S.T., Zhao, Y.Q., Li, H.L. and Hu, Z.A., 2005. Template synthesis of highly ordered hydroxyapatite nanowire arrays. *Journal of materials science*, 40, pp.1121-1125.

Yang, Y.L., Chang, C.H., Huang, C.C., Kao, W.M.W., Liu, W.C. and Liu, H.W., 2014. Osteogenic activity of nanonized pearl powder/poly (lactide-co-glycolide) composite scaffolds for bone tissue engineering. *Bio-medical materials and engineering*, 24(1), pp.979-985.

Yar, M., Shahzad, S., Siddiqi, S.A., Mahmood, N., Rauf, A., Anwar, M.S., Chaudhry, A.A. and ur Rehman, I., 2015. Triethyl orthoformate mediated a novel crosslinking method for the preparation of hydrogels for tissue engineering applications: characterization and in vitro cytocompatibility analysis. *Materials Science and Engineering: C*, 56, pp.154-164.

Yavari, S.A., van der Stok, J., Chai, Y.C., Wauthle, R., Birgani, Z.T., Habibovic, P., Mulier, M., Schrooten, J., Weinans, H. and Zadpoor, A.A., 2014. Bone regeneration performance of surface-treated porous titanium. *Biomaterials*, 35(24), 6172-6181.

Yuan, Y., Liu, C., Qian, J., Wang, J. and Zhang, Y., 2010. Size-mediated cytotoxicity and apoptosis of hydroxyapatite nanoparticles in human hepatoma HepG2 cells. *Biomaterials*, 31(4), pp.730-740.

Yui, T., Kobayashi, H., Kitamura, S. and Imada, K., 1994. Conformational analysis of chitobiose and chitosan. *Biopolymers: Original Research on Biomolecules*, 34(2), pp.203-208.

Zakaria, F.Z., Mihály, J., Sajó, I., Katona, R., Hajba, L., Aziz, F.A. and Mink, J., 2008. FT-Raman and FTIR spectroscopic characterization of biogenic carbonates from Philippine venus seashell and *Porites* sp. coral. *Journal of Raman Spectroscopy: An International Journal for Original Work in all Aspects of Raman Spectroscopy, Including Higher Order Processes, and also Brillouin and Rayleigh Scattering*, 39(9), pp.1204-1209.

Zeller-Plumhoff, B., Malich, C., Krüger, D., Campbell, G., Wiese, B., Galli, S., Wennerberg, A., Willumeit-Römer, R. & Wieland, D. C. F. (2019). Analysis of the bone ultrastructure around biodegradable Mg-xGd implants using small angle X-ray scattering and X-ray diffraction. *Acta Biomaterialia*, 101, 637-645.

Zeng, M., Qi, C. and Zhang, X.M., 2013. Chitosan microspheres supported palladium heterogeneous catalysts modified with pearl shell powders. *International journal of biological macromolecules*, 55, pp.240-245.

Zhang, J. and Chen, Z., 1996. Advance of research of pearls in the field of biomedicine. *Natu Prod Res and Deve*, 8(2), pp.63-68.

Zhang, R. and Ma, PX, 1999. Poly (α -hydroxyl acids)/hydroxyapatite porous composites for bone-tissue engineering. I. Preparation and morphology. *Journal of Biomedical Materials Research: An Official Journal of The Society for Biomaterials, The Japanese Society for Biomaterials, and The Australian Society for Biomaterials*, 44(4), 446-455.

Zhang, Y. and Zhang, M., 2001. Synthesis and characterization of macroporous chitosan/calcium phosphate composite scaffolds for tissue engineering. *Journal of Biomedical Materials Research: An Official Journal of The Society for Biomaterials, The Japanese Society for Biomaterials, and The Australian Society for Biomaterials and the Korean Society for Biomaterials*, 55(3), pp.304-312.

Zhang, Y. and Zhang, M., 2002. Calcium phosphate/chitosan composite scaffolds for controlled in vitro antibiotic drug release. *Journal of Biomedical Materials Research: An Official Journal of The Society for Biomaterials, The Japanese Society for Biomaterials, and The Australian Society for Biomaterials and the Korean Society for Biomaterials*, 62(3), pp.378-386.

Zhang, S., Wang, Y., Wei, K., Liu, X., Chen, J. and Wang, X., 2007. Template-assisted synthesis of lamellar mesostructured hydroxyapatites. *Materials Letters*, 61(6), pp.1341-1345.

Zhang, G., Guo, Y., Ao, J., Yang, J., Lv, G. and Shih, K., 2013. Thermally induced phase transformation of pearl powder. *Materials Science and Engineering: C*, 33(4), pp.2046-2049.

Zhang, G., Brion, A., Willemin, A.S., Piet, M.H., Moby, V., Bianchi, A., Mainard, D., Galois, L., Gillet, P. and Rousseau, M., 2017. Nacre, a natural, multi-use, and timely biomaterial for bone graft substitution. *Journal of Biomedical Materials Research Part A*, 105(2), pp.662-671.

Zhang, X., Du, X., Li, D., Ao, R., Yu, B. and Yu, B., 2018. Three dimensionally printed pearl powder/poly-caprolactone composite scaffolds for bone regeneration. *Journal of Biomaterials Science, Polymer Edition*, 29(14), pp.1686-1700.

Zhao, X., Ng, S., Heng, B.C., Guo, J., Ma, L., Tan, T.T.Y., Ng, K.W. and Loo, S.C.J., 2013. Cytotoxicity of hydroxyapatite nanoparticles is shape and cell dependent. *Archives of toxicology*, 87, pp.1037-1052.

Zheng, L.Y. and Zhu, J.F., 2003. Study on antimicrobial activity of chitosan with different molecular weights. *Carbohydrate polymers*, 54(4), pp.527-530.

Innovative incorporation of pearl and calcium phosphate composite in bone regenerative scaffolds

Zhou, J., Zhang, X., Chen, J., Zeng, S. and De Groot, K., 1993. High temperature characteristics of synthetic hydroxyapatite. *Journal of materials science: materials in medicine*, 4, pp.83-85.

Zhou, L., Ramezani, H., Sun, M., Xie, M., Nie, J., Lv, S., Cai, J., Fu, J. and He, Y., 2020. 3D printing of high-strength chitosan hydrogel scaffolds without any organic solvents. *Biomaterials Science*, 8(18), pp.5020-5028.

Zulli, A., 2011. Taurine in cardiovascular disease. *Current Opinion in Clinical Nutrition & Metabolic Care*, 14(1), pp.57-60.

Appendix A. BET (Brunauer, Emmett and Teller) analysis

The surface measurement by BET was performed on commercial HA, commercial pearl powders, synthesized HA samples and pearl/HA composite powders. Pearl/HA samples synthesized from three different strategies, as well as the HA samples, were also evaluated that the following figures demonstrate some BET plots and the table 4.2.3 included the whole information of the analysis.

In comparison with the results from the porosity estimation aforementioned, the mixture of pearl powders and HA during the synthetic process demonstrates a significant agglomeration of crystals that higher surface area was observed compared to the pure crystals.

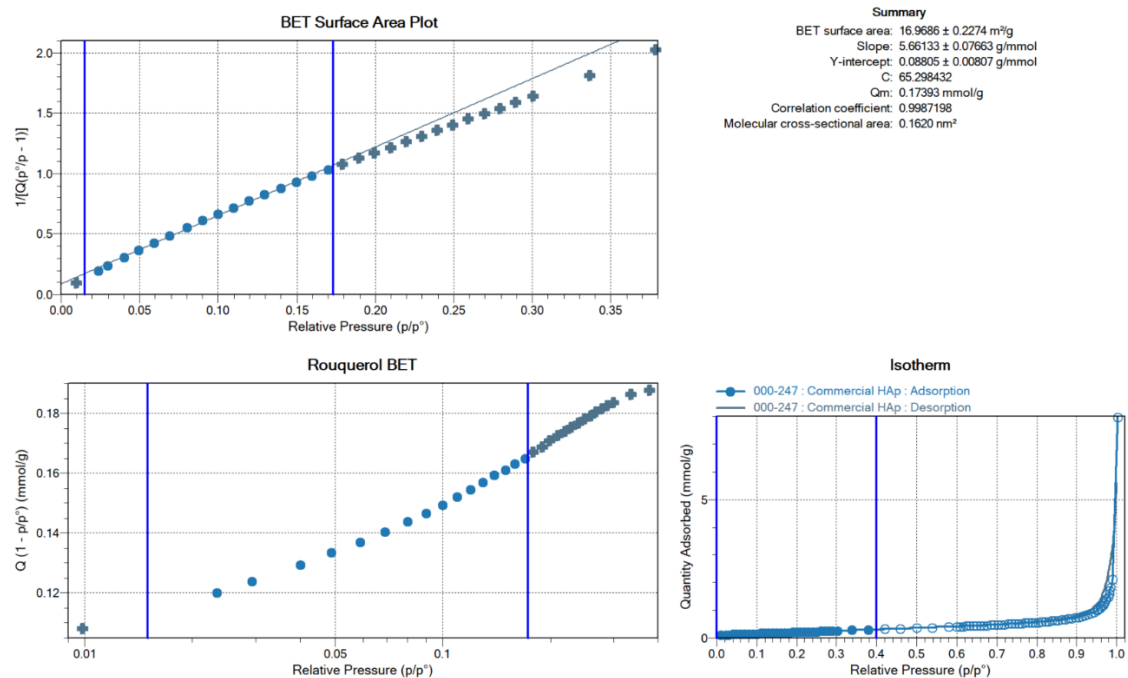


Fig. 4.2.12 Surface area measurement by BET plot of commercial HA sample using points collected at the pressure range 0.01 to 0.4 (Y-axis stands for the specific surface area, calculated from the BET equation); the Rouquerol BET plot and the isotherm BET plot. The equation of the best-fit line ($y=5.66133x+0.08805$) and R^2 (0.99871) was shown in the summary.

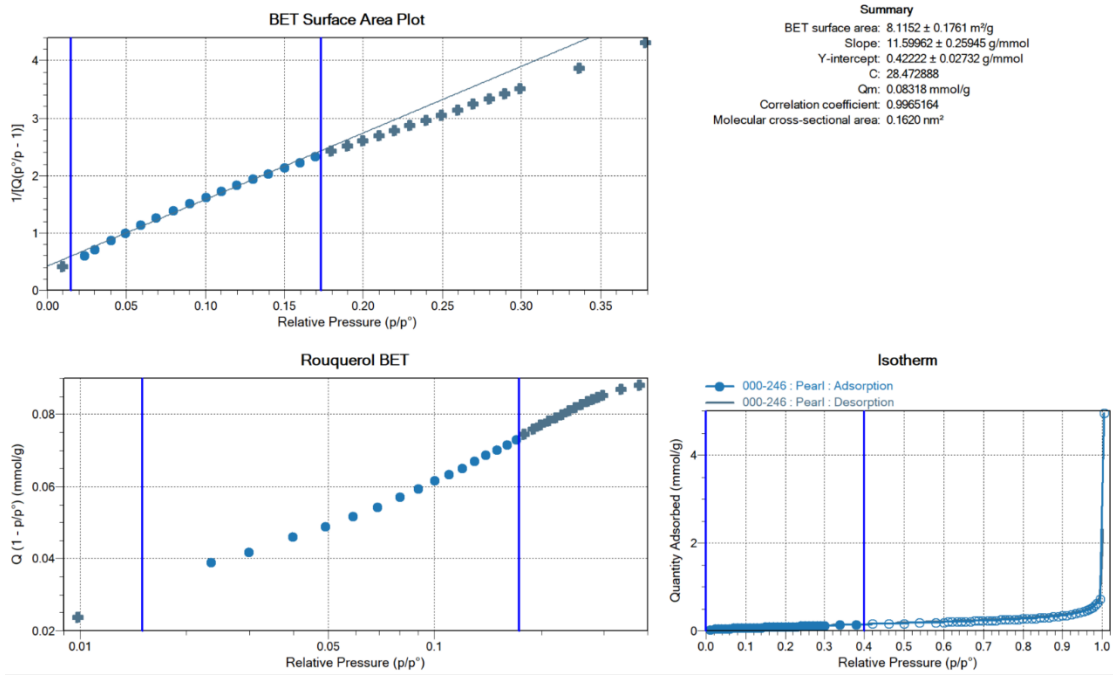


Fig. 4.2.13 Surface area measurement by BET plot of commercial pearl sample using points collected at the pressure range 0.01 to 0.4 (Y-axis stands for the specific surface area, calculated from the BET equation); the Rouquerol BET plot and the isotherm BET plot. The equation of the best-fit line ($y=11.55962x+0.422222$) and R^2 (0.99651) was shown in the summary.

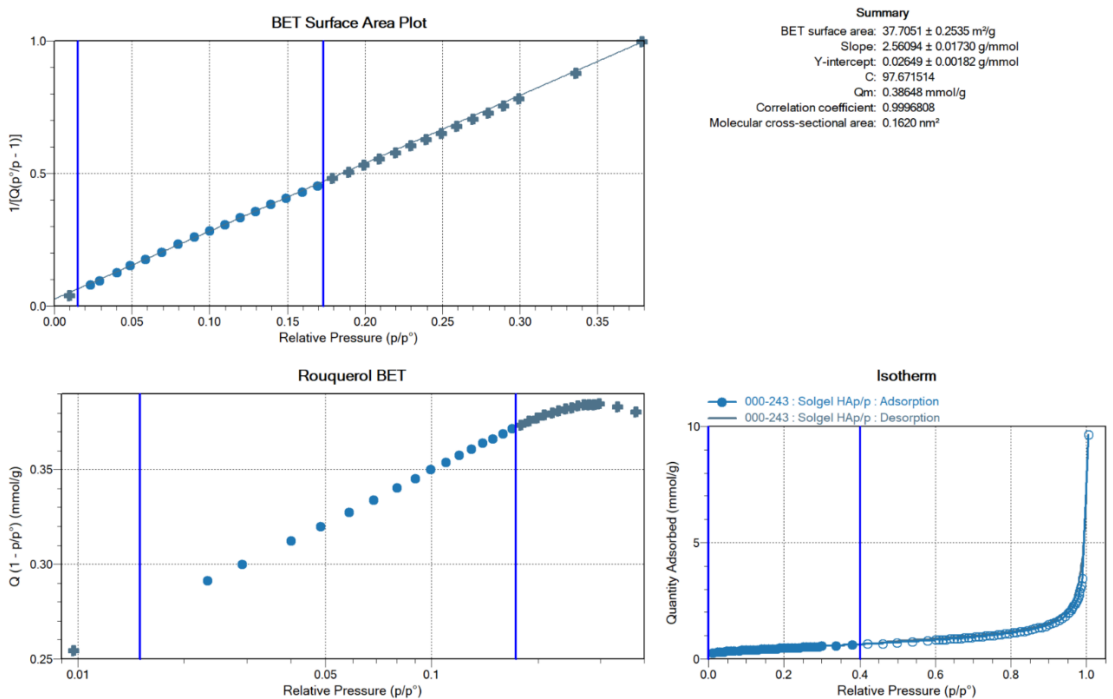


Fig. 4.2.14 Surface area measurement by BET plot of commercial p/CaP sample using points collected at the pressure range 0.01 to 0.4 (Y-axis stands for the specific surface area, calculated from the BET equation); the Rouquerol BET plot and the isotherm BET plot. The equation of the best-fit line ($y=2.56094x+0.026489$) and R^2 (0.99968) was shown in the summary.

Appendix A: Bibliography

Table 4.2.3 BET results of commercial HA, pearl, synthesized HA and pearl/HA composites.

Sample names	BET surface area (m ² /g)	specific area (g/cm ³)	density	Average pore radius (nm)
Commercial HA	16.99 ± 0.23	3.17		1.62
Pearl	8.12 ± 0.18	2.73		1.98
Precipitation HA	18.74 ± 0.26	3.16		1.73
Sol-gel HA	17.23 ± 0.35	3.18		1.68
Hydrothermal HA	17.79 ± 0.28	3.15		1.68
Precipitation pearl/HA	38.23 ± 0.19	2.95		1.72
Sol-gel pearl/HA	37.71 ± 0.25	2.97		1.67
Hydrothermal pearl/HA	37.74 ± 0.22	2.93		1.70